

MINISTRY OF EDUCATION AND SCIENCE, YOUTH AND SPORT OF UKRAINE

Odessa I. I. Mechnikov National University

PHOTO ELECTRONICS

PHOTOELECTRONICS
INTER-UNIVERSITIES SCIENTIFIC ARTICLES

Founded in 1986

Number 20

Odessa
«Astroprint»
2011

«PHOTOELECTRONICS»

No 20 — 2011

INTER-UNIVERSITIES
SCIENTIFIC ARTICLES

Founded in 1986

Certificate of State Registration
KB No 15953

«ФОТОЭЛЕКТРОНИКА»

№ 20 — 2011

МЕЖВЕДОМСТВЕННЫЙ
НАУЧНЫЙ СБОРНИК

Основан в 1986 г.

Свидетельство
о Государственной регистрации
KB № 15953

The results of theoretical and experimental studies in problems of the semiconductor and micro-electronic devices physics, opto- and quantum electronics, quantum optics, spectroscopy and photophysics of nucleus, atoms, molecules and solids are presented in the issue. New directions in the photoelectronics, stimulated by problems of the super intense laser radiation interaction with nuclei, atomic systems and substance, are considered. Scientific articles «Photoelectronics» collection abstracted in ВИНІТИ and «Джерело».

The issue is introduced to the List of special editions of the Ukrainian Higher Certification Commission in physics-mathematics and technical sciences.

For lecturers, scientists, post-graduates and students.

У збірнику наведено результати теоретичних і експериментальних досліджень з питань фізики напівпровідників та мікроелектронних приладів, опти- та квантової електроніки, квантової оптики, спектроскопії та фотофізики ядра, атомів, молекул та твердих тіл. Розглянуто нові напрямки розвитку фотоелектроніки, пов'язані із задачами взаємодії надінтенсивного лазерного випромінювання з ядром, атомними системами, речовиною.

Збірник включено до Переліку спеціальних видань ВАК України з фізико-математичних та технічних наук. Збірник «Photoelectronics» реферується у ВІНІТИ (Москва) та «Джерело» (Київ).

Для викладачів, наукових працівників, аспірантів, студентів.

В сборнике приведены результаты теоретических и экспериментальных исследований по вопросам физики полупроводников и микроэлектронных приборов, опти- и квантовой электроники, квантовой оптики, спектроскопии и фотофизики ядра, атомов, молекул и твердых тел. Рассмотрены новые направления развития фотоэлектроники, связанные с задачами взаимодействия сверхинтенсивного лазерного излучения с ядром, атомными системами, веществом.

Сборник включен в Список специальных изданий ВАК Украины по физико-математическим и техническим наукам. Сборник «Photoelectronics» реферируется в ВИНІТИ (Москва) и «Джерело» (Київ).

Для преподавателей, научных работников, аспирантов, студентов.

Editorial board «Photoelectronics»:

Editor-in-Chief **V. A. Smyntyna**

Kutalova M. I. (Odessa, Ukraine, responsible editor);

Vaxman Yu. F. (Odessa, Ukraine);

Litovchenko V. G. (Kiev, Ukraine);

Gulyaev Yu. V. (Moscow, Russia);

D'Amiko A. (Rome, Italy)

Mokrickiy V. A. (Odessa, Ukraine);

Neizvestny I. G. (Novosibirsk, Russia);

Starodub N. F. (Kiev, Ukraine);

Vikulin I. M. (Odessa, Ukraine)

Address of editorial board:

Odessa I. I. Mechnikov National University 42, Pasteur str., Odessa, 65026, Ukraine

e-mail: wadz@mail.ru, tel.: +38-0482-7266356.

Information is on the site: <http://www.photoelectronics.onu.edu.ua>

TABLE OF CONTENTS

<i>K. V. Avdonin.</i> Integral representation of quasirelativistic wave equation and Dirac equation for an electron in periodic field.....	4
<i>A. Tereschenko, A. Kusevitch, R. Viter, V. Smyntyna, J. Buk, J. M. Macak, A. Gurov, I. Konup, S. Gevuluk.</i> Optical and structural properties of TiO ₂ nanofibers prepared by the electrospinning method.....	8
<i>O. Yu. Khetselius.</i> Determination of the hyperfine and electroweak interactions parameters and parity non-conservation amplitudes in heavy atoms and nuclei within nuclear-qed theory.....	12
<i>O. I. Konopelnyk, O. I. Aksimentyeva.</i> Thermochromic effect in conducting polyaminoarenes.....	18
<i>A. S. Melnik, Y. N. Karakis, M. I. Kutalova, G. G. Chemeresjuk.</i> Features of thermo-optical transitions from the re-combinational centers excited states.....	23
<i>D. A. Andrusenko, R. M. Burbelo, A. G. Kuzmich, S. A. Alekseev.</i> Photoacoustic transformation in “porous silicon — fluid” composite systems: influences of fluid motion.....	29
<i>O. I. Vlasenko, V. P. Veleschuk, M. P. Kisseluk, O. V. Lyashenko.</i> Changes in electrophysical characteristics of InGaN/GaN heterostructures of high power light-emitting diodes at increased current.....	33
<i>A. V. Loboda, G. P. Prepelitsa, A. A. Svinarenko.</i> Positron-atom collisional spectroscopy: energy approach.....	40
<i>F. O. Ptashchenko, O. O. Ptashchenko, G. V. Dovganyuk.</i> Negative sensitivity of silicon <i>p—n</i> junctions as gas sensors.....	44
<i>V. V. Halyan, A. H. Kevshyn, G. Ye. Davydyuk, M. V. Shevchuk, S. V. Voronyuk.</i> The features of infrared photoluminescence in glasses of the system Ag _{0.05} Ga _{0.05} Ge _{0.95} S ₂ —Er ₂ S ₃ at various intensity and wavelength of excitation....	49
<i>V. V. Kovalchuk.</i> The optical properties, stability and reactivity of solid nanocluster subsystem.....	53
<i>A. V. Glushkov, A. P. Fedchuk, P. A. Kondratenko, Ya. I. Lepikh, Yu. M. Lopatkin, A. A. Svinarenko.</i> The green’s functions and density functional approach to vibrational structure in the photoelectronic spectra: molecules of CH ₄ , HF.....	58
<i>V. A. Smyntyna, O. A. Kulinich, I. R. Iatsunskyi, I. A. Marchuk, N. N. Pavlenko.</i> Investigation of nanostructured silicon surfaces using fractal analysis.....	63
<i>Yu. A. Nitsuk.</i> Influence of 3d-impurities (Cr, Fe, Co, Ni) on the position of absorption edge in zinc chalcogenides.....	67
<i>A. S. Kvasikova, A. V. Ignatenko, T. A. Florko, D. E. Sukharev, Yu. G. Chernyakova.</i> Photoeffect and spectroscopy of the hydrogen atom in the crossed dc electric and magnetic field.....	71
<i>O. V. Bondarenko, D. M. Stepanov, O. M. Stastchuk.</i> Technique of determination of modules tube diameter and possible lengthening of optical cables construction.....	76
<i>M. V. Chizhov, M. V. Eingorn.</i> The electrostatic field in the two-dimensional region between uneven electrodes.....	81
<i>Sh. D. Kurmashev, I. M. Vikulin, A. I. Nimtsoviich.</i> Saturation current of the thermosensitive field-effect transistors under β -irradiation.....	86
<i>A. V. Glushkov, A. A. Svinarenko, A. V. Ignatenko.</i> Spectroscopy of autoionization resonances in spectra of the lanthanides atoms.....	90
<i>A. V. Ignatenko.</i> Microwave ionization of lithium rydberg atoms: link of quasiscrete states with continuum.....	95
<i>T. A. Florko.</i> Determination of the radiative transition characteristics in spectra of heavy ions: relativistic scheme.....	99
<i>L. V. Nikola.</i> Resonant auger spectroscopy of the atoms of inert gases.....	104
<i>I. N. Serga.</i> Electromagnetic and strong interactions effects in x-ray spectroscopy of pionic atoms.....	109
<i>Yu. V. Dubrovskaya, D. E. Sukharev, L. A. Vitavetskaya.</i> Relativistic theory of the beta decay: environment and final state interaction effects.....	113
<i>N. G. Serbov, V. Kuzakon, O. Yu. Khetselius, G. P. Prepelitsa, E. P. Solyanikova.</i> Non-linear analysis methods of signal’s temporal series in modeling of interactions in the non-linear vibrational systems of the quantum generators type.....	117
<i>D. E. Sukharev.</i> Sensing electromagnetic and strong interactions effects in spectroscopy of kaonic atoms.....	124
<i>R. M. Balabai, E. N. Chernikova.</i> Quantum-chemical simulation of the oxidation process of ethylene glycol to glyoxal at presence of copper nanocatalysts.....	128
Information for contributors of “Photoelectronics” articles.....	134
Информация для авторов научного сборника «Photoelectronics».....	134
Інформація для авторів наукового збірника «Photoelectronics».....	135

Kyiv National University of technology and design,
01011, Ukraine, Kyiv, Nemyhovycha-Dahchenko, 2,
tel: 256-29-27, 419-32-59; e-mail: alexandrisukr@rambler.ru

INTEGRAL REPRESENTATION OF QVASIRELATIVISTIC WAVE EQUATION AND DIRAC EQUATION FOR AN ELECTRON IN PERIODIC FIELD

Integral representation of quasirelativistic wave equation and Dirac equations for an electron in periodic electromagnetic field is proposed. It allows finding wave functions by iterative way in some cases and obtaining information about distribution of power.

INTRODUCTION

The most complete information about means of integral equation construction corresponding to Schroedinger and Dirac equations are contained in monograph [1]. To date there are quite enough amount of works dedicated to this course. For example, in works [2–3] for case of homogeneous electric and magnetic field, which are not parallel, as well as for case of plane wave Green true functions of Klein—Gordon—Foc—and Dirac equations are received by means of Maslov canonical operator. Green function is received for combination of external electric and magnetic field with plane wave in work [4]. In this work integral equations of Fredholm type are builded corresponding quasirelativistic wave equation and Dirac equation for an electron in periodic field by means of summarizing of results of work [5].

PROBLEM STATEMENT

Quasirelativistic wave equation is as follows:

$$(\hat{H}_0 - e\varphi(\mathbf{r}))\psi(\mathbf{r}) = E\psi(\mathbf{r}), \quad (1)$$

де $\hat{H}_0 = c\sqrt{-\hbar^2\Delta + \mu^2c^2}$, laying out periodical scalar potential in fourier series:

$$e\varphi(\mathbf{r}) = v_0 + v_k \exp\{i\mathbf{k}\mathbf{r}\}, \quad (2)$$

draw an equation (1) as follows:

$$(\hat{H}_0 - \chi)\psi(\mathbf{r}) = \exp\{i\mathbf{k}\mathbf{r}\}v_k\psi(\mathbf{r}), \quad (3)$$

де $\chi = E + v_0$.

For Dirac equation we choose the follow arrays:

$$\gamma_1 = \begin{pmatrix} \sigma_1 & 0 \\ 0 & \sigma_1 \end{pmatrix}; \quad \gamma_2 = \begin{pmatrix} \sigma_2 & 0 \\ 0 & -\sigma_2 \end{pmatrix}; \quad \gamma_3 = \begin{pmatrix} \sigma_3 & 0 \\ 0 & \sigma_3 \end{pmatrix};$$

$$\gamma_4 = \begin{pmatrix} 0 & -i\sigma_2 \\ i\sigma_2 & 0 \end{pmatrix},$$

where

$$\sigma_1 = \begin{pmatrix} 0 & 1 \\ 1 & 0 \end{pmatrix}; \quad \sigma_2 = \begin{pmatrix} 0 & -i \\ i & 0 \end{pmatrix}; \quad \sigma_3 = \begin{pmatrix} 1 & 0 \\ 0 & -1 \end{pmatrix} -$$

Pauli array, then:

$$\left\{ c\gamma_\alpha \left(-i\hbar \frac{\partial}{\partial x_\alpha} - \frac{e}{c} A_\alpha \right) + \gamma_4 \mu c^2 - e\varphi \right\} \psi = E\psi, \quad (4)$$

де $\alpha = 1, 2, 3$.

Laying out components of vector potential in fourier series:

$$\frac{e}{c\hbar} A_\alpha(\mathbf{r}) = a_{\alpha,k} \exp\{i\mathbf{k}\mathbf{r}\},$$

and introducing designations as follows:

$$\hat{\mathbf{P}} = -i\gamma_\alpha \frac{\partial}{\partial x_\alpha}; \quad \mathfrak{D} = \frac{E + v_0}{c\hbar}; \quad \eta = \frac{\mu c}{\hbar};$$

$$\omega_0 = \mathfrak{D}\mathbf{I} - \eta\gamma_4; \quad \omega_k = \gamma_\alpha a_{\alpha,k} + \mathbf{I}v_k,$$

where \mathbf{I} — unit matrix, $\mathbf{u}(\mathbf{r}) = \omega_k \exp\{i\mathbf{k}\mathbf{r}\}$, writ down the equation (4) as follows:

$$(\hat{\mathbf{P}} - \omega_0)\psi = \mathbf{u}(\mathbf{r})\psi. \quad (5)$$

Translation vector for potential would be designated using $\lambda = \{\lambda_1, \lambda_2, \lambda_3\}$.

INTEGRAL REPRESENTATION OF QVASIRELATIVISTIC WAVE EQUATION

Let vector $\mathbf{m} = \left\{ \frac{2\pi m_1}{\lambda_1}, \frac{2\pi m_2}{\lambda_2}, \frac{2\pi m_3}{\lambda_3} \right\}$, where

m_1, m_2, m_3 — whole numbers, satisfied condition:

$$g_m = \chi, \quad (6)$$

де $g_m = c\sqrt{\hbar^2 m^2 + \mu^2 c^2}$, then free addend in integral equation could be choosed as simple plane wave: $\exp\{i\mathbf{m}\mathbf{r}\}$, since

$$\{\hat{H}_0 - \chi\} \exp\{i\mathbf{m}\mathbf{r}\} = 0. \quad (7)$$

Let examine the equation:

$$\psi = \exp\{i\mathbf{m}\mathbf{r}\} + \frac{\exp\{i(\mathbf{k}' + \mathbf{k})\mathbf{r}\}v_k B_k}{g_{\mathbf{k}+\mathbf{k}} - g_m}, \quad (8)$$

where B_k — expansion coefficient in fourier series of wave $\psi(\mathbf{r})$.

Acting on both parts of the expression (8) by operator $\{\hat{H}_0 - \chi\}$ we have:

$$\{\hat{H}_0 - \chi\}\psi = v_k B_k \exp\{i(\mathbf{k}' + \mathbf{k})\mathbf{r}\} = \exp\{i\mathbf{k}\mathbf{r}\}v_k \psi.$$

Let substitute in expression (8) instead of fourier series ratios their presentation through original function:

$$v_k = \frac{e}{V} \int_0^\lambda \varphi(\rho) \exp\{-i\mathbf{k}\rho\} d\rho;$$

$$B_k = \frac{1}{V} \int_0^\lambda \psi(\rho') \exp\{-i\mathbf{k}'\rho'\} d\rho',$$

then, shifted start of series summation on vector \mathbf{k} at \mathbf{k}' , we have:

$$\psi = \exp\{i\mathbf{m}\mathbf{r}\} + \int_0^\lambda \Omega(\mathbf{r}, \rho) \varphi(\rho) \psi(\rho) d\rho, \quad (9)$$

де

$$\Omega(\mathbf{r}, \rho) = \frac{e}{V} \left(\frac{\exp\{i\mathbf{k}(\mathbf{r} - \rho)\}}{g_{\mathbf{k}} - g_m} \right). \quad (10)$$

If we consider function boundary case $\Omega(\mathbf{r}, \rho)$, in other words if we pass on from summation to integral, then integrating using residues theories, we have:

$$\tilde{\Omega}(\mathbf{r}, \rho) = \frac{e\chi}{2\pi c^2 \hbar^2 |\mathbf{r} - \rho|} \exp\{ik|\mathbf{r} - \rho|\}. \quad (11)$$

Expression received (11), accurate to fixed multiplier, coincide with known Green function for Schroedinger equation. The function, determined with the expression (10) has singular addends for vectors, module of which is equal to scalar of vector \mathbf{m} . Let $\mathbf{m}^{(1)}, \mathbf{m}^{(2)}, \dots, \mathbf{m}^{(j)}, \dots, \mathbf{m}^{(N)}$, — be the vectors full set, equal in absolute value to vector \mathbf{m} , then using adjusted radius-vector: $\tilde{\mathbf{r}} = \mathbf{r} - \lambda_{\max}$, where λ_{\max} — maximal translation vector, which is in radius-vector \mathbf{r} , we can eliminate singularity in the expression (10), changing it as follows:

$$\Omega(\mathbf{r}, \rho) = -\frac{ie\chi\mathbf{m}^{(j)}\tilde{\mathbf{r}}}{Vm^2c^2\hbar^2} \exp\{i\mathbf{m}^{(j)}(\mathbf{r} - \rho)\} + \frac{e}{V} \sum_{\substack{\mathbf{k} \\ |\mathbf{k}| \neq |\mathbf{m}|}} \frac{\exp\{i\mathbf{k}(\mathbf{r} - \rho)\}}{g_{\mathbf{k}} - g_m}. \quad (12)$$

It is easy to be sure that the function (12) satisfied the condition by the direct substitution:

$$\{\hat{H}_0 - \chi\}\Omega(\mathbf{r}, \rho) = \delta(\mathbf{r} - \rho), \quad (13)$$

in other words is regular spectral decomposition of Green function for equation (3). Discrete part

of energetic spectrum should be find, according to integral equation theory, from homogeneous equation, corresponding with (9), which we can draw using the expression (12) as follows:

$$\psi(\mathbf{r}) = -\frac{i\chi\mathbf{m}^{(j)}\tilde{\mathbf{r}}}{m^2c^2\hbar^2} \exp\{i\mathbf{m}^{(j)}\mathbf{r}\}L(\mathbf{m}^{(j)}) + \sum_{\substack{\mathbf{k} \\ |\mathbf{k}| \neq |\mathbf{m}|}} \frac{\exp\{i\mathbf{k}\mathbf{r}\}}{g_{\mathbf{k}} - g_m} L(\mathbf{k}), \quad (14)$$

where

$$L(\mathbf{k}) = \frac{e}{V} \int_0^\lambda \psi(\rho) \varphi(\rho) \exp(-i\mathbf{k}\rho) d\rho.$$

Multiplying both parts of equation (14) with function $\frac{e}{V} \varphi(\mathbf{r}) \exp\{-i\mathbf{k}'\mathbf{r}\}$ and integrating on \mathbf{r} , we receive a system of linear, homogeneous equations for values $L(\mathbf{k})$:

$$(Q(\mathbf{m}, \mathbf{k}, \mathbf{k}') - \delta_{\mathbf{k}, \mathbf{k}'}L(\mathbf{k})), \quad (15)$$

where

$$Q(\mathbf{m}, \mathbf{k}, \mathbf{k}') = \delta_{\mathbf{k}, \mathbf{m}^{(j)}} C(\mathbf{k}', \mathbf{m}^{(j)}) + \frac{v_{\mathbf{k}' - \mathbf{k}}}{g_{\mathbf{k}} - g_m} \prod_{j=1}^N \{1 - \delta_{\mathbf{k}, \mathbf{m}^{(j)}}\};$$

$$C(\mathbf{k}', \mathbf{m}^{(j)}) = -\frac{ie}{Vm^2c^2\hbar^2} \int_0^\lambda \mathbf{m}^{(j)}\mathbf{r} \varphi(\mathbf{r}) \exp\{-i(\mathbf{k}' - \mathbf{m}^{(j)})\mathbf{r}\} d\mathbf{r}.$$

Then it is obvious, that discrete part of spectrum can be found, putting to zero system determinant (15).

INTEGRAL VIEW OF DIRAC EQUATION

Free four-dimensional vector ψ_0 in integral equation have to satisfy the follow condition:

$$(\hat{\mathbf{P}} - \omega_0)\psi_0 = 0. \quad (16)$$

It can be presented as follows: $\psi_0 = \exp\{i\mathbf{m}\mathbf{r}\}\mathbf{A}$, where \mathbf{A} — constant four-dimensional vector. From the condition (16), we have homogeneous system of equations:

$$(\mathbf{P}(\mathbf{m}) - \omega_0)\mathbf{A} = 0, \quad (17)$$

де $\mathbf{P}(\mathbf{m}) = \gamma_\alpha m_\alpha$.

System determinant (17) Δ_0 is equal to:

$$\Delta_0 = (\vartheta^2 - m^2 - \eta^2). \quad (18)$$

Putting to zero the determinant (18) we find possible value of scalar of vector \mathbf{m} :

$$m = \pm\sqrt{\vartheta^2 - \eta^2}, \quad (19)$$

which are well fill in with module of a particle's relativistic wave number. Components of four-dimensional vector \mathbf{A} , depend on two arbitrary constants, marked as C_1 , C_2 , and on

two arbitrary component of wave vector m_1 ; m_2 , sum of squares of absolute value does not exceed the meaning (19), in other words: $m_1^2 + m_2^2 \leq \vartheta^2 - \eta^2$. Choice of component for \mathbf{A} is not the unique solution. For instance, they can be presented as follows:

$$\begin{aligned} A_1 &= -\eta C_1; \quad A_2 = \eta C_2; \\ A_3 &= (m_1 + im_2)C_1 + (\vartheta + \sqrt{\vartheta^2 - \eta^2 - m_1^2 - m_2^2})C_2; \\ A_4 &= (m_1 - im_2)C_2 + \\ &+ (\vartheta - \sqrt{\vartheta^2 - \eta^2 - m_1^2 - m_2^2})C_1. \end{aligned} \quad (20)$$

Nuclear constitution of integral equation is analogical to the nuclears of the equation (9). It is as follows:

$$\mathbf{G} = \frac{\exp\{i\mathbf{k}(\mathbf{r}-\boldsymbol{\rho})\}(\gamma_\alpha k_\alpha + \mathbf{I}\vartheta + \gamma_4\eta)}{V(k^2 - \vartheta^2 + \eta^2)}. \quad (21)$$

When boundary case for array \mathbf{G} is under examination, in other words if we pass on from summarizing to integral, then integrating by means of розглянути граничний випадок для матриці \mathbf{G} , тобто, перейти від сумування до інтегралу, то, інтегруючи за допомогою residue theory, we have:

$$\tilde{\mathbf{G}} = \left[\mathbf{I}\vartheta + \left(m + \frac{i}{|\mathbf{r}-\boldsymbol{\rho}|} \right) \gamma_3 + \eta\gamma_4 \right] \frac{\exp\{im|\mathbf{r}-\boldsymbol{\rho}|\}}{4\pi|\mathbf{r}-\boldsymbol{\rho}|}. \quad (22)$$

Using different representation of four-dimensional vectors \mathbf{A} , we build square four-dimensional array \mathbf{D} as follows:

$$\mathbf{D}(\mathbf{m}) = \begin{pmatrix} -i\eta\sigma_2 & \mathbf{M}_1 \\ \mathbf{M}_2 & \eta\mathbf{I} \end{pmatrix}, \quad (23)$$

where $\mathbf{M}_1 = \begin{pmatrix} m_{12}^* & -q_+ \\ q_- & -m_{12} \end{pmatrix}$, $\mathbf{M}_2 = \begin{pmatrix} q_+ & m_{12} \\ m_{12}^* & q_- \end{pmatrix}$, $m_{12} = m_1 + im_2$, $q_+ = \vartheta + m_3$, $q_- = \vartheta - m_3$,

for which parity is equitable:

$$(\mathbf{P}(\mathbf{m}) - \omega_0)\mathbf{D} = 0. \quad (24)$$

Array (21), such as the function (10), has singular addends for vectors, module of which is equaled to module vector \mathbf{m} . Divergence can be removed by changing the expression (21) as follows:

$$\begin{aligned} \mathbf{G} &= \frac{\exp\{i\mathbf{k}(\mathbf{r}-\boldsymbol{\rho})\}(\gamma_\alpha k_\alpha + \mathbf{I}\vartheta + \gamma_4\eta)}{V(k^2 - \vartheta^2 + \eta^2)} + \\ &+ \frac{1}{V} \mathbf{D}(\mathbf{m}^{(j)}) \hat{\mathbf{b}} \tilde{\mathbf{r}} \exp\{im^{(j)}(\mathbf{r}-\boldsymbol{\rho})\}, \end{aligned} \quad (25)$$

where summarizing in first addend is conducted by all vectors, which vectors are not equal to the vector module \mathbf{m} , $\hat{\mathbf{b}} = \{\mathbf{b}_\alpha\}$ — array-vector, which components are three square four-dimensional arrays, which can be found from the following condition:

$$\gamma_\alpha \mathbf{D}(\mathbf{m}) \mathbf{b}_\alpha = \mathbf{I}. \quad (26)$$

Array vector $\hat{\mathbf{b}}$ has a lot of representations, which satisfy the condition (26). The most simple is as follows:

$$\begin{aligned} \mathbf{b}_1 &= \frac{1 - \delta_{m_3, m}}{2(m_1^2 + m_2^2)} \begin{pmatrix} 0 & F & m_{12}^* & 0 \\ F & 0 & 0 & m_{12} \\ 0 & m_{12}^* & -F^* & 0 \\ -m_{12} & 0 & 0 & F^* \end{pmatrix} + \\ &+ \frac{\delta_{m_3, m}}{4\eta m_3} \begin{pmatrix} -q_- & 0 & 0 & 0 \\ 0 & -q_+ & 0 & 0 \\ 0 & 0 & 0 & q_+ \\ 0 & 0 & -q_- & 0 \end{pmatrix}; \end{aligned} \quad (27)$$

$$\begin{aligned} \mathbf{b}_2 &= \frac{1 - \delta_{m_3, m}}{2(m_1^2 + m_2^2)} \begin{pmatrix} 0 & S^* & im_{12}^* & 0 \\ S^* & 0 & 0 & -im_{12} \\ 0 & im_{12}^* & -S & 0 \\ im_{12} & 0 & 0 & S \end{pmatrix} + \\ &+ \frac{\delta_{m_3, m}}{2\eta m_3} \begin{pmatrix} -iq_- & 0 & 0 & 0 \\ 0 & iq_+ & 0 & 0 \\ 0 & 0 & 0 & iq_+ \\ 0 & 0 & iq_- & 0 \end{pmatrix}; \end{aligned} \quad (28)$$

$$\begin{aligned} \mathbf{b}_3 &= \frac{1 - \delta_{m_3, m}}{\eta} \begin{pmatrix} -\sigma_1 & 0 \\ 0 & \sigma_3 \end{pmatrix} + \\ &+ \frac{\delta_{m_3, m}}{2m\eta^2} \begin{pmatrix} -2\eta m & \eta q_- & 0 & -2\eta m \\ -\eta q_+ & 2mq_+ & 2mq_+ & 0 \\ 2mq_+ & 0 & \eta q_+ & 2mq_+ \\ 0 & -2\eta m & -2\eta m & \eta q_- \end{pmatrix}, \end{aligned} \quad (29)$$

where $F = m_3 m_1 + i\vartheta m_2$; $S = m_3 m_2 + i\vartheta m_1$.

We can be sure that the array (25) meet the conditions, by direct substitution:

$$(\hat{\mathbf{P}} - \omega_0)\mathbf{G} = \mathbf{I}\delta(\mathbf{r}-\boldsymbol{\rho}), \quad (28)$$

in other words, the expression (25) is regular matrix notation of Green function for the equation (5). Using the expression (25) we can draw an integral equation of Fredholm type, corresponding to the equation (5):

$$\boldsymbol{\psi}(\mathbf{r}) = \exp\{im\mathbf{r}\}\mathbf{A} + \int_0^\lambda \mathbf{G}(\mathbf{r}, \boldsymbol{\rho}, m) \mathbf{u}(\boldsymbol{\rho}) \boldsymbol{\psi}(\boldsymbol{\rho}) d\boldsymbol{\rho}. \quad (29)$$

Homogeneous equation corresponding to the equation (29), can be represented as follows:

$$\begin{aligned} \boldsymbol{\psi} &= \frac{\exp\{i\mathbf{k}\mathbf{r}\}(\gamma_\alpha k_\alpha + \mathbf{I}\vartheta + \gamma_4\eta) \mathbf{N}(\mathbf{k})}{(k^2 - \vartheta^2 + \eta^2)} + \\ &+ \mathbf{D}(\mathbf{m}^{(j)}) \hat{\mathbf{b}} \tilde{\mathbf{r}} \exp\{im^{(j)}\mathbf{r}\} \mathbf{N}(\mathbf{m}^{(j)}), \end{aligned} \quad (30)$$

where $\mathbf{N}(\mathbf{k}) = \frac{1}{V} \int_0^\lambda \mathbf{u}(\boldsymbol{\rho}) \boldsymbol{\psi}(\boldsymbol{\rho}) \exp\{-i\mathbf{k}\boldsymbol{\rho}\} d\boldsymbol{\rho}$, and summarizing in first addends is conducted at

all \mathbf{k} , module of which is not equal to vector \mathbf{m} . Multiplying both parts of the equation (30)

from the left with array: $\frac{1}{V} \mathbf{u}(\mathbf{r}) \exp\{-i\mathbf{k}'\mathbf{r}\}$ and integrating at \mathbf{r} , we can receive a system of linear, homogeneous equation for values $\mathbf{N}(\mathbf{k})$:

$$(\mathbf{R}(\mathbf{m}, \mathbf{k}, \mathbf{k}') - \mathbf{I} \delta_{\mathbf{k}, \mathbf{k}'}) \mathbf{N}(\mathbf{k}), \quad (31)$$

where

$$\begin{aligned} \mathbf{R}(\mathbf{m}, \mathbf{k}, \mathbf{k}') &= \delta_{\mathbf{k}, \mathbf{m}^{(i)}} \mathbf{T}(\mathbf{k}', \mathbf{m}^{(i)}) + \\ &+ \frac{v_{\mathbf{k}-\mathbf{k}'} (\gamma_{\alpha} k_{\alpha} + \mathbf{I} \vartheta + \gamma_4 \eta)}{k^2 - \vartheta^2 + \eta^2} \prod_{j=1}^N \{1 - \delta_{\mathbf{k}, \mathbf{m}^{(j)}}\}; \\ \mathbf{T}(\mathbf{k}', \mathbf{m}^{(i)}) &= \\ &= \frac{\mathbf{D}(\mathbf{m}^{(i)})}{V} \int_0^{\lambda} (\hat{\mathbf{b}}\mathbf{r}) \mathbf{u}(\mathbf{r}) \exp\{-i(\mathbf{k}' - \mathbf{m}^{(i)})\mathbf{r}\} d\mathbf{r}. \end{aligned}$$

Then, it is obviously that fixed spectrum part can be found, by putting to zero the system determinant (31).

RESULTS

Using method, developed in the work [5] integral equations of Fredholm (9), corresponding with quasirelativistic equation (1), and integral equation (29), corresponding with Dirac equation (5) were received. The proportions (15) and (31) are proposed for finding of energetic spectrum.

LITERATURE

1. Н. Н. Боголюбов, Д. В. Ширков. Введение в теорию квантованных полей. — М., 1999. — 442 с.
2. В. В. Белов. Точная функция Грина уравнений квантовой механики в электромагнитном поле // Изв. вузов, физика, 1999, № 11, С. 45—56.
3. В. В. Белов, О. Ю. Горчинская. Точная функция Грина релятивистских уравнений квантовой механики в поле плоской волны // ВИНТИ, 3026—76, деп., 14 с.
4. С. П. Гаврилов, Д. М. Гитман, Ш. М. Шварцман. Функции Грина во внешнем электрическом поле и комбинации с магнитным полем и полем плоской волны // ЯФ, 1999, т. 29, № 5, С. 1392—1405.
5. К. В. Авдонин. Побудова хвильових функцій частинки у модельному періодичному полі // Фотоелектроника, 2009, т. 18, С. 140—147.

UDC 539.125.5

K. V. Avdonin

INTEGRAL REPRESENTATION OF QUASIRELATIVISTIC WAVE EQUATION AND DIRAC EQUATION FOR AN ELECTRON IN PERIODIC FIELD

Abstract

Integral representation of quasirelativistic wave equation and Dirac equation for an electron in periodic electromagnetic field is proposed. This representation permeates one in same cases to find wave function by the iterative procedure and to obtain information about energy spectrum.

Key words: integral, equation, Dirac, electron, field, period.

УДК 539.125.5

К. В. Авдонин

ИНТЕГРАЛЬНЫЙ ВИД РЕЛЯТИВИСТСКОГО ВОЛНОВОГО УРАВНЕНИЯ ДЛЯ ЭЛЕКТРОНА В ПЕРИОДИЧЕСКОМ ПОЛЕ

Резюме

В работе предложены интегральные представления квазирелятивистского волнового уравнения и уравнения Дирака для электрона, которые позволяют, итерационным путем, находить волновые функции и получать информацию об энергетическом спектре релятивистской частицы в периодическом поле.

Ключевые слова: интеграл, уравнение, Дирак, поле, период.

УДК 539.125.5

К. В. Авдонин

ІНТЕГРАЛЬНИЙ ВИГЛЯД РЕЛЯТИВІСТСЬКОГО ХВИЛЬОВОГО РІВНЯННЯ ДЛЯ ЕЛЕКТРОНУ У ПЕРІОДИЧНОМУ ПОЛІ

Резюме

У роботі запропоновані інтегральні представлення квазірелятивістського хвильового рівняння та рівняння Дірака для електрону в періодичному електромагнітному полі, які дозволяють, в окремих випадках, ітераційним шляхом знаходити його хвильові функції та отримувати інформацію про енергетичний спектр.

Ключові слова: інтеграл, рівняння, Дірак, поле, період.

*A. TERESCHENKO*¹, *A. KUSEVITCH*¹, *R. VITER*¹, *V. SMYNTYNA*¹, *J. BUK*²,
*J. M. MACAK*³, *A. GUROV*¹, *I. KONUP*¹, *S. GEVULUK*¹

¹ Odessa National I. I. Mechnikov University, Odessa, Ukraine

² Kertak Nanotechnology, Prague, Czech Republic

³ Elmarco, Liberec, Czech Republic

OPTICAL AND STRUCTURAL PROPERTIES OF TiO₂ NANOFIBERS PREPARED BY THE ELECTROSPINNING METHOD

The presented paper is devoted to investigation of structural and optical properties of titania nanofibers. The investigated samples were prepared by the electrospinning method from polymeric solutions, containing TiO₂ precursor, followed by a calcination procedure to obtain highly crystalline, pure inorganic nanofiber materials. The structural properties have been investigated by Scanning electron microscopy (SEM, FEI Nova) and X-ray diffractometry (XRD, Rigaku Ultima). The phase identification of the samples showed the anatase phase of TiO₂. Linear dimensions of nanofibers were calculated. Optical properties were studied with use of UV—VIS spectrophotometer Shimadzu UV-1700 and photoluminescence (PL) setup (excitation with $\lambda = 355$ nm) in the range 350—1100 nm and 370—900 nm, correspondingly. The absorption edge of the samples was in the range of 395—410 nm. The PL maximums appeared at the range of 420—510 nm and 550—710 nm. The mechanisms of luminescence were discussed.

INTRODUCTION

TiO₂ is well known material for optical, catalytic and sensing applications. It has polymorphic nature and three different phases: rutile, anatase and brookite. The development of various deposition techniques allows synthesis of novel titanium dioxide structures with dimensions on the nanometer scale. The decrease of the dimensions below certain levels may lead to the formation of quantum-size effects such as the absorbance edge shift and the room temperature photoluminescence peaks appearance [1].

In the recent decades the attention of scientists was attracted to fabricate metal oxide nanofibers with 2—300 nm cross-section and 0,001—1 mm in length. In these nanostructures the depletion layer width is bigger or in the same range as nanofiber diameter. It results in the relevant influence of surface state on optical and electrical properties of such nanostructures [1]. There have been developed a great number of technological routes to fabricate TiO₂ nanostructures: hydrothermal method [2], magnetron sputtering [3], thermal evaporation method and so on. The mentioned technological routes allow to obtaining TiO₂ nanostructures with different shapes: nanoparticles, nanorods and nanotubes.

In the last decade, electrospinning deposition is to be prospective for nanofibers fabrication. It is based on interaction between charged jet of polymeric solution with electrostatic field. The jet is narrowed by electrostatic effects to the cylindrical shape and hardened because of solvent evaporation. The precipitated nanofibers are 20—200 μm in length and with diameter of 50—500 nm [5—8].

In the presented paper the structural and optical properties of titania nanofibers, fabricated by electrospinning method, are reported. The influence of Li doping on these properties was investigated. The peculiarities of optical properties have been discussed.

EXPERIMENTAL

Electrospinning deposition setup is shown in fig. 1. Ethanol solution of Titanium (IV) isopropoxide (TIP) with initial concentration 1 mol/l was mixed with polyvinyl alcohol in ratio 1:20. Lithium doping was provided by addition of the corresponding alkaline dopant (LiNO₃) in ethanol. The solutions were supplied by capillary to the rotating template, preheated to 150 °C. High voltage was applied between capillary and template. The voltage value and distance between capillary and template were kept constant for all depositions 5 kV and 1 cm, correspondently. After fabrication, as-deposited nanofibers were collected and calcinated in air atmosphere at 600 °C for 2 hours.

Structural properties of annealed samples have been investigated by Scanning electron microscopy (SEM) and X-ray diffractometry (XRD).

XRD tests were measured by Rigaku Ultima XRD-setup (CuK α , $\lambda = 0,154$ nm) in the range of 2θ angle 20—80°. Scanning electron microscopy FEI Nova has been used to obtain surface images of the investigated nanofibers.

Optical properties were studied with use of UV—VIS spectrophotometer Shimadzu UV-1700 in the range 350—1100 nm. Photoluminescence (PL) spectra were measured by setup, presented in fig. 2. The luminescence was stimulated

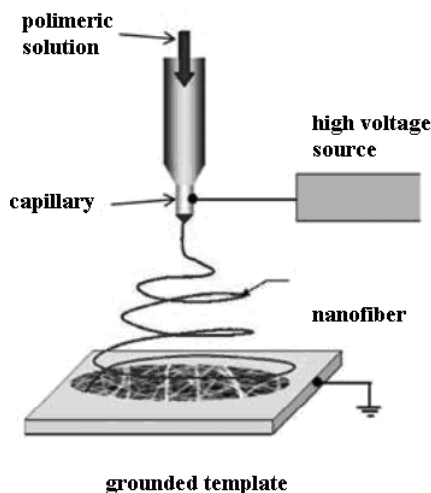


Fig. 1. Electrospinning deposition setup

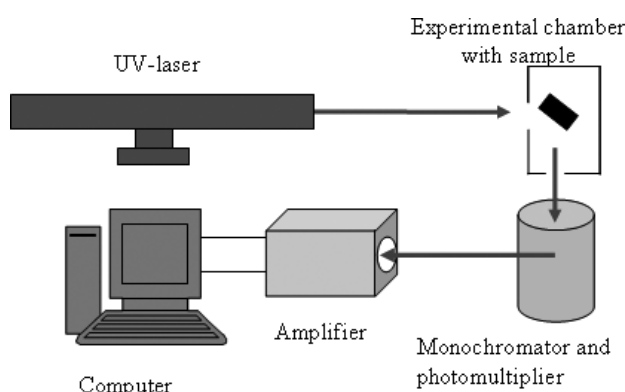


Fig. 2. Photoluminescence setup

by UV laser LCS-DTL-374QT with excitation wavelength $\lambda = 355$ nm. The emission spectra were amplified and recorded in the wavelength range 370–900 nm.

RESULTS AND DISCUSSION

XRD spectrum of the obtained powder is plotted in fig. 3. The one can see XRD peaks at following 2θ values: $25,96^\circ$; $38,56^\circ$; $55,06^\circ$; $62,12^\circ$; $70,28^\circ$ и $76,02^\circ$. The obtained peaks correspond to TiO_2 anatase phase with (hkl) indices (101), (004), (211), (204), (220) and (215) [9–11].

Surface morphology of TiO_2 nanopowder, obtained by SEM is shown in fig. 4. The SEM image reveals a geometry of the obtained nanostructures. The one can claim that the fabricated TiO_2 nanopowder was formed by nanofibers with 295 ± 70 nm in diameter and 20 mkm in length.

Absorbance spectrum of TiO_2 nanopowder $\alpha(h\nu)$ is presented in fig. 5. The absorption edge lies in the region of photon energies 3,1–3,3 eV. It is known that titanium dioxide is semiconductor with indirect band gap. So, absorbance spectrum of TiO_2 nanofibers was plotted in specific scale $(\alpha h\nu)^{1/2}$ vs $h\nu$ (fig. 6). Band gap was estimated from the linear plot at the absorp-

tion edge region as intersection with $(h\nu)$ axis. As one can see, the E_g value is about 2,5 eV. This value is much lower than for anatase single crystal band gap value ($E_g = 2,8$ eV) [11]. The effect of decreasing of particles size to nano dimensions is expected to bring to blue

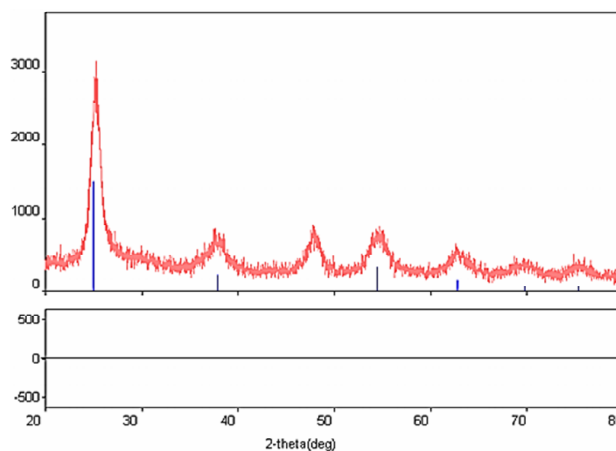


Fig. 3. XRD spectrum of TiO_2 nanopowder

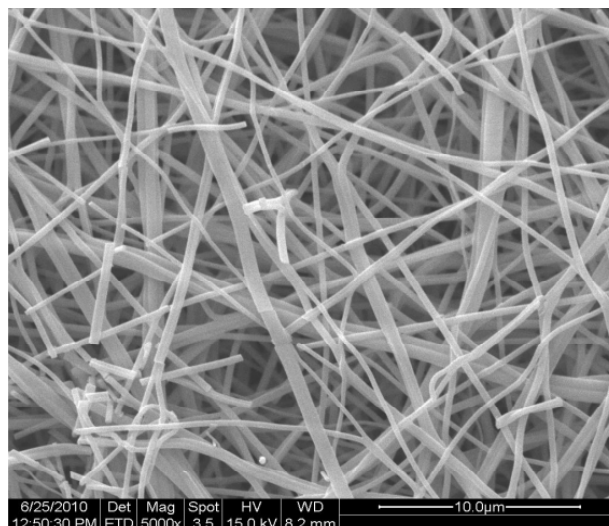


Fig. 4. SEM image of TiO_2 nanopowder

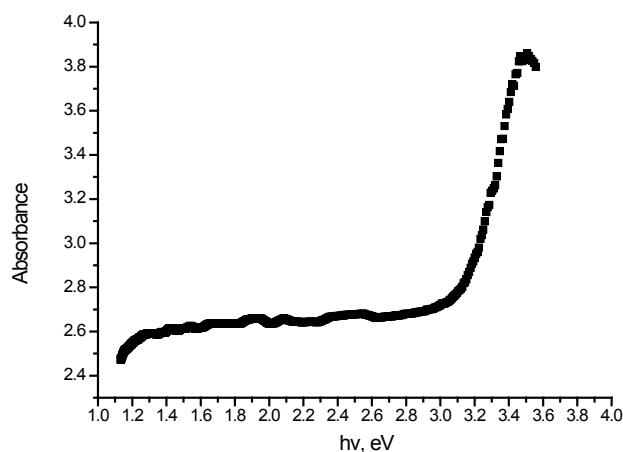


Fig. 5. Absorption spectrum of TiO_2 nanopowder

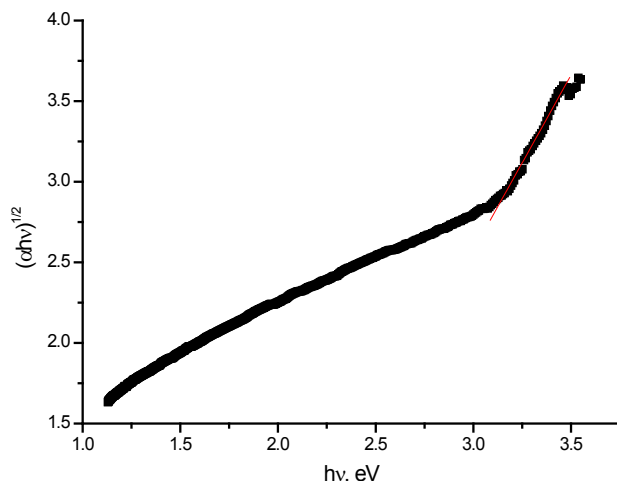


Fig. 6. Graphical evaluation of band gap value

shift of band gap [11]. The physical properties of the nanopowder drastically depend on its density, which is characterized by a parameter called compaction [12]. It may happen that, because of the shapes of nanofibers the compaction of nanopowder is low and it includes the material and intergranular gaps, filled in with air. In this case E_g value will differ from the real number and represent only average value of material + void system [12].

The phenomenon can be explained by another mechanism. The random compaction of nanofibers on the plane can cause the high scattering coefficient, what can support red shift of band gap value [11].

PL spectrum of TiO_2 nanofibers is plotted in fig. 7. It can be seen that PL curve had a kind of complexity. By means of Origin Pro 7.0 software, the PL spectrum was split onto separate peaks. The PL peaks, located at 423, 481, 508, 555, 601, 632 and 702 nm have been found. The full explanation of photoluminescence in TiO_2 has not been done yet. The peaks at 423 and 481 nm are connected with excitons, located in TiO_6 octahedron. It is supposed that peaks at 508 and 555 nm are formed by oxygen vacancies and peaks, appeared at 601, 632 and 702 nm

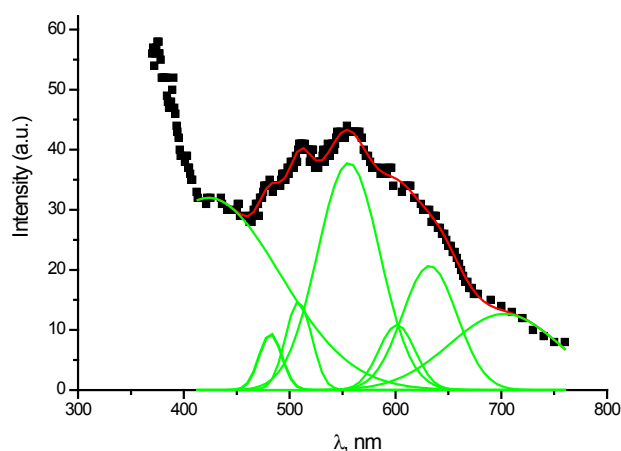


Fig. 7. PL spectrum of TiO_2 nanofibers, measured at room temperatures

relate to structural defects on the surface of nanofibers. In [11, 13, 14] it was discussed that Ti^{3+} surface states are responsible for emission peaks at 600–632 nm and peaks at higher wavelengths correspond to structural defects.

The PL peaks at room temperature at UV region verify quantum-size effects appeared in the studied titania nanofibers. However, red shift of the peaks in comparison with lower dimensional TiO_2 nanostructures suggests to tailor the diameter of the nanotubes to lower values [13,14]. The PL peaks at 500–700 nm demonstrate the defect presence at the surface of nanofibers. At this stage it is quite difficult to explain the nature of these defects and additional measurements will be performed in future works.

CONCLUSION

TiO_2 nanofibers were successfully fabricated by electrospinning route. The obtained samples had pure anatase edge phase of titania and linear dimensions 295 ± 70 nm in diameter and 20 μm in length. Absorption of the samples lies in the region of photon energies 3.1–3.3 eV. Scattering and compaction effects in nanofibers make it difficult to estimate band gap value with standard calculations. Room temperature photoluminescence of the samples was measured. PL peaks at UV region correspond to excitons in TiO_2 lattice and Vis-IR peaks are related with structural defects.

REFERENCES

1. Pavlova E., Lapcikova M., Slouf M., Kuzel R. Preparation and structure of TiO_2 nanotubes // *Materials Structure*. — 2006. — Vol. 12. — P. 156–157.
2. Lin Y.-J., Wang L., Chiu W.-Y. Preparation and characterization of titania nanotubes and hybrid materials derived from them // *J. Vac. Sci. Technol. B*. — 2005. — Vol. 23. — P. 2398–2402.
3. More A. M., Gujar T. P., Gunjekar J. L., Lokhande C. D., Joo O.-S. Growth of TiO_2 nanorods by chemical bath deposition method. // *Applied Surface Science*. — 2008. — Vol. 255. — P. 2682–2687.
4. Yoshida R., Suzuki Y., Yoshikawa S. Syntheses of $\text{TiO}_2(\text{B})$ nanowires and TiO_2 anatase nanowires by hydrothermal and post-heat treatments // *Journal of Solid State Chemistry*. — 2005. — Vol. 178. — P. 2179–2185.
5. Матвеев А. Т., Афанасов И. М. Получение нановолокон методом электроформования: Учеб. пособие. — М.: МГУ имени М. В. Ломоносова, 2010. — 83 с.
6. Yarin A. L., Zussman E. Electrospinning of nanofibers from polymer solutions // *XXI ICTAM*. — Warsaw, Poland, 2004. — P. 12–15.
7. Frenot A., Chronakis I. S. Polymer nanofibers assembled by electrospinning // *Current Opinion in Colloid and Interface Science*. — 2003. — Vol. 8. — P. 64–75.
8. Grafe T. H., Graham K. M. Nanofiber webs from electrospinning // *Nonwovens in Filtration* — Fifth International Conference. — Stuttgart, Germany, 2003. — P. 15–18.
9. Malina Raileanu, Maria Crisan, Nicolae Dragan, Dorel Crisan, Anouk Galtayries, Ana Braileanu, Adelina Ianculescu, Valentin S. Teodorescu, Ines Nitoi, Mihai Anastasescu. Sol-gel doped TiO_2 nanomaterials: a comparative study/ 5th international conference on sol-gel materials. — Trzebiezowice, Poland. — 2009. — P. 315–329.
10. D. Reyes-Coronado, G. Rodriguez-Gattorno, M. E. Espinosa-Pesqueira, C. Cab, R. de Cossel and G. Osakam. Phase-pure TiO_2 nanoparticles: anatase, brookite and rutile // *Nanotechnology* 19. — 2008. — P. 2–11.

11. Ma Yutao, Lin Yuan, Xiao Xurui, Li Xueping & Zhou Xiaowen. Synthesis of TiO_2 of nanotubes film and its light scattering property // Chinese Science Bulletin 2005. — Vol. 50. — No. 18. — P. 1985—1990.

12. Peter R. Laity, Ruth E. Cameron. Changes in small-angle X-ray scattering during powder compaction — An explanation based on granule deformation // Powder Technology. — 2010. — V. 198. — P. 404—411.

13. Wu J.-M., Shih H. C., Wu W.-T., Tseng Y.-K., Chen I.-C. Thermal evaporation growth and the luminescence property of TiO_2 nanowires. // Journal of Crystal Growth — 2005. — Vol. 281. — P. 384—390.

14. Y. Lei and L. D. Zhang. Fabrication, characterization, and photoluminescence properties of highly ordered TiO_2 nanowire arrays // J. Mater. Res. — 2005. — Vol. 16. — No. 4. — P. 1138—1144.

UDC 621.315.592

A. Tereschenko, A. Kusevitch, R. Viter, V. Smyntyna, J. Buk, J. M. Macak, A. Gurov, I. Konup, S. Gevulok.

OPTICAL AND STRUCTURAL PROPERTIES OF TiO_2 NANOFIBERS PREPARED BY THE ELECTROSPINNING METHOD

Abstract

The presented paper is devoted to investigation of structural and optical properties of titania nanofibers and the influence of Li doping on these properties. The investigated samples were prepared by the electrospinning method from polymeric solutions, containing TiO_2 precursor, followed by a calcination procedure to obtain highly crystalline, pure inorganic nanofiber materials. The structural properties have been investigated by Scanning electron microscopy (SEM, FEI Nova) and X-ray diffractometry (XRD, Rigaku Ultima). The phase identification of the samples showed the anatase phase of TiO_2 . Linear dimensions of nanofibers were calculated. Optical properties were studied with use of UV—VIS spectrophotometer Shimadzu UV-1700 and photoluminescence (PL) setup (excitation with $\lambda = 355$ nm) in the range 350—1100 nm and 370—900 nm, correspondingly. The absorption edge of the samples was in the range of 395—410 nm. The PL maximums appeared at the range of 420—510 nm and 550—710 nm for both samples. The mechanisms of luminescence were discussed.

Key words: optical properties, nanofibers, electrospinning.

УДК 621.315.592

A. Терещенко, А. Кусевич, Р. Витер, В. Смынтна, І. Бук, М. Макак, А. Гуков, І. Конуп, С. Гевелюк

ОПТИЧЕСКИЕ И СТРУКТУРНЫЕ СВОЙСТВА НАНОВОЛОКОН TiO_2 ПОЛУЧЕННЫХ МЕТОДОМ ЭЛЕКТРОСПИННИНГА

Резюме

Представленная работа посвящена исследованию структурных и оптических свойств нановолокон TiO_2 и влиянию легирования Li на эти свойства. Исследованные образцы были приготовлены методом электроспиннинга из полимерных растворов, содержащих прекурсор TiO_2 , и далее отжигались для формирования кристаллической структуры. Структурные свойства были исследованы с помощью сканирующей электронной микроскопии и рентгеновской дифракции. Рентгеноструктурный анализ показал, что данные нановолокна принадлежат фазе анатаза. Линейные размеры нановолокон были рассчитаны. Оптические свойства были изучены с использованием спектрофотометра Shimadzu UV-1700 и установки для исследования фотолюминесценции (длина волны возбуждения $\lambda = 355$ nm) в диапазоне 350—1100 nm и 370—900 nm соответственно. Край поглощения образцов приходится на диапазон 395—410 nm. Пики фотолюминесценции возникают в диапазоне 420—510 nm и 550—710 nm для обоих образцов. Механизм люминесценции обсуждается в данной статье.

Ключевые слова: оптические свойства, нановолокна, электроспиннинг.

УДК 621.315.592

A. Терещенко, А. Кусевич, Р. Витер, В. Смынтна, І. Бук, М. Макак, А. Гуков, І. Конуп, С. Гевелюк

ОПТИЧНІ ТА СТРУКТУРНІ ВЛАСТИВОСТІ НАНОВОЛОКОН TiO_2 , ОТРИМАНИХ МЕТОДОМ ЕЛЕКТРОСПІНІНГУ

Резюме

Представлена робота присвячена дослідженню структурних та оптичних властивостей нановолокон TiO_2 та впливу легування Li на ці властивості. Досліджені зразки були приготовлені методом електроспінінгу з полімерних розчинів, що містять прекурсор TiO_2 , та відпалених для формування кристалічної структури. Структурні властивості були досліджені за допомогою скануючої електронної мікроскопії та рентгенівської дифракції. Рентгеноструктурний аналіз показав, що дані нановолокна належать фазі анатаза. Лінійні розміри нановолокон були розраховані. Оптичні властивості були досліджені з використанням спектрофотометра Shimadzu UV-1700 та приладу для дослідження фотолюмінесценції (довжина хвилі збудження $\lambda = 355$ nm) у діапазоні 350—1100 nm і 370—900 nm відповідно. Край поглинання зразків припадає на діапазон 395—410 nm. Піки фотолюмінесценції виникають у діапазоні 420—510 nm і 550—710 nm для обох зразків. Механізм люмінесценції обговорюється у даній статті.

Ключові слова: оптичні властивості, нановолокна, електроспінінг.

DETERMINATION OF THE HYPERFINE AND ELECTROWEAK INTERACTIONS PARAMETERS AND PARITY NON-CONSERVATION AMPLITUDES IN HEAVY ATOMS AND NUCLEI WITHIN NUCLEAR-QED THEORY

It is presented new approach to determination of the electroweak and hyperfine interactions parameters and parity non-conservation effect in heavy atomic and nuclear systems, based on the combined QED perturbation theory formalism and relativistic nuclear mean-field theory. Results of estimating some fundamental hyperfine and electroweak constants in the Cs, Tl and Yb isotopes are presented. Firstly it is predicted the weak charge for the Yb nucleus.

1. INTRODUCTION

Different topics of the modern physics of electroweak interactions are now a subject of intensive theoretical and experimental interest. From the other side, the parity violation (non-conservation) experiments in atomic physics provide an important possibility to deduce information on the Standard Model independently of high-energy physics experiments [1–8]. The recent LEP experiments are fulfilled [1, 2], that yield extremely accurate values for Z-boson properties. Although the spectacular experimental achievements of particle physics in the last decade have strengthened the Standard Model (SM) as an adequate description of nature, they have also revealed that the SM matter represents a mere 5 % or so of the energy density of the Universe, which clearly points to some physics beyond the SM despite the desperate lack of direct experimental evidence. The sector responsible for the spontaneous breaking of the SM electroweak symmetry is likely to be the first to provide experimental hints for this new physics. The fundamental purposes of the high-precision atomic PNC studies are to search for new physics beyond the SM of the electroweak interaction by precise evaluation of the weak charge Q_W and to probe parity violation in the nucleus by evaluation of the nuclear anapole moment. The detailed review of these topics can be found in refs. [1–10], in particular, speech is about brief introducing the SM physics and the conventional Higgs mechanism and a survey of recent ideas on how breaking electroweak symmetry dynamics can be explained.

The most popular multiconfiguration Dirac–Fock (MCDF) method for calculating parity and time reversal symmetry violations in many-electron atoms has some serious disadvantages [3, 17, 26]. This fact has stimulated a devel-

opment of different versions of the many-body perturbation theory (PT), namely, the PT with relativistic Hartree-Fock (RHF) and DF zeroth approximations, QED-PT and nuclear-QED PT [11–44].

In present paper the new theoretical approach, namely, nuclear-QED PT is used for detection of the hyperfine structure and electroweak interaction parameters, scalar-pseudo-scalar interaction constant and parity non-conservation (PNC) effect in atomic system. In fact the N-QED PT is based on the combining ab initio QED PT formalism and nuclear relativistic middle-field (RMF) model and allows to fulfil studying the spectra for atomic systems with an account of the relativistic, correlation, nuclear, radiative effects [10, 38–44]. The important feature is the correct accounting for the inter electron correlations, nuclear, Breit and QED radiative corrections. All correlation corrections of the second order and dominated classes of the higher orders diagrams are taken into account [10]. The results of studying the different atomic systems are presented.

2. NUCLEAR-QED PT APPROACH TO ELECTROWEAK INTERACTIONS IN HEAVY FINITE FERMI-SYSTEMS AND PARITY-NON-CONSERVATION TRANSITION AMPLITUDE DETERMINATION

The wave electron functions zeroth basis is found from the Dirac equation solution with potential, which includes the core ab initio potential, electric, polarization potentials of nucleus. All correlation corrections of the second and high orders of PT (electrons screening, particle-hole interaction etc.) are accounted for [10]. The concrete nuclear model is based on

the relativistic mean-field (RMF) model for the ground-state calculation of the nucleus. Though we have no guaranty that these wave-functions yield a close approximation to nature, the success of the RMF approach supports our choice [35]. These wave functions do not suffer from known deficiencies of other approaches, e. g., the wrong asymptotics of wave functions obtained in a harmonic oscillator potential. The RMF model has been designed as a renormalizable meson-field theory for nuclear matter and finite nuclei. The realization of nonlinear self-interactions of the scalar meson led to a quantitative description of nuclear ground states. As a self-consistent mean-field model (for a comprehensive review see ref. [35]), its ansatz is a Lagrangian or Hamiltonian that incorporates the effective, in-medium nucleon-nucleon interaction. Recently the self-consistent models have undergone a reinterpretation, which explains their quantitative success in view of the facts that nucleons are composite objects and that the mesons employed in RMF have only a loose correspondence to the physical meson spectrum. They are seen as covariant Kohn-Sham schemes and as approximations to the true functional of the nuclear ground state. As a Kohn-Sham scheme, the RMF model can incorporate certain ground-state correlations and yields a ground-state description beyond the literal mean-field picture. RMF models are effective field theories for nuclei below an energy scale of 1 GeV, separating the long- and intermediate-range nuclear physics from short-distance physics, involving, i. e., short-range correlations, nucleon form factors, vacuum polarization etc, which is absorbed into the various terms and coupling constants.

In our approach we have used so called NL3-NLC and generalized Ivanov et al approach (see details in refs. [37, 39, 4]), which are among the most successful parameterizations available. Further one can write the Dirac—Fock-like equations for a multi-electron system $\{\text{core-}nlj\}$. Formally they fall into one-electron Dirac equations for the orbitals nlj with the total potential $V(r)$. Radial parts F and G of two components of the Dirac function for electron, which moves in the potential $V(r, R)$ are defined by solution of the Dirac equations (PT zeroth order). The total potential includes the electric potentials of a nucleus with using the RNF charge distribution, exchange-correlation and radiative potentials. The radiative QED (the self-energy part of the Lamb shift and the vacuum polarization contribution in the lower order plus corrections of the high QED orders) are accounted for within the QED formalism [4]. The continuum pressure effects and contribution of the autionization states are taken onto account by means the Dirac-Sturm approach. The full description of the corresponding models and other details of the general method are presented in refs. [4, 10, 37–44].

Below we are limited by presenting the key formulae for determination of the PNC transi-

tion amplitude. The dominative contribution to the PNC amplitude is provided by the spin-independent part of the operator for a weak interaction, which should be added to the atomic Hamiltonian [5]:

$$H = H_{at} + \mu \sum_j H_W(j),$$

$$H_W^1 = \frac{G_F}{2\sqrt{2}} Q_W \gamma_5 \rho(r), \quad (1)$$

where $G_F = g^2/4\sqrt{2}m_W^2$ is the Fermi constant of the weak interaction, γ_5 — is the Dirac matrice, m_W is the mass of the W boson, $\rho(r)$ is a density of the charge distribution in a nucleus and Q_W is a weak charge of a nucleus, linked with number of neutrons N and protons Z and the Weinberg angle θ_W in the Standard Model as follows:

$$Q_W = Z(1 - 4\sin^2\theta_W) - N. \quad (2)$$

The latter can be rewritten with accounting for the radiative corrections as [5, 18]:

$$Q_W = \{Z(1 - [4,012 \pm 0,010]\sin^2\theta_W) - N\} \times \\ \times (0,9857 \pm 0,0004)(1 + 0,0078T), \\ \{\sin^2\theta_W = 0,2323 + 0,00365S - 0,00261T\} \quad (3)$$

The parameters S, T parameterize the looped corrections in the terms of conservation (S) and violation (T) of an isospin. The spin-dependent contribution to the PNC amplitude has three distinct sources: the nuclear anapole moment ((that is considered as an electromagnetic characteristics of system, where the PNC takes a place; generally speaking, speech is about the arisen spin structure and the magnetic field distribution is similar to the solenoid field), the Z -boson exchange interaction from nucleon axial-vector currents ($A_n V_e$), and the combined action of the hyperfine interaction and spin-independent Z -boson exchange from nucleon vector ($V_n A_e$) currents [7, 9, 34]. The anapole moment contribution strongly dominates.

The above-mentioned interactions can be represented by the Hamiltonian

$$H_W^i = \frac{G_F}{\sqrt{2}} k_i (\alpha \cdot I) \rho(r), \quad (4)$$

where $k(i=a)$ is an anapole contribution, $k(i=2) = k_{z0}$ — axial-vector contribution, $k(i=kh) = k_{Q_W}$ is a contribution due to the combined action of the hyperfine interaction and spin-independent Z exchange. The estimate of the corresponding matrix elements is in fact reduced to the calculation of the integrals as [10]:

$$\langle i | H_W^1 | j \rangle = i \frac{G_F}{2\sqrt{2}} Q_W \delta_{k_i - k_j} \delta_{m_i m_j} \times \\ \times \int_0^\infty dr [F_i(r) G_j(r) - G_i(r) F_j(r)] \rho(r). \quad (5)$$

The reduced matrix element is as follows:

$$\begin{aligned} \langle i \| H_W^1 \| j \rangle &= i \frac{G_F}{2\sqrt{2}} Q_W \times \\ &\times \int_0^\infty dr [F_i(r)G_j(r) - G_i(r)F_j(r)]\rho(r). \end{aligned} \quad (6)$$

Further the general expression for the corresponding nuclear spin-independent PNC amplitude for a-b transition is written as follows:

$$\begin{aligned} \langle a | \text{PNC} | b \rangle &= - \sum_n \frac{\langle b | e\alpha_v A^v | n \rangle \langle n | H_W^{(1)} | a \rangle}{\varepsilon_a - \varepsilon_n} + \\ &+ \frac{\langle b | H_W^{(1)} | n \rangle \langle n | e\alpha_v A^v | a \rangle}{\varepsilon_b - \varepsilon_n}. \end{aligned} \quad (7)$$

Here the following notations are used: $|a\rangle = |aIF_F M_F\rangle$, $|b\rangle = |bIF_I M_I\rangle$, I — spin of a nucleus, $F_{I,F}$ — is a total momentum of an atom and M — its z component (I, F are the initial and final states).

The corresponding spin-dependent PNC contribution is as follows:

$$\begin{aligned} \langle a | \text{PNC} | b \rangle^{sd} &= k_a \langle a | \text{PNC} | b \rangle^{(a)} + \\ &+ k_2 \langle a | \text{PNC} | b \rangle^{(2)} + k_{\text{hf}} \langle a | \text{PNC} | b \rangle^{(\text{hf})}. \end{aligned} \quad (8)$$

It should be noted the expressions for the matrix elements $\langle a | \text{PNC} | b \rangle^{(a)}$ and others in Eq. (8) are similar to equation (12), however have much more complicated form.

3. RESULTS AND FUTURE PROSPECTS

In table 1 we listed the calculated and experimental values of the hyperfine structure (hfs) energy and magnetic moments (in nuclear magnetons) in the $^{207}\text{Tl}^{80+}$, which are determined within the nuclear-QED theory and other different theoretical models [12–14]. The key quantitative factor of agreement between our N-QED theory and experimental data is

connected with the correct accounting for the inter electron correlations, nuclear, Breit and QED radiative corrections (including magnetic moment distribution in a nucleus and nuclear corrections).

Table 1

The hfs energy and magnetic moment (in nuclear magnetons) in $^{207}\text{Tl}^{80+}$ [12–14]

Magn. moment [μ_N]	HS	NLC	Tomaselli	N-QED
Theory	1.8769	1.8758	1.6472	1.8764
Exp. [14]	1.8765(5)			
HFS [eV]	HS	NLC	Tomaselli	N-QED
ΔE^1_{HFS}	3,721	3,729	3,2592	3,5209
ΔE_{QED}	−0,0201		−0,0178	−0,0207
Total	3,701	3,708	3,2592	3,5002

In table 2 there are listed the PNC amplitudes (in units of $10^{-11}iea_B(-Q_W)/N$) for a number of radiative transitions in spectra of the Cs, Tl, Yb isotopes, which are calculated by the different methods (without the Breit corrections): DF, RHF, MCDF, many-body perturbation theory (MBPT) and our nuclear-QED PT results (other data from refs. [25–34]).

Let us underline that the values of the weak charge are firstly predicted by us for ^{173}Yb atoms. The analysis of results shows that in principle a majority of theoretical approaches provides physically reasonable agreement with the Standard model data, but the important question is how much exact this agreement. In our opinion, however, the precise estimates indicate on the tiny deviation from the Standard model. In any case analysis of the data allow to conclude that the SM violation has a place, however it can be hardly stated on significant violation. Nevertheless, one could turn to attention on the “sensitivity” of the PNC experiments to New Physics for energies, which are hardly reached at the modern colliders. This fact is clearly illustrated by the figure 1, where the

Table 2

The PNC amplitudes (in units of $10^{-11}iea_B(-Q_W)/N$) and estimated values of the weak charge Q_W for different heavy atoms, predicted in different approaches (see text)

Isotope, transition	$E_{\text{PNC}} Q_W$	N-QED	MCDF	MBPT-DF	MCDF-QED	TDRHF-C	RCC
^{133}Cs 6s-7s	E_{PNC}	−0.8985	−0.935 −0.905	−0.897 −0.904	−0.8981 −0.9055	−0.898 −0.910 −0.902	−0.9054 −0.899
^{133}Cs 6s-7s $Q_W^{\text{SM}} = -73,19$	Q_W	−72.62	−69.78 −71.09	−72.69 −72.18	−72.65 −72.06	−72.66 −71.70 −72.42	−72.06 −72.58
^{173}Yb 6s ²¹ S ₀ -5d6s ³ D ₁ $Q_W^{\text{SM}} = -95,44$	E_{PNC} Q_W	−97.07 −92.31	— —	— —	— —	— —	— —
^{205}Tl 6p _{1/2} -6p _{3/2}	E_{PNC}	26.5114	−26.75	−26.5	—	—	—
^{205}Tl 6p _{1/2} -6p _{3/2} $Q_W^{\text{SM}} = -116,81$	Q_W	−116.15	−112.4	−116.2	—	—	—

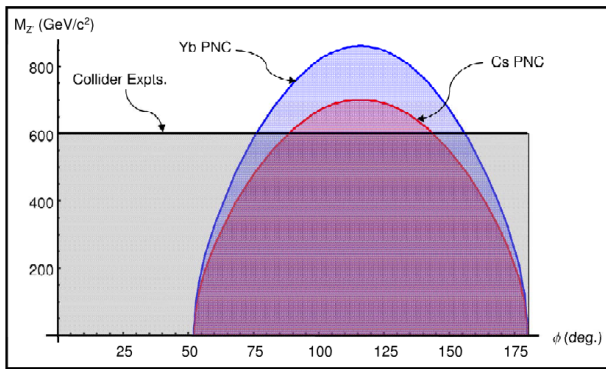


Figure 1. The limitations on the Z' boson mass and missing angle in the models beyond the Standard Model (see comment in the text)

darkened region is eliminated from the measurements in the PNC and colliders experiments.

Therefore, in this paper we presented new more accurate data on some fundamental hyperfine and electroweak constants in the Cs, Tl and Yb isotopes using a new approach to determination of the electroweak and hyperfine interactions parameters and parity non-conservation effect in heavy atomic and nuclear systems, based on the combined QED perturbation theory formalism and relativistic nuclear mean-field theory. Some listed data on the indicated constants directly stimulate carrying out new sufficiently precised experiments in order to provide the low-energy test of the Standard Model. The rare-earth elements have to be especially interesting as they have very complicated spectra of autoionization resonances (with very unusual from physical point of view their behavior in a weak electric and laser fields; the known effect of resonances giant broadening [4]). The elementary comments show that the prospects of the PNC experiments with Stark pumping (or a polarization plane rotation) of the individual states (in the considered isotopes,

including the rare-earth elements; probably more effective possibility is given by studying multicharged ions of these elements) and simultaneously polarized laser field dressing (with a cold-atom fountain or interferometer) could provide comfortable conditions for precised experimental observation of the weak effects.

REFERENCES

1. Grojean C., New approaches to electroweak symmetry breaking // *Physics — Uspekhi.* — 2007. — Vol. 50. — P. 3—42; Review of Particle Properties, Particle Physics Booklet (AIP). — July, 2006.
2. Shabalin E. P., What future for CP- and T-violation studies and CPT-invariance tests? // *Physics — Uspekhi.* — 2001. — Vol. 171. — P. 951—976.
3. Grant I. P., *Relativistic Quantum Theory of Atoms and Molecules.* — Oxford, 2008. — 650 P.
4. Glushkov A. V., *Relativistic Quantum Theory. Quantum, mechanics of Atomic Systems.* — Odessa: Astroprint, 2008. — 900 P.
5. Khriplovich I. B., *Parity Nonconservation in Atomic Phenomena.* — Gordon and Breach, Philadelphia, 1999. — 250 P.
6. Grojean C., New approaches to electroweak symmetry breaking // *Physics — Uspekhi.* — 2007. — Vol. 177. — P. 3—42.
7. Khriplovich I. B., Discovery of anapole moment // *Physics — Uspekhi.* — 1999. — Vol. 167. — 1214—1216.
8. Auerbach N., Search for electric dipole moments in atoms of radioactive nuclei // *J. Phys. G: Nucl. Part. Phys.* — 2008. — Vol. 35. — P. 014040.
9. Safronova M. S., Rupsi Pal, Jiang D., Kozlov M. G., Johnson W. R., Safronova U. I., New directions in atomic PNC // *Nucl. Phys. A.* — 2009. — Vol. 827. — P. 411—413.
10. Khetselius O. Yu., *Hyperfine structure of spectral lines of the heavy atoms and multicharged ions.* — Odessa: Astroprint, 2008. — 210 P.
11. Gaigalas G., Gaidamauskas E., Jonsson P., Multiconfiguration Dirac—Hartree—Fock calculations for the hyperfine-structure parameters and the scalar-pseudoscalar interaction constant of ^{133}Cs // *Journal of Physics CS.* — 2008. — Vol. 130. — P. 012008.
12. Nagasawa T., Haga A., Nakano M., Hyperfine splitting of hydrogenlike atoms based on relativistic mean field theory // *Phys. Rev. C.* — 2004. — Vol. 69. — P. 034322: 1—10.
13. Bouchiat M. A., Linear Stark effect in dressed atoms as a signal to measure a nuclear anapole moment with a cold-atom fountain or interferometer // *Phys. Rev. Lett.* — 2007. — Vol. 98. — P. 043003.
14. Tomaselli M., Kuhl T., Seelig P., Holbrow C. and Kankeleit E., Hyperfine splittings of hydrogenlike ions and the dynamic-correlation model for one-hole nuclei // *Phys. Rev. C.* — 1998. — Vol. 58, N 3. — P. 1524—1534.
15. Tomaselli M., Schneider S. M., Kankeleit E., Kuhl T., Ground state magnetization of ^{209}Bi in a dynamic-correlation model // *Phys. Rev. C.* — 1995. — Vol. 51, N 6. — P. 2989—2997.
16. Labzowsky L. N., Johnson W. R., Soff G., Schneider S. M., Dynamic proton model for the hyperfine structure of H-like ion $^{209}\text{Bi}^{+82}$ // *Phys. Rev. A.* — 1995. — Vol. 51, N 6. — P. 4597—4602.
17. Bieron J., Pyykko P., Degree of accuracy in determining the nuclear electric quadrupole moment of radium // *Phys. Rev. A.* — 2005. — Vol. 71. — P. 032502.
18. Porsev S. G., Rakhilina Yu. G., Kozlov M. G., Non-conservation of spatial parity in atomic ytterbium // *JETP Lett.* — 1995. — Vol. 61. — P. 449—453.
19. Dzuba V. A., Flambaum V. V., Sushkov O. P., Polarizabilities and parity nonconservation in the Cs atom and limits on the deviation from the standard electroweak model // *Phys. Rev. A.* — 1997. — Vol. 56. — P. R4357—4360.
20. Safronova M. S., Johnson W. R., Derevianko A., Relativistic many-body calculations of energy levels, hyperfine constants, electric-dipole matrix elements, and static polarizabilities for alkali-metal atoms // *Phys. Rev. A.* — 1999. — Vol. 60. — P. 044103.
21. Bennett S. C., Roberts J. L., Wieman C. E., Measurement of the dc Stark shift of the 6S-7S transition in atomic caesium // *Phys. Rev. A.* — 1999. — Vol. 59. — P. 3254—3260.
22. Dzuba V. A., Flambaum V. V., Off-diagonal hyperfine interaction and parity nonconservation in cesium // *Phys. Rev. A.* — 2000. — Vol. 62. — P. 052101.
23. Johnson W. R., Bednyakov I., Soff G., Vacuum-polarization corrections to the parity-nonconserving 6s-7s transition amplitude in ^{133}Cs // *Phys. Rev. Lett.* — 2001. — Vol. 87. — P. 233001.
24. Dzuba V. A., Harabati C., Johnson W. R., Safronova M. S., Breit correction to the parity-nonconservation amplitude in cesium // *Phys. Rev. A.* — 2001. — Vol. 63. — P. 044103.
25. Kozlov M. G., Porsev S. G., Tupitsyn I. I., High-Accuracy calculation of 6s-7s parity-nonconserving amplitude in Cs // *Phys. Rev. Lett.* — 2001. — Vol. 86. — P. 3260—3263.
26. Johnson W. R., Sapistein J., Blundell S. A., Atomic structure calculations associated with PNC experiments in atomic caesium // *Phys. Scripta T.* — 1999. — Vol. 46. — P. 184—192.
27. Vasilyev A. A., Savukov I. M., Safronova M. S., Berry H. G., Measurement of 6s-7p transition probabilities in atomic Cs and revised value for the weak charge Q_W // *Phys. Rev. A.* — 2002. — Vol. 66. — P. 020101.

28. Johnson W. R., Safronova M. S., Safronova U. I., Combined effect of coherent Z exchange and hyperfine interaction in parity-nonconserving interaction // Phys. Rev. A. — 2003. — Vol. 67. — P. 062106.
29. Shabaev V. M., Tupitsyn I. I., Pachucki K., Plunien G., Yerokhin V. A., Radiative and correlation effects and parity-nonconserving transition amplitude in heavy alkali-metal atoms // Phys. Rev. A. — 2005. — Vol. 72. — P. 062105.
30. Safronova M. S., Johnson W. R., Safronova U. I., Cowan T. E., Relativistic many-body theory calculation of the Stark-induced amplitude of the 6p-7p transition in thallium // Phys. Rev. A. — 2006. — Vol. 74. — P. 022504.
31. Dzuba V. A., Flambaum V. V., Safronova M. S., Breit interaction and parity-nonconservation in many-electron atoms // Phys. Rev. A. — 2006. — Vol. 73. — P. 022112.
32. Glushkov A. V., Ambrosov S. V., Khetselius O. Yu., et al, QED calculation of the super heavy elements ions: energy levels, radiative corrections and hfs for different nuclear models // Nucl. Phys. A: Nucl. and Hadr. Phys. — 2004. — Vol. 734. — P. 21—28.
33. Kuchiev M. Yu., Flambaum V. V., Radiative corrections to parity nonconservation in atoms and test of the standard model // J. Phys. B. — 2003. — Vol. 36. — P. R191—222.
34. Johnson W. R., Safronova M. S., Safronova U. I., Combined effect of coherent Z exchange and the hyperfine interaction in the atomic parity-non-conserving interaction// Phys. Rev. A. — 2003. — Vol. 67. — P. 062106.
35. Serot B. D., Walecka J. D., Advances in Nuclear Physics Vol. 16: The Relativistic Nuclear Many Body Problem. Plenum Press, New York, 1999.
36. Sahoo B. K., Gopakumar G., Chaudhuri R. K., Das B. P., Merlitz H., Mahapatra U. S., Makherjee D., Magnetic dipole hyperfine interactions in $^{137}\text{Ba}^+$ and the accuracies of neutral weak interaction matrix elements // Phys. Rev. A. — 2003. — Vol. 68. — P. 040501.
37. Glushkov A. V., Ivanov L. N., Ivanova E. P., Radiation decay of atomic states. Generalized Energy approach // Autoionization Phenomena in Atoms. — M.: Moscow State University. — 1986. — P. 58—160.
38. Glushkov A. V., Khetselius O. Yu., Ambrosov S. V. et al, QED calculation of heavy ions with account for the correlation, radiative and nuclear effects // Recent Advances in Theory of Phys. and Chem. Systems (Berlin, Springer). — 2006. — Vol. 15. — P. 285—300.
39. Glushkov A. V., Khetselius O. Yu., Lovett L., Floriko T. A. et al, Gauge-invariant QED perturbation theory approach to calculating nuclear electric quadrupole moments, hyperfine structure constants for heavy atoms and ions // Frontiers in Quantum Systems in Chemistry and Physics (Berlin, Springer). — 2008. — Vol. 18. — P. 505—522.
40. Khetselius O. Yu., On sensing nuclei of the lanthanide isotopes by means of laser spectroscopy of hyperfine structure ^{165}Ho , ^{169}Tm // Sensor Electr. Microsyst. Techn. — 2008. — N 2. — P. 5—9.
41. Khetselius O. Yu., On possibility of sensing nuclei of the rare isotopes by means of laser spectroscopy of hyperfine structure // Sensor Electr. Microsyst. Techn. — 2008. — N 3. — P. 28—33.
42. Khetselius O. Yu., Relativistic calculating the hyperfine structure parameters for heavy-elements and laser detecting the isotopes and nuclear reaction products // Phys. Scripta T. — 2009. — Vol. 135. — P. 014023.
43. Khetselius O. Yu., On sensing nuclei of the ^{207}Bi & ^{207}Pb isotopes by means of laser spectroscopy of hyperfine // Sensor Electr. and Microsyst. Techn. — 2009. — N 2. — P. 26—29.
44. Khetselius O. Yu., Relativistic perturbation theory calculation of the hyperfine structure parameters for some heavy-element isotopes // Int. Journ. of Quantum Chemistry. — 2009. — Vol. 109. — P. 3330—3335.

UDC539.19

O. Yu. Khetselius

DETERMINATION OF THE HYPERFINE AND ELECTROWEAK INTERACTIONS PARAMETERS AND PARITY NON-CONSERVATION AMPLITUDES IN HEAVY FINITE FERMI-SYSTEMS WITHIN NUCLEAR-QED THEORY

Abstract

It is presented new approach to determination of the electroweak and hyperfine interactions parameters and parity non-conservation effect in heavy atomic and nuclear systems, based on the combined QED perturbation theory formalism and relativistic nuclear mean-field theory. Results of estimating some fundamental hyperfine and electroweak constants in the Cs, Tl and Yb isotopes are presented. Firstly it is predicted the weak charge for the Yb nucleus.

Key words: electroweak interaction, parity non-conservation, nuclear-QED theory.

УДК 539.19

О. Ю. Хецелиус

ОПРЕДЕЛЕНИЕ ПАРАМЕТРОВ СВЕРХТОНКОГО И ЭЛЕКТРОСЛАБОГО ВЗАИМОДЕЙСТВИЯ И АМПЛИТУД ПЕРЕХОДОВ С НЕСОХРАНЕНИЕМ ЧЕТНОСТИ В ТЯЖЕЛЫХ КОНЕЧНЫХ ФЕРМИТ-СИСТЕМАХ В РАМКАХ ЯДЕРНО-КЭД ТЕОРИИ

Резюме

На основе нового подхода к определению параметров сверхтонкого, электрослабого взаимодействий и амплитуд переходов с несохранением четности в тяжелых атомных и ядерных системах, базирующегося на ядерно-КЭД теории возмущений и релятивистской ядерной модели среднего поля, получены уточненные данные по параметрам сверхтонкого и электрослабого взаимодействий для ряда изотопов Cs, Tl, Yb. Впервые предсказано уточненное значение слабого заряда для ядра Yb.

Ключевые слова: электрослабое взаимодействие, несохранение четности, ядерно-КЭД теория.

**ВИЗНАЧЕННЯ ПАРАМЕТРІВ ПОНАДТОНКОЇ ТА ЕЛЕКТРОСЛАБКОЇ ВЗАЄМОДІЇ І АМПЛІТУД ПЕРЕХОДІВ
З НЕЗБЕРЕЖЕННЯМ ПАРНОСТІ У ВАЖКИХ СКІНЧЕННИХ ФЕРМІ-СИСТЕМАХ
У МЕЖАХ ЯДЕРНО-КЕД ТЕОРІЇ**

Резюме

На основі нового підходу до визначення параметрів понадтонкої, електрослабкої взаємодії та амплітуд переходів з незбереженням парності у важких атомних та ядерних системах, який базується на ядерно-КЕД теорії збурень та релятивістській моделі середнього поля, отримані уточнені дані по параметрах понадтонкої, електрослабкої взаємодії для ряду ізотопів Cs, Tl, Yb. Вперше передбачено уточнене значення слабого заряду для ядра Yb.

Ключові слова: електрослабка взаємодія, незбереження парності, ядерно-КЕД теорія.

¹ Physical Department of Ivan Franko National University of Lviv6 Kyryla-Mefodia, Lviv, 79005, Ukraine; (0322) 394500; e-mail: konopel@ukr.net

² Chemical Department of Ivan Franko National University of Lviv8 Kyryla-Mefodia, Lviv, 79005, Ukraine; (0322) 600397; e-mail: aksimen@ukr.net

THERMOCHROMIC EFFECT IN CONDUCTING POLYAMINOARENES

Effect of temperature on absorption spectra of sulfate-doped polyaminoarenes — polyaminophenol, polyaniline, polyorthotoluidine, polyorthoanisidine films in temperature interval of 293—523 K has been investigated. On the basis of optical spectroscopy and thermal behavior investigations it shown that changes of electron transport energy and film's optical density may be caused by macro chain conformation and connected with temperature depending electronic properties of conjugated polymers.

INTRODUCTION

Conjugated polyaminoarenes such as polyaniline and its derivatives have a potential technological application in chemical power sources, electrochromic displays and recently attract a great attention as sensor materials [1—4]. Polyaminoarenes are known chromogenic polymers changing their visible optical properties in response to the external stimulus [5—7]. In terms of the specific stimulus they are subclassified as thermochromic (temperature), photochromic (light), electrochromic (electric field), piezochromic (pressure), ionochromic (ion concentration) or biochromic (biochemical reaction). The chromogenic phenomena enable the integration of sensor and actuator functionality or any kind of information respectively into a material itself [5].

Thermochromism is the ability of substance to change color (and optical spectrum) due to a change in temperature and may be used for many novel applications including sensor devices, flat thermometers, battery testers, clothing, and the indicators [6, 8]. Due to very high temperature sensitivity, liquid crystals are used in precision applications; however, their color range is limited by their principle of operation [9]. In contrast, conjugated polymers allow wider range of colors to be used, but their temperature response has not clear understood.

From the physical point of view, the origin of the thermochromic effect in conducting polymers can be multifarious — from conformation state of polymer chain to the freezing of the movement of the dopant substituents and of the movements of polymer-dopant anion association, respectively [10]. Generally the color change is based on alteration of the electron states of molecules, especially the π - or d -electron state. Thermochromic effect can be correlated with the temperature dependence of conductivity [8, 10] and at low temperatures ($T < 100$ K) the sam-

ple is in the insulating state which is another manifestation of the increasing localization of charge carriers [10]. Most interesting is thermochromic effect developing in the temperature interval near human body and ambient temperature (300—400 K) for applying in color indicators that would respond to human touch, environment temperature, etc.

In this paper the influence of polymer link structure on thermochromic effect in the films of sulfate-doped polyaminoarenes — polyaminophenol (PoAP), polyaniline (PAN), polyorthotoluidine (POTI), polyorthoanisidine (PoA) together with their thermal behavior has been studied.

EXPERIMENTAL

Preparation of polyaminoarene films was carried out in tree-compartment electrochemical cell by electrolysis of 0,1M monomer solutions (o-aminophenol, o-anisidine, o-toluidine and aniline) in 0,5M H_2SO_4 at oxidative potential of 0,8—1,0 V. The glass coated by SnO_2 working electrodes, Pt-wire counter electrodes and Ag/AgCl (in saturated KCl) as a reference was employed. After electrolysis during 10—15 minutes the glass electrode with polymer film were rising in distilled water and dried in vacuum at $T = 295—300$ K. Obtained polyaminoarenes are self-doped by sulfate acid in the process of electropolymerization [3]. The molecular structure of main polymer chain (without dopant) supporting by IR-spectroscopy ("Specord M-80") for samples pressed in KBr pellets are presented in the Figure 1.

The UV-vis. absorption spectra in the range of $\lambda = 320—1000$ nm were obtained using the spectrophotometer SF-46 after 10 minutes of film heating at constant temperature in the interval of 293...473 K. Studies of polyaminoarenes thermal behaviour were carried out for powder samples on the derivatograph Q-1500 D in the

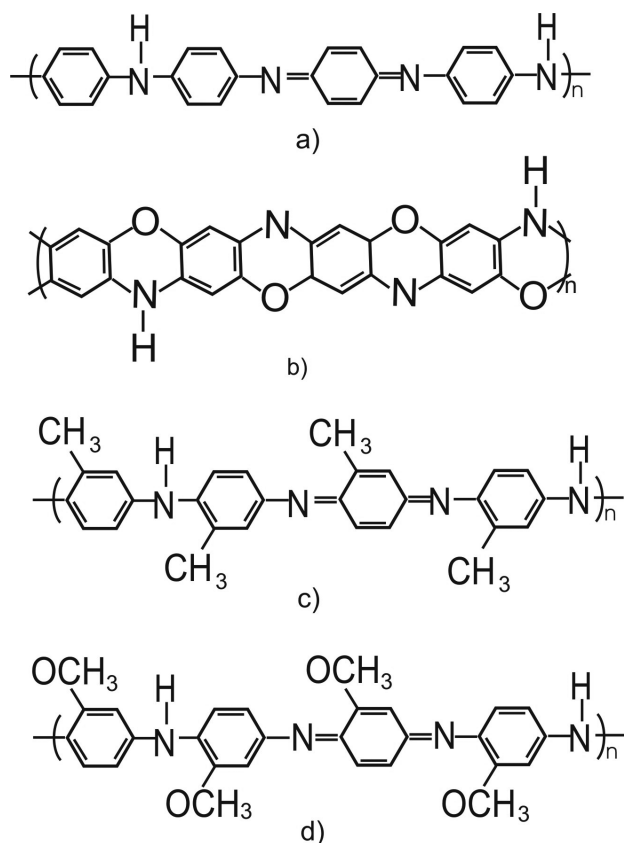


Figure 1. Molecular structure of polyaniline (a), polyaminophenol (b), poly-ortho-toluidine (c), poly-ortho-anisidine (d)

temperature interval of 273–1273 K in air with Al_2O_3 standard at heating rate of 10 K/min.

RESULTS AND DISCUSSION

It has been found that under temperature change in the interval of $T = 293\text{--}473$ K the variations of the colour in conjugated polyaminoarene — PAN and PoTI films may proceed [7]. Recently such effect was manifested also in other polyaminoarenes — PoA and PoAP [8], but detail analysis of the observed phenomenon was not done.

According to electron spectroscopy, for all investigated films in near-UV and visible spectral range (Fig. 2) there are observed three bands typical for polyaminoarenes absorption. The maximum of absorption at 1.4–1.65 eV is characteristic of the free charge carriers, delocalized along conjugated polymer chain [11]. Absorption near 1.9 eV is probably caused by transition in imino-quinoid fragments of polyaminoarene [12]. The band corresponding to energy interval of 3.2–3.4 eV may be assigned to electron transition between π and π^* levels, which associated with energy of band-gap [13]. With temperature increasing the “blue shift” of absorption maximums and changing of their intensity are observed.

Character of the spectral changes in the polyaminoarene films significantly depends on

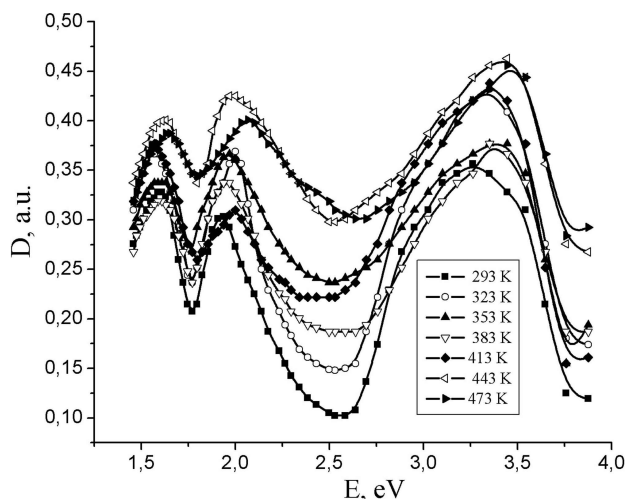


Figure 2. Absorption spectra of PAN (a), PoAP (b), PoTI (c), PoA (d) films heated at the following temperatures

the molecular structure of polymers, namely — presence, position and mutual disposition of substitutes. In particular, for unsubstituted polyaminoarene — PAN (characterized by linear structure presented in Fig. 1, a) — with temperature increasing a shift of absorption maximums is accompanied by the total increasing of the absorption intensity (Fig. 2, a). In the optical spectra of substituted polyaminoarenes character of thermochromic changes is some distinguish.

In the case of PoAP characterized by ladder heterocycle structure (presented in the Fig. 1, b) with temperature rising a monotonic increasing of absorption to temperature of 413–433 K and higher takes a place. At this observed a clear shift of the bands corresponded to $\pi \rightarrow \pi^*$ transitions to the high energy field (Fig. 2, b). At higher temperatures one wide band forms in the interval of $E = 2.9\text{--}3.05$ eV.

For PoTI macrochain with methyl substitute in aminoarene ring (Fig. 1, c) before the temperature of 383–393 K an optical absorption decreases (films become lighter) while in the case of PAN in the temperature interval of 293–473 K the deepness of coloration take a place (Fig. 2, a). It found that for electron spectra of the PoTI films investigated a total decreasing of the second band intensity of absorption is characteristic and almost full disappearance of this band at $T > 413$ K.

An existence of methoxy substitute ($-\text{O}-\text{CH}_3$) in ortho-position to amino group in the molecule of PoA (Fig. 1, d) causes a very interesting thermochromic behavior of this polymer. There are observed two temperature intervals (from 293 to 353 K and 383 to 413 K), in which a decreasing of absorption intensity of PoA is proceeds at overall low wavelength shift of maximum positions (Fig. 2, c).

From the studies of polyaminoarenes thermal behaviour it is established the four extreme points for all samples (Table 1). A first endothermic maximum at $T = 383\text{--}403$ K associ-

ates with a loss of chemisorbed moisture [14, 15]. Sequence of peaks on DTA and DTG curves in the region $T=413\text{--}600\text{ K}$ are evidences to cross-linking of polymer chains (second extreme at $463\text{--}513\text{ K}$), following desorption of doping admixtures ($513\text{--}563\text{ K}$). Attached to temperatures of this maximum the sign change of temperature coefficient of resistance can be observed [3], that have been associated with a loss of doping admixtures and starting the macro chains destruction processes at the temperature $T > 700\text{ K}$.

Table 1

Characteristic temperatures of the conjugated polyaminoarenes thermal behavior

Polyaminoarene	Peak temperature, K			
	Water desorption	Cross-linking in macrochains	Desorption of dopant	Thermal decomposition
PAN	403—413	463—483	533—553	> 723
POTI	373—393	487—498	513—533	> 713
PoA	353—373	463—483	513—533	> 700
PoAP	383—398	473—513	543—563	> 790

To understand a nature of thermochromic effect in conjugated polyaminoarenes we have analyze a temperature dependence of the change in peak position (ΔE) and absorption intensity (ΔD) of the bands corresponded to $\pi\text{--}\pi^*$ transition.

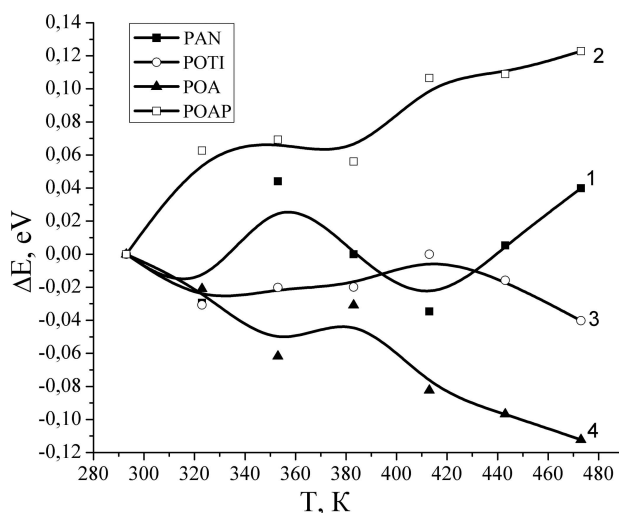


Figure 3. (a) Temperature dependence of intensity and (b) position of absorption band of $\pi \rightarrow \pi^*$ transition in polyaniline (1), polyaminophenol (2), poly-ortho-toluidine (3), polyorthoanisidine (4)

From the fig. 3, a one can see that for PAN and PoA films the intensity changes are not so significant as for PoAP and PoTI films and characterized by some extremes at the temperatures of 320 K, 380 K and in the interval of 430—450 K. It may be suggested that at the temperatures less than 360 K the variations

in optical spectra may be caused by conformation rotation of the substituted phenyl rings [16—18]. Consideration the thermal behavior of polyaminoarenes make it possible to connect the changes at $T > 373\text{ K}$ with the processes of evacuation of chemisorbed water and cross-linking in polymer chains [14]. Probably at these temperatures in PoTI films structure changes in direct to space network formation take place. This decreases a kinetic mobility of polymer segments and breaks an internal rotation. That's why a thermochromic change in PoTI films become irreversible and darkness of polymer film that causes an increasing of optical density is observed. For the PoTI film is observed a decreasing of ΔD to 390 K and in further an increasing of absorption intensity. This temperature associated with moisture evacuation (Table 1). In the case of PoAP is observed almost uniform increasing of band intensity at $E = 1,6\text{ eV}$ when temperature is rising.

In the fig. 3, b presented the temperature dependences of the changes in position of the absorption band corresponded to $\pi \rightarrow \pi^*$ transition. These dependences for all investigated polymers are complex and characterized by some folds. So, for PAN the folds observed at 320, 360 and 410 K, for PoTI — at 320 and 410 K, for PoA — —350 and 380 K, for PoAP — at 340 and 390 K. The first fold may be associated with conformation transition in polymer change, but last — with the changes in electron structure and conductivity in results of water desorption and decreasing the level of protonation in polymers doped by sulfate acid.

It's known, that phenyl group disposition in polyaminoarenes lies under rotation angles, and phenyl ring may revolve around --C--N-- bond [16]. In solid state (in the film) the polymer chain mobility is considerably limited, in comparison with solution, since an absence of large lateral substitutes made impossible the creation of sufficient for conformation change free volume.

In the presence of methyl or methoxy substitute in PoTI and PoA macromolecules the increasing of spatial repulsion between phenyl rings and between neighboring chains [16, 17] occurs in contrast to unsubstituted PAN. Increasing of macrochain repulsion leads to decreasing of conductivity in result of charge localization [18]. From the other hand this repulsion considerably relieves an internal rotation [16]. Therefore in the region of $T = 293\text{--}363\text{ K}$ a thermochromic changes in mainly caused by change of polymer chains conformations and "enlightenment" of the films is observed. In the case of sulfate doped PAN and PoAP when doping leads to structure ordering [3] the difficulty of internal rotation take place. At this time an increasing of charge carriers mobility along polymer chains occurs, that causes an increasing of PAN and PoAP conductivity [3, 10, 11]. This leads to conclusion that variations in electron transition energy and film's optical density is depended on the nature of substitutes

in benzene ring of conjugated polyaminoarene. Thermochromic effect in the temperature interval of 293–363 K are caused by changing in macrochain conformation and connected with depended on temperature electronic properties of polymers, but do not caused by the thermal induced transformation in polymer chain composition.

This work was supported by the budget cost of Ministry of Education and Science of Ukraine given as Ukraine President Grant № GP-f27/0125 (Agreement F27/61-2010).

REFERENCES

1. S. A. Wilson, R. P. Jourdain, Q. Zhang, R. A. Dorey, C. R. Bowen et al. New materials for micro-scale sensors and actuators. An engineering review // *Materials Science and Engineering R: Reports* 2007, 56(1-6), pp. 1–129.
2. P. Kar, C. Narayan, N. C. Pradhan, B. Adhikari, Application of sulfuric acid doped poly (m-aminophenol) as aliphatic alcohol vapour sensor material // *Sensors and Actuators B* 2009, 140, pp. 525–531.
3. O. I. Konopelnik, O. I. Aksimentyeva, B. R. Tsizh, M. I. Chokhan, Physical and Technological Properties of the Sensor Materials Based on Conjugated Polyaminoarenes // *Physics and Chemistry of the Solid State* 2007, 8 (4), pp. 786–790.
4. S. Bhadra, D. Khastgir, N. K. Singha, J. H. Lee, Progress in preparation, processing and applications of polyaniline // *Progress in Polymer Science* 2009, 34, pp. 783–810.
5. A. Seeboth, D. Löttsch, *Thermochromic Phenomena in Polymers*. — Smithers Rapra. 2008, 103 p.
6. A. A. Argun, P. H. Aubert, B. C. Thompson, I. Schwendeman, L. Carleton et al., Multicolored Electrochromism in Polymers: Structures and Devices // *Chem. Mater.* 2004, 16, pp. 4401–4412.
7. O. I. Аксіментьєва, О. І. Конопельник, В. П. Загородський, М. Я. Гриців, Г. В. Мартинюк. Термохромний

ефект в тонких шарах спряжених поліаміноаренів // *Журнал фізичних досліджень* 2004, 8 (4), С. 369–372.

8. O. I. Konopelnik, O. I. Aksimentyeva, G. V. Martynuk, Effect of temperature on the optical properties of conducting polyaminoarenes and their composites with elastic polymer matrix // *Molec. Cryst. Liq. Cryst.* 2005, 427, pp. 37–46.
9. С. А. Пикин, Л. М. Блинов, *Жидкие кристаллы*. Мир Москва, 1999, С. 386.
10. P. Rannou, B. Dufour, J.-P. Travers, A. Pron, D. Djurado, H. Janeczek, D. Sek, Temperature-Induced Transitions in Doped Polyaniline: Correlation between Glass Transition, Thermo-chromism and Electrical Transport // *J. Phys. Chem. B*. 2002, 106(41), pp. 10553–10559.
11. A. J. Heeger, Semiconducting and metallic polymers: the four generation of polymeric materials // *Synth. Met.* 2002, 123, pp. 23–42.
12. О. В. Свердлов, *Электронные спектры в органической химии*, Химия, Ленинград, 1999, С. 298.
13. Ж. Симон, *Молекулярные полупроводники* / Ж. Симон, Ж.-Ж. Андре; пер. с англ. Б. Б. Страумала. Мир, Москва, 1999, С. 344.
14. L. Abella, S. J. Pomfret, P. N. Adamsa, A. P. Monkman, Thermal studies of doped polyaniline // *Synth. Metals* 1999, 84, pp. 127–131.
15. O. I. Aksimentyeva, V. M. Beluh, D. O. Poliovyi, V. V. Cherpak, P. Y. Stakhira, D. Y. Volynyuk, Thermovacuum Deposition and Electrooptical Properties of Polyaniline Thin Films // *Molec. Cryst. Liq. Cryst.*, 2007, 467, pp. 143–152.
16. J. M. Ginder, A. J. Epstein, A. G. MacDiarmid, Phenyl ring rotation, structural order and electronic states in polyaniline // *Synth. Metals*, 1999, 37, pp. 45–48.
17. M. I. Winokur, D. Spiegel, Y. Kim, S. Hotta, A. J. Heeger, Structural and absorption studies of the thermochromic transition in poly (3-hexylthiophene) // *Synth. Metals*, 1999, 28, pp. 419–425.
18. W.-Y. Zheng, K. Levon, J. Laakso, J. -E. Osterholm, Characterization of Solid-State Properties of Processable N-Alkylated Polyanilines in the Neutral State // *Macromolecules*, 1999, 27, pp. 7754–7763.
18. I. D. Norris, L. A. P. Kane-Maguire, G. G. Wallace, Thermochromism in Optically Active Polyaniline Salts // *Macromolecules*, 1999, 31, pp. 6529–6538.

UDC 78.40, 78.66

Konopelnik O. I., Aksimentyeva O. I.

THERMOCHROMIC EFFECT IN CONDUCTING POLYAMINOARENES

Abstract

Effect of temperature on absorption spectra of sulfate-doped polyaminoarenes — polyaminophenol, polyaniline, polyortho-toluidine, polyortho-anisidine films in temperature interval of 293–523 K has been investigated. On the basis of optical spectroscopy and thermal behavior investigations it shown that changes of electron transport energy and film's optical density may be caused by macro chain conformation and connected with temperature depending electronic properties of conjugated polymers.

Keywords: thermochromic effect, polyaminoarenes, optical spectroscopy, thermal behavior, conjugation.

УДК 78.40, 78.66

Конопельник О. І., Аксіментьєва О. І.

ТЕРМОХРОМНИЙ ЕФЕКТ В ЕЛЕКТРОПРОВІДНИХ ПОЛІАМІНОАРЕНАХ

Резюме

Досліджено вплив температури на спектри поглинання плівок сульфатно допованих поліаміноаренів — полі-орто-амінофенолу, поліаніліну, полі-орто-толуїдину, полі-орто-анізидину в інтервалі температур 293–523 К. На основі даних оптичної спектроскопії та дослідження термічної поведінки поліаміноаренів показано, що зміни енергії електронного переносу і оптичної густини плівок можуть бути спричинені конформаційними перетвореннями макроланцюга і пов'язані із залежними від температури електронними властивостями спряжених полімерів.

Ключові слова: термохромний ефект, поліаміноарени, оптична спектроскопія, термогравіметрія, спряження.

ТЕРМОХРОМНЫЙ ЭФФЕКТ В ПРОВОДЯЩИХ ПОЛИАМИНОАРЕНАХ

Резюме

Исследовано влияние температуры на спектры поглощения пленок сульфатно-легированных полиаминоаренов — поли-орто-аминофенола, полианилина, поли-орто-толуидина, поли-орто-анизидина в интервале температур 293—523 К. На основании данных оптической спектроскопии и термического поведения полиаминоаренов показано, что изменения энергии электронного переноса полиаминоаренов и оптической плотности пленок могут быть вызваны конформационными превращениями макроцепи и связаны с зависимыми от температуры электронными свойствами сопряженных полимеров.

Ключевые слова: термохромный эффект, полиаминоарены, оптическая спектроскопия, термогравиметрия, сопряжение.

FEATURES OF THERMO-OPTICAL TRANSITIONS FROM THE RECOMBINATIONAL CENTERS EXCITED STATES

The model of thermo-optical transitions created is confirmed experimentally. The process of hole release from ground state through excited one to valence band includes firstly the transition at phonon absorption $E_R \rightarrow E_{R'}$ with energy 0,2 eV and then excitation to the free state $E_{R'} \rightarrow E_v$ at the expense of photon energy $h\nu = 0,9$ eV.

The research in effect of photocurrent infrared quenching to determine the priority of optical-thermal transitions at hole release from R-centers was carried out.

The optical quenching of photocurrent [1] is the direct consequence in recharge of slow recombination centers as the result of additional impurity excitation. The ground of this phenomenon is that photocurrent excited by light from self-absorption area can be decreased (quenched) by light of definite spectral content. This process can be carried out in the crystals that have S- and R-centers. In the most cases the mentioned effect is accompanied by two maxima in the plot for spectral distribution of quenching ratio $Q(\lambda)$ (Fig. 1, *a*). And so R. Bube [2] offered to observe the excited state of R-levels which corresponding zone band presented by Fig. 1, *b*.

Two-leveled model of R. Bube explains the phenomenon of semiconductor sensitization at presence of slow recombination centers. At the same time the model created is semi-phenomenological. The points mentioned below can be considered as its shortcomings:

I. If localized holes from R' -levels transit thermally with activation energy 0,2 eV to the free state (Fig. 1, *b*), the light quanta with en-

ergy from 0,2 up to 0,9 eV could release them too. In this case the hot vacancies simply appeared in valence band, but longwave sensitivity within the range 1400–1600 μm did not decrease (Fig. 1, *a* — “*a*”).

II. The minimum between two maxima in Fig. 1, *a* — “*b*” could not be observed. The light quanta within the range from $\lambda_1 = 1000$ μm up to $\lambda_2 = 1400$ μm (from 1,1 up to 0,9 eV) can release the carriers from R' -states.

III. In maximum point at 1400 μm (Fig. 1, *a*, — “*c*”) the value Q should be lower than in shortwave range (1000 μm). It should occur because R- and R' -centers have the equal capture cross-sections for holes, but R' -level is influenced by thermal withdrawal of carriers. As the result the steady-state population of R' should be lower than for the basic state R. At the moment of illumination by energy 0,9 eV the pattern becomes indistinct because the additional non-equilibrium charge has appeared as the result of vacancies transition from R- to R' -centers. But resonance light excitation of holes does not occur both to the right and to

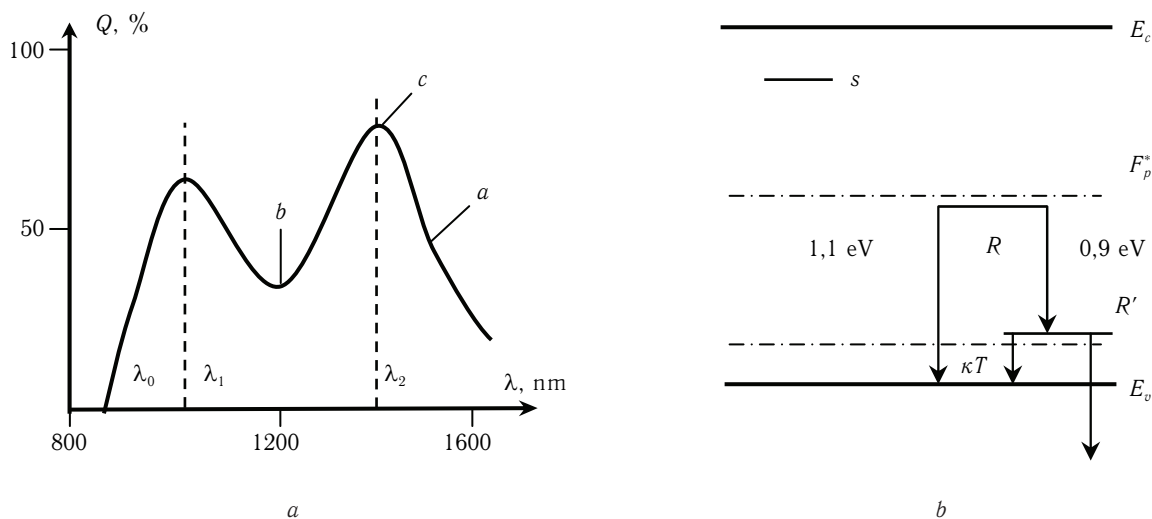


Figure 1. Spectral distribution of quenching ratio (*a*) and band model of R. Bube (*b*) observed experimentally

the left of point "c" in Fig. 1, *a* ($\lambda_{\max} + d\lambda$ and $\lambda_{\max} - d\lambda$). If the curve $Q(\lambda)$ is smooth, and only such curves were observed experimentally, $Q(\lambda_2)$ in this case would be lower than $Q(\lambda_1)$.

So the interpretation of Bube model required the additional research. In papers [3,4] the authors showed that intensity of IR-light could not be too much. The number of absorbed IR-photons should correspond approximately to concentration of R -centers in order to observe the quenching effect. Since capture cross-sections $S_{pr} = S_{pr'}$, IR-photons divide approximately in two between R - and R' -centers. Two photons are required for transit passage of holes firstly from R to R' -level and then to valence band. So the longwave maximum would be provided by the smaller number of released holes than the shortwave one. And investigation of such processes requires the greater period of time.

IV. If the model in Fig. 1, *b* was realized, the additional quenching maximum with energy 0.2 eV ($\lambda \sim 7500$ nm) might exist in the remote IR-region when thermal transitions are changed by the optical ones. At the same time, if the maximum is shadowed by phonon activity, its intensity should be raised with increase of crystal illumination by intrinsic light when population of R' -levels increases. But such maximum of quenching has not been already observed [5]. We observed that the height of quenching maxima in the nearest IR-region (1000 и 1400 μm) decreases with increase of intrinsic excitation.

V. The symmetry of quenching maxima at λ_1 and λ_2 was observed (Fig. 1, *a*). Two wide bands were determined experimentally, both were slightly smeared to the left of maxima directed to the higher energies. This result explains that hole release from R and R' levels is carried out directly to the band. At photon energies exceeded activation energy of a trap the vacancies have the possibility to transit to the deeper levels in valence band. Meanwhile, the longwave maximum at 0,9 eV ($\lambda = 1400$ μm) should be weaker than the shortwave one and strongly symmetrical because the transitions $R \rightarrow R'$ bears the resonance view.

VI. Proceeding from the same suppositions, the straight line should be observed after the second maximum at Fig. 1, *a*. Photons with energy being lower than 0,9 eV can not shift holes from the basic state to the excited one.

VII. If the model from Fig. 1, *b* operates, the distance between the basic and the excited states of sensitization centers $E_R - E_{R'} = = h\nu(\lambda_2) = 0,9$ eV. That means that at room temperature when spectrum $Q(\lambda)$ was registered (Fig. 1, *a*) this distance is greater by 36 folds than phonon energy $kT = 0,025$ eV. If one takes into consideration that namely this temperature causes the splitting of R' -centers excited state out of the basic one, such divergence is seemed unlike.

VIII. In accordance with the model, at illumination by light of wavelength λ_2 the intra-center transitions $R \rightarrow R'$ take place (Fig. 1, *b*) and occupation of R' levels should increase but for the basic levels R — decreases. Experimentally we observe the smooth dependencies on intensity of longwave light. This shows that the processes occur in the common way without changes of mechanism along the whole range and large illuminations $p_{R'} \gg p_R$. Owing to large concentration of holes at R' , they should be located **under** Fermi quasi-level, i. e. value F_p^* lies within the range between $E_{R'}$ and E_v . But since occupation p_R at large intensities is low these levels are **over** Fermi quasi-level, i. e. the value F_p^* is lower than E_R . These processes can not occur simultaneously because $E_R \gg E_{R'}$.

IX. The excited state of hole interacts with the basic one at any temperature [6]. In the model the states R' exchange holes with valence band solely at 300 K. And owing to its depth the basic level can only capture the carriers from there. The interaction between levels is not supposed.

The basis to create the band model in Fig. 1, *b* was taken the shape of spectral characteristics $Q(\lambda)$ in Fig. 1, *a*. But the presence of two quenching maxima with the same activation energies can be explained differently as it was shown in Fig. 2, *b*. The following ex-

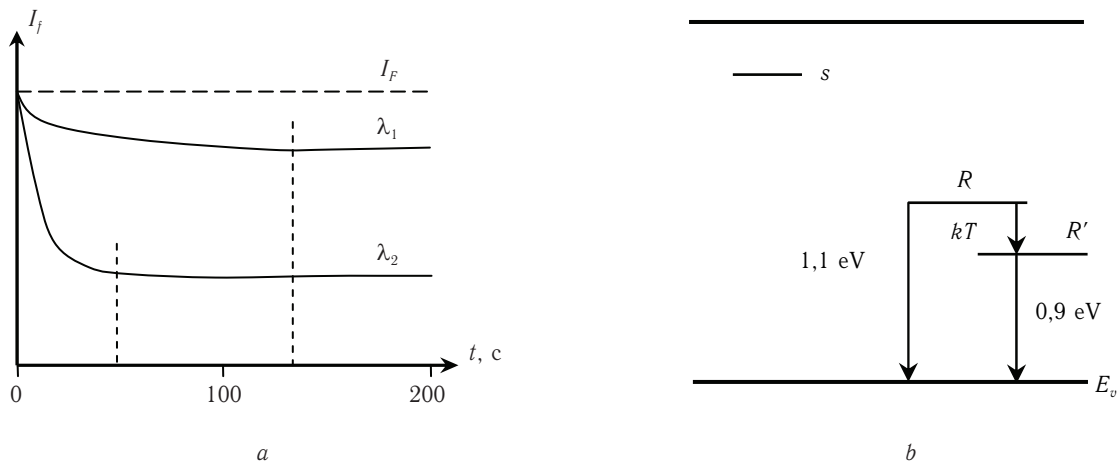


Figure 2. Photocurrent relaxation at additional illumination from quenching maxima (*a*) and the alternative band scheme (*b*)

perimental data support the abovementioned situation.

1. RELAXATION CURVES

The sample was excited by intrinsic light and then additionally by infrared illumination from quenching bands either λ_1 or λ_2 (Fig. 1, *a*) to research photocurrent relaxation (Fig. 2, *a*). The intensities of intrinsic and quenching light were chosen as recommended in [3, 7, 8]. The curves of both plots began from one and the same point corresponded to the value of intrinsic current. The ordinary mechanism of quenching was carried out with the additional influence of IR-light.

A) The steady-state value I_F is defined by level population. The smaller change in photocurrent was observed that fully corresponded to Fig. 1, *a* for lower value Q at illumination light of λ_1 wavelength.

B) The slope of plot at $t=0$ for the same curve is smaller because it was defined by number of dislodged carriers proportional to concentration of holes in R -levels.

C) Fig. 2, *a* shows that a period to adjust steady-state photocurrent differs approximately by three times that is caused by interaction of levels at both quenching procedures. The light of wavelength λ_1 knock out holes from the basic state R and the excited state R' plays as damper — the part of its holes drops to R centers and delays relaxation. When levels R' are activated by light of λ_2 wavelength, this role transmitted to R centers. And relaxation finishes considerably quicker because the number of holes there is lower. Hence, three particularities of relaxation curves point out the lower occupation in basic state of R -centers (point III).

2. MIGRATION-RELAXATION CHANGES. LARGE INTERELECTRODE DISTANCE

Filamentary CdS crystals with interelectrode distance 2—3 mm were chosen to research coordinative redistribution of impurity. The investigation in effect of photocurrent IR-quenching confirmed the existence of R - and S -centers which concentrations being approximately equal and.

Photosensitivity was not observed completely when samples exposed by intrinsic light and located in darkness for a long time (2—3 months). Then photosensitivity restored during several days besides crystals were exposed by monochromatic light with wavelength 515 nm [9]. The process took place and was independent on number and duration of exposures and remained identical even at one illumination of 10 sec per day. The rate of photosensitivity restoration was observed maximal at the beginning and then its raise decreased. Af-

ter approximately 100 hours photocurrent became stable and did not respond to 24-hour exposures.

The intensity of photocurrent longtime relaxation was managed to activate at higher temperatures (approximately up to 40—50 °C to avoid photocurrent temperature quenching). The restoration of sensitivity was considerably broken by infrared light with $\lambda = 1400$ nm, 0,9 eV.

The durations of the observed phenomena excluded any electron processes. And ion-migration model were taken to explain the situation.

It was shown the presence of considerable cut-off barriers. After preliminary exposure R -centers trapped the positive charge [10] are drawn by near-contact field ($\sim 10^5$ V/cm) into space-charge region and accumulate there. These traps with depth ~ 1 eV can keep holes for a long time and thus migrate even in darkness. As positive charge accumulates in barrier region the height of barrier decreases and the situation becomes more stable. If R -centers continue to locate in steady-state-conditions, they slowly recombine and transit to the neutral state but remain in space-charge region as before.

At the following illumination by intrinsic light and under external voltage applied the charged R -centers at the expense of diffusion and drift migrate to the central part of crystal and sensitize it. The higher temperatures increase their mobility without changes in charge state because thermal transitions are intra-center (Fig. 2, *b*). According to this model IR-light (λ_2) knock out holes from the most occupied R -levels. Then both diffusion and drift are delayed.

If the other model would exist (Fig. 1, *b*), IR-light caused intra-center transitions and temperature devastated the excited states. The depth of R' levels 0,2 eV can not provide the longterm keeping of charge in darkness and accumulation of traps in space-charge region.

3. MIGRATION-RELAXATION CHANGES

Small interelectrode distance. Since near-contact barriers play the significant role in longtime relaxation of photocurrent it was interesting to make this influence enhanced. The contacts on the same samples shifted up 0,1—0,2 mm. In this case the interelectrode distance is comparable to width of space-charge region. Thus, contact barriers and processes occurred control current. In crystals with small intercontact distance after stay in equilibrium conditions we observed the unusual form of photocurrent relaxation.

Photocurrent at low level of intrinsic illumination (1—3 lx) reached the steady-state during several seconds. For higher illuminations

(10—15 lx) photocurrent firstly raised during 3—4 min (1 stage), then during 15 min its value decreased approximately 30 % (2 stage) and then reverted to the same value and stabilized during 45—50 minutes.

These processes can be explained as follows. At the first stage the raise I_F is defined by usual relaxation increase of electron concentration. R -levels collected in barrier area captured the charge resulting in lowering of Schottky barrier that could not keep them. Space-charge region widens at the second stage as R -centers migrate from here [11]. Its resistance raises and current drops. At the third stage current increases because of two reasons: widening of contact leads to reduction in central part of crystal. Simultaneously it is sensitizing by extracted R -centers. This process is longterm because the time to distribute impurity along the crystal is required. As result, current stabilized at the same level as before will formation because the number of centers leaving space-charge region corresponds to the number of centers causes the changes in the central part of the crystal.

Obviously at weak illumination the mentioned processes are not observed — the number of R^+ is considerably small and their doping is seemed to be negligible.

In order to research this model we decreased concentration of charged impurity by IR-radiation with energy 0,9 eV. And all the particularities of relaxation disappeared. Photocurrent curve without minimum point came to saturation during longer periods that in several times prevailed the period when maximum I_F was reached. The absolute value of photocurrent I_F is observed by an order of magnitude lower.

This confirmed the structure of band diagram 2, *b* but do not agree with model in Fig. 1, *b*.

4. ILLUMINATION-CURRENT DEPENDENCIES

A) The dependence of quenching ratio Q on intensity of exciting and quenching light based on model of Fig. 2, *b* was obtained in [3] and the formula has been confirmed experimentally. When the value for absorbed photons of intrinsic light raises Q drops, but with raise in intensity of longwave light quenching increases and this is not agree with model 1, *b*. Two-stage transition should minimize the influence of this light on quenching ratio.

B) The analysis in rate for quenching maxima increase was carried out. With raise in number of infrared photons the value of minimum between maxima decreases. This can be explained (see Fig. 2, *b*) as follows: photons with energy between maxima from 0,9 up to 1,1 eV can effectively absorbed by both levels.

C) The conditions when the first maximum of Figure 1a was practically absent were created in the narrow region of relationship between applied field, temperature and intensity of longwave light with $\lambda_1 \sim 1000$ nm [8].

This was explained by the repeated capturing of traps. Directly after activation the hole locates in the vicinity of mother center and has the energy benefits to come back. This is confirmed by the value of quantum yield for IR-light within the range 0,03—0,07 determined in [7] to be anomalously low.

These processes combine very well with the alternative model 2, *b*. And the probability to capture holes to these levels being proportional to the number of free places is considerably lower.

D) In paper [12] it was shown that illumination-current characteristics $I_F(L)$ observed linear when crystal was influenced only by intrinsic light. They became superlinear under additional infrared illumination but at lower absolute values of current. This process was observed both for wavelengths λ_1 and λ_2 .

This corresponds completely to band diagram of Fig. 2, *b*. The transitions either from R - and R' -levels are equivalent here.

5. REVERSAL PLOTS

The performance of $Q(\lambda)$ parameter at reversal mode of excitation was investigated in [13] The plots measured with different rate of wavelength change to increase and then to decrease were compared. The difference consisted in the sequence of center excitation.

Model 1, *b* does not suppose the interaction between levels (see item IX). So the shape of maxima $Q(\lambda)$ should not changes at any procedure of measurements independently on rate of wavelength raise or decrease. Infrared light simply indicates the stage of R and R' level occupation with holes.

If the levels thermally interacts as shown by the alternative model the pattern changes. In this case the influence on one level changes the dependence on the on the other. If the measurements are carried out beginning from the longer waves to the shorter ones, R' centers exited firstly. The holes increase their transitions from the basic states to the released places. So maximum $Q(\lambda_1)$ will be smaller when wavelength decreases up to λ_1 because of smaller occupation of R -centers. The time is required for thermal transitions $R \rightarrow R'$. So the value of decrease will be dependent on rate for changes in wavelength $\frac{d\lambda}{dt}$. The higher it will be the smaller changes take place. So, in this case maximum $Q(\lambda_2)$ is observed without changes, but maximum $Q(\lambda_1)$ decreases depending on applied $\frac{d\lambda}{dt}$ value.

If the spectrum is measured to the direction of wavelength increase, the maximum $Q(\lambda_1)$ observed stable. But namely light influence at measurements decreases thermal flow of holes to R' centers. When light energy will drop up to $E_{R'}$, the number of hole transitions from spectrum to free state decreases. In this case the maxi-

imum $Q(\lambda_2)$ decreases the strongly the longer time was needed for thermal transitions from R -levels, i. e. the slower changes in wavelength the slower rate $\frac{d\lambda}{dt}$.

The decrease of maxima $Q(\lambda)$ by turn in spectral area being remote from the beginning of wavelength change was observed in [13] that was the additional argument in favour of the model 2, *b*.

6. THE PROCESSES ON SHORTWAVE BOUND OF QUENCHING

The authors [14] show that the value I_F does not change at shortwave bound of quenching area because the intensities of photoexcitation and quenching processes are equal. Since each of them depends differently on external effects — the values of light beams, temperature, applied voltage — the changes of these parameters should result in displacement of wavelength to start quenching.

A) We can not observe the changes in λ_0 area (Fig. 1, *a*) connected with variation of voltage applied to sample or intensity of intrinsic light. The raise of intrinsic excitation takes place similarly in both models. This leads to increase of level occupation. On exposure the yield is observed higher, recombination rate increases quickly that rate of photoexcitation at absorption edge. The bound λ_0 shifted to the shorter wavelengths.

One and the same result was reached for the different intensities of IR-light in measurements of spectral dependencies from shorter to longer wavelengths. The greatest effect on λ_0 position gives the followed spectral area $Q(\lambda_1)$ that is connected with transitions from basic states operating similarly in both models.

B) The transitions with energy 0,9 eV and 1,1 eV have the different rates and take place in measurement of $Q(\lambda)$ from longer wavelengths to shorter ones. The higher the intensity of light the more evident particularities observed.

If model 1, *b* operates at preliminary illumination by light with energy 0,9 eV levels R are devastated and at the following excitation with energy 1,1 eV their photoresponse will be lower. The rate of quenching in λ_0 decreases respectively. The value λ_0 should shift to the right and the higher the rate $\frac{d\lambda}{dt}$ the evident the picture. But the opposite situation was observed in experiments. The higher the rate of wavelength change the smaller shift of quenching bound λ_0 to the higher values.

This corresponds to the alternative model 2, *b*. Illumination with energy 0,9 eV devastated R centers. Thermal ejection of holes $R \rightarrow R'$ increases because there are larger free places. The shoots of holes from R -centers at the moment of illumination with energy 1,1 eV will be less because of the smaller occupation. The

decrease in recombination rate results in shift of λ_0 to the longer wavelengths, but this process is inertial because of the additional stage of thermal transitions limited by probability phenomena.

C) The differentiation connected with temperature change at registered voltage and light intensity is carried out better that is observed at measurement in the increasing wavelength of quenching light.

In model 1b the holes are knocked out from R' -states by thermal energy. The occupation of basic levels does not change there. And the influence of maximum $Q(\lambda_1)$ remains stable. One should expect the registered value λ_0 but it shifted from 920 up to 940 μm along the measurements with temperature raise. This situation takes place because holes shift from R -levels to R' ones. And illumination with wavelength λ_1 knocks out the smaller number of carriers. The processes of quenching are oppressed and the restoration of equality with rate of excitation is possible only at longer wavelengths.

6. CONCLUSION

The experiment which results are unambiguously defined by the active model of Fig. 1, *b* or 2, *b* is described in [3]. The plots $Q(\lambda)$ for room and increased (up to 45—50°) temperatures were compared to avoid the effects connected with temperature quenching.

Spectral position of maximum $Q(\lambda_1)$ did not change under heating. In both models it is bound with hole release from basic state of R -levels.

A) Its height with heating slightly decrease. This testifies to favour of diagram 2, *b*. In this case the number of holes coming to R' -centers should increase. Occupation of R -levels drops. Light of wavelength λ_1 knocks out the smaller number of carriers than in model 1, *b*, where the temperature influences only on R' -levels. When light with wavelength λ_2 is absent the optical transitions $R \rightarrow R'$ should not take place. The occupancy, the number of holes released from R -levels and the height of maximum $Q(\lambda_1)$ with temperature increase should be stable.

B) The second maximum $Q(\lambda_2)$ undergoes the greatest changes at heating. The increase of temperature in model 1, *b* results in devastation of R' -centers. In the alternative model occupation of R' -levels should increase because the number of transitions there from the basic state increases. In experiment we observe the increase of longwave maximum $Q(\lambda_2)$.

C) The change in energy position of R' -levels should occur with temperature changes. At $T=0$ the changes are not observed. With temperature raise the walls of energy well for holes widen in space of quasi-impulse. And the moment when two quantum wavelengths for holes are along between them comes. The excited state R' appears. In model 1, *b* this occurs at 170—190 K for cadmium sulphide [2].

The gap from the basic state (~ 1 eV) is rather big — see item VII. At the further temperature raise the walls of hole continue to wide. The energy $E_{R'}$ raises. For both models the heating should be accompanied by approach of energy for $E_{R'}$ to E_R .

Our temperature range 20—50 °C was very narrow to observed the mentioned process. But with changes in energy distances the probability to absorb phonons by bound holes changes exponentially. If the model 1b operates, as R' -levels remove from the top of valence band the probability of holes release from them decreases. The probability to absorb photons λ_2 should decrease too. Maximum $Q(\lambda_2)$ becomes shorter. If the gap $E_R - E_{R'}$ decreases in case of model 2, b , the greater number of phonons in Maxwell distribution provides the transition of equilibrium holes to R' -levels and their concentration there increases. And light is possible to transit the greater value of charge to free state. Maximum $Q(\lambda_2)$ raises.

Hence, the diagram of Fig. 2, b confirms experimentally.

So, the created model of thermal-optical transitions reduces the shortcomings I—IX of model 1, b and is confirmed by experimental data 1—7. The process of hole release from the basic state — through the excited one — to the valence band begins from transition with absorption $E_R \rightarrow E_{R'}$ of phonon with energy 0,2 eV and only then the excitation to free state $E_{R'} \rightarrow E_v$ at the expense photon energy $h\nu = 0,9$ eV. Band diagram of Fig. 2, b is realized.

Thus, proposed model of thermo-optical transitions proves to be true by the experimental data 1—7. The mechanism of holes release from the ground state through excited in the valence band includes first a transition with a phonon absorption $E_R \rightarrow E_{R'}$ at 0,2 eV energy, and only then excitation in the $E_{R'} \rightarrow E_v$ free state due to phonon energy $h\nu = 0,9$ eV. The zonal plot Fig. 2, b is realized.

UDC 621.315.592

A. S. Melnik, Y. N. Karakis, M. I. Kutalova, G. G. Chemeresjuk

FEATURES OF THERMO-OPTICAL TRANSITIONS FROM THE RECOMBINATIONAL CENTERS EXCITED STATES

Abstract

The model of thermo-optical transitions created is confirmed experimentally. The process of hole release from ground state through excited one to valence band includes firstly the transition at phonon absorption $E_R \rightarrow E_{R'}$ with energy 0,2 eV and then excitation to the free state $E_{R'} \rightarrow E_v$ at the expense of photon energy $h\nu = 0,9$ eV.

The research in effect of photocurrent infrared quenching to determine the priority of optical-thermal transitions at hole release from R -centers was carried out.

Key words: photocurrent infrared quenching, optico-thermal transitions, R -center.

УДК 621.315.592

А. С. Мельник, Ю. Н. Каракис, М. И. Куталова, Г. Г. Чемересюк

ОСОБЕННОСТИ ТЕРМО-ОПТИЧЕСКИХ ПЕРЕХОДОВ С ВОЗБУЖДЁННЫХ СОСТОЯНИЙ РЕКОМБИНАЦИОННЫХ ЦЕНТРОВ

Резюме

Созданная модель термооптических переходов подтверждается экспериментальными данными. Процесс освобождения дырок с основного состояния — через возбуждённое — в валентную зону включает в себя сначала переход с поглощением фонона $E_R \rightarrow E_{R'}$ с энергией 0,2 eV, и лишь затем возбуждение в свободное состояние $E_{R'} \rightarrow E_v$ за счёт энергии фотона $h\nu = 0,9$ eV.

Проведены исследования эффекта инфракрасного гашения фототока для определения очерёдности оптико — термических переходов при освобождении дырок с R -центров.

Ключевые слова: эффект инфракрасного гашения, оптико-термические переходы, R -центр.

УДК 621.315.592

А. С. Мельнік, Ю. Н. Каракіс, М. І. Куталова, Г. Г. Чемересюк

ОСОБЛИВОСТІ ТЕРМО-ОПТИЧНИХ ПЕРЕХОДІВ ЗБУДЖЕНИХ СТАНІВ РЕКОМБІНАЦІЙНИХ ЦЕНТРІВ

Резюме

Розроблена модель термооптичних переходів підтверджена дослідним шляхом. Процес звільнення дірок з основного стану через збудження — у валентну зону складається спочатку з переходу з поглинанням фонону $E_R \rightarrow E_{R'}$ з енергією 0,2 eV, і потім збудження у вільний стан $E_{R'} \rightarrow E_v$ за рахунок енергії фотона $h\nu = 0,9$ eV. Проведені дослідження ефекту інфрачервоного гасіння фотоструму для визначення послідовності оптико-термічних переходів при звільненні дірок з R -центрів.

Ключові слова: ефект інфра-червоного гасіння, оптико-термічні переходи, R -центр.

PHOTOACOUSTIC TRANSFORMATION IN “POROUS SILICON — FLUID” COMPOSITE SYSTEMS: INFLUENCES OF FLUID MOTION

In the present work we demonstrate that thermally induced pressures inside the pores of mesoporous “PS — fluid” composite systems have significant influence on the value and time dependence of PA signal under its piezoelectric registration. This pressure causes an increment of front steepness of the PA signal. Besides, the relaxation of this pressure resulted in extremums on the oscillograms of composites with low-viscous liquids. Experimental value of thermally induced nonequilibrium pressure relaxation time exceeds its theoretical estimation on one order of magnitude. The most important factor of this deviation can be caused by variability of the pore's cross — section. The results of this work can be applied for study of porous materials morphology and also development of sensor systems.

INTRODUCTION

Methods of photoacoustic (PA) spectroscopy are widely applied for investigation of optical, thermophysical, transport, adsorption and other properties of porous materials and powders [1—3]. Application to porous materials of PA methods possesses several advantages comparing to traditional ones.

The PA methods are based on the PA effect, which consists in excitation of elastic vibrations in the substance under absorption of modulated irradiation. Processes of fluid percolation inside the porous matrix under the thermally induced pressures (TIP) determine some peculiarities of PA effect in the composites “porous matrix — fluid”. Previously these peculiarities were successfully applied for estimation of the porosity of the materials with open pore geometry [4]. In this case classical gas-microphone method of PA signal formation was used, and the pores were filled with gas. As it was shown in [2, 4], part of the gas releases from the pores under the heating due to TIP induced gas movement, which resulted in impact to PA signal, additional to common “gas pistol” mechanism [5]. It is obviously, that in some range of pore size (D), where viscous resistance of gas flow inside the pores is significant, but the percolation of gas still takes place, the value of TIP inside the pores as well as PA signal parameters (phase and amplitude) are sensitive to D . This state usually appears when D is in order of microns.

According to preliminary estimations, the effects related to viscous flow of liquids in porous composites under the TIP should appear for significantly smaller D values than for gases, first of all due to much lower compressibility of liquids. Hence the above mentioned effects could be used for the characterization of morphology

of nanostructured porous materials (in particular for the determination of D).

An application of gas-microphone methods for the composites with liquids should be straitened due to significantly lower thermal expansion of liquids comparing to gases. Furthermore, the volume of liquid, participating in signal formation (in the layer with thickness equal to thermal diffusion length $d_c = (2k_c/c_c\rho_c\omega)^{1/2}$, where k_c — is a thermal conductivity of the composite, c_c , ρ_c — its thermal capacity and density, $\omega = 2\pi f$, f — light modulation frequency), is significantly smaller than the volume of gas pistol (gas layer with thickness $d_g = (2k_g/c_g\rho_g\omega)^{1/2}$ near the sample surface, the index g here relates to the gas). Hence, the component of gas-microphone PA signal, appeared due to the expansion of liquid, is small in comparison with usual mechanism of its formation, and therefore is difficult to be registered.

In case of piezoelectric registration the situation is significantly different. In this case under the low frequencies of modulation [6] the signal is caused by the quasi-static deformations appeared due to thermoelastic stresses in the sample. For the composite “porous matrix-liquid” these stresses are resulted by joint action of two comparable factors: thermoelastic stresses in porous matrix and TIP of the liquid inside the pores. The percolation of liquid results in the relaxation of TIP, which should be displayed in modulation of parameters of PA signal registered by piezotransducer. That is why in the present work we have used a piezoelectric method of PA signal formation.

EXPERIMENT

To clarify the role of TIP in PA signal formation in the composites the porous silicon (PS)

was applied as a porous solid matrix. The PS has uniform open pores, the diameter of which can be varied in a wide range by anodization parameters tuning. That is why it is possible to choose a material with the value of D , providing the peculiarities of PA experiment, related to viscous flow of liquid. Besides, the PS is usually obtained as a layer on a monocrystalline Si (c-Si) substrate. Presence of the substrate significantly simplifies the realization of PA experiment; this eliminates the problem of thermal and acoustic contacts with the porous material.

The geometry of experimental the sandwich structure is represented on the Fig. 1. The layers 1 and 2 with a total thickness of $h = 300 \mu\text{m}$, the layer 1 with $h_1 = 50 \mu\text{m}$ is a composite of the PS with the pores filled with liquid. The porosity of the PS (ϵ) is approximately 60 %, the pores are opened and a characteristic pore diameter of $\sim 20 \text{ nm}$. The layer 2 with the thickness $h_2 = 250 \text{ nm}$ is a single crystal silicon substrate. The layers 3–6 transducer: layer 3 — buffer glass-ceramic plate, layer 5 — 200 μm thick piezoceramic (PZT) with the polarization axis perpendicular to the layers, layers 4 and 6 — electrodes. An alternating electric potential was taken from the electrode 6 through the preamplifier with an input impedance of 100 $\text{M}\Omega$ to a lock in nanovoltmeter and fed to an oscilloscope.

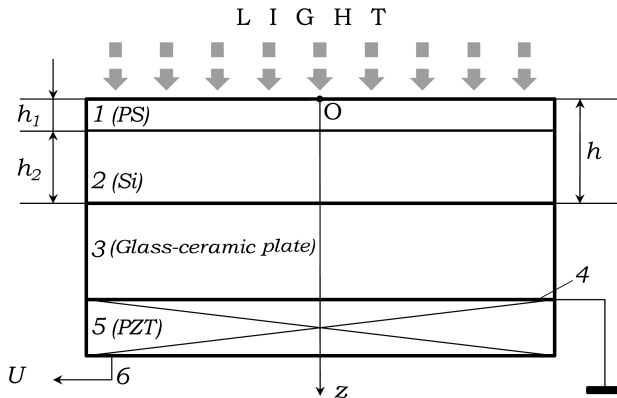


Fig. 1. Geometry of the system “sample — piezotransducer”:

Layers 1 and 2 — sample: 1 — the composite PS with liquid or air in the pores; 2 — c-Si. 3–6 — transducer: layer 3 — buffer glass-ceramic plate, 5 — piezoceramic (PZT); 4 and 6 — electrodes

Low thermal conductivity (k) and temperature conductivity coefficient (α) of glass-ceramic layer in the transducer allow localization of alternating component of the temperature and therefore of the region of thermoelastic forces formation within the boundaries of the sample in all studied range of modulation frequencies. Besides that due to the presence of glass-ceramic layer overall thickness of the layered structure (1.2 mm) is much higher than the thickness of the sample (h), Fig. 1. In this case, in accordance with the results of the work [7], an alternating potential \tilde{U} on the electrode 6 (the

PA signal) can be assigned as proportional to the value of deformational force:

$$\tilde{U} \sim F = \int_0^h \tilde{T}(z, t) dz. \quad (1)$$

Here \tilde{T} is a variable component of thermoelastic stresses in the transverse section of the sample plate, z is the transverse coordinate, and t is the time.

In assumption of independence of stresses in the solid matrix from the TIP of liquid the thermoelastic stresses in the composite can be represented as:

$$\tilde{T}(z, t) = \alpha \cdot \tilde{\theta}(z, t) \cdot \hat{E} + \epsilon \cdot \tilde{P}(z, t). \quad (2)$$

If the material of the layers is assumed as homogeneous and isotropic, then: $\hat{E} = E/(1 - \sigma)$, where E — modulus of elasticity, σ — Poisson coefficient, $\tilde{P}(z, t)$ — fluid pressure inside the pores, $\tilde{\theta}(z, t)$ — variable component of the temperature.

Periodic thermal perturbations (thermal waves) were excited in the samples by radiation of a blue LED operating at an electric power of 3 W, which was modulated by rectangular pulses (at an off/duty ratio of two) and frequency 40 Hz. The intensity of light collected and uniformly distributed over the sample surface was about 1 mW/cm^2 . The light flux was modulated by interrupting the pump current to the LED.

Time dependencies of the potential $U(t)$ taken from the piezotransducer (the PA signal) for the composites with pores, filled with mineral oil (1) and ethanol (2) are represented on the Fig. 2. These two liquids were chosen due to their perfect wetting of the PS and significantly different viscosities. The dependence for the porous composite without liquid (3) is also shown for the comparison.

As it can be seen from the Fig. 2, the rate of potential increase for the composites is significantly higher than for the sample without liquid. Besides that, the dependencies $U(t)$ are signifi-

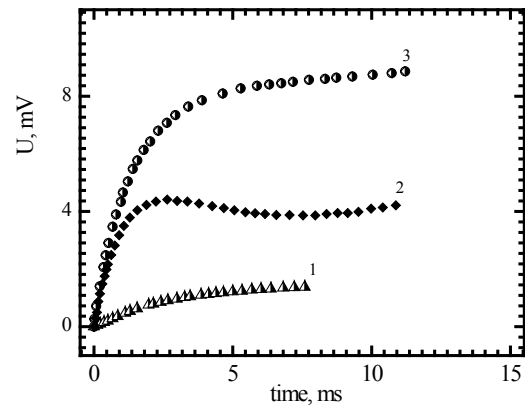


Fig. 2. Experimental dependencies of voltage on piezotransducer electrodes from the time after LED switching on

cantly different for both composites. A minimum can clearly be seen on the oscillograms of the samples with ethanol, but for the samples with oil no minimum was observed [7]. In all studied frequency range (10 Hz — 2 kHz) the amplitudes of PA signals for the composites are several times higher than the amplitude of the PA signal of the PS without liquid at the same frequency. For high frequencies the ratio of the amplitudes reaches 9 for the composite with ethanol and 20 for the sample with oil.

DISCUSSION

Changes of the front slope and amplitude of the PA signal from the composites "PS-liquid" in comparison with initial PS are resulted from the impact of TIP in the thermoelastic stresses in the composite. This impact increases the coefficient of thermal expansion of the composite in comparison with initial PS as well as silicon. Thermal conductivity (and hence the thermal activity) of c-Si substrate is significantly higher than for the PS-based composite. That is why, when the front of thermal perturbation reaches c-Si substrate, rise in temperature significantly slows down due to the superposition of primary and secondary thermal perturbations. The heat, additionally coming into the sample, redistributes into the substrate, thermal expansion coefficient of which is significantly lower in comparison with corresponding coefficient of the PS-liquid composite. As a result, the steepness of curves 1 and 2 decreases when thermal perturbation reaches the substrate (approximately in 1—2 ms after switching on the LED, see Fig. 2).

The heat, additionally coming into the sample, comes into the support, thermal expansion coefficient of which is significantly lower in compare to corresponding coefficient of the PS-liquid composite. As a result, the steepness of curves 1 and 2 (Fig. 2 decreases when thermal perturbation reaches the support (approximately in 1 — 2 ms after the light diode is on).

Minimum on the curve 2 can be related to the relaxation of TIP due to the percolation of ethanol in the composite pores. The viscosity of oil is much higher than of the ethanol, so the TIP of the sample with oil can not significantly relax during the time of modulation period, so the minimum on the curve 1 (Fig. 2) is absent.

Let's estimate the relaxation time τ for the TIP in the composite layer. The length of attenuation (l_p) of periodic pressure perturbations with the frequency f can be equated with the thickness of the composite layer h_1 . For the pores filled with the gas the l_p can be calculated according to the equation [3, 4]:

$$l_p = \frac{v \cdot D}{2 \cdot \gamma \cdot \sqrt{2\pi}} \cdot \sqrt{\frac{\rho}{\eta \cdot f}}, \quad (3)$$

where v is the sound velocity in the gas, γ is the adiabatic index, ρ is the density, η is the viscosity.

For the liquids the sound velocity is $v = 1/\sqrt{\chi \cdot \rho}$, where χ is the compressibility of the liquid, and taking into account that the heat capacity at constant pressure (CP) and the heat capacity at constant volume (CV) are almost equal for liquid let us assume that $\gamma \cong 1$ so the equation (3) can be rewritten as:

$$l_p \cong \frac{D}{2 \cdot \sqrt{2\pi \cdot \chi \cdot \eta \cdot f}}. \quad (4)$$

An equation (5) for the calculation of τ can easily be derived from (4), taking into account that $h_1 = l_p$ and $f = 1/\tau$:

$$\tau = 8\pi(h_1/D)^2 \cdot \chi \cdot \eta. \quad (5)$$

Top region of the curve 2 (Fig. 2) can be approximated by the superposition of linear increment (due to the heat of overall sample after reach of c-Si substrate by thermal perturbation) and exponential decay (due to TIP relaxation). This allows to estimate τ of TIP relaxation as 10 ms. This value approximately one order of magnitude higher than the estimation from the equation (5).

CONCLUSIONS

In the present work we demonstrate that thermally induced pressures inside the pores of mesoporous composite have significant influence on the value and time dependence of PA signal under its piezoelectric registration. This pressure causes an increment of front steepness of the PA signal. Besides, the relaxation of this pressure resulted in extremism on the oscillograms of composites with low-viscous liquids.

Experimental value of thermally induced non-equilibrium pressure relaxation time exceeds its theoretical estimation on one order of magnitude. This deviation can be caused by increase of viscosity the change of thermal expansion coefficient of liquid in thin capillaries [8] and also by increase of efficient capillary length in the porous media in comparison with the layer thickness [9]. Furthermore, real shape of the pore is significantly different from cylindrical one and variability of the pore size with length is the most important factor among above mentioned.

The results of this work can be applied for study of porous materials morphology, development of sensor systems and also they should be considered, if PA method is applied for the composites "porous matrix — liquid".

REFERENCE

1. A. C. Tam: Applications of photoacoustic sensing techniques // *Rev. Mod. Phys.* — 1999. — V. 58. — № 2, pp. 381—431.
2. J.-P. Monchalain, L. Bertrand, G. Rousset and F. Lepoutre: Photoacoustic spectroscopy of thick powdered or porous samples at low frequency // *J. Appl. Phys.* — 1999. — V. 56, pp. 190—210.

3. H. Vargas, L. C. M. Miranda. Photoacoustic and related photothermal techniques // *Physics Reports*. — 1999. — V. 161, № 2, pp. 43—101.

4. M. T. Yasuda, W. L. B. Melo. A new method to determine open porosity and permeability constants of open-pore sintered glasses by photoacoustic technique // *Ceramica*. — 2005. — V. 51, pp. 259—264.

5. A. Rosenzweig, Photoacoustics and Photoacoustic Spectroscopy. John Wiley and Sons, New-York, (1999).

6. D. A. Andrusenko, I. Ya. Kuchеров. Photothermoacoustic effect in solids with piezoelectric detection // *Technical Physics*. — 1999. — V. 44, № 12, pp. 1397—1401.

7. D. A. Andrusenko, R. M. Burbelo, A. G. Kuzmich. Photothermoacoustic conversion in porous matrix — liquid filler systems // *Technical Physics Letters*. — 2010. — V. 36, No. 12, pp. 1121—1124.

8. S. Xu, G. C. Simmons, G. W. Scherer, Thermal expansion and viscosity of confined liquids // *Mat. Res. Soc. Symp. Proc.* — 2004. — V. 790, Materials Res. Soc., Warrendale, P. 6.8.1—P. 6.8.7.

9. Heui-Seol Roh, Richard Raspet and Henry E. Bass, Parallel capillary-tube-based extension of thermoacoustic theory for random porous media // *J. Acoust. Soc. Am.* — 2007. — V. 121 — № 3, pp. 1413—1422.

UDC 537.311.33

D. A. Andrusenko, R. M. Burbelo, A. G. Kuzmich, S. A. Alekseev

PHOTOACOUSTIC TRANSFORMATION IN “POROUS SILICON — FLUID” COMPOSITE SYSTEMS: INFLUENCE OF FLUID MOTION

Abstract

In the present work we demonstrate that thermally induced pressures inside the pores of mesoporous “PS — fluid” composite systems have significant influence on the value and time dependence of PA signal under its piezoelectric registration. This pressure causes an increment of front steepness of the PA signal. Besides, the relaxation of this pressure resulted in extremums on the oscillograms of composites with low-viscous liquids. Experimental value of thermally induced nonequilibrium pressure relaxation time exceeds its theoretical estimation on one order of magnitude. The most important factor of this deviation can be caused by variability of the pore's cross — section. The results of this work can be applied for study of porous materials morphology and also development of sensor systems

Key words: photoacoustic transformation, development, sensor system.

УДК 537.311.33

Д. А. Андрусенко, Р. М. Бурбело, А. Г. Кузьмич, С. А. Алексеев

ФОТОАКУСТИЧЕСКИЙ ЭФФЕКТ В КОМПОЗИТНЫХ СИСТЕМАХ «ПОРИСТАЯ МАТРИЦА — ФЛЮИД»: ВЛИЯНИЕ ПРОЦЕССА ПЕРЕТЕКАНИЯ

Резюме

В представленной работе показано, что термоиндуцированное давление жидкости в порах мезопористого композита существенно влияет на величину и характер зависимости от времени ФА сигнала при его пьезоэлектрической регистрации. Данное влияние проявляется в росте крутизны фронтов ФА сигнала, а в случае композитов с жидкостями малой вязкости, кроме того и в появлении на осциллограммах экстремумов, связанных с релаксацией давления жидкости в порах. Полученное из эксперимента время релаксации термоиндуцированного неравновесного давления в порах композита на порядок превышает оцененное теоретически. Наиболее существенной причиной этого является переменный по длине характер сечения пор. Приведенные в работе результаты могут быть использованы для исследования морфологии пористых материалов, а также при разработке сенсорных систем на их основе.

Ключевые слова: фотоакустический эффект, исследование, сенсорные системы.

УДК 537.311.33

Д. А. Андрусенко, Р. М. Бурбело, А. Г. Кузьмич, С. О. Алексеев

ФОТО АКУСТИЧНИЙ ЕФЕКТ В КОМПОЗИТНИХ СИСТЕМАХ «ПОРИСТА МАТРИЦА — ФЛЮЇД»: ВПЛИВ ПРОЦЕСУ ПЕРЕТІКАННЯ

Резюме

В роботі показано, що термоіндукований тиск рідини у порах мезопоруватого композиту суттєво впливає на величину та характер залежності ФА сигналу від часу при його п'єзоелектричній реєстрації. Цей вплив виявляється в зростанні крутизни фронту ФА сигналу, а у випадку композитів з рідинами, що мають малу в'язкість на осцилограмах, крім того, з'являються екстремуми, що пов'язані з релаксацією тиску рідини в порах. Отримане експериментальне значення часу релаксації, термоіндукованого нерівноважного тиску в порах композиту на порядок перевищує теоретичні оцінки. Найбільш суттєвою причиною цього є нерівномірний за довжиною перетин пор. Отримані у роботі результати можуть бути використані для дослідження морфології пористих матеріалів, а також при розробці сенсорних систем на їх основі.

Ключові слова: фото акустичний ефект, розробка, сенсорні системи.

¹ V. E. Lashkaryov Institute of Semiconductor Physics of NASU,
45 Prospect Nauki, 03028, Kyiv, Ukraine² Kyiv National University of Taras Shevchenko,
4 Prospect Glushkova, 03680, Kyiv, Ukraine

CHANGES IN ELECTROPHYSICAL CHARACTERISTICS OF InGaN/GaN HETEROSTRUCTURES OF HIGH POWER LIGHT-EMITTING DIODES AT INCREASED CURRENT

Changes in electrophysical characteristics of InGaN/GaN high power light-emitting diodes (structure area is 1 mm²) were investigated. It was shown that differential slope parameter of CVC m in the case of direct bias from 0 to 3.2 V changes from 2.2 to 8 and its usual value comprises 5–6. It was revealed that CVC of InGaN/GaN high power LED at $T = 77$ K demonstrates S-shaped view, which is caused by the transfer from a monopolar mode of currents injection to bipolar one and is sensitive for defects, which create deep levels. Infrared band of electroluminescence is revealed in InGaN/GaN heterostructures.

INTRODUCTION

Development of optoelectronics and energy-saving technologies requires both comprehensive investigation of physical properties and operation parameters of heterostructures, and application of effective methods of not-destructive wasteless diagnostic and degradation control. The most perspective radiation and illumination sources in visible range from the efficiency point of view are InGaN/GaN heterostructures [1–6]. Increase of area of epitaxial heterostructures [2, 3] and production of matrixes from structures of high power light-emitting diodes (LED) are the trends in development of this direction.

However, in high power (the area of structure 1 mm²) and super-power (2–3 mm²) InGaN/GaN LED inhomogeneity of distribution of internal mechanical stresses, dislocations, dopants and indium or aluminium components in InGaN and AlGaIn layers increases with area. Therefore, when significant current (0.35...1.4 A) passes through the structure, the problem of thermomechanical stresses and current in local low-resistance sections and near contacts arises. In these places the local current density can exceed its average value in tens times [4]. As a result, quantum efficiency of LED electroluminescence (EL) decreases. Deep levels (DL), which appear due to various defects and impurities, also adversely affect LED performance parameters. DL play the significant role in recombination processes, the majority of them are responsible for formation of channels of nonradiative recombination [5–7]. Therefore timely detection of DL with the purpose to prevent their further activation is the important problem of non-destructive diagnostic, control and reliability prediction of high power light-emitting diodes [8]. Recombination, degradation processes

and centres of nonradiative recombination in heterostructures of high power light-emitting diodes on the basis of GaN, InGaIn, AlGaIn compounds have not been adequately investigated, especially such processes, which are directly responsible for degradation of high power light-emitting diodes.

Therefore the purpose of this work is the comprehensive study of features of electrical and luminescent parameters of InGaIn/GaN heterostructures of high power LED, and also their changes at current increase over typical (nominal) values.

1. EXPERIMENT

Current-voltage characteristics (CVC) were measured with a step of 10 mV, which corresponds to a procedure of determination of a non-ideality factor and energy location of the deep levels using differential coefficient of CVC [8–10]. This procedure of LED structures diagnostic by slope differential index of CVC and its derivative with respect to voltage is very sensitive to character of recombination and degradation processes that offers the means of determining degradation at very beginning and revealing energy levels of defects in light-emitting diodes.

High power light-emitting diodes of Golden Dragon⁺ LUW-W5AM-LXLY-6P7R (Osram) brand and also, for comparison, FYLP-1W-UBB (Foryard) and other high power LED were explored. Heterostructures with area of 1×1 mm² were located on a sapphire wafer and contained quantum well InGaIn = 30 Å in breadth; GaIn n -area doped with Si, and GaIn—Mg p -area.

Holding at the fixed direct current of 500 mA is chosen with the aim to increase electroluminescence intensity in comparison with

nominal $I_{\text{nom}} = 350$ mA, to reveal deep levels and possible degradation changes at testing of these light-emitting diodes. Thus the temperature of own LED radiator was lower than the highest possible admissible passport value of 80 °C and comprised ~ 57 °C in our studies. LED was disposed on a metal heat sink in the form of a plate with sizes $3 \times 2 \times 0.1$ cm³.

2. ANALYSIS OF CVC OF HIGH POWER InGaN/GaN LIGHT-EMITTING DIODES

For detection of changes in electrophysical parameters of LED, CVC of power LED before and after loading by 500 mA current during 15, 30 and 60 days are presented in Fig. 1. Within one day the loading was carried out during 12 hours, the full term of a cycle made 180, 360 and 720 hours respectively. It is seen that for voltages lower than 2.4 V current growth and decrease of the slope of linear (in logarithmic scale) section of CVC take place.

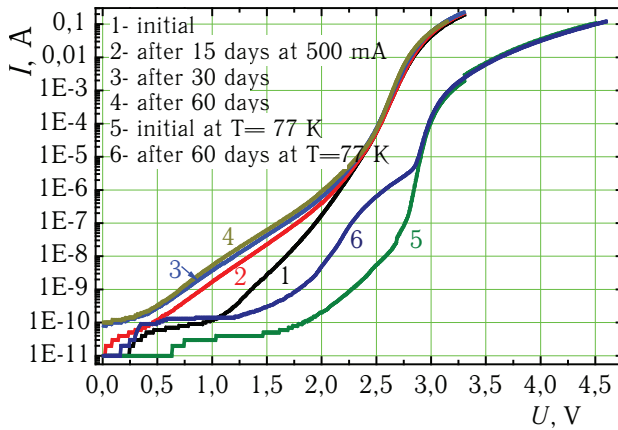


Fig. 1. CVCs of Golden Dragon+ high power light-emitting diode before (1, 5) and after holding at 500 mA current (2, 3, 4, 6)

CVC measuring at direct voltage and temperatures of 300 and 77 K have shown that at $U \sim 1.2\text{--}2.25$ V (at 300 K) and at $2\text{--}2.65$ V (at 77 K) (currents $I = 10^{-9}\dots 10^{-6}$ A) dependence $I \sim I_0 \exp(eU/E_i)$ is observed, and the exponential curve index $1/E_i$ depends only slightly on temperature, *i. e.* the slope of this section of CVC is invariable, that is in agreement with data of [11]. In this voltage range the tunnel component of the current predominates [5, 11].

At voltages $U > 2.6$ V and $T = 300$ K (the interval $I \sim 10^{-5}\dots 10^{-3}$ A) injection component of current predominates, and thus CVC is described by dependence $I = I_0 \exp(eU/mkT)$, where m is differential slope coefficient, or the non-ideality factor. For gallium nitride LED structures the non-ideality factor $m \sim 6.8$ [12], that testifies to the dominating tunnel current component, while for diffuse or recombination currents the factor m should lie within the range of 1—2. The main reason for that

is low concentration of intrinsic equilibrium charge carriers $n_i^2 = 4 \cdot 10^{-20}$ cm⁻⁶ (for instance, in GaAs/AlGaAs structure $n_i^2 = 4 \cdot 10^{12}$ cm⁻⁶) owing to high bandwidth of GaN, and for observation of significant diffuse currents significant voltages should be applied. High values of non-ideality factor (6...10 and more) were observed in [13].

On CVC in logarithmic scale at room temperature in the range of voltages 1—2.3 V (currents 0.1—4.5 μ A) in non-degraded and degraded at 500 mA structures the characteristic shoulder is observed, which is related to influence of significant number of defects — imperfect and grown-in dislocations, which are typical for gallium nitride structures on the sapphire wafer. Comparing strength of current in this range, one can determine relative (in comparison) concentration of defects (dislocations) in different light-emitting diodes. CVC of LED at holding at 350 mA practically did not change — there were only insignificant positive and negative equal current deviations through the whole range of voltages.

Source currents at small biases are determined by processes of the tunnel nonradiative recombination, localised in system of distributed defects in vicinity of a active area of light-emitting diodes, and their number is in many respects determined by a degree of order of this system [14]. In the voltages interval $U = 2.3\text{--}2.7$ V sharp exponential growth, which corresponds to injection in the active area, is observed. At large currents the current grows sublinearly with certain saturation on voltage, which is caused by sequential resistance R_s of contact areas. In the range of large currents saturation observed in Fig. 1 in logarithmic scale is caused by a voltage drop on spurious sequential resistances of light-emitting diode structure — contacts, a buffer layer, weakly doped and compensated thin technological layers.

It should be noted that the injection component of the current after turn-on voltage after 15 and 30 days holding at 500 mA has grown a little, as it is seen from CVC in Fig. 1, though at degradation it should always decrease [15].

One can concede that growth of the tunnel current and lack of degradation of the recombination current testifies to activation of already existing defects in electrical, thermal and thermoelastic fields and their gradients, and due to recharge of defects at increased temperature. In particular, it is known that dislocations in GaN and the sections enriched by indium in InGaN quantum well modulate the energy band diagram and capture (localise) charge carriers of both signs at the expense of fluctuations of the band potential [1] and states on boundaries of layers [7].

The significant growth of the current in the range of 2—2.8 V on CVC at $T = 77$ K after holding at 500 mA within 60 days is important (see curve 6 in Fig. 1). On initial CVC at $T = 77$ K such singularity was not observed.

Such growth of the current at degradation processes (appearance of “humps” on CVC) is typical for LED structures and is related to distributed defects, when current carriers are capable to tunnel by the localised states of defects — tunnel current transmission by the mechanism of multistage tunnelling takes place, when field space charge (FSC) width exceeds a tunnelling reference length (for example, on a dislocation line or on DL of point defects systems on heteroboundaries).

For InGaN/GaN epitaxial structures on the sapphire wafer the significant number of the localised states in the band gap is typical, therefore charge carriers can move outside of the conduction band, especially in the region of heteroboundaries. Such non-classical motion represents tunnelling between two adjusting localised states.

It should be noted that despite very high dislocation density (10^9 – 10^{10} cm $^{-2}$) in structures InGaN/GaN on sapphire, their high efficiency of the radiating recombination is explained by such fluctuations of solid solution compositions, clusters and phases decomposition in solid solutions, which lead to appearance of local potential wells on the band diagram. In this case localisation of charge carriers and suppression of their diffusion to dislocations take place. In comparison with GaAsP, GaP, GaAlAs, GaAs, diffuse path length of charge carriers in GaN is smaller.

There are localised states related to dislocations, inhomogeneity of In concentration by the area of the active layer, segregated atoms of hydrogen and oxygen [7, 15, 16], complexes with doping atoms, *etc.* on boundaries of heterojunctions of GaN/InGaN/GaN. Tunnelling of charge carriers happens on these states at small voltages. Energy levels of defects are practically always nonradiative recombination centres; therefore their detection and analysis are actual for the control of degradation and reliability prediction of heterostructures of high power LED.

3. ANALYSIS OF CVC DIFFERENTIAL COEFFICIENT AND THE DEEP LEVELS OF HIGH POWER LED

Let us use a method of recombination spectroscopy, which is based on differentiation of CVC for determination of non-ideality factor and the deep levels, which participate in formation of the recombination channel [5, 6, 8–10].

After CVC numerical differentiation it has appeared that the non-ideality factor

$$m = \frac{e}{kT} \left(\frac{d(\ln I)}{dU} \right)^{-1} \text{ behaves non-monotonically}$$

on voltage U and changes after holding at 500 mA throughout days. The deep levels, which are activated or formed, participate in formation of recombination channel. Value m in the

range of 0.7...1 V — 2.5 V is high and varies from 8 to 3. Quantity m has the characteristic minimum in the field of 2.6 V (see Fig. 2), it testifies to the change of mechanism of charge carriers transfer from tunnelling to injection in the active area at voltage growth. The current near “turn-on” voltage of electroluminescence U_{EL} — 2.6 V on CVC sharply increases. The “turn-on” voltage is approximately equal to E_g of InGaN layer and corresponds to the beginning of effective injection in the quantum well.

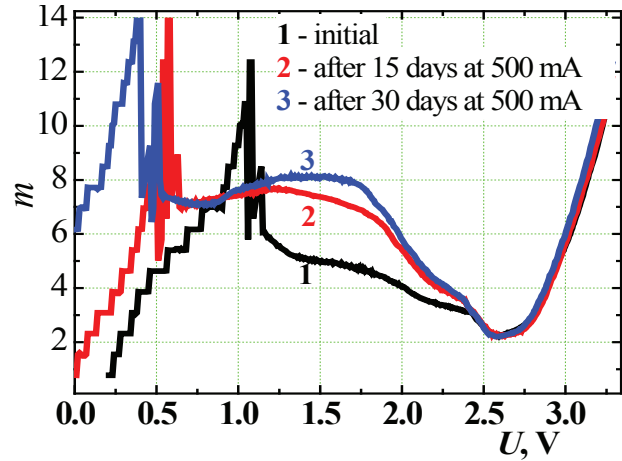


Fig. 2. Dependence of slope differential coefficient of CVC m on voltage

It is seen from Fig. 2 (curves 2 and 3), that m after the holding behaves non-monotonically in the range of voltages 1.8–2.5 V, and in the range of voltages 0.8–1.9 V the non-ideality factor is practically constant.

In the range of 0...1.2 V coefficient m sharply increases to significant value — 12...13 at 0.5...1 V, after that a sharp drop is observed (see Fig. 2). It, possibly, corresponds to the beginning of charge carriers transfer from n to p area and is a special feature of the tunnel current. The section, where m varies only slightly and is practically constant with the activation energy $1/E_a$, corresponds to the linear section of CVC. Then the drop is observed, which corresponds to the growth of concentration of minority carriers in the FSC, which screen other charge carriers (the change of Debye screening distance) with simultaneous further decrease of field (volume) of FSC with voltage growth. The valley corresponds to the turn-on voltage.

Generally, the differential non-ideality factor m of the structures under investigation varies from 2.2 to 14 (see Fig. 2). High m values are explained by the significant bandwidth of GaN and small lifetimes (10–20 nanoseconds) and mobilities of minority carriers. It results in violation of condition $L_D > L_e$, where L_D and L_e are length of diffusion and depth of Debye screening [12]. It testifies to high and ultrahigh levels of majority current carriers injections into the high-resistance layer of the structure. Obtained dependences $m(U)$ and values m for GaN struc-

tures as a whole are in fair agreement with literary data, in particular with [11, 12, 16].

In Fig. 3 the dependence of differential slope coefficient of CVC dm/dU at 300 K is presented. It is seen that at U from ~ 2.5 V value dm/dU increases, as after the turn-on voltage 2.6 V the injection current component predominates. For U lower than the turn-on voltage, $dm/dU \approx \text{const}$ or varies slightly. It is known from [5, 6, 8–10] that maximums on dependence of differential slope coefficient of CVC dm/dU on U correspond to energy positions of the deep levels in the bandgap. An observable peak (oscillation) at 2 V in Fig. 3 corresponds to the recombination level E_t . Calculation of its value is performed by formula [5, 6]

$$E_t = (E_g/2) - eU_{\max} + kT \ln([m_n^*/m_p^*]^{3/2} \cdot \omega N/c_p n_i), \quad (1)$$

where U_{\max} is the maximum on the curve dm/dU , $E_g(\text{GaN}) = 3.34$ eV, $\omega = 1.768 \cdot 10^{-12}$ cm³/s is probability of tunnelling for InGaN/GaN structures [6], N is concentration of the deep levels, c_p is hole capture coefficient for the localised states of DL, n_i is concentration of intrinsic charge carriers, $m_{n(p)}^*$ is effective mass of energy-level density for conduction band (valence band); $m_n^* = 0.22 \cdot m_0$, $m_p^* = 0.32 \cdot m_0$, m_0 is free electron mass.

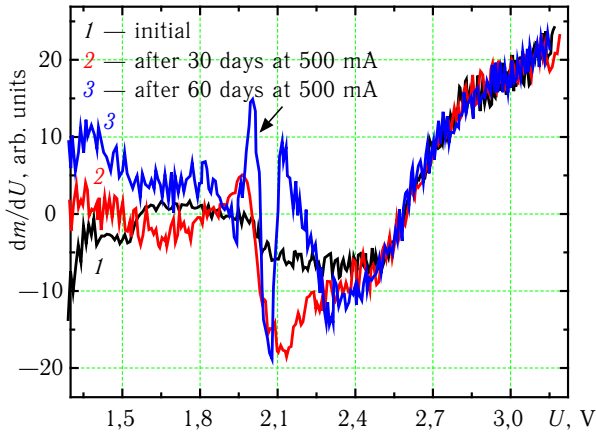


Fig. 3. Derivative of differential slope coefficient of CVC m of high power light-emitting diode with respect to U

Then $E_t = (3.34/2)$ eV $- 2$ eV $+ 1.56$ eV ≈ 1.23 eV, as for calculation of an activation energy of the level data from [5, 6] were used, where last addend of formula (1) for similar heterostructures of indicator light-emitting diodes was calculated. However, its exact calculation requires the further analysis.

Let us note that in article [6] the peak 3.08 V is determined on the derivative dm/dU . This peak corresponds to the level $E_t = 0.15$ eV for InGaN/GaN structures, which is identified as magnesium level ($E_t(\text{Mg}) = 0.15 \dots 0.2$ eV). Thus on dependence dm/dU on U in high power LED based on GaN the presence of DL after holding at 500 mA is determined. Its amplitude increases with holding time.

In works [7, 16] the possible mechanism of degradation is proposed, in which a pinning (fixing) of Fermi level on heteroboundaries of structure p-GaN/InGaN/n-GaN is caused by segregation of the residual impurities of hydrogen and oxygen. Process of degradation of EL intensity and CVC is associated with the increase of energy-level density at heteroboundaries and change of their distribution in the band gap. Correlation of singularities of CVC of light-emitting diodes before and after degradation indicates that the defects generated during degradation on heteroboundaries are characterised by the same energy levels as those before degradation [16]. Activation of dislocations at the current loading (for example, deposition of point defects on dislocations) and formation/decomposition of complexes of defects are also possible. Formation of channels of current sources on initial stage of degradation is connected with electrical activity of the residual impurities rather than electromigration of atoms of metals from contacts [16].

Decrease of intensity of electroluminescence spectra is evidence for defects formation and activation of existing defects (Fig. 4 a), as the

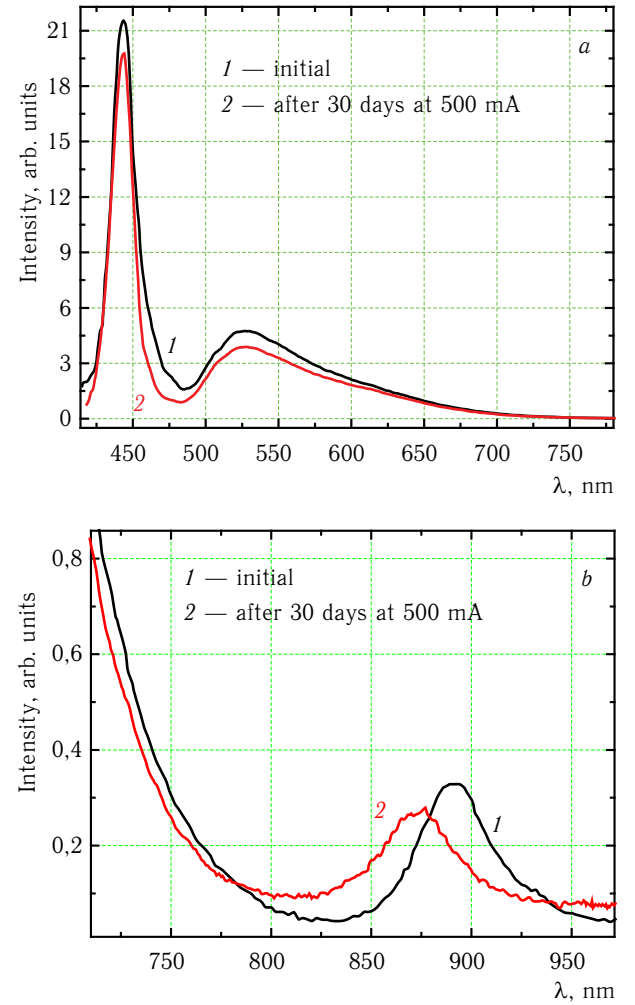


Fig. 4. Electroluminescence spectrum of high power InGaN/GaN Golden Dragon⁺ LED ($T_{\text{col}} = 5700$ K) at 350 mA

activated and formed defects play a role of non-radiative recombination centres. This process dominates over an opposite one — it is known that at the current holding decomposition of Mg—H complexes and activation of doping atoms of magnesium take place, which results in a certain growth of EL intensity [15].

In addition to blue band of heterostructure and green band of the luminophor, a band in IR range is observed (see Fig. 4 *b*). After holding its shift to the short-wave range and intensity decrease are observed. This band concerns to InGaN/GaN heterostructure itself and is observed in other high power light-emitting diodes (in the range of 850—1000 nanometers) without luminophor. Its halfwidth and intensity distribution are typical for injection electroluminescence in the semiconductors with an impurity level. From the energy position of the possible level, responsible for the IR band, follows that it is deep, so, this band is informative at analysis of DL. Authors do not possess any information concerning this band. Possibly, the specified level is caused by the level of complexes of magnesium or zinc with vacancy of nitrogen. Through this level a part of the recombination current passes, which does not participate in formation of blue basic band of LED EL.

Intensity of EL spectrum slightly decreased, thus the differential index and its derivative point up essential changes in LED crystal, associated with degradation.

4. S-SHAPED CVC OF HIGH POWER LIGHT-EMITTING DIODES

It has been determined that CVCs of high power InGaN/GaN LED at nitrogen temperature have S-shaped view with a section of the negative differential resistance (NDR) (see Fig. 5), similar to those in indicator InGaN/GaN LED [17]. Heterostructures of different types have different view of S—CVC: for example, CVC of FYLP-1W-UBB (Foryard) LED has wide section of NDR (curves 1 and 2 in Fig. 5), S—CVC of Golden Dragon⁺ LUW-W5AM-LXLY-6P7R (Osram) has hysteresis (curve 3). After holding at 500 mA throughout 30 days such CVC considerably changes. The voltage of “break-down” U_{th} is approximately 6.05 V, $I = 180$ mA (see Fig. 5, curve 1), negative differential comes to the end from $I = 1140$ mA, $U = 5.3$ V, (curve 1). For Golden Dragon⁺ $U_{th} = 5.78$ V, current $I = 460$ mA (Fig. 5, curve 3).

So, view of S—CVCs of high power InGaN/GaN LED of different producers strongly differ, more considerably than CVCs at 300 K. On S-CVC of identical LEDs differences are also observed. For FYLP-1W-UBB LED section of NDR is considerably longer than that for Golden Dragon⁺ LED that is caused by technological differences at manufacture of different producers and, accordingly, degree of deficiency (Golden Dragon⁺ LED has better radiating

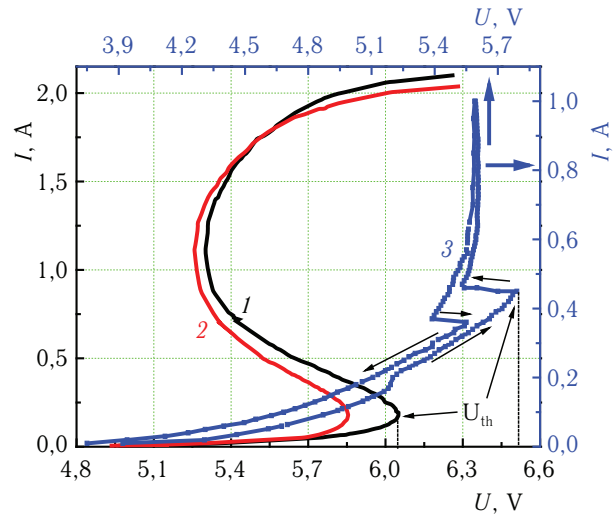


Fig. 5. CVC of high power InGaN/GaN light-emitting diode at $T = 77$ K: 1 — initial; 2 — after holding at 500 mA throughout 30 days (Foryard); 3 — initial (Osram)

and electrical parameters than FYLP-1W-UBB). As such view of CVC is caused by levels in active area of LED, let us carry out the analysis of such CVC.

Such view of CVC at temperatures ~ 100 K and lower for structures of such type is caused by the presence of the deep level and can be described by Ashley—Milnce theory [18, 19]. In their model trap levels can be either neutral (then they are traps for electrons), or single negative charged (then they are traps for holes). The capture cross-section of holes by hole traps is considerably higher than the capture cross-section of electrons by electron traps, therefore the lifetime of electrons is much longer than that of the holes. The lifetime of electrons is eventually infinite, so at very low voltages the injection current is the electronic current, restricted by space charge and proportional to the voltage quadrate (monopolar injection). With growth of the voltage to the threshold value U_{th} (Fig. 5), the deep acceptor levels (traps) are gradually occupied by the injected holes, accordingly the lifetime of holes in the active area increases, and at $U = U_{th}$ holes start to pass through the whole structure. Hence occupation of DL causes the increase of holes lifetime and decrease of electrons lifetime. At the break-down voltage holes can easily pass through the active area at much lower voltages (Fig. 5), and NDR section appears. When lifetimes of electrons and holes become equal, the current is caused by transmission of charge carriers of both signs (bipolar injection), restricted by recombination. Then injection rate exceeds the recombination rate. It corresponds to saturation section after the end of NDR section.

Hence the voltage of NDR beginning or voltage of S—CVC break-down corresponds to the time of transmission of holes through i -area, which is approximately equal to time of holes life. As soon as holes start to transit i -area without recombination, CVC suddenly changes,

as conductivity from the monopolar condition of injection of charge carriers is switched to the bipolar one. The deep trapping and recombination sites correspond to acceptor levels of Mg [18] (or zinc in case of alloying with Zn).

Thus the strength of current through p - n — junction increases by orders (Fig. 5). Return into a high-ohmic state can happen also at lower voltages, forming hysteresis curve on CVC (Fig. 5). Let us note that in some high power LED S —CVC at $T=77$ K only slightly manifests itself or is even unavailable (such cases are rare).

Thus, summing up the aforesaid, one can say the following. View of CVC in the range of tunnel and injection current and its derivative with respect to voltage, S -shaped CVC, the determined infra-red band of electroluminescence in high power InGaN/GaN light-emitting diodes are caused by the deep levels of defects and are very sensitive to degradation. Accordingly, their changes (in comparison with initial parameters) are informative at study of degradation processes for the control technique and reliability prediction of InGaN/GaN heterostructures of high power light-emitting diodes.

5. CONCLUSIONS

In high power InGaN/GaN light-emitting diodes ($I_{\text{nom}}=350$ mA) the changes of CVC, differential non-ideality factor of CVC m , and the derivative dm/dU after holding at 500 mA throughout 1—2 months are determined. They are accompanied by decrease of electroluminescence intensity and caused by the deep levels of defects. Using differential coefficient of CVC, the deep level is determined.

It is revealed that differential non-ideality factor of CVC of high power InGaN/GaN light-emitting diodes at direct bias from 0 to 3.2 V varies — $m=2.2$ —8 and usually its value comprises 5—6.

It is determined that CVC of InGaN/GaN high power light-emitting diodes at $T=77$ K has S -shaped view caused by the deep level and changes after long-term holding at 500 mA. Such view of CVC is caused by transition from the monopolar condition of charge carriers injection to the bipolar one and is sensitive to defects, which create the deep levels.

In InGaN/GaN heterostructures of high power light-emitting diodes IR-band of electroluminescence, associated with the deep level, is determined. Data on the nature and properties of this electroluminescence band are not available in literature.

It is shown that simultaneous single and double differentiation and analyses of CVC of LEDs for determination of their non-ideality factor and detection of the deep levels, which cause degradation of their functional electrical and luminescent parameters, suggest reliability prediction of InGaN/GaN structures of high

power light-emitting diodes and can be applied for development of a method for their rapid control.

Acknowledgments

This work was fulfilled at financial support of the State target scientific and technical program "Development and implementation of energy saving LED light sources and lighting devices on their base" (state registration No. 0109U004882).

REFERENCES

1. E. F. Schubert. *Light Emitting Diodes. Second edition.* — Cambridge University Press, 2006. — P. 422.
2. M. R. Krames, O. B. Shchekin, R. Mueller-Mach, G. O. Mueller, Ling Zhou, G. Harbers, M. G. Craford. Status and Future of High-Power Light-Emitting Diodes for Solid-State Lighting // *Journal of Display Technology.* — 2007, 3(2), pp. 160—175.
3. Hu Jianzheng, Lianqiao Yang and Moo Whan Shin. Electrical, optical and thermal degradation of high power GaN/InGaN light-emitting diodes // *Journal of Physics D: Appl. Phys.* — 2008, 41(3), pp. 035107.
4. K. A. Bulashevich, I. Yu. Evstratov, V. F. Mymrin and S. Yu. Karpov. Current spreading and thermal effects in blue LED dice // *Phys. Stat. Solidi (C).* 2007, 4(1), pp. 45—48.
5. N. S. Grushko, E. A. Loginova, L. N. Potanakhina. A tunnel recombination process in spatially heterogeneous structures // *Fiz. Tech. Polupr.* — 2006, 40(5), pp. 584—588.
6. A. S. Ambrozevich, S. A. Ambrozevich, N. S. Grushko and L. N. Potanakhina. Determining the energies of deep centers in heterostructures based on InGaN Solid solutions // *Pis'ma v Jour. Tech. Fiz.* 2006, 32(4), pp. 16—23.
7. N. I. Bochkareva, E. A. Zhirnov, A. A. Efremov, Y. T. Rebane, R. I. Gorbunov, A. V. Klochkov, D. A. Lavrinovich, Y. G. Shreter. Effects of interface states on capacitance and efficiency of electroluminescence in InGaN/GaN light-emitting diodes // *Fiz. Tech. Polupr.* — 2005, 39(7), pp. 829—833.
8. С. В. Булярский, Н. С. Грушко. *Физические принципы функциональной диагностики p — n -переходов с дефектами.* — Кишинев, Изд. "Штиинца", 1992. — С. 236.
9. S. V. Bulyarskii, M. O. Vorob'ev, N. S. Grushko and A. V. Lakalin. Determination of the parameters of deep levels using the differential coefficients of the current-voltage characteristics // *Pis'ma v Jour. Tech. Fiz.* — 1999, 25(5), pp. 22—27.
10. S. V. Bulyarskii and N. S. Grushko. Generalized model of recombination in inhomogeneous semiconductor structures // *Zh. Exp. and Theor. Phys.* — 2000, 118(5), pp. 1222—1229.
11. Е. А. Логинова. Исследование электрических и электролюминесцентных характеристик гетероструктур на основе нитрида галлия: Дисс. канд. физ.-мат. наук, спец. 01.04.10. — Ульяновск, 2005. — С. 118.
12. S. V. Svechnikov, P. F. Oleksenko, G. A. Sucach, P. S. Smertenko, S. I. Vlaskina, A. V. Bushma, A. B. Bogoslovskaya. Investigation of thermal-injection processes in GaN light emitting diodes // *Ukrainian Journal of Physics.* — 1998, 43(10), pp. 1290—1294.
13. S. H. Shamirzaev, G. Gulyamov, M. G. Dadamirzaev, A. G. Gulyamov. Nonideality coefficient of current-voltage characteristic of p — n -junctions in strong superhigh-frequency (microwave) field // *Fiz. Tech. Polupr.* — 2009, 43(1), pp. 53—57.
14. N. S. Averkhev, M. E. Levinshstein, P. V. Petrov, A. E. Chernyakov, E. I. Shabunina and N. M. Schmidt. Features of the recombination processes in InGaN/GaN based LEDs at high densities of injection current // *Pis'ma v Jour. Tech. Fiz.* — 2009, 35(19), pp. 97—102.
15. A. N. Kovalev, F. I. Manyakhin, V. E. Kudryashov, A. N. Turkin, A. E. Yunovich. Changes of luminescent and electrical properties of InGaN/AlGaIn/GaN light-emitting diodes during a long work // *Fiz. Tech. Polupr.* — 1999, 33(2), pp. 224—232.
16. N. I. Bochkareva, A. A. Efremov, Y. T. Rebane, R. I. Gorbunov, A. V. Klochkov, Y. G. Shreter. Charge car-

rier injection non-uniformity and degradation of blue light-emitting diodes // *Fiz. Tech. Polupr.* — 2006, 40(1), pp. 122—127.

17. V. P. Veleschuk, O. I. Vlasenko, O. V. Lyashenko, A. Baidullaeva, B. K. Dauletmuratov. Acoustic emission and changes of luminescent and electrical characteristics of InGaN/GaN heterostructures at the current loading

// *Physics and Chemistry of Solid State.* — 2008, 9(1), pp. 169—174.

18. N. I. Kuznetsov, K. G. Irvine. Current-voltage characteristics of GaN and AlGaIn $p-i-n$ diodes // *Fiz. Tech. Polupr.* — 1998, 32(3), pp. 369—372.

19. A. G. Milnes. *Deep impurities in semiconductors.* — Moscow: "Mir", 1999. — P. 562.

UDC 621.383:621.381.2

O. I. Vlasenko, V. P. Veleschuk, M. P. Kisseljuk, O. V. Lyashenko

CHANGES IN ELECTROPHYSICAL CHARACTERISTICS OF InGaN/GaN HETEROSTRUCTURES OF HIGH POWER LIGHT-EMITTING DIODES AT INCREASED CURRENT

Abstract

Changes in electrophysical characteristics of InGaN/GaN high power light-emitting diodes (structure area is 1 mm²) were investigated. It was shown that differential slope parameter of CVC m in the case of direct bias from 0 to 3.2 V changes from 2.2 to 8 and its usual value comprises 5—6. It was revealed that CVC of InGaN/GaN high power LED at $T=77$ K demonstrates S-shaped view, which is caused by the transfer from a monopolar mode of currents injection to bipolar one and is sensitive for defects, which create deep levels. Infrared band of electroluminescence is revealed in InGaN/GaN heterostructures.

Key words: high power InGaN/GaN light-emitting diode, deep levels, S—CVC.

УДК 621.383:621.381.2

О. І. Власенко, В. П. Велешук, М. П. Киселюк, О. В. Ляшенко

ЗМІНИ ЕЛЕКТРОФІЗИЧНИХ ХАРАКТЕРИСТИК InGaN/GaN ГЕТЕРОСТРУКТУР ПОТУЖНИХ СВІТЛОДІОДІВ ПРИ ПІДВИЩЕНОМУ СТРУМІ

Резюме

Вивчено зміни електрофізичних характеристик потужних InGaN/GaN світлодіодів (площа структури 1 мм²). Визначено, що диференційний показник нахилу ВАХ при прямому зміщенні від 0 до 3,2 В змінюється — $m=2,2...8$ та зазвичай має величину 5—6. Виявлено, що ВАХ InGaN/GaN потужних СД при $T=77$ К має S-подібний вигляд, зумовлений переходом від монополярного режиму інжекції носіїв до біполярного та є чутливим до дефектів, які створюють глибокі рівні. В InGaN/GaN гетероструктурах виявлено інфрачервону смугу електролюмінесценції.

Ключові слова: потужний InGaN/GaN світлодіод, глибокі рівні, S—ВАХ.

УДК 621.383:621.381.2

А. И. Власенко, В. П. Велешук, М. П. Киселюк, О. В. Ляшенко

ИЗМЕНЕНИЯ ЭЛЕКТРОФИЗИЧЕСКИХ ХАРАКТЕРИСТИК InGaN/GaN ГЕТЕРОСТРУКТУР МОЩНЫХ СВЕТОДИОДОВ ПРИ ПОВЫШЕННОМ ТОКЕ

Резюме

Изучены изменения электрофизических характеристик мощных InGaN/GaN светодиодов (площадь структуры 1 мм²). Определено, что дифференциальный показатель наклона ВАХ при прямом смещении от 0 до 3,2 В изменяется — $m=2,2...8$ и обычно имеет величину 5—6. Выявлено, что ВАХ InGaN/GaN мощных СД при $T=77$ К имеет S-образный вид, обусловленный переходом от монополярного режима инжекции носителей к биполярному и является чувствительным к дефектам, которые создают глубокие уровни. В InGaN/GaN гетероструктурах выявлена инфракрасная полоса электролюминесценции.

Ключевые слова: мощный InGaN/GaN светодиод, глубокие уровни, S—ВАХ.

POSITRON-ATOM COLLISIONAL SPECTROSCOPY: ENERGY APPROACH

A new advanced energy approach in the positron-atom collisional spectroscopy is developed and based on the S-matrix Gell-Mann and Low formalism and relativistic many-body perturbation theory. Some results of calculation of the positron impact ionization cross-sections are presented for helium and argon.

Now days positron-atomic and positron-molecular spectroscopy is one of the quickly developed fields of scientific research as in atomic physics, physics of particles as in quantum electronics and plasma physics. A positron being the antiparticle of an electron is a unique projectile particle for collision experiments with atomic systems. Moreover, positron-atomic spectroscopy becomes a powerful tool for studying molecular and cluster systems [1—22]. Surely, this is one of the effective methods for investigation of the different elementary processes in the gases and plasma [4]. Comparison of electron and positron scattering are affected by differences, for example, there is no exchange interaction, for positrons, the static interaction is repulsive for positrons and attractive for electrons, at last, the positronium formation and annihilation can occur for positrons. From other hand, there are some similarities such as the polarization interaction is attractive for both particles. Besides, the known in the electron-atom collisional spectroscopy methods can be naturally generalized in the case of the positron-atomic interactions, collisions, impact ionization etc.). Over the years there has been a lot of speculation about whether positrons could bind to atoms. The interaction between a positron and the electrostatic field of any neutral atom is repulsive. Therefore the initial reaction would be that it is impossible to bind a positron to an atom. However, this simplistic argument does not take into account the polarisation of the atom. The positron will cause a redistribution of the electronic charge cloud of the parent atom with the electrons migrating to the side of the atom nearest to the positron. This “polarisation” of the atom leads to an additional attractive interaction between the positron and the atom, the polarisation potential. There is another possible mechanism to that promotes positron binding. One of the atomic electrons can be attached to the positron, thereby forming a positronium atom on the perimeter of the residual positively charged atomic ion. This positronium cluster will tend to align itself so that the electron is closest to the nucleus. Therefore, the positron

is attached to one of the electrons, and the resulting Ps cluster is attracted to the rest of the atom. This interaction is reasonably strong since the dipole polarizability of the positronium is $36 a_0^3$. This additional attractive interaction makes a strong contribution to the binding of the positron. Whether these interactions are strong enough to overcome the electrostatic interaction has been one of the longest standing and most interesting questions in the field of positron physics. The question has been finally settled (see, for example, [1—4]).

Above theoretical approaches one can note the standard Born approximation, Coulomb distorted-wave models, R -matrix method, classical trajectory Monte Carlo method etc [2—5]. The popular approaches are based on using the Coulomb approximation with using the plane waves (CPE) with full energy range and distorted wave CPE approximation (DCPE). It should be noted that the main problems of the correct description of the positron-atom interactions are arisen under low and middle collision energies, while at the high energies it is acceptable even the first Born approximation. Earlier we developed new relativistic energy approach to electron atom collisions (including the elementary collision processes in plasmas) and obtained many data about the low- and middle-energy electron-atom and electron-ion collision cross-sections with correct accounting for the different groups of the exchange-correlation effects. In particular, new consistent relativistic and QED versions for calculations of the spectroscopic characteristics of the multicharged ions in plasma have been developed. Namely, within the uniform energy approach we have defined the cross-sections of electron-collisional excitation and ionization for neon and argon atoms, Ne-like multicharged ions, Ne- and Ar-like plasma etc. The purpose of this paper is to develop a new advanced energy approach in the positron-atom collisional spectroscopy (collisional energy approach (CEA)), which is based on the S-matrix Gell-Mann and Low formalism and relativistic many-body perturbation theory. The results of calculation of the positron impact ion-

ization cross-sections are presented for helium and krypton.

Let us present the key moments of the new consistent approach for calculation of the positron-impact (collision) atom ionization cross-sections. General formulation is in full degree similar to the electron-impact ionization theory, however, with some differences (look above). It bases on the gauge invariant QED energy approach to construction of the relativistic functions basis's [17, 18] and using the Green's function method for accounting of the complex exchange-correlation, radiation and others corrections. Within the Gell-Mann and Low approach with the QED scattering matrix (c. f. [17, 22]) the secular matrix elements are already complex in the second order of the perturbation theory (PT). The imaginary parts are connected with the radiation decay (radiation) possibility. The total energy shift of the state is usually presented in the form:

$$\Delta E = \text{Re}\Delta E + i\text{Im}\Delta E, \quad (1)$$

$$\text{Im}\Delta E = -\Gamma/2, \quad (2)$$

where Γ is interpreted as the level width, and the decay possibility $P = \Gamma$. The whole calculation of the energies and decay probabilities of a non-degenerate excited state is reduced to calculation and diagonalization of the complex matrix M . Usually one uses for this purpose a one-electron Hamiltonian with a central potential that can be treated as a bare potential in the formally exact QED PT. The bare potential includes the electric potential of the atomic nucleus and some model potential that is to be compensated for in all orders of PT. There are many well-known attempts to find the more fundamental optimization principles for the bare one-electron Hamiltonian. The minimization of the gauge dependent multielectron contribution of the lowest QED PT corrections to the radiation widths of atomic levels is proposed in [17] as "ab initio" optimization principle (see below). In our calculations of different characteristics we dealt with atoms and ions having one, two or three quasi-particles (electron or vacancies) outside the core of closed electron shells. For example, the excited states $[\text{Ne}]3s^23p^5nl$ of the Ar-like ion is a two-quasi-particle (2QP) state. It is usually accepted, as the bare potential, a potential including the electric nuclear potential V_N and some parameterized potential V_C , that imitates the interaction of closed-shell electrons with quasi-particles. The parameters of the model bare potential are chosen so as to generate accurate eigen-energies of all one-quasi-particle (1QP) states, i. e. $3s3p^6$, $3s^23p^5$ states of the Cl-like ion and $3s^23p^6nl$ states of K-like ions, with the same nucleus. Usually the experimental one-quasi-particle energies are used for determination of parameters of the model potential (c. f. [8—10, 18—22]).

In the PT second order the energy shift is expressed in terms of two-particle matrix elements:

$$V(1, 2; 4, 3) = \sqrt{(2j_1 + 1)(2j_2 + 1)(2j_3 + 1)(2j_4 + 1)} \times \\ \times (-1)^{j_1 + j_2 + j_3 + j_4 + m_1 + m_2} \sum_{\lambda, \mu} (-1)^\mu \times \\ \times \begin{bmatrix} j_1 \dots j_3 \dots \lambda \\ m_1 \dots m_3 \dots \mu \end{bmatrix} \begin{bmatrix} j_2 \dots j_4 \dots \lambda \\ m_2 \dots m_4 \dots \mu \end{bmatrix} (Q_\lambda^{\text{Qul}}). \quad (3)$$

Here Q_λ^{Qul} is corresponding to the Coulomb inter-particle interaction, which expresses through the radial integrals of the Coulomb inter-particle interaction [17, 22]. To calculate all necessary matrix elements one must use the basis's of the 1QP relativistic functions. In many calculations of characteristics of the atomic elementary processes it has been shown that adequate description of these characteristics requires using the optimized basis's of wave functions. In ref. [17] it has been proposed "ab initio" optimization principle for construction of cited basis's. There is used the minimization of the gauge dependent multielectron contribution of the lowest QED PT corrections to the radiation widths of atomic levels. The details of procedure can be found in [22]. Here we briefly describe the key moments. In the fourth order of QED PT there appear diagrams, whose contribution into the $\text{Im}\Delta E$ accounts for the core polarization effects (polarization of the closed shell core by the quasi-particle). This contribution describes collective effects and it is dependent upon the electromagnetic potentials gauge (the gauge non-invariant contribution). Let us examine the multi-electron atom with 1QP in the first excited state, connected with the ground state by the radiation transition. In the zeroth order of QED PT we use the one-electron bare potential $V_N(r) + V_C(r)$. The core potential $V_C(r)$ is related to the core electron density $\rho_C(r)$ in a standard way [19, 20]. Moreover, all the results of the approximate calculations are the functionals of the density $\rho_C(r)$. The minimization of the density functional $\text{Im}\Delta E_{\text{minv}}$ leads to the integral differential equation for the ρ_C , that is numerically solved. In result one can get the optimal one-electron basis of PT. Below we first use such a basis in calculation of the electron-collision cross-sections and strengths. Further we briefly discuss the energy approach in scattering theory [17, 22] and give main formulas. We briefly outline the main idea using, as an example, the collisional de-excitation of the argon atom: $((3j_{iv})^{-1}4j_{ie}[J_i M_i], \epsilon_{in}) \rightarrow (\Phi_0, \epsilon_{sc})$. Here Φ_0 is the state of the ion with closed shells (ground state of the Ar); J_i is the total angular moment of the initial target state; indices iv , ie are related to the initial states of vacancy and electron; indices ϵ_{in} and ϵ_{sc} are the incident and scattered energies, respectively to the incident and scattered positron (the positronium forming case is treated analogously with accounting another positron final state). It is convenient to use the second quantization representation. In particular, the initial state of the system "atom plus free positron" can be written as

$$|I\rangle = a_{in}^+ \sum_{m_{iv}, m_{ie}} a_{ie}^+ a_{iv} \Phi_0 C_{m_{ie}, m_{iv}}^{J_i, M_i}. \quad (4)$$

Here $C_{m_{ie}, m_{iv}}^{J_i, M_i}$ is the Clebsh—Gordan coefficient. Final state is: $|F\rangle = a_{sc}^+ \Phi_0$, where Φ_0 is the state of an atom with closed electron shells (ground state of Ar-like ion). For the state (4) the scattered part of energy shift $\text{Im}\Delta E$ appears first in the PT second order in the form of integral over the scattered electron energy ϵ_{sc} :

$$\int d\epsilon_{sc} G(\epsilon_{iv}, \epsilon_{ie}, \epsilon_{in}, \epsilon_{sc}) / (\epsilon_{sc} - \epsilon_{iv} - \epsilon_{ie} - \epsilon_{in} - i0) \quad (5)$$

with

$$\text{Im}\Delta E = \pi G(\epsilon_{iv}, \epsilon_{ie}, \epsilon_{in}, \epsilon_{sc}). \quad (6)$$

Here G is a definite squared combination of the two-particle matrix elements (2). The value $\sigma = -2 \cdot \text{Im}\Delta E$ represents the collisional cross-section if the incident electron eigen-function is normalized by the unit flow condition and the scattered positron eigen-function is normalized by the energy δ function. The cross-section is as follows:

$$\sigma(0 \rightarrow IF) = 2\pi(2J_f + 1) \sum_{j_{in}, j_{sc}} (2j_{sc} + 1) \left\{ \sum_{j_{ie}, j_{iv}} B_{j_{ie}, j_{iv}}^{FK} \langle j_{ie}, j_{iv}, J_f | j_{in}, j_{sc} | 0 \rangle \right\}^2 \quad (7)$$

with

$$\begin{aligned} & \langle j_{ie}, j_{iv}, J_f | j_{in}, j_{sc} | 0 \rangle = \\ & = \sqrt{(2j_{ie} + 1)(2j_{iv} + 1)} (-1)^{j_{ie} + 1/2} \times \sum_{\lambda} (-1)^{\lambda + J_f} \times \\ & \times \{ \delta_{\lambda, J_f} (1/(2J_f + 1)) \cdot Q_{\lambda}(sc, ie; iv, in) \}. \end{aligned} \quad (8)$$

Here $Q_{\lambda}^{\text{Quil}}$ is defined as follows [11].

$$Q_{\lambda}^{\text{Quil}} = \{ R_{\lambda}(1243)S_{\lambda}(1243) + R_{\lambda}(\tilde{1}24\tilde{3})S_{\lambda}(\tilde{1}24\tilde{3}) + R_{\lambda}(1\tilde{2}\tilde{4}3)S_{\lambda}(1\tilde{2}\tilde{4}3) + R_{\lambda}(\tilde{1}\tilde{2}\tilde{4}\tilde{3})S_{\lambda}(\tilde{1}\tilde{2}\tilde{4}\tilde{3}) \}, \quad (9)$$

where $R_{\lambda}(1,2;4,3)$ is the radial integral of the Coulomb inter-electron interaction with large radial components; the tilde denotes a small component. The different normalization conditions are used for the incident and for the scattered positron wave functions. The details of the whole numerical procedure of calculation of the impact ionization cross-section can be found in [17—22].

We applied our approach to estimate of the positron-impact ionization cross-sections for a number of the noble gases atoms (He, Ne, Ar, Kr). To test our theory we compared our calculations results on available experimental results and theoretical cross-sections data for some atoms. In tables 1, 2 we present available theoretical and experimental (measured) data on the positron-impact ionization cross-sections for He and Ar, namely: Experiment — (A) Danish group: A1 — Jacobsen et al [4], A2 — Knudsen et al [5, 6]; (B) — Bielefeld group of Fromme et al [7, 8]; Theory — the Coulomb approximation CPE and distorted CPE approximation

DCPE [9, 11, 12] and our theoretical results (CEA). One can see the wide dispersion of the measured data. The detailed analysis shows that the latest experimental data by Knudsen et al et al are considered as the most exact. The difference between different theory is provided by using different bases of the wave functions; at low energies, the approaches with more exact functions give much better agreement with experiment in comparison with the CPE model.

Table 1

The positron impact ionization cross-sections (in 10^{-16} cm^2) for neutral helium (see text)

Impact energy, eV	Measured A1	Measured A2	Measured B	Theory CPE	Theory DCPE	Theory CEA
40	—	0.20	0.19	0.22	0.22	0.20
50	—	0.30	0.28	0.25	0.31	0.31
60	—	0.38	0.34	0.31	0.33	0.36
100	0.53	0.51	0.44	0.42	0.45	0.49
150	0.49	0.49	0.42	0.39	0.44	0.48
200	0.44	0.42	0.40	0.37	0.39	0.42
250	—	0.39	0.36	0.35	0.36	0.38
300	0.37	0.35	0.33	0.32	0.30	0.34
400	0.29	0.28	0.27	0.27	0.24	0.28
500	—	0.24	—	0.23	0.19	0.25

Table 2

The positron impact ionization cross-sections (in 10^{-16} cm^2) for neutral argon (see text)

Impact energy, eV	Measured A1	Measured A2	Theory CPE	Theory DCPE	Theory CEA
40	0.15	0.18	—	—	0.19
50	0.20	0.26	0.21	0.22	0.25
60	0.24	0.35	0.23	0.31	0.34
100	0.29	0.37	0.28	0.32	0.36
150	0.25	0.35	0.26	0.29	0.35
200	0.22	0.28	0.23	0.25	0.29
250	—	—	0.22	0.23	0.26
300	0.20	0.23	0.19	0.21	0.23
400	0.17	0.19	0.17	0.17	0.18
500	0.15	0.17	0.14	0.13	0.17

REFERENCES

1. Douglas W. R., Dujko S., Robson Robert, Petrovic Z. Lj., McEachran R., Non-equilibrium transport of positron and electron swarms in gases and liquids // Plasma Sources Science and Technology. — 2010. — Vol. 19. — P. 3—12.
2. Eds. Aumar F. and Winter H. 1999 Photonic, Electronic and Atomic Collisions. (Singapore: World Sci.).
3. Hamada A., Sueoka O., Total cross-section measurements for positrons and electrons colliding with molecules: CCl_4 // Applied Surface Science. — 1999. — Vol. 85, N 2. — P. 64—68.
4. Jacobsen F. M., Frandsen N. P., Knudsen H., Mikkelsen U., Schrader D. M., Single ionization of He, Ne and Ar by positron impact // J. Phys. B. Atom. Opt. Phys. — 1995. — Vol. 28, N 21. — P. 4691—4695.
5. Nielsen K. A., Bluhme H., Knudsen H., Merrison J. P., Ionization of noble gases by positron impact // Hyperfine Interactions. — 2005. — Vol. 127, N 1—4. — P. 523—527.
6. Bluhme H., Knudsen H., Merrison J. P., Nielsen K. A., Ionization of helium, neon and xenon by positron impact // J. Phys. B. Atom. Opt. Phys. — 1999. — Vol. 32, N 22. — P. 5237—5245.

7. Fromme D., Kruse G., Raith W., Sinapius G., Partial-Cross-Section Measurements for Ionization of Helium by Positron Impact // *Phys. Rev. Lett.* — 1986. — Vol. 57. — P. 3031—3034.
8. Sperber W., Becker D., Lynn K. G., Raith W., Schwab A., Sinapius G., Spicher G., Weber M., Measurement of positronium formation in positron collisions with hydrogen atoms // *Phys. Rev. Lett.* — 1992. — Vol. 68. — P. 3690—3693.
9. Campeanu R. I., McEachran R. P., Stauer A. D., Distorted-wave models in positron impact ionization of atoms // *Nucl. Instr. and Methods in Phys. Research. B.* — 2002. — Vol. 192. — P. 146—149.
10. Parcell L. A., McEachran R. P., Stauffer A. D., Positron Scattering from Xenon // *Nuclear Instruments and Methods in Physics Research: Section B.* — 2002. — Vol. 192. — P. 180—184.
11. McEachran R. P., Stauffer A. D., Excitation of the 4s 1P_1 and 3P_1 States of Argon by Positron Impact // *Phys. Rev. A.* — 2002. — Vol. 65. — P. 034703.
12. Campeanu R. I., McEachran R. P., Stauffer A. D., Positron impact ionization of hydrogen and the noble gases // *Canad. Journ. of Phys.* — 2001. — Vol. 79. — P. 1231—1236.
13. McEachran R., Stauffer A. D., An optical potential method for elastic electron and positron scattering from argon // *J. Phys. B: At. Mol. and Opt. Phys.* — 2009. — Vol. 42. — P. 075202 (6p.).
14. Jones A., Caradonna P., Makochekanwa C., Slaughter D., McEachran R., Machacek J., Sullivan J., Buckman S., Observation of Threshold Effects in Positron Scattering from the Noble Gases // *Phys. Rev. Lett.* — 2010. — Vol. 105. — P. 073201 (4p.).
15. Chen Z., Msezane A. Z., Calculation of the cross sections for positron- and proton-impact ionization of helium // *Phys. Rev. A.* — 1994. — Vol. 49. — P. 1752—1756.
16. Tokesi K., Barna I. F., Burgdorfer J., Ionization of helium in positron impact // *Nucl. Instr. and Methods in Phys. Research. B.* — 2005. — Vol. 233. — P. 307—311.
17. Glushkov A. V., Ivanov L. N., Ivanova E. P. Radiation decay of Atomic States: generalized Energy Approach // *Autoionization Phenomena in Atoms.* — M.: Moscow Univ. — 1986.
18. Glushkov A. V., Malinovskaya S. V., Loboda A. V., Shpinareva I. M., Gurnitskaya E. P., Korchevsky D. A., Diagnostics of the collisionally pumped plasma and search of the optimal plasma parameters of x-ray lasing: Calculation of electron-collision strengths and rate coefficients for Ne-like plasma // *J. Phys. CS.* — 2005. — Vol. 11. — P. 188—198.
19. Glushkov A. V., Gurnitskaya E. P., Ambrosov S. V., Loboda A. V., Prepelitsa G. P., Consistent QED approach to calculation of electron-collision excitation cross-sections and strengths: Ne-like ions // *Int. Journ. Quant. Chem.* — 2005. — Vol. 104. — P. 562—569.
20. Glushkov A. V., Ambrosov S. V., Loboda A. V., Gurnitskaya E. P., Khetselius O. Yu., QED calculation of heavy multicharged ions with account for the correlation, radiative and nuclear effects // *Frontiers in Quantum Systems* (Berlin, Springer). — 2006. — Vol. 15. — P. 285—300.
21. Gurnitskaya E. P., Korchevsky D. A., Loboda A. V., Sensing the optimal plasma parameters for x-ray lasing: calculation of electron-collision excitation cross-sections for Ar-like plasma ions // *Sensor Electr. and Microsyst. Techn.* — 2006. — N 1. — P. 21—25.
22. Glushkov A. V., *Relativistic Quantum Theory. Quantum, mechanics of Atomic Systems.* — Odessa: Astroprint, 2008.

UDC 539.182

A. V. Loboda, G. P. Prepelitsa, A. A. Svinarenko

POSITRON-ATOM COLLISIONAL SPECTROSCOPY: ENERGY APPROACH

Abstract

A new advanced energy approach in the positron-atom collisional spectroscopy is developed and based on the S-matrix Gell-Mann and Low formalism and relativistic many-body perturbation theory. The results of calculation of the positron impact ionization cross-sections are presented for helium and krypton.

Key words: positron-impact ionization, relativistic energy approach.

УДК 539.182

А. В. Лобода, Г. П. Препелица, А. А. Свиноренко

ПОЗИТРОН-АТОМНАЯ СТОКНОВИТЕЛЬНАЯ СПЕКТРОСКОПИЯ: ЭНЕРГЕТИЧЕСКИЙ ПОДХОД

Резюме

Развит новый усовершенствованный энергетический подход в спектроскопии позитрон-атомных столкновений, который базируется на S-матричном формализме Гелл-Мана и Лоу и релятивистской многочастичной теории возмущений. Приведены результаты расчета сечений позитрон-ударной ионизации для гелия и криптона.

Ключевые слова: позитрон-ударная ионизация, релятивистский энергетический подход.

УДК 539.182

А. В. Лобода, Г. П. Препелица, А. А. Свиноренко

ПОЗИТРОН-АТОМНА СПЕКТРОСКОПІЯ ЗА РАХУНОК ЗІТКНЕНЬ: ЕНЕРГЕТИЧНИЙ ПІДХІД

Резюме

Розвинуто новий удосконалений енергетичний підхід у спектроскопії позитрон — атомних зіткнень, який базується на S-матричному формалізмі Гелл-Мана та Лоу і релятивістській багаточастинковій теорії збурень. Наведені результати розрахунку перерізів позитрон-ударної іонізації для гелію та криптону.

Ключові слова: позитрон-ударна іонізація, релятивістський енергетичний підхід.

NEGATIVE SENSITIVITY OF SILICON $p-n$ JUNCTIONS AS GAS SENSORS

The influence of ammonia vapors on $I-V$ characteristics of the forward and reverse currents in silicon $p-n$ junctions with different doping levels was studied. Some samples had anomalous high forward and reverse currents. They had negative sensitivity to ammonia vapors. The forward and reverse currents decreased with increasing ammonia partial pressure in the ambient atmosphere. This effect is explained under an assumption that some ionized acceptor centers are present on the n -region surface and form a surface conductive channel, which shorts the $p-n$ junction. Adsorption of ammonia molecules, which are donors in Si, compensates the surface acceptors and diminish the conductivity of the channel.

1. INTRODUCTION

$P-n$ junctions as gas sensors [1, 2] have some advantages in comparison with oxide polycrystalline films [3] and Schottky diodes [4]. $P-n$ junctions on wide-band semiconductors have high potential barriers for charge carriers, which results in low background currents. $P-n$ junctions on III-V semiconductors exhibit high sensitivity and selectivity to the gas components [5, 6]. The advantage of silicon $p-n$ junctions as gas sensors is that they are compatible with silicon amplifying elements. Characteristics of silicon $p-n$ junctions as gas sensors were studied in previous works [7–9].

The sensitivity of studied $p-n$ structures to donor vapors such as ammonium was explained with the field effect. In the electric field of adsorbed positive ions a surface conductive channel is formed, which shorts the $p-n$ junction [5–9]. It results in an increase of the forward and reverse currents in a $p-n$ junction in presence of a donor gas.

The purpose of this work is a comparative study of the influence of ammonia vapors on stationary $I-V$ characteristics of silicon $p-n$ junctions with different surface currents.

2. EXPERIMENT

The measurements were carried out on silicon $p-n$ junctions with different gradients of the doping concentrations. The n regions were doped with phosphorus and p regions with boron. The surface of $p-n$ junctions was not covered, so there was only a natural oxide layer. The parameters of the studied samples are presented in Table 1. The samples were ranged in breakdown voltage. $C-V$ characteristics of all the samples were linear in a plot $C^{-3}(V)$, so

the $p-n$ junctions were linear. The values of the doping concentrations gradient correlated with the breakdown voltages and were in the range between $4.5 \cdot 10^{21} \text{ cm}^{-4}$ and $4.5 \cdot 10^{23} \text{ cm}^{-4}$, as evident from Tab. 1.

Table 1

Parameters of samples

Number of the sample	1	2	3	4
Breakdown voltage, Volts	3.3	5.1	8.2	18
Gradient of the doping concentrations, cm^{-4}	$4.5 \cdot 10^{23}$	$5.1 \cdot 10^{22}$	$2.6 \cdot 10^{22}$	$4.6 \cdot 10^{21}$
Ideality coefficient of $I-V$ curve	1.82	2.89	1.44	2.92
Depletion layer width from $C-V$ curve, nm	60	93	125	248
Depletion layer width from $I-V$ curve, nm	44	37	54	36

$I-V$ curves of the forward current in all the samples are presented in Fig. 1. Over the current range between 10 nA and 1 mA the $I-V$ curve can be described with the expression

$$I(V) = I_0 \exp[qV/(n_i kT)], \quad (1)$$

where I_0 for each sample is a constant; q is the electron charge; V denotes bias voltage; k is the Boltzmann constant; T is temperature; n_i is the ideality coefficient. The ideality coefficients for all the studied samples are presented in Tab. 1.

Ideality coefficients of all the $I-V$ characteristics essentially exceed the ideal value $n_i = 1$.

Deviation from the value $n_t = 1$ can be ascribed to the local phonon-assisted tunnel recombination on deep levels in non-homogeneities of the p – n junction [10]. The local depletion layer wide in these non-homogeneities can be estimated from the expression [10]

$$n_t = n_{t0} \left[1 - \frac{qh^2}{6m_t(\omega_V kT)^2} \right]^{-1}, \quad (2)$$

where $n_{t0} = 1$ or $n_{t0} = 2$ for related recombination mechanisms; h is the Plank constant; m_t is the tunnel effective mass of current carriers; ω_V is a parameter of the non-homogeneity of the p – n junction, which is used in the expression

$$\omega = \omega_V \left(\frac{\Phi_0}{q} - V \right)^{\frac{1}{2}}, \quad (3)$$

where ω is the local p – n junction width at voltage V ; Φ_0 is the equilibrium barrier height in the p – n junction.

The local depletion layer widths of the p – n junctions, obtained from such analysis of I – V curves, are presented in Tab. 1. It is evident that the depletion layer widths in the non-homogeneities, responsible for the recombination current, are remarkably smaller, than the values, estimated from C – V curves. The maximum difference between these values is for the sample with a breakdown voltage of 18 V.

Fig. 2 presents I – V characteristics of reverse current in the p – n junctions. The samples with breakdown voltages of 3.3 and 5.1 V exhibit exponential rise of the current with the voltage. This corresponds to the tunnel breakdown mechanism. In the sample with a breakdown voltage of 8.2 V the current does not exceed 10^{-8} A at $V < 5$ Volts. And the sample with a breakdown voltage of 18 V exhibit anomalous high reverse current. This is in accordance with high forward current in this sample and anomalous thin depletion layer in the non-homogeneities, which are responsible for the recombination current.

Fig. 3 shows I – V characteristics of reverse current in the p – n junction with breakdown voltage of 5.1 Volts, measured in air and in air with ammonia vapors of several partial pressures. Adsorption of ammonia molecules strongly increases the current.

The (absolute, current-) gas sensitivity of a p – n junction as gas sensor can be defined as

$$S_I = \Delta I / \Delta P, \quad (4)$$

where ΔI is the change in the current (at a fixed voltage), which is due to a change ΔP in the corresponding gas partial pressure [11]. An analysis of the data in Fig. 3 yields an estimation $S_I = 0.5 \mu\text{A/kPa}$ at a reverse bias voltage of 1 V.

Fig. 4 presents I – V characteristics of reverse current in the p – n junction with break-

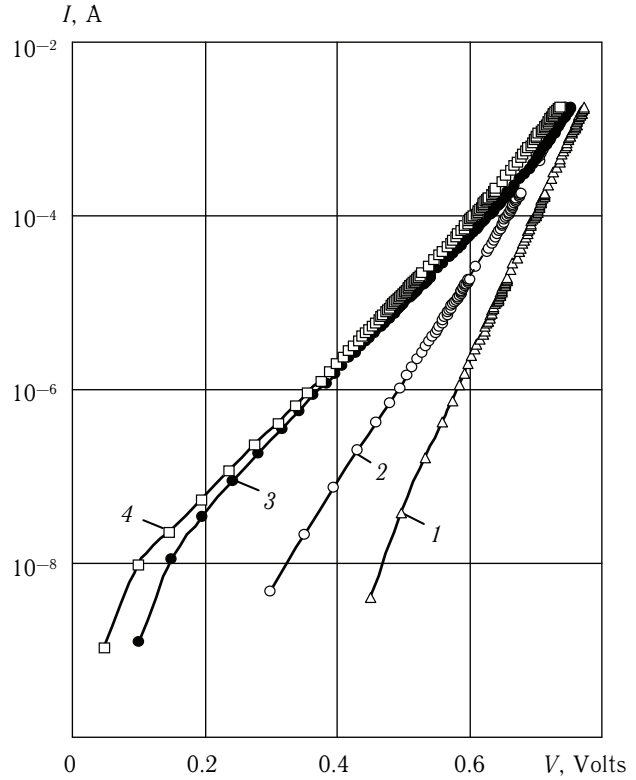


Fig. 1. I – V characteristics of the forward current in p – n structures with different breakdown voltages, Volts: 1 – 8.2; 2 – 3.3; 3 – 5.1; 4 – 18

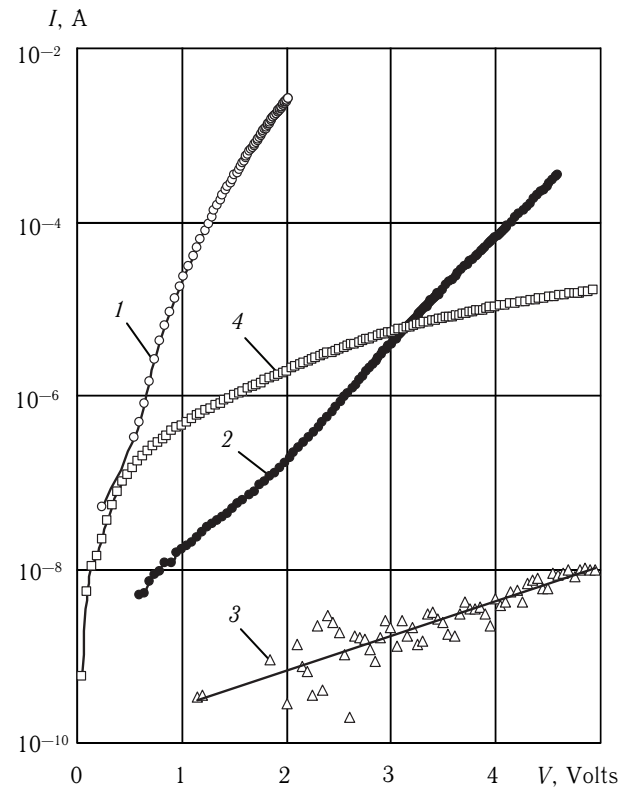


Fig. 2. I – V characteristics of the reverse current in p – n structures with different breakdown voltages, Volts: 1 – 3.3; 2 – 5.1; 3 – 8.2; 4 – 18

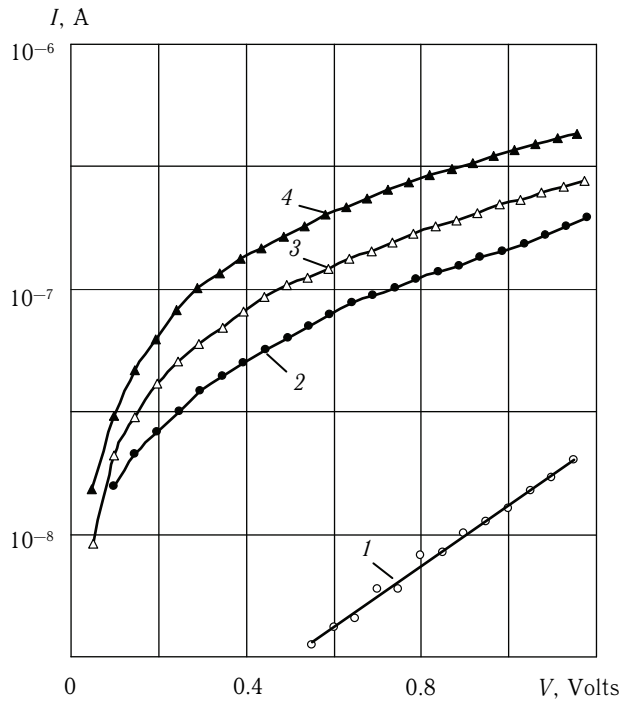


Fig. 3. I — V characteristics of the reverse current in p — n structure with breakdown voltage of 5.1 Volts, measured in air (1) and in air with ammonia vapors of partial pressure: 2 — 100 Pa; 3 — 500 Pa; 4 — 1000 Pa

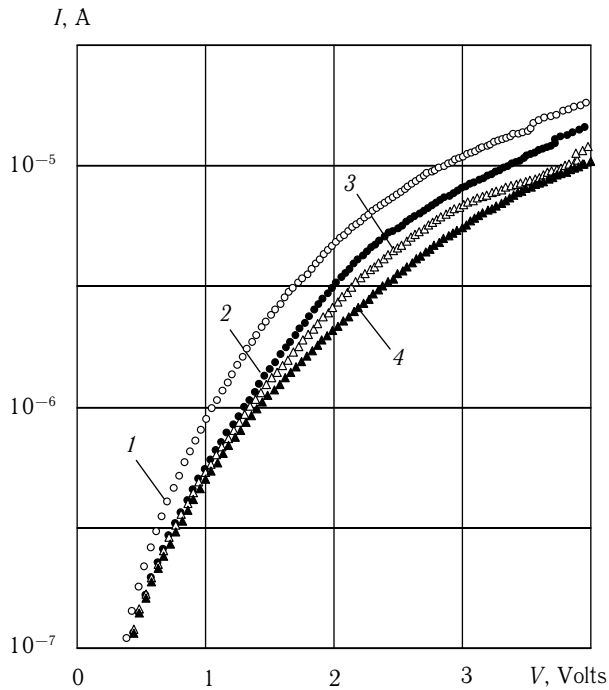


Fig. 4. I — V characteristics of the reverse current in p — n structure with breakdown voltage of 18 Volts, measured in air (1) and in air with ammonia vapors of partial pressure: 2 — 100 Pa; 3 — 500 Pa; 4 — 1000 Pa

down voltage of 18 Volts (“anomalous sample”), obtained in air and in air with ammonia vapors of various partial pressures. A comparison between curves 1—4 shows that adsorption of ammonia molecules does not increase the cur-

rent. The current in ammonia vapors is lower, than in dry air. And the sensitivity of this sample is negative, namely $S_I = -20 \mu\text{A/kPa}$ at a bias voltage of 4 V and $S_I = -0.7 \mu\text{A/kPa}$ at $V = 1$ V. The absolute value of the negative sensitivity of this sample is some higher, than the sensitivity of “normal” samples.

The relative sensitivity of a gas sensor is defined as

$$S_R = \Delta I / (I_0 \Delta P), \quad (5)$$

where I_0 denotes the current in the pure air at the same bias voltage. An analysis of the data in Figs. 3 and 4 gives for the relative sensitivity of a “normal” sample $S_R = 10 \text{ kPa}^{-1}$ at $V = 1$ V and for the “anomalous” one $S_R = -0.7 \text{ kPa}^{-1}$ at the same bias. A relative sensitivity of this sample reaches a value of -10 kPa^{-1} at $V = 4$ V. It is remarkable that the current noise in “anomalous” samples is higher, than in “normal” junctions. It is because the current of the “anomalous” samples in the pure air is high.

3. DISCUSSION

The negative sensitivity to a donor gas, namely, a decrease in the current as a result of the donor molecules adsorption can be explained under an assumption that some acceptor centers are present on the n -region surface. The corresponding schematic of the p — n structure is presented in Fig. 5. Ionized acceptors (not shown) at (on) the surface of n -region form an electric field, which bends up the c - and v -bands. Therefore the depletion region 3 is bent, as shown in Fig. 5. A channel of p -type conductivity 4 is produced at enough high number of ionized acceptors. This channel shorts the p — n junction, and therefore the forward and reverse currents in dry air are high. When the p — n

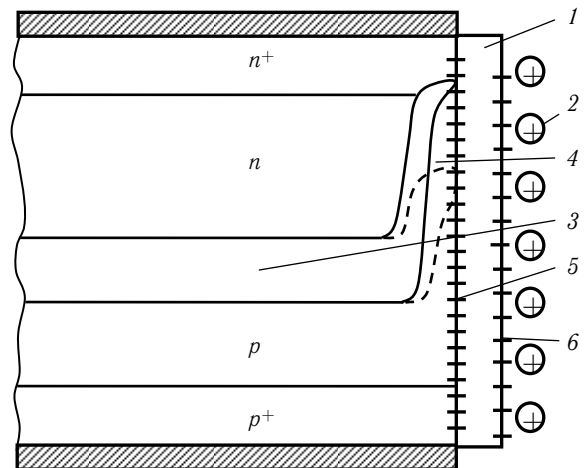


Fig. 5. Schematic of the p — n structure in NH_3 vapors: 1 — oxide layer; 2 — ions; 3 — depletion layer; 4 — conducting channel; 5 — surface states (rapid centers); 6 — states on the oxide surface (slow centers). Dashed — the depletion layer after adsorption of donor molecules

junction is placed in ammonia vapors, NH_3 molecules are adsorbed and ionized on the crystal surface. The ionized donors partly compensate the acceptors mentioned and decrease the band bending. Therefore the conduction channel becomes shorter, as shown with dashed lines in Fig. 5, and the current in the channel decreases.

4. CONCLUSIONS

Silicon p – n junctions can have negative sensitivity to donor vapors, such as ammonia. In these structures the forward and reverse currents decrease in the atmosphere of donor gases. Such p – n structures have acceptor centers on (at) the surface of the n -layer. The electric field of the ionized acceptors bends up c - and v -bands and, at enough high density of acceptors, forms a channel with p -conductivity at the n -layer surface. This channel shorts the p – n junction, causing an additional current at forward and reverse biases. Adsorption of donor molecules, such as NH_3 , partly compensates acceptors mentioned and decreases the surface currents at forward and reverse biases.

The absolute (current-) and relative sensitivities of such p – n structures is negative, which extends the functional possibilities of p – n junctions as gas sensors.

The negative sensitivity to ammonia vapors of the silicon p – n junctions with acceptor surface doping is of the same order, as the positive sensitivity of p – n structures without such doping.

The response time of the sensors with positive and negative sensitivity at room temperature is of 100 s.

The current noise in the sensors with negative sensitivity is higher, than in other structures of positive sensitivity because of higher current in pure air.

REFERENCES

1. Ptashchenko O. O., Artemenko O. S., Ptashchenko F. O. Vliyanie gazovoi sredy na poverkhnostnyi tok v p – n geterostrukturakh na osnove GaAs–AlGaAs // *Fizika i khimiya tverdogo tila*. — 2001. — V. 2, № 3. — P. 481–485.
2. Ptashchenko O. O., Artemenko O. S., Ptashchenko F. O. Vplyv pariv amiaku na poverkhnevyy strum v p – n perekhodakh na osnovi napivprovodnykh A^3B^5 // *Journal of physical studies*. — 2003. — V. 7, № 4. — P. 419–425.
3. Bugayova M. E., Koval V. M., Lazarenko B. I. et al. Gazovi sensory na osnovi oksydu tsynku (oglyad) // *Sensorna elektronika i mikrosystemni tehnologii*. — 2005. — № 3. — P. 34.
4. Baluba V. I., Gritsyk V. Y., Davydova T. A. et al. Sensory ammiaka na osnove diodov Pd– n –Si // *Fizika i tekhnika poluprovodnikov*. — 2005. — V. 39, № 2. — P. 285–288.
5. Ptashchenko O. O., Artemenko O. S., Dmytruk M. L. et al. Effect of ammonia vapors on the surface morphology and surface current in p – n junctions on GaP. // *Photoelectronics*. — 2005. — No. 14. — P. 97–100.
6. Ptashchenko F. O. Effect of ammonia vapors on surface currents in InGaP p – n junctions // *Photoelectronics*. — 2007. — No. 17. — P. 113–116.
7. Ptashchenko F. O. Vplyv pariv amiaku na poverkhnevyy strum u kremniyevykh p – n perekhodakh // *Visnyk ONU, ser. Fizyka*. — 2006. — V. 11, № 7. — P. 116–119.
8. Ptashchenko O. O., Ptashchenko F. O., Yemets O. V. Effect of ammonia vapors on the surface current in silicon p – n junctions // *Photoelectronics*. — 2006. — No. 16. — P. 89–93.
9. Ptashchenko O. O., Ptashchenko F. O., Yemets O. V. Effect of ambient atmosphere on the surface current in silicon p – n junctions // *Photoelectronics*. — 2009. — No. 18. — P. 28–32.
10. Ptashchenko A. A., Ptashchenko F. A. Tunnel surface recombination in p – n junctions // *Photoelectronics*. — 2000. — № 10. — P. 69–71.
11. Vashpanov Yu. A., Smyntyna V. A. Adsorbtsionnaya chuvstvitel'nost' poluprovodnikov. — Odessa: Astroprint, 2005. — 216 p.

UDC 621.315.592

F. O. Ptashchenko, O. O. Ptashchenko, G. V. Dovganyuk

NEGATIVE SENSITIVITY OF SILICON p – n JUNCTIONS AS GAS SENSORS

Abstract

The influence of ammonia vapors on I – V characteristics of the forward and reverse currents in silicon p – n junctions with different doping levels was studied. Some samples had anomalous high forward and reverse currents. They had negative sensitivity to ammonia vapors. The forward and reverse currents decreased with increasing ammonia partial pressure in the ambient atmosphere. This effect is explained under an assumption that some ionized acceptor centers are present on the n -region surface and form a surface conductive channel, which shorts the p – n junction. Adsorption of ammonia molecules, which are donors in Si, compensates the surface acceptors and diminish the conductivity of the channel.

Key words: gas sensor, p – n junction, surface states, conductive channel, sensitivity.

УДК 621.315.592

Ф. О. Птащенко, О. О. Птащенко, Г. В. Довганюк

НЕГАТИВНА ЧУТЛИВІСТЬ КРЕМНІЄВИХ p – n ПЕРЕХОДІВ ЯК ГАЗОВИХ СЕНСОРІВ

Резюме

Досліджено вплив парів аміаку на ВАХ прямого і зворотного струмів кремнієвих p – n переходів з різним рівнем легування. Деякі зразки мали аномально високі прямий і зворотний струми. Вони мали негативну чутливість до парів аміаку. Прямий і зворотний струми зменшувалися зі зростанням парціального тиску аміаку в навколишній атмосфері. Даний ефект пояснюється у припущенні, що на поверхні n -області знаходяться іонізовані акцепторні центри і формують провідний канал, який закорочує p – n перехід. Адсорбція молекул аміаку, які є донорами в Si, компенсує поверхневі акцептори і зменшує електропровідність каналу.

Ключові слова: газовий сенсор, p – n перехід, поверхневі стани, провідний канал, чутливість.

ОТРИЦАТЕЛЬНАЯ ЧУВСТВИТЕЛЬНОСТЬ КРЕМНИЕВЫХ $p-n$ ПЕРЕХОДОВ КАК ГАЗОВЫХ СЕНСОРОВ

Резюме

Исследовано влияние паров аммиака на ВАХ прямого и обратного токов кремниевых $p-n$ переходов с различным уровнем легирования. Некоторые образцы имели аномально высокие прямой и обратный токи. Они имели отрицательную чувствительность к парам аммиака. Прямой и обратный токи уменьшались с ростом парциального давления аммиака в окружающей атмосфере. Данный эффект объясняется в предположении, что на поверхности n -области находятся ионизированные акцепторные центры и формируют проводящий канал, который закорачивает $p-n$ переход. Адсорбция молекул аммиака, которые являются донорами в Si, компенсирует поверхностные акцепторы и уменьшает электропроводность канала.

Ключевые слова: газовый сенсор, $p-n$ переход, поверхностные состояния, проводящий канал, чувствительность.

¹ Department of Solid State Physics, Volyn National University, Voli Ave 13, 43025 Lutsk, Ukraine² Department of Chemistry, Lutsk National Technical University, 75 Lvivska St., 43018 Lutsk, Ukraine³ Department of Solid state Physics, Volyn National University, Voli Ave 13, 43025 Lutsk, Ukraine
Tel/fax: +30332249221; E-mail address: halyan@univer.lutsk.ua

THE FEATURES OF INFRARED PHOTOLUMINESCENCE IN GLASSES OF THE SYSTEM $\text{Ag}_{0.05}\text{Ga}_{0.05}\text{Ge}_{0.95}\text{S}_2\text{—Er}_2\text{S}_3$ AT VARIOUS INTENSITY AND WAVELENGTH OF EXCITATION

Photoluminescence and optical absorption spectra of the glasses $(100 - X)\text{Ag}_{0.05}\text{Ga}_{0.05}\text{Ge}_{0.95}\text{S}_2\text{—}(X)\text{Er}_2\text{S}_3$, where $X = 0.42, 0.25, 0.18$ mol% Er_2S_3 were investigated in the spectral range 1450–1650 nm at room temperature. Excitation of luminescence was carried out using wavelengths of 532 and 980 nm at various power of excitation. Higher intensity of the luminescence was observed at $\lambda_{\text{ex}} = 980$ nm at equal power of excitation. Observed nonlinear dependence of the photoluminescence intensity on power of excitation is due to up-conversion processes.

1. INTRODUCTION

Glassy alloys activated by the ions of rare-earth elements (RE) are of considerable interest for development of optical communication and photonics for fabrication of optical amplifiers and microlasers. Special attention has been turned to the glasses that doped with erbium, as wavelength of emission of erbium ions (1.54 μm) is optimum for transferring information via fiber-optic communication lines. In the telecommunication devices, simultaneously with a space-saving, it is necessary to increase emission efficiency of active environments. It can be achieved by increasing concentration of erbium ions, setting optimum wavelength and power of excitation (PE). Increase of RE concentration is limited by solubility of RE in the host matrix, and also results the concentration extinguishing of photoluminescence (PL) [1-3]. Increase of the power and variation of the excitation wavelength can change spectral distribution of PL, and consequently efficiency of telecommunication devices.

In this work we studied influence of PE and excitation wavelength on PL of glassy alloys of the system $\text{Ag}_{0.05}\text{Ga}_{0.05}\text{Ge}_{0.95}\text{S}_2\text{—Er}_2\text{S}_3$.

2. EXPERIMENTAL

Technology of synthesis and X-ray diffraction analysis of the glassy alloys are presented in detail in our previous work [4]. Investigation of absorption spectra and PL was carried out using MDR-206 monochromator with Si and PbS photodetectors. Excitation of luminescence was carried out using diode laser KLM H980-200-5 with power of 200 mW ($\lambda_{\text{max}} = 980$ nm) and laser LDM532U with power of 150 mW ($\lambda_{\text{max}} = 532$ nm). Receiving of the PL signal was carried out from the same side

of surface of the sample that excitation. Thickness of the samples that were used for investigation of absorption spectra was 1 mm.

3. RESULTS

In the system $\text{AgGaSe}_2 + \text{GeS}_2 \rightleftharpoons \text{AgGaS}_2 + \text{GeSe}_2$ [4] we chose the glassy alloy $\text{Ag}_{0.05}\text{Ga}_{0.05}\text{Ge}_{0.95}\text{S}_2$ which has the widest transparency window in comparison to other glasses of this system. Investigation of PL spectra was performed using the glassy alloys $(100 - X)\text{Ag}_{0.05}\text{Ga}_{0.05}\text{Ge}_{0.95}\text{S}_2\text{—}(X)\text{Er}_2\text{S}_3$, where $X = 0.42, 0.25, 0.18$ mol% Er_2S_3 (0.27, 0.16, 0.12 at% Er, respectively).

Spectral dependences of PL at various PE for the glassy alloy with maximal content of Er_2S_3 that are typical for all glasses of the investigated system are shown in Fig. 1. The comparative analysis of the PL spectra at maximal PE was carried out in our previous work [5]. Fig. 1 shows that intensity of PL at both excitation wavelengths ($\lambda_{\text{ex}} = 980, 532$ nm) increases with increase of PE. Maximum of the PL intensity for both excitation wavelengths is 1540 ± 1.5 nm and does not depend on power of excitation as well as shape of the spectra (as shown in the insertion).

For the investigated glassy alloys increase of PL intensity with increase of PE takes place differently. It can be seen well in Fig. 2 where dependence of PL intensity on PE (at $\lambda = 1540$ nm) is shown. At 0.16, 0.12 at% Er intensity of luminescence I_{PL} is proportional to the power of excitation P at $\lambda_{\text{ex}} = 980$ nm as well as $\lambda_{\text{ex}} = 532$ nm. Functional dependence $I_{\text{PL}}(P)$ at $\lambda_{\text{ex}} = 980, 532$ nm is nonlinear for the sample with maximal content of erbium. Obviously, in the glassy alloys interatomic distance between erbium ions decreases with increasing of Er^{3+} concentration. This may lead to the emergence

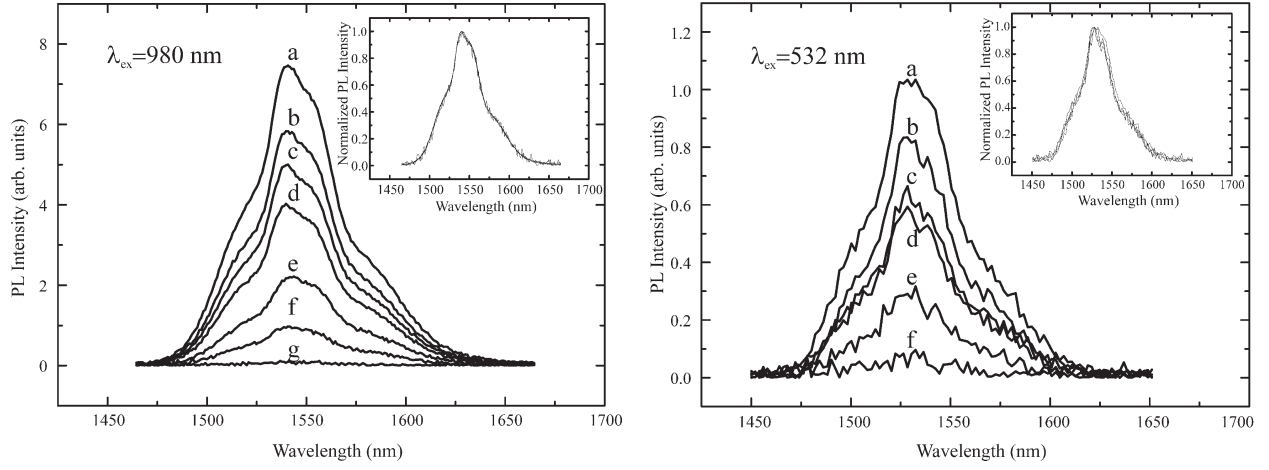


Fig. 1. PL spectra at different powers of excitation (*a* — 200 mW, *b* — 140 mW, *c* — 108 mW, *d* — 87 mW, *e* — 53 mW, *f* — 23 mW, *g* — 5 mW) at temperature of 290 K

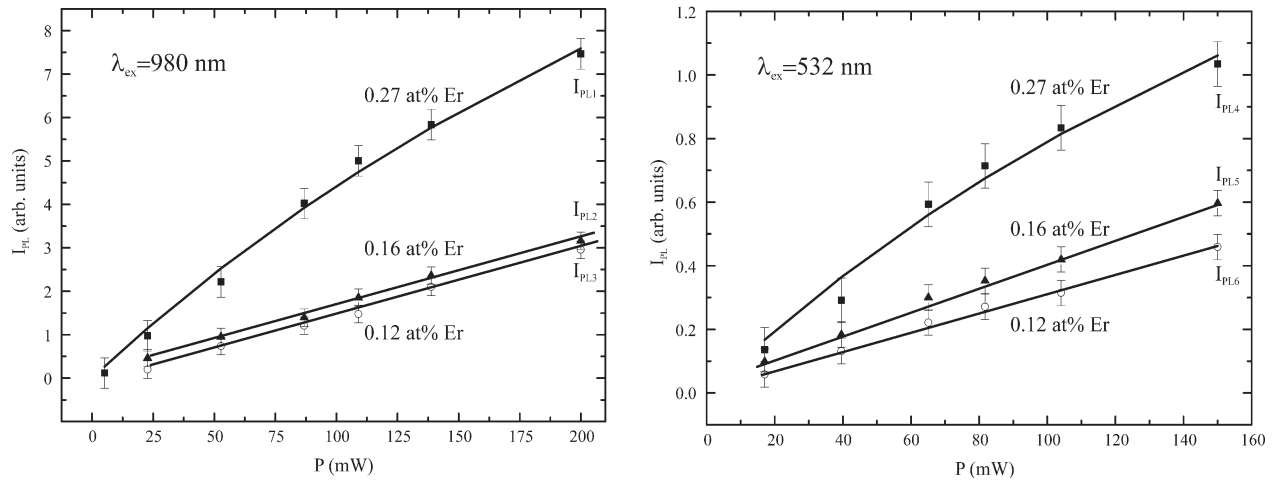


Fig. 2. PL intensity of the glasses as a function of excitation power at different excitation wavelengths at temperature of 290 K

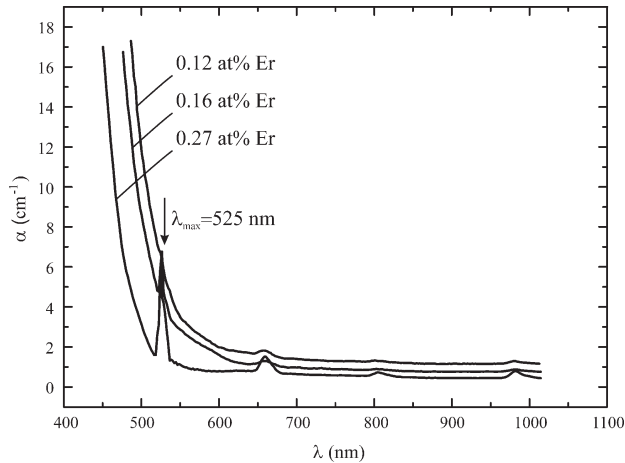


Fig. 3. Absorption spectra of the glasses at temperature of 290 K

of up-conversion processes, and therefore less effective emission at 1540 nm, and, consequently, the nonlinearity of $I_{PL}(P)$.

During excitation of the glassy alloys with wavelength $\lambda_{ex} = 980$ nm energy of light quanta

is directly transferred to the erbium ions, namely the $^4I_{15/2} \rightarrow ^4I_{11/2}$ transition in the 4f-shell of the Er^{3+} ion takes place [6]. At lighting of the sample with wavelength of 532 nm transfer of light energy is not so single-valued as with $\lambda_{ex} = 980$ nm. We have studied spectra of optical absorption of the glasses (Fig. 3). For the sample with maximal erbium content an intensive absorption band was observed in the range of 518—540 nm ($\lambda_{max} = 525$ nm) which diminishes with decreasing content of Er. According to Refs., this absorption band is related to the intra-4f transition $^4I_{15/2} \rightarrow ^2H_{11/2}$ in the Er^{3+} ion [7]. Moreover, the light quanta with wavelength of 532 nm can be absorbed by the glass matrix, as according to Fig. 3, this wavelength is near the edge of the intrinsic absorption area.

4. DISCUSSION

As clearly apparent from absorption spectra (Fig. 3), during excitation of the glasses by light with wavelength of 532 nm energy of photons: at first — is transferred directly to the Er^{3+} ions;

secondly — is absorbed by the glass matrix and in the case of good energy connection of the glass matrix with the Er^{3+} ions can be transferred to the last. Taking this into account, obviously that losses of energy at excitation of PL with wavelength of 532 nm considerably exceed the losses of energy at excitation with 980 nm. Erbium ions excited by light of 532 nm spend its energy on the radiative transition 1540 nm ($^4\text{I}_{13/2} \rightarrow ^4\text{I}_{15/2}$). In addition, energy losses can occur with or without light emission in the other transitions of the Er^{3+} ion, namely: 550 nm ($^4\text{S}_{3/2} \rightarrow ^4\text{I}_{15/2}$), 660 nm ($^4\text{F}_{9/2} \rightarrow ^4\text{I}_{15/2}$), 800 nm ($^4\text{I}_{9/2} \rightarrow ^4\text{I}_{15/2}$), 980 nm ($^4\text{I}_{11/2} \rightarrow ^4\text{I}_{15/2}$). Figs. 1, 2 show that intensity of PL at $\lambda_{\text{ex}} = 980$ nm is approximately 6 times higher than the intensity at $\lambda_{\text{ex}} = 532$ nm (for $P = 100\text{--}110$ mW). In the last case (at $\lambda_{\text{ex}} = 532$ nm) the role of competitive channels increases both in the process of excitation and during transition to the ground state of the rare-earth ions that our experimental results confirm.

Intensity of PL increases with increase of the erbium concentration, as Fig. 2 shows. At maximal PE ($\lambda_{\text{ex}} = 532$ nm) increase of the PL intensity is proportional to increase of erbium concentration in the glasses:

$$\frac{I_{\text{PL4}}}{I_{\text{PL5}}} \approx \frac{0.27 \text{ at } \%}{0.16 \text{ at } \%} = 1.69; \quad \frac{I_{\text{PL4}}}{I_{\text{PL6}}} \approx \frac{0.27 \text{ at } \%}{0.12 \text{ at } \%} = 2.25.$$

Consequently, PL intensity increases due to increase of atomic content of the rare-earth element. At excitation of the samples with wavelength $\lambda_{\text{ex}} = 980$ nm at maximal PE ratios of PL intensities are:

$$\frac{I_{\text{PL1}}}{I_{\text{PL2}}} \approx 2.36; \quad \frac{I_{\text{PL1}}}{I_{\text{PL3}}} \approx 2.52.$$

In the latter case, increase of PL intensity is due to several factors: increasing erbium content, reducing energy losses compared with $\lambda_{\text{ex}} = 532$ nm, and also we assume that there is an increase of fraction of the optically active erbium ions. This supposition can be verified considering functional dependences $I_{\text{PL}}(P)$ for each of the glassy alloys. Dependence of PL intensity on power of excitation for Er-containing materials is defined as following [8, 9]:

$$I_{\text{PL}} = \frac{abP}{(1 + bP)}, \quad (1)$$

where $b = Q \cdot \tau$; $a \sim N_0^{\text{Er}} \tau_d$; $I_{\text{PL}} \sim N^{\text{Er}} \omega_{\text{rad}}$; P is the power of excitation; Q is a factor which includes the quantum efficiency of the process (which is dependent on the temperature, excitation wavelength and geometrical parameters); N^{Er} , N_0^{Er} are the concentrations of excited and optically active Er^{3+} ions, respectively; τ , τ_d are total and radiative lifetime of Er^{3+} in the excited state, respectively; $\omega_{\text{rad}} = \frac{1}{\tau_d}$ is the probability of radiative transition.

In partial case PL intensity linearly depends on PE if $bP \ll 1$, then from Eq. (1) we will get:

$$I_{\text{PL}} = abP. \quad (2)$$

In Fig. 2 the dependencies for 0.16 and 0.12 at% Er are described actually by Eq. (2). Consequently, in the samples the equation (2) is ensured by low quantum efficiency Q and low total lifetime τ in all range of P variation. In Fig. 2 for the glassy alloy with 0.27 at% Er a solid line represents the fitted dependence calculated using Eq. (1) with following values of coefficients: $a = 26.84$ arb. units, $b = 0.002 \text{ mW}^{-1}$ at $\lambda_{\text{ex}} = 980$ nm; $a = 3.378$ arb. units, $b = 0.003 \text{ mW}^{-1}$ at $\lambda_{\text{ex}} = 532$ nm. Calculations show that b parameter diminishes insignificantly ($b_{980} = 0.67 \cdot b_{532}$) while a increases approximately in 8 times (for $\lambda_{\text{ex}} = 980$ nm). Taking into account the variations of both parameters we can obtain increase of PL intensity with variation of excitation wavelength from 532 to 980 nm approximately in 5.36 times. Consequently, calculated increase of PL intensity is due to increase of the a parameter which is proportional to the concentration of optically active Er^{3+} ions N_0^{Er} and radiative lifetime τ_d . However, it should be noted that the factor of increase of the fraction of optically active erbium ions may be less influential on the increase of PL compared to the energy losses that occur at $\lambda_{\text{ex}} = 980$ nm than at $\lambda_{\text{ex}} = 532$ nm.

5. CONCLUSIONS

Position of the intensity maximum and shape of the spectral dependences of PL do not depend on power and wavelength ($\lambda_{\text{ex}} = 980, 532$ nm) of excitation. During excitation of the glasses with wavelength of 532 nm energy of photons is transferred directly to the Er^{3+} ions ($^4\text{I}_{15/2} \rightarrow ^2\text{H}_{11/2}$ transition) and also absorbed by the glass matrix. Nonlinear dependence of PL on PE when doping the alloy with 0.27 at% Er is associated with the emergence of up-conversion processes that reduce the effectiveness of PL emission. The increase in PL intensity with variation of the excitation wavelength from 532 to 980 nm is due to the less losses of energy transfer both during excitation of the erbium ions and transition to the ground state and, possibly, to the increasing concentration of the optically active Er^{3+} ions.

REFERENCES

1. A. Tverjanovich, Ya. G. Grigoriev, S. V. Degtyarev, A. V. Kurochkin, A. A. Man'shina, Yu. S. Tver'yanovich. *J. Non-Cryst. Solids*, 2001, 286(1–2), p. 89–92.
2. Z. G. Ivanova, R. Ganesana, K. V. Adarsha, V. S. Vassilev, Z. Aneva, Z. Cernosek, E. S. R. Gopala. *J. Optoelectron. Adv. Mater.*, 2005, 7(1), p. 345–348.
3. Z. G. Ivanova, E. Cernosekova, Z. Cernosek. *J. Phys. Chem. Solids*, 2007, 68(5–6), p. 1260–1262.
4. V. V. Halyan, M. V. Shevchuk, G. Ye. Davydyuk, S. V. Voronyuk, A. H. Kevshyn, V. V. Bulatetsky. *Semicon.*

Phys. Quant. Electr. Optoelectron., 2009, 12(2), p. 138—142.

5. V. V. Halyan, A. H. Kevshyn, Yu. M. Kogut, G. Ye. Davydyuk, M. V. Shevchuk, V. Kažukauskas, A. Ziminskij. *Phys. Stat. Sol. (c)*, 2009, 6(12), p. 2810—2813.

6. J. Fick, É. J. Knystautas, A. Villeneuve, F. Schiettekatte, S. Roorda, K. A. Richardson, *J. Non-Cryst. Solids*, 2000, 272(2—3), p. 200—208.

7. T. Yu. Ivanova, A. A. Man'shina, A. V. Kurochkin, Yu. S. Tver'yanovich, V. B. Smirnov. *J. Non-Cryst. Solids*, 2002, 298(1), p. 7—14.

8. R. Serna, Jung H. Shin, M. Lohmeier, E. Vlieg, A. Polman, P. F. A. Alkemade. *J. Appl. Phys.*, 1999, 79(5), p. 2658—2662.

9. B. A. Andreev, Z. F. Krasil'nik, V. P. Kuznetsov, A. O. Soldatkin, M. S. Bresler, O. B. Gusev, I. N. Yassievich. *Physics of Solid State*, 2001, 43(6), p. 979—984.

UDC 621.315.592

V. V. Halyan, A. H. Kevshyn, G. Ye. Davydyuk, M. V. Shevchuk, S. V. Voronyuk

THE FEATURES OF INFRARED PHOTOLUMINESCENCE IN GLASSES OF THE SYSTEM $\text{Ag}_{0.05}\text{Ga}_{0.05}\text{Ge}_{0.95}\text{S}_2\text{—Er}_2\text{S}_3$ AT VARIOUS INTENSITY AND WAVELENGTH OF EXCITATION

Abstract

Photoluminescence and optical absorption spectra of the glasses $(100 - X)\text{Ag}_{0.05}\text{Ga}_{0.05}\text{Ge}_{0.95}\text{S}_2\text{—}(X)\text{Er}_2\text{S}_3$, where $X = 0.42, 0.25, 0.18$ mol% Er_2S_3 were investigated in the spectral range 1450—1650 nm at room temperature. Excitation of luminescence was carried out using wavelengths of 532 and 980 nm at various power of excitation. Higher intensity of the luminescence was observed at $\lambda_{\text{ex}} = 980$ nm at equal power of excitation. Observed nonlinear dependence of the photoluminescence intensity on power of excitation is due to up-conversion processes.

Keywords: Photoluminescence; Glasses; Optical spectroscopy; Rare-earth in glasses; Power of excitation.

УДК 621.315.592

В. В. Галян, А. Г. Кевшин, Г. Е. Давидюк, Н. В. Шевчук, С. В. Воронюк

ОСОБЕННОСТИ ИНФРАКРАСНОЙ ФОТОЛЮМИНЕСЦЕНЦИИ В СТЕКЛАХ СИСТЕМЫ $\text{Ag}_{0.05}\text{Ga}_{0.05}\text{Ge}_{0.95}\text{S}_2\text{—Er}_2\text{S}_3$ ПРИ РАЗНОЙ ИНТЕНСИВНОСТИ И ДЛИНЕ ВОЛНЫ ВОЗБУЖДЕНИЯ

Резюме

В спектральном диапазоне 1450—1650 нм при комнатной температуре мы исследовали спектры люминесценции и оптического поглощения стекол $(100 - X)\text{Ag}_{0.05}\text{Ga}_{0.05}\text{Ge}_{0.95}\text{S}_2\text{—}(X)\text{Er}_2\text{S}_3$, где $X = 0,42, 0,25, 0,18$ мол%. Возбуждение люминесценции проводилось длиной волны 532 и 980 нм при различной мощности возбуждения. Большая интенсивность люминесценции при одинаковой мощности возбуждения зафиксирована при $\lambda_{\text{вз}} = 980$ нм. Зафиксирована нелинейная зависимость интенсивности фотолюминесценции от мощности возбуждения, обусловлена апконверсионными процессами.

Ключевые слова: стеклообразные сплавы, оптическое поглощение, фотолюминесценция.

УДК 621.315.592

В. В. Галян, А. Г. Кевшин, Г. Е. Давидюк, М. В. Шевчук, С. В. Воронюк

ОСОБЛИВОСТІ ІНФРАЧЕРВОНОЇ ФОТОЛЮМІНІСЦЕНЦІЇ В СТЕКЛАХ СИСТЕМИ $\text{Ag}_{0.05}\text{Ga}_{0.05}\text{Ge}_{0.95}\text{S}_2\text{—Er}_2\text{S}_3$ ПРИ РІЗНІЙ ІНТЕНСИВНОСТІ ТА ДОВЖИНІ ХВИЛІ ЗБУДЖЕННЯ

Резюме

В спектральному діапазоні 1450—1650 нм при кімнатній температурі ми дослідили спектри люмінесценції і оптичного поглинання стекол $(100 - X)\text{Ag}_{0.05}\text{Ga}_{0.05}\text{Ge}_{0.95}\text{S}_2\text{—}(X)\text{Er}_2\text{S}_3$, де $X = 0,42, 0,25, 0,18$ мол%. Збудження люмінесценції проводилось довжиною хвилі 532 і 980 нм при різній потужності збудження. Вища інтенсивність люмінесценції при однаковій потужності збудження зафіксована при $\lambda_{\text{вз}} = 980$ нм. Зафіксована нелінійна залежність інтенсивності фотолюмінесценції від потужності збудження обумовлена апконверсійними процесами.

Ключові слова: склоподібні сплави, оптичне поглинання, фотолюмінесценція.

THE OPTICAL PROPERTIES, STABILITY AND REACTIVITY OF SOLID NANOCLUSTER SUBSYSTEM

In this paper we will present the parametrized density-functional theory (PDFT) in the realisation of Kohn and Sham, using a few empirical parameters. The accuracy of the method is illustrated by the results of calculations for nanocluster silicon subsystems (Si-NCS). The extreme simplicity of the method allows one to calculate the geometry and the electronic structure of nanoclusters. The PDFT method with the combination of the molecular dynamics the simulated process makes very useful tool for the determination of the optical properties, stability, reactivity and covalent-metallic bonding of Si-NCS

The interest to research of atomic clusters systems (ACS) is called not only clearing up of fundamental features of a cluster state of substance [1], but also is boosted by research of possibilities of synthesising of perspective materials for modern optoelectronics [2]. ACS is a small piece of the nature in the range from nanometers to micrometer. ACS is not molecule, and can not to represent itself as the bulk material also. It is real nanodimensional object [3]. The small ACS has properties very different from the bulk material. This is due to of their small physical size.

There are direct experiments (Fig. 1) on the geometry of the nanodimensional cluster subsystem (NCS) as a systems of the spherical-like particles (NDSP) of Si [1]. This fact became motivation of our computer researches of the NCS. To attack this problem we investigated electronic and geometry structures of cage ball-like (CBL) Si-ACS theoretically. Probably, the NDSP are consisting from these structures. To study the dynamics of the CBL-ACS simulation we needs the optimal approximate calculation scheme.

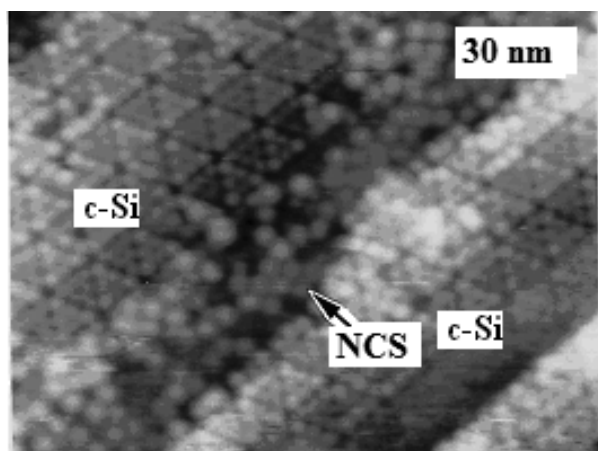


Fig. 1. Experimental results of the surface investigation Si(111)—(7x7). c-Si — crystal phase (by Prof. M. O. Watanabe using STM Omicron, UHV)

In this paper we will present the density-functional theory (DFT) in the realisation of Kohn and Sham (KS), using a few empirical parameters. This is method, which named by us parameterised DFT-PDFT is based on the Hartree—Fock scheme plus a proper treatment of the electron correlation [3, 4]. The use of only a few parameters minimises the effort for the determination of the parameters, it yields a close relation to full ab initio DFT schemes (for example, GAMESS [5]). This is guarantee of the good “transferability” of the parameters, going from one system to another. On the other hand the use of some approximations in connection with a few empirical parameters makes the scheme computationally extremely fast. PDFT allows also the study of dynamical processes through the coupling with molecular dynamics (MD) [6].

THE APPROXIMATION OF THE PDFT METHOD

The method is based on an LCAO ansatz for the KS wave functions:

$$\Psi(\vec{r}) = \sum_{\mu} C_{\mu} \zeta_{\mu}(\vec{r} - \vec{R}_j). \quad (1)$$

Here ζ_{μ} — atomic orbital, which we shall utilise as basic wave functions (BWF) [4, 5]:

$$\zeta_{\mu} = N_{\mu} r^{n^{*-1}} e^{-\alpha_{\mu} r} Y_{lm}, \quad (2)$$

where N_{μ} is constant; α_{μ} is the Slater's parameter which defined on algorithm; Y_{lm} are spherical harmonic functions, n^{*} is an effective quantum number. The LCAO ansatz leads to the secular problem. The matrix elements of the Hamiltonian $H_{\mu\nu}$ and the overlap matrix elements $S_{\mu\nu}$ are defined as

$$H_{\mu\nu} \equiv \langle \zeta_{\mu} | \hat{H} | \zeta_{\nu} \rangle, S_{\mu\nu} \equiv \langle \zeta_{\mu} | \zeta_{\nu} \rangle. \quad (3)$$

In an offered method PDFT, the Hamiltonian of the system is:

$$\hat{H} = \hat{T} + V_{\text{eff}}(\vec{r}), \quad (4)$$

where \hat{T} is the operator of a kinetic energy, $V_{\text{eff}}(\vec{r})$ is an effective KS potential. It is approximated as a simple superposition of the potentials of the neutral atoms V_j^0 :

$$V_{\text{eff}}(\vec{r}) = \sum_j V_j^0(\vec{r}_j), \quad (5)$$

where $r_j \equiv |\vec{r} - \vec{R}_j|$. Such approximation for the potential is consistent with the following approximations in the matrix elements of the Hamiltonian,

$$H_{\mu\nu} = \begin{cases} \langle \zeta_\mu | \hat{T} + V_j + V_k | \zeta_\nu \rangle, & \mu \cap \nu \in \{j, k\}, \\ 0 & \end{cases} \quad (6)$$

Thus, only two-centre terms in the Hamiltonian matrix are considered, but all two-centre terms $H_{\mu\nu}$, $S_{\mu\nu}$ are calculated exactly.

The approximations formulated above lead to the same structure of the secular equations as in (non-orthogonal) tight-binding (TB) or Iterative Extended Huckel (IEHT) [7] schemes, but it has the important advantage that all matrix elements are calculated, and non of them is handled as an empirical parameter. Quite recently [1], it has been shown that the quality of the results, especially concerning binding energies, can be improved distinctly by using basis functions and potentials from slightly “compressed atoms” rather than from free atoms. This “compression” is achieved by the introduction of an artificial additional repulsive potential of the form $(r/r_0)^k$ in the atomic calculations. The main effect of this term is a damping of the long-range part of the basis functions. Practically, it optimizes the basis functions concerning the approximations, mainly the neglect of 3-centre terms.

The total energy $E[\rho(\vec{r})]$ may be written in a form using the KS eigenvalues ϵ_i

$$E[\rho(\vec{r})] = \sum_i^{\text{occ}} \epsilon_i - \frac{1}{2} \left[\int d^3r V_{\text{eff}} \rho - \int d^3r V_{\text{ext}} \rho \right] + E_{\text{xc}} - \frac{1}{2} \int d^3r V_{\text{xc}} \rho + E_N, \quad (7)$$

The external potential V_{ext} is the electron-nucleus potential, E_{xc} is the exchange-correlation energy, V_{xc} is the corresponding potential, and E_N stands for the nuclear repulsion energy.

The representation of the density and the potential as a superposition of atomic-like contributions i. e.: $\rho = \sum_i \rho_i$, $V = \sum_i V_i$ allows one to write the total energy in the following form:

$$E[\rho(\vec{r})] = \sum_i^{\text{occ}} \epsilon_i - \frac{1}{2} \sum_j \sum_{j'} \int d^3r V_j \rho_{j'} -$$

$$- \frac{1}{2} \sum_j \sum_{j'} \int d^3r \frac{Z_j \rho_{j'}}{r_j} + \frac{1}{2} \sum_j \sum_{j'} \int d^3r \tilde{V}_{\text{xc}j} \rho_{j'} + \frac{1}{2} \sum_j \sum_{j' \neq j} \int d^3r \frac{Z_j Z_{j'}}{R_{jj'}}. \quad (8)$$

$R_{jj'}$ is the inter nuclear distance: $R_{jj'} = |\vec{R}_j - \vec{R}_{j'}|$, Z_j is the charge which has of the j -atom, ρ_j is electronic density, which localised on the j -atom, ϵ_i is one-electron energy.

For large inter nuclear distances the electron-nucleus energy compensates strongly the nuclear repulsion energy, and the two-centre terms with the potential vanish also: $\int d^3r V_j \rho_{j'} = 0$, $j \neq j'$, due to the screening of the potential. Assuming additionally that $\int d^3r \tilde{V}_{\text{xc}} \rho_{j'} = 0$, and writing the total energy $E[\rho(\vec{r})]$ of a single atom in a corresponding form as (8), one can evaluate the binding energy approximately by the KS eigenvalues ϵ_B and the KS energies ϵ_{n_j} of the atomic orbital n_j :

$$\epsilon_B \equiv E - \sum_j E_j \approx \sum_i^{\text{occ}} \epsilon_i - \sum_j \sum_{n_j} \epsilon_{n_j}. \quad (9)$$

The binding energy calculated in this way and the binding energy from a full SCF-LDA calculation, using algorithm GAMESS [6] ($\Delta E \equiv \epsilon_B - E_B^{\text{GAMESS}}$) for the Si clusters has a good agreement, as was illustration in [3]. The differences between these energies are increase with decreasing internuclear distance (r). However, this increase is rather smooth and the difference has practically vanished already at about 3/2 times the equilibrium distance (r_0). For a more detailed discussion of the approximate calculation of the binding energy, and even the justification for heteronuclear systems, as well as the extension to charged systems see [1].

With PDFT approximations the forces on the atoms (F_m) can be calculated easily using the LCAO coefficients ($C_{i\mu}$) and the derivatives of the Hamilton and overlap matrices ($\partial H_{\mu\nu}/\partial x_j$, $\partial S_{\mu\nu}/\partial x_j$), respectively:

$$F_m = \sum_i^{\text{occ}} \sum_\mu \sum_\nu C_{i\mu} C_{i\nu} \left[-\frac{\partial H_{\mu\nu}}{\partial x_j} + E_i \frac{\partial S_{\mu\nu}}{\partial x_j} \right] + \sum_{j \neq k} \frac{\Delta E_{jj'}}{\partial x_k}. \quad (10)$$

Having the forces, MD simulations may be performed easily (see e. g. [6]). The PDFT scheme may be viewed as a “hybrid” between pure ab initio method — based on DFT — and the use of purely empirical potentials. It has the advantage over the latter in overcoming the “transferability” problem, and it requires much less computational effort than full “ab initio” methods. And even in comparison to traditional TB schemes, which are computationally as fast as our method, the transferability is much better, since only very few parameters are used and their determination is straightforward.

SIMULATION'S RESULTS

In the following we will report the results of test calculations for some clusters and small particles of silicon. The PDFT method (with different of basis sets: STO — 3G, HF/3 — 21G) was utilised for the analysis of geometry and electronic structures of Si-CBL-ACS. The calculated geometry of the clusters are in good agreement with results from corresponding DFT (GAMESS) ab initio calculations. The nearest neighbour distances in silicon lattice are obtained correctly [2]. The energetic positions and equilibrium distances of high-pressure modifications of silicon are described rather well [9].

Nonetheless, all of these calculations find that major changes occur in the geometric structures of silicon clusters as a function of size below 50 atoms. Such changes are mirrored in the photoelectron spectra measured for Si-ACS anions containing 3—12 atoms [3]. Structural differences in our cluster size range for positively charged Si-ACS have also been inferred from mobility and chemical reactivity data [1]. Thus, we are quite surprised to find that the electronic spectra of neutral Si-ACS larger than Si_{18} show no evidence for any such structural changes. This leads us to conclude that all of these small Si-ACS share one or more common structural entities which are strong chromophores.

One possibility is that small Si-ACS share a common bonding network which persists and extends as the cluster grows in size. As described below, this network may be related to that of bulk Si. Another possibility is that all of these Si-ACS contain at least one loosely bound smaller ACS such as the abundant Si_{10} , which is responsible for the sharp spectral structure. This explanation is less appealing since the smaller Si-ACS would have to have an appreciable binding interaction in order to remain bound to the quite warm Si-ACS for a long time. This interaction would have to be similar for all of the ACS in order to produce the observed spectral similarity. However, we cannot rule this excitation spectra of these small Si-ACS are known at this time in the energy range of interest.

PDFT calculations have been recently performed to study the size dependence of the absorptions of diamond-lattice-like silicon clusters with 10—100 Å diameters [1]. These calculations predict that direct gap transitions in small Si crystallites should redshift with decreasing size and that new features should appear greatly shifted to the blue as a result of lifting of the degeneracy's of the critical points.

Given that Si-ACS containing only few tens of atoms are too small to have either band structures or bulk excitations, the similarity of their optical signature to crystalline silicon is unexpected. Moreover, these cluster spectra are far more similar to the spectrum of the most stable crystalline form of Si than to the spectra of other Si forms.

In the next step the nanodimensional particle structure was constructed. For inter CBL ACS interaction the pairwise additive approximation (PAA) was used. The calculations analyse of Si-ACS, which has spherical symmetry, were performed using periodic boundary conditions. Formally, the total energy of an ensemble of N Si-CBL-ACS can be written as:

$$E_N = \sum_{i < j}^N E_{ij}(r_{ij}, \Omega_{ij}) + \sum_{i < j < k}^N E_{ijk}(r_{ij}, r_{ik}, r_{jk}, \Omega_{ijk}) + \dots \\ + \dots \sum_{i < j < k < l}^N E_{ijkl}(r_{ij}, r_{ik}, r_{il}, r_{jk}, r_{jl}, r_{lk}, \Omega_{ijkl}) + \dots, \quad (11)$$

where the first term is the sum of all two-body (pair, E_{ij}) interactions (each a function of the separation r_{ij} and relative orientation Ω_{ij} of the two “ball”). The three-body term E_{ijk} provides the difference between the actual energy of a trio of Si-CBL-ACS in a given orientation and the sum of the three pair potential terms; similarly, E_{ijkl} is the corresponding correction to give the correct energy of a quartet of “ball”; and so on. For the system which consist of the Si-CBL-ACS the pairwise additive approximation by only using the first term in this expansion was used. NDSP consists of Si-CBL-ACS with an average diameter d (as shown in Fig. 2).

Vapour-phase clusters of Si_n^+ have been prepared and analysed for trends in relative abundance and chemical reactivity for $3 < n < 60$ or 24, respectively [10, 11]. Magic numbers (extreme) for these properties are observed which presumably reflect differences in cluster structures. Here we show how these magic numbers can be understood based on structures predicted by a thermodynamic classical force field developed by us to fit the equations of state of bulk phases and energies and average co-ordination numbers of small Si-ACS. As we anticipated, our classical method becomes quite accurate for

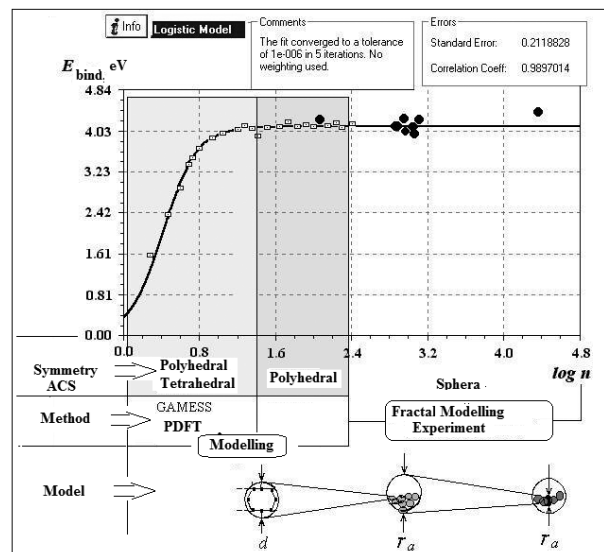


Fig. 2. Algorithm of the nanodimensional cluster subsystem's modelling

$n > 10$. PDFT quantum-mechanical calculations have successfully predicted the structures and properties of Si_n^+ clusters for $n < 10$.

Covalent-metallic phase transitions are the key to the functional form used to construct our force field. The primary reason for the stability of our theory, as compared to the kaleidoscopic variations in analytic detail and parametric values which have characterised almost all other work, is that our treatment of bond-bending forces is physically consistent. We use a novel angular cut-off, which means that bond-bending forces are strong only for smaller bond angles, in parallel with the usual radial cut-off, which makes radial forces strong only for nearer neighbours. Moreover, our bond-bending angular function is $\cos 3\theta$, not $\cos \theta$, because the former provides the rapid angular variation needed to describe the "phase transition" between metallic ($\theta = 60^\circ$) and covalent ($\theta = 110^\circ$) bonding.

Other forms of more compact silicon such as the beta-tin and primitive hexagonal metallic phases, and the BC-8 and ST-12 metastable phases are also candidates for comparison in light of the theoretical calculations which predict high co-ordination numbers in small silicon clusters. None of these alternative structures have optical properties which are as closely related to our cluster spectra as diamond c-Si [11].

In author's monography [3] we show our results for the bulk phases of Si. In our previous work [1, 2, 7] we fitted our parameters for the bulk energy to the equations of state for the covalent diamond and metallic simple, body-centred and face-centred cubic phases. In this figure we show, in addition, the results for the metallic hexagonal close-packed and semi-metallic $\beta = Sn$ phases with both our functions both our parameters unchanged. The sign and magnitude of the very small fcc-hcp difference agrees very well with the calculation of the article [12]. This confirms the accuracy of our cut-off functions. Of greater importance to our central theme, the metal-semiconductor transition, is the excellence of the unadjusted fit to the equation of state for $\beta = Sn$.

We now turn to the structure of Si_n ACS for $10 \leq n \leq 25$. These were determined by a combination of Monte Carlo and molecular-dynamics techniques. The latter has been partially optimised and is now essentially as effective as such simulations using much simpler potentials, so that our practical upper limit for n is much larger than 25. However, the structures of the clusters with $3 \leq n \leq 23$ already show striking properties that have immediate application to chemical reactivities.

First, we show in [3] the smaller bond-angle distribution for all ACS in the range $3 \leq n \leq 20$. While previous potentials based on $\cos \theta$ were always designed to favour tetrahedral angles θ_t , [usually trivially through a term in the energy proportional to $(\cos \theta - \cos \theta_t)^2$], there is no such bias in our functions. Instead what we received that the smaller bond angles are all

concentrating near $\theta = \pi/3$ (close packing) or near θ_t (tetrahedral packing). This is what one would have expected from a bond-bending energy dependent on $\cos 3\theta$, but the virtual absence of bond angles near $\theta = \pi/2$ reflects, in addition, certain geometrical constraints, which one might not have anticipated. These packing constraints in effect amplify the significance of the covalent-metallic distinction.

For $n > 10$, the ACS geometries turn out to be very different from what one might have expected, based on the bulk phase diagram. At $n = 13$ the structure is that of an atom-centred icosahedron. Several clusters from this sequence are shown in Fig. 2.

The icosahedral-pentagonal growth sequence is well known for two-body central forces appropriate to inert gases, and indeed magic numbers $n = 13, 19, 23, 25, \dots, 55$ etc. have been observed for Xe and other inert gas clusters. Our calculations show that back-bonding forces in small Si-ACS can cause a remarkable reappearance of these simple geometrical structures.

Our results indicate that in the range $n = 10$ –20 the Si_n ACS oscillate between metallic pentagonal growth structures and covalent molecular structures. In effect, in this range Si_n clusters are vicinal to a covalent-metallic "phase transition".

It may well be that in the addition reaction the covalent molecule C_2H_4 remains intact and reacts strongly only with covalent Si_n structures ($n = 10$ and 16) and much more weakly with metallic structures ($n = 13$ and 19). This appears to be a case of "like prefers like," which often occurs in covalent network structures. This preference originates from the persistence of the covalent energy gap, accompanied by phase-matched occupied valence orbital, from the rings of Si_n into interlocking rings including C_2H_4 segments. In earlier days this phenomenon was sometimes described as resonant valence bonds, in which case large capture cross sections near $n = 16$ could also be described as resonant addition.

SUMMARY

We have presented a simplified PDFT scheme. Due to the neglect of all three-centre integrals and the use of a short-range repulsive interaction potential in the energy calculations the method is computationally extremely fast. It gives reliable results for geometry's, binding energies and vibration frequencies for different ACS. The bond lengths and angles are obtained with an error less than 5 %.

REFERENCES

1. Kovalchuk V. V. Cluster morphology of silicon nanoparticles // *Sem. Phys., Quant. Electr. & Optoelectr.* — 2007. — V. 10, № 4. — P. 81–86.
2. Drozdov V. A., Kovalchuk V. V. Electronic processes in nanostructures with silicon subphase // *J. of Phys. Studies.* — 2003. — Vol. 4, № 7. — P. 393–401.

3. Kovalchuk V. V. Cluster modification semiconductor's heterostructures. — Kiev: Hi-Tech, 2007. — 309 p.

4. Blaudeck P., Freuenheim Th., Porezag D., Seifert G., Fromm E. Calculation of Molecules, Clusters and Solids with DFT-LDA Scheme // J. Phys. Condensed Matter. — 2000. — V. 4. — P. 6368—6371.

5. Schmidt M. W., Baldrige K. K., Boatz J. A., Gordon M. S., Jensen J. H., Koseki S., Matsunaga N., Su S., Windus T. L., Dupus M., Montgomery J. General Atomic and Molecular Electronic Structure System // J. Comp. Chem. — 1999. — V. 14. — P. 1347—1363.

6. Laasonen K., Nieminen R. M. Molecular dynamics the tight-binding approximation // J. Phys.: Condens. Matter. — 1999. — V. 2. — P. 1509—1520.

7. Kovalchuk V. V., Chislov V. V., Yanchuk V. A. Cluster Model of the Real Silicon Surface // Phys. Stat. Sol. (b). — 1999. — V. 187. — P. K47—K50.

8. Watanabe M. O., Murakami H., Miyazaki T., Kanayama T. Three types of stable structures of hydrogenated silicon clusters // Appl. Phys. Lett. — 1999. — V. 71. — P. 1207—1209.

9. Jarrold M. F. Nanosurface Chemistry on Size-Selected Silicon Clusters // Science. — 2000. — V. 252. — P. 1085—1092.

10. Vansant E. F., Van der Voort P., Vrancken K. C. Characterisation and chemical modification of silica surface. Amsterdam: Elsevier, 1999. — 334 p.

11. Garcia-Ruiz J. M., Louis E., Meakin P., Sander L. M. Growth Patterns in Physical Sciences and Biology. NATO ASI Series B: Physics, V. 304, N. Y.: Plenum Publ. — 1999. — 456 p.

12. Honea E. C., Ogura A., Murray C. A., Raghavachari K., Sprenger W., Jarrold M., Brown W. L. Raman spectra of size-selected silicon clusters and comparison with calculated structures // Nature. — 2000. — V. 366. — P. 42—44.

UDC 40+82.20

V. V. Kovalchuk

THE OPTICAL PROPERTIES, STABILITY AND REACTIVITY OF SOLID NANOCLUSTER SUBSYSTEM

Abstract

In this paper we will present the parametrized density-functional theory (PDFT) in the realisation of Kohn and Sham, using a few empirical parameters. The accuracy of the method is illustrated by the results of calculations for nanocluster silicon subsystems (Si-NCS). The extreme simplicity of the method allows one to calculate the geometry and the electronic structure of nanoclusters. The PDFT method with the combination of the molecular dynamics the simulated process makes very useful tool for the determination of the optical properties, stability, reactivity and covalent-metallic bonding of Si-NCS.

Key words: optical properties, stability, empirical parameters.

УДК 40+82.20

В. В. Ковальчук

ОПТИЧЕСКИЕ СВОЙСТВА, СТАБИЛЬНОСТЬ И РЕАКТИВНОСТЬ ТВЕРДОТЕЛЬНОЙ НАНОКЛАСТЕРНОЙ ПОДСИСТЕМЫ

Резюме

В этой статье представлен параметризованный метод функционала электронной плотности (ПФЭП) в приближении Кона-Шема, с применением нескольких эмпирических параметров. Точность метода иллюстрируется результатами расчетов нанокластерной подсистемы кремния (Si-НКП). Простота метода позволяет эффективно рассчитать геометрическую и электронную структуру нанокластеров. В рамках молекулярной динамики моделирование процесса делает метод ПФЭП полезным инструментом для определения оптических свойств, стабильности и реактивности Si-НКП.

Ключевые слова: оптические свойства, стабильность, эмпирические параметры.

A. V. GLUSHKOV², A. P. FEDCHUK¹, P. A. KONDRATENKO³, Ya. I. LEPIKH¹,
Yu. M. LOPATKIN⁴, A. A. SVINARENKO²

¹ I. I. Mechnikov Odessa National University, Odessa

² Odessa State Environmental University, e-mail: glushkov@paco.net

³ Kiev National Aviation University, Kiev

⁴ Sumy State University, Sumy

THE GREEN'S FUNCTIONS AND DENSITY FUNCTIONAL APPROACH TO VIBRATIONAL STRUCTURE IN THE PHOTOELECTRONIC SPECTRA: MOLECULES OF CH, HF

The combined theoretical approach to vibrational structure in photo-electronic spectra (PES) of molecules is used for quantitative treating of PES of the CH, HF molecules. The method is based on the density functional theory (DFT) and the Green's-functions (GF) approach.

Many papers have been devoted to the treatment of the vibrational spectra by construction of potential curves for the reference molecule (the molecule due to be ionized) and the molecular ion (c. f. [1—19]). The most sophisticated method is provided by the GF approach. Usually, the electronic GF is defined for the fixed position of the nuclei. The cited method, however, requires as input data, the geometries, frequencies, and potential functions of the initial and final states.

Since at least a part of these data are unavailable, the calculations have been carried out with the objective of determining the missing data through comparison with experiment. To avoid this difficulty and to gain the additional information about the ionization process, L. S. Cederbaum et al [11] have extended the GF approach to include the vibration effects and shown that the GF method allows *ab initio* calculation of the intensity distribution of the vibrational lines etc. For large molecules far more approximate but more easily applied methods such as DFT [16, 17] or from the wave-function world the simplest correlated model MBPT are preferred [2, 8, 10].

Earlier, has been developed the combined GF-DFT approach [12—15] to the vibration structure in PES of the molecules, which has been successfully applied to quantitative treatment of the CO and N₂ molecules. Here we have applied this method to the determination of the key parameters of the CH, HF molecules PES. It is important to note that the calculation procedure of the GF-DFT method is significantly simplified. As the key aspects of the GF-DFT method has been in details earlier considered, we are only limited to presentation of the main formulae.

The quantity which contains the information about the ionization potentials (IP) and molecular vibration structure due to quick ionization is the density of occupied states [2, 8]:

$$N_k(\Gamma) = (1/2\pi\hbar) \int dt e^{i\hbar^{-1}\Gamma t} \langle \Psi_0 | a_k^\dagger(0) a_k(t) | \Psi_0 \rangle, \quad (1)$$

where $|\Psi_0\rangle$ is the exact ground state wave

function of the reference molecule and $a_k(t)$ is an electronic destruction operator, both included into the Heisenberg picture. For particle attachment, the quantity of interest is the density of unoccupied states:

$$N_k(\Gamma) = (1/2\pi\hbar) \int dt e^{i\hbar^{-1}\Gamma t} \langle \Psi_0 | a_k(t) a_k^\dagger(0) | \Psi_0 \rangle, \quad (2)$$

Usually, in order to calculate the value (1) states for photon absorption one should express the Hamiltonian of the molecule in the second quantization formalism. The Hamiltonian is as follows:

$$H = T_E(\partial/\partial x) + T_N(\partial/\partial X) + U_{EE}(x) + U_{NN}(X) + U_{EN}(x, X), \quad (3)$$

where T_E and T_N are the kinetic energy operators for electrons and nuclei, and U represents the interaction; U_{EE} represents the Coulomb interaction between electrons, etc; x (X) denotes electronic or nuclear coordinates. As usually, introducing a field operator $\Psi(R, \theta, x) = \sum_i \phi_i(x, R, \theta) a_i(R, \theta)$ assuming that

Hartree—Fock (HF) one—particle functions ϕ_i ($\epsilon_i(R)$ are the one-particle HF energies and i denotes the set of orbitals occupied on the HF ground state; R_0 is the equilibrium geometry on the HF level) and dimensionless normal coordinates Q_s one could write the standard Hamiltonian as follows [10, 11]:

$$\begin{aligned} H &= H_E + H_N + H_{EN}^{(1)} + H_{EN}^{(2)}, \quad (4) \\ H_E &= \sum_i T_i(R_0) a_i^\dagger a_i + \frac{1}{2} \sum_{ijkl} V_{ijkl}(R_0) a_i^\dagger a_j^\dagger a_l a_k - \\ &\quad - \sum_{i,j} \sum_{k \in f} [V_{ikjk}(R_0) - V_{ikkj}(R_0)] a_i^\dagger a_j, \\ H_N &= \hbar \sum_{s=1}^M \omega_s \left(b_s^\dagger b_s + \frac{1}{2} \right), \\ H_{EN}^{(1)} &= 2^{-1/2} \sum_{s=1}^M \left(\frac{\partial T_i}{\partial Q_s} \right)_0 (b_s + b_s^\dagger) [a_i^\dagger a_i - n_i] + \\ &\quad + \frac{1}{4} \sum_i \sum_{s,s'=1}^M \left(\frac{\partial^2 T_i}{\partial Q_s \partial Q_{s'}} \right)_0 (b_s + b_s^\dagger) (b_{s'} + b_{s'}^\dagger) [a_i^\dagger a_i - n_i], \end{aligned}$$

$$H_{EN}^{(2)} = 2^{-3/2} \sum_{s=1}^M \sum_{s'=1}^M \left(\frac{\partial V_{ijkl}}{\partial Q_s} \right)_0 (b_s + b_s^t) [\delta v_1 a_i^t a_j^t a_k + \delta v_2 a_i a_k a_i^t a_j^t + 2\delta v_3 a_i^t a_k a_i a_j^t] + \frac{1}{8} \sum_{s,s'=1}^M \left(\frac{\partial^2 V_{ijkl}}{\partial Q_s \partial Q_{s'}} \right)_0 (b_s + b_s^t)(b_{s'} + b_{s'}^t) [\delta v_1 a_i^t a_j^t a_k + \delta v_2 a_i a_k a_i^t a_j^t + 2\delta v_3 a_i^t a_k a_i a_j^t],$$

with $n_i = 1$ (0), $i \in f$ ($i \notin f$), $\delta\sigma_i = 1$ (0), $(ijkl) \in \sigma_f$, where the index set v_1 means that at least ϕ_k and ϕ_l or ϕ_i and ϕ_j are unoccupied, v_2 that at most one of the orbitals is unoccupied, and v_3 that ϕ_k and ϕ_i or ϕ_l and ϕ_j are unoccupied. Here for simplicity all terms leading to non-harmonicities, are being neglected. The ω_s are the HF frequencies; b_s , b_s^t are destruction and creation operators for vibration-
al quanta as

$$Q_s = (1/\sqrt{2})(b_s + b_s^t), \quad \partial/\partial Q_s = (1/\sqrt{2})(b_s - b_s^t). \quad (5)$$

The interpretation of the above Hamiltonian and the exact solution of the one-body HF problem are given in refs. [5, 6]. The HF-single-particle component H_0 of the Hamiltonian (4) is as follows:

$$H_0 = \sum_i T_i(R_0) a_i^t a_i + \sum_{s=1}^M \hbar \omega_s \left(b_s^t b_s + \frac{1}{2} \right) + \sum_{s=1}^M \sum_i 2^{-1/2} \left(\frac{\partial T_i}{\partial Q_s} \right) [a_i^t a_i - n_i] (b_s + b_s^t)_0 + \sum_{s,s'=1}^M \sum_i \frac{1}{4} \left(\frac{\partial^2 T_i}{\partial Q_s \partial Q_{s'}} \right) [a_i^t a_i - n_i] (b_s + b_s^t)(b_{s'} + b_{s'}^t). \quad (6)$$

Correspondingly, in the frame of one-particle picture, the density of occupied states is given by

$$N_k^0(\epsilon) = \frac{1}{2\pi\hbar} \int_{-\infty}^{\infty} dt e^{i\hbar^{-1}(\epsilon - \epsilon_k)t} \langle 0 | e^{\pm i\hbar^{-1}\tilde{H}_0 t} | 0 \rangle, \quad (7)$$

$$\tilde{H}_0 = \sum_{s=1}^M \hbar \omega_s b_s^t b_s + \sum_{s=1}^M g_s^k (b_s + b_s^t) + \sum_{s,s'=1}^M \gamma_{ss'}^k (b_s + b_s^t)(b_{s'} + b_{s'}^t), \quad (8)$$

$$g_s^i = \pm \frac{1}{\sqrt{2}} \left(\frac{\partial T_i}{\partial Q_s} \right)_0, \quad \gamma_{ss'}^i = \pm \frac{1}{4} \left(\frac{\partial^2 T_i}{\partial Q_s \partial Q_{s'}} \right)_0. \quad (9)$$

Introducing new operators

$$c_s = \sum_{l=1}^M (\lambda_1^{sl} b_l + \lambda_2^{sl} b_l^t). \quad (10)$$

with real coefficients λ_1^{sl} , λ_2^{sl} , defined in such a way that \tilde{H}_0 in new operators is

$$\tilde{H}_0 = \sum_{s=1}^M \hbar \hat{\omega}_s c_s^t c_s + \sum_{s=1}^M \hat{g}_s (c_s + c_s^t) + k. \quad (11)$$

Eq. (7) is as follows:

$$N_k^0(\epsilon) = \sum_{n_1 \dots n_M} |\langle \hat{n} | U | 0 \rangle|^2 \delta(\epsilon - \epsilon_k \pm \Delta\epsilon_k \pm n \cdot \hbar \hat{\omega}), \quad (12)$$

where δ function in (12) naturally contains the information about adiabatic ionization potential and the spacing of the vibration peaks; while $|\langle \hat{n} | U | 0 \rangle|^2$ is the well-known Franck—Condon factor.

In a diagrammatic method to get function $N_k(\epsilon)$ one should calculate the GF $G_{kk'}(\epsilon)$ first [3, 10, 11]:

$$G_{kk'}(T) = -i\hbar^{-1} \int_{-\infty}^{\infty} dt e^{i\hbar^{-1}Tt} \langle \psi_0 | \{ a_k(t) a_k^t(0) \} | \psi_0 \rangle \quad (13)$$

and the function $N_k(\epsilon)$ could be found from the relation

$$\pi N_k(\epsilon) = a \text{Im} G_{kk}(\epsilon - a i \eta), \quad a = -\text{sign} \epsilon_k. \quad (14)$$

Choosing the unperturbed Hamiltonian H_0 to be $H_0 = \sum \epsilon_i a_i^t a_i + H_N$ one finds the GF. In the known approximation GF is as follows:

$$G_{kk'}^{\text{OB}}(t) = \pm \delta_{kk'} i \exp[-in^{-1}(\epsilon_k \mp \Delta\epsilon)t] \times \sum_n |\langle \hat{n}_k | U_k | 0 \rangle|^2 \exp(\pm i n_k \cdot \hat{\omega}_k t). \quad (15)$$

The corresponding Dyson-like equation ($\Sigma = O$) looks as follows:

$$G_{kk'}(\epsilon) = G_{kk'}^{\text{OB}}(\epsilon) + \sum_{kk'} G_{kk'}^{\text{OB}}(\epsilon) \Phi_{kk'} G_{kk'}(\epsilon), \quad (16)$$

$$\Phi_{kk'}(\epsilon) = \sum_{\substack{i,j \in F \\ l \notin F}} \sum_{n_i, n_j, n_l} \frac{(V_{klij} - V_{k'lij}) V_{k'lij} U_{n_i} U_{n_j} U_{n_l}}{\epsilon + E_i - E_j - E_l} + \sum_{\substack{i,j \in F \\ l \notin F}} \sum_{n_i, n_j, n_l} \frac{(V_{klij} - V_{k'lij}) V_{k'lij} U_{n_i} U_{n_j} U_{n_l}}{\epsilon + E_i - E_j - E_l},$$

where $U_{n_i} = |\langle \hat{n}_i | U_i | 0 \rangle|^2$ and

$$E_i = \epsilon_i \mp \Delta\epsilon_i \mp \hat{n}_i \cdot \hat{\omega}_i. \quad (17)$$

The direct method for calculation of $N_k(\epsilon)$ as the imaginary part of the GF includes a definition of the vertical IP (VIP) of the reference molecule and then of $N_k(\epsilon)$. The zeros of the functions

$$D_k(\epsilon) = \epsilon - [\epsilon^{\text{OP}} + \Sigma(\epsilon)]_k, \quad (18)$$

where $(\epsilon^{\text{OP}} + \Sigma)_k$ denotes the k -th eigen-value of the diagonal matrix of the one-particle energies added to matrix of the self-energy part, are the negative VIP for a given geometry. One could write according to [10, 11]:

$$(V.I.P.)_k = -(\epsilon_k + F_k), \quad F_k = \Sigma_{kk}(- (V.I.P.)_k) \approx \frac{1}{1 - \partial \Sigma_{kk}(\epsilon_k) / \partial \epsilon} \Sigma_{kk}(\epsilon_k). \quad (19)$$

Expanding the ionic energy E_k^{N-1} about the equilibrium geometry of the reference molecule in a power series of the normal coordinates of this molecule leads to a set of linear equations in the unknown normal coordinate shifts δQ_s , and new coupling constants are then:

$$g_l = \pm(1/\sqrt{2})[\partial(\epsilon_k + F_k)/\partial Q_l]_0, \\ \gamma_{ll'} = \pm\left(\frac{1}{4}\right)[\partial^2(\epsilon_k + F_k)/\partial Q_l \partial Q_{l'}]_0. \quad (20)$$

The coupling constants g_l and $\gamma_{ll'}$ are calculated by the well-known perturbation expansion of the self-energy part using the Hamiltonian H_{EN} of Eq. (3). In second order one obtains:

$$\sum_{kk}^{(2)}(\epsilon) = \sum_{\substack{i,j \\ s \notin F}} \frac{(V_{ksij} - V_{ksji})V_{ksij}}{\epsilon + \epsilon_s - \epsilon_i - \epsilon_j} + \sum_{\substack{i,j \\ s \notin F}} \frac{(V_{ksij} - V_{ksji})V_{ksji}}{\epsilon + \epsilon_s - \epsilon_i - \epsilon_j} \quad (21)$$

and the coupling constant g_l , could be written as

$$g_l \approx \pm \frac{1}{\sqrt{2}} \frac{\partial \epsilon_k}{\partial Q_l} \frac{1 + q_k(\partial/\partial \epsilon) \sum_{kk} [-(V.I.P.)_k]}{1 - (\partial/\partial \epsilon) \sum_{kk} [-(V.I.P.)_k]}, \quad (22)$$

$$q_k = \frac{\sum \frac{(V_{ksij} - V_{ksji})^2}{[-(V.I.P.)_k + \epsilon_s - \epsilon_i - \epsilon_j]^2} \left[\frac{\partial \epsilon_s}{\partial Q_l} - \frac{\partial \epsilon_i}{\partial Q_l} - \frac{\partial \epsilon_j}{\partial Q_l} \right]}{\frac{\partial \epsilon_k}{\partial Q_l} \sum \frac{(V_{ksij} - V_{ksji})^2}{[-(V.I.P.)_k + \epsilon_s - \epsilon_i - \epsilon_j]^2}}. \quad (23)$$

It is suitable to use the pole strength of the corresponding GF in the form of [12]:

$$\rho_k = \left\{ 1 - \frac{\partial}{\partial \epsilon} \sum_{kk} [-(V.I.P.)_k] \right\}^{-1}; \quad 1 \geq \rho_k \geq 0, \quad (24)$$

$$g_l \approx g_l^0 [\rho_k + q_k(\rho_k - 1)], \\ g_l^0 = \pm 2^{-1/2} \partial \epsilon_k / \partial Q_l. \quad (25)$$

Below we give the DFT definition of the pole strength corresponding to VIP and confirm the earlier data [10, 11]: as $p_k \approx 0.8-0.95$. The coupling constant is:

$$\gamma_{ll} = \gamma_{ll}^0 \left(\frac{g_l}{g_l^0} \right) + \frac{1}{4} \sqrt{2} g_l^0 \frac{\partial}{\partial Q_l} \left(\frac{g_l}{g_l^0} \right). \quad (26)$$

Further, we consider the quasi-particle Fermi-liquid version of the DFT, following to Refs. [12, 13, 19]. The master equation could be derived using an expansion for self-energy part Σ into set on degrees of x , $\epsilon - \epsilon_F$, $p^2 - p_F^2$ (here ϵ_F and p_F are the Fermi energy and pulse correspondingly):

$$[p^2/2 - \sum_{\alpha} Z_{\alpha}/r_{\alpha} + \sum_0(x) + p(\partial \Sigma / \partial p^2)p] \Phi_{\lambda}(x) = \\ = (1 - \partial \Sigma / \partial \epsilon) \epsilon_{\lambda} \Phi_{\lambda}(x). \quad (27)$$

The functions Φ_{λ} in (27) are orthogonal with a weight $\rho_k^{-1} = a^{-1} = [1 - \partial \Sigma / \partial \epsilon]$. Now one can introduce the wave functions of the quasi-particles

$\phi_{\lambda} = a^{-1/2} \Phi_{\lambda}$, which are, as usually, orthogonal with weight 1. The equations (27) could be obtained on the basis of variational principle, if we start from a Lagrangian of a system L_q (DF). It should be defined as a functional of quasi-particle densities:

$$\mathbf{v}_0(r) = \sum_{\lambda} n_{\lambda} |\Phi_{\lambda}(r)|^2, \\ \mathbf{v}_1(r) = \sum_{\lambda} n_{\lambda} |\nabla \Phi_{\lambda}(r)|^2, \\ \mathbf{v}_2(r) = \sum_{\lambda} n_{\lambda} [\Phi_{\lambda}^* \Phi_{\lambda} - \Phi_{\lambda}^* \Phi_{\lambda}].$$

The densities \mathbf{v}_0 and \mathbf{v}_1 are similar to the HF electron density and kinetic energy density correspondingly; the density \mathbf{v}_2 has no analogs in the HF or DFT theory and appear as a result of the account for the energy dependence of the mass operator Σ . A Lagrangian L_q could be written as a sum of a free Lagrangian and Lagrangian of interaction: $L_q = L_q^0 + L_q^{\text{int}}$, where a free Lagrangian L_q^0 has a standard form:

$$L_q^0 = \int dr \sum_{\lambda} n_{\lambda} \Phi_{\lambda}^* (i\partial/\partial t - \epsilon_p) \Phi_{\lambda}, \quad (28)$$

The interaction Lagrangian is defined in the form, which is characteristic for a standard (Kohn—Sham [16]) DFT (as a sum of the Coulomb and exchange-correlation terms), however, it takes into account for the energy dependence of a mass operator Σ :

$$L_q^{\text{int}} = L_K - \frac{1}{2} \sum_{i,k=0}^2 \int \beta_{ik} F(r_1, r_2) \mathbf{v}_i(r_1) \mathbf{v}_k(r_2) dr_1 dr_2, \quad (29)$$

where β_{ik} are some constants (please, look below), F is an effective potential of the exchange-correlation interaction. The Coulomb interaction part L_K looks as follows [19]:

$$L_K = -\frac{1}{2} \int [1 - \sum_2(r_1)] \mathbf{v}_0(r_1) [1 - \sum_2(r_2)] \times \\ \times \mathbf{v}_0(r_2) / |r_1 - r_2| dr_1 dr_2, \quad (30)$$

where $\Sigma_2 = \partial \Sigma / \partial \epsilon$. In the local density approximation, the potential F could be expressed through the exchange-correlation pseudo-potential V_{xc} as follows [20]:

$$F(r_1, r_2) = \delta V_{xc} / \delta \mathbf{v}_0 \cdot \delta(r_1 - r_2).$$

Further, one can get the following expressions for $\Sigma_i = -\delta L_q^{\text{int}} / \delta \mathbf{v}_i$, for example:

$$\Sigma_0 = (1 - \Sigma_2) V_K + \Sigma_0^{\text{ex}} + \frac{1}{2} \beta_{00} \delta^2 V_{xc} / \delta \mathbf{v}^2 \mathbf{v}_0^2 + \\ + \beta_{00} \delta V_{xc} / \delta \mathbf{v}_0 \mathbf{v}_0 + \beta_{01} \delta V_{xc} / \delta \mathbf{v}_0 \mathbf{v}_1 + \\ + \beta_{01} \delta^2 V_{xc} / \delta \mathbf{v}_0^2 \cdot \mathbf{v}_0 \mathbf{v}_1 + \beta_{02} \delta^2 V_{xc} / \delta \mathbf{v}_0^2 \cdot \mathbf{v}_0 \mathbf{v}_2 + \\ + \beta_{02} \delta V_{xc} / \delta \mathbf{v}_0 \cdot \mathbf{v}_2. \quad (31)$$

$$\Sigma_2 = \beta_{02} \delta V_{xc} / \delta \mathbf{v}_0 \cdot \mathbf{v}_0 + \beta_{12} \delta V_{xc} / \delta \mathbf{v}_0 \cdot \mathbf{v}_1 + \\ + \beta_{22} \delta V_{xc} / \delta \mathbf{v}_0 \cdot \mathbf{v}_2. \quad (32)$$

Here V_K is the Coulomb term, Σ_0^{ex} is the exchange term. Using the known canonical relationship, one can derive the quasi-particle Hamiltonian [10, 14], corresponding to L_q .

In refs. [12, 13, 15] it has been given the comment regarding the constants β_{ik} . Indeed, in some degree they have the same essence as the similar constants in the well-known Landau Fermi-liquid theory and the Migdal finite Fermi-system theory. The value of β_{00} depends on the definition of V_{xc} . If for V_{xc} one of the DFT exchange-correlation potentials form is used, then, without losing a generality of the statement, $\beta_{00} = 1$. The constant β_{02} can be in principle calculated by the analytical way, but it is very useful to remember its connection with a spectroscopic factor F_{sp} of the system [19]:

$$F_{sp} = \left\{ 1 - \frac{\partial}{\partial \epsilon} \Sigma_{kk} [-(V.I.P.)_k] \right\}. \quad (33)$$

One could see that this definition is corresponding to the pole strength of the corresponding Green's function [2, 11]. As potential V_{xc} , we use the Gunnarsson—Lundqvist exchange-correlation functional [17]:

$$V_{xc}(r) = -(1/\pi)[3\pi^2 \cdot \rho(r)]^{1/3} - 0,0333 \times \ln[1 + 18,376 \cdot \rho^{1/3}(r)]. \quad (34)$$

Using the above written formula, one can simply define the values (24), (33).

In refs. [15, 20], the above presented combined approach has been applied to analysis of the photoelectron spectrum for the sufficiently complicated from the theoretical point of view N_2 and CO molecules, where the known Koopmans' theorem even fails in reproducing the sequence of the V.I.P.'s in the PE spectrum (c. f. [5—7]). It is stressing, however that it has been possible to get the full sufficiently correct description of the diatomics PES already in the effective one-quasiparticle approximation [11, 13]. Another essential aspect is the sufficiently simple calculating procedure, provided by using the DFT. Moreover, the cumbersome calculation is not necessary here, if the detailed Hartree—Fock (Hartree—Fock—Roothaan) data (separate HF-potential curves of molecule and ion) for the studied diatomic molecule are available.

Further, it is easily to estimate the pole strengths p_k and the values q_k . When the change of frequency due to ionization is small, the density of states could be well approximated using only one parameter g :

$$N_k(\epsilon) = \sum_{n=0}^{\infty} e^{-s} \frac{S^n}{n!} \delta(\epsilon - \epsilon_k + \Delta\epsilon_k + n \cdot \hbar\omega),$$

$$S = g^2(\hbar\omega)^{-2}. \quad (35)$$

In case the frequencies change considerably, the intensity distribution of the most intensive lines can analogously be well approximated by

an effective parameter S . In table 1 the experimental (S^{exp}) and theoretical (S^{th}) values of the S parameter are presented for the molecules of CH and HF: S^0 is the value without accounting correlation and reorganization corrections; $S^{(b)}$ — the values of the parameter with accounting of the correlation and reorganization, in total synergistic, corrections within our combined GF—DFT method.

Table 1

The experimental (S^{exp}) and theoretical (S^{theor}) values of the S parameter presented for different molecules (CH, HF): S^0 is the value without accounting correlation and reorganization corrections; $S^{(b)}$ — the combined GF-DFT method (b).

Molecule	Theory	S^{theor}		S^{exp}	
		1	2	1	2
CH	S^0	0.22(1 π)	0.105(3 σ)	—	—
	$S^{(b)}$	0.2711	0.1134		
HF	S^0	0.126(1 π)	1.90(3 σ)	0.35	2.13
	$S^{(b)}$	0.1920	2.0534		

One could guess that there a physically reasonable agreement between the theoretical and experimental results for all bands. This example also confirms that quite effective theory become an effective tool in interpreting the vibrational structure of the molecular PES, especially taking into account an essential simplification (implementation of the DFT scheme) of the standard GF approach.

In conclusion let us indicate on the prospects of the presented method application to the problems of the cooperative laser-electron-vibrational gamma-nuclear effects in the di-atomics and multi-atomic molecules [21].

REFERENCES

1. Thouless D J, Quantum Mechanics of Many-Body Systems // Academic Press, N.-Y., 2001.
2. Wilson W., Handbook on Molecular Physics and Quantum Chemistry // Chichester: Wiley, 2003. — 680 pp.
3. Lindgren I., Morrison M., Atomic Many-Body Theory // Berlin: Springer, 1999. — 370 pp.
4. Abrikosov A., Gorkov L., Dzyaloshinskii E., Quantum Field Theoretical Methods in Statistical Physics // Oxford: Pergamon, 1965. — 400 pp.
5. Turner D. W., Baker C., Baker A. D., Brunelle C. R., Molecular Photoelectronic Spectroscopy. — N.-Y.: Wiley, 2002.
6. Herzberg G., Molecular Spectra and Molecular Structure // Moscow: Mir Publishers, 1999. — Vol. 1.
7. Cade D. E., Wahl A. L., Hartree—Fock—Roothaan Wave Functions for Diatomic Molecules // Atomic Data and Nucl. Data Tabl. — 1974. — vol. 13, N 4. — p. 2339—2389.
8. Bartlett R. J., Musiał M. N., Coupled-cluster theory in quantum chemistry // Rev. Mod. Phys. — 2007. — Vol. 79. — P. 291—328.
9. Dorofeev D., Zon B. A., Kretinin I., Chernov V. E., Method of Quantum Defect Green's Function for Calculation of Dynamic Atomic Polarizabilities // Optics and Spectroscopy. — 2005. — vol. 99. — p. 540—548.
10. Glushkov A. V., Relativistic and Correlation Effects in Spectra of Atomic Systems. — Odessa: Astropoint, 2006. — 450 pp.

11. Köppel H., Domcke W., Cederbaum L. S., Green's Function Method in Quantum Chemistry // *Adv. Chem. Phys.* — 1999. — vol. 57. — p. 59—132.
12. Glushkov A. V., An Effective Account for Energy Effects of Exchange and Correlation in a Theory of Multi-Electron Systems // *Journ. Struct. Chem.* — 1990. — vol. 31, N 4. — p. 3—7.
13. Glushkov A. V., New Approach to Theoretical Definition of Ionization Potentials for Molecules on the Basis of Green's Function Method // *Journ. of Phys. Chem.* — 1992. — vol. 66. — p. 2671—2677.
14. Glushkov A. V., Malinovskaya S. V., Loboda A. V., Shpinareva I. M., Prepelitsa G. P., Consistent Quantum Approach to New Laser-Electron-Nuclear-Effects in Diatomic Molecules // *J. Phys. C.* — 2006. — vol. 35. — p. 420—424.
15. Glushkov A. V., Lepikh Ya. I., Fedchuk A. P., Loboda A. V., The Green's Functions and Density Functional Approach to Vibrational Structure in the Photoelectron Spectra of Molecules // *Photoelectronics.* — 2009. — N 18. — p. 119—127.
16. Kohn W., Sham L. J. Quantum Density Oscillations in an Inhomogeneous Electron Gas // *Phys. Rev. A.* — 1965. — vol. 137, N 6. — p. 1697.
17. The Fundamentals of Electron Density, Density Matrix and Density Functional Theory in Atoms, Molecules and the Solid State, Eds. Gidopoulos N. I., Wilson S. — Amsterdam: Springer, 2004. — vol. 14. — 244 pp.
18. Ivanova E. P., Ivanov L. N., Glushkov A. V., Kramida A. E., High-order Corrections in Relativistic Perturbation Theory with the Model Zeroth Approximation, Mg-like and Ne-Like Ions // *Physica Scripta.* — 1985. — vol. 32(4). — p. 512—524.
19. Glushkov A. V., An Universal Quasi-particle Energy Functional in a Density Functional Theory for Relativistic Atom // *Optics and Spectroscopy.* — 1989. — Vol. 66, N 1. — P. 31—36.
20. Fedchuk A. P., Glushkov A. V., Lepikh Ya. I., Loboda A. V., Lopatkin Yu. M., Svinarenko A. A., The Green's functions and density functional approach to vibrational structure in the photoelectron spectra of carbon oxide molecule // *Photoelectronics.* — 2010. — N 19. — p. 115—120.
21. Glushkov A. V., Khetselius O. Yu., Malinovskaya S. V., Spectroscopy of Cooperative Laser-Electron-Nuclear Effects in Multi-Atomic Molecules // *Mol. Physics (UK).* — 2008. — vol. 106. — p. 1257—1262.

UDC 539.186

A. V. Glushkov, A. P. Fedchuk, P. A. Kondratenko, Ya. I. Lepikh, Yu. M. Lopatkin, A. A. Svinarenko

THE GREEN'S FUNCTIONS AND DENSITY FUNCTIONAL APPROACH TO VIBRATIONAL STRUCTURE IN THE PHOTOELECTRONIC SPECTRA: MOLECULES CH AND HF

Abstract

The improved theoretical approach to vibration structure of photo-electronic spectra (PES) of molecules is used for quantitative treatment of the CH, HF molecules PES. The method is based on the density functional theory (DFT) and the Green's-functions (GF) approach including synergistic corrections.

Key words: photo-electronic spectra, Green's functions, density functional theory, CH and HF molecules, synergistic corrections.

УДК 539.186

А. В. Глушков, А. П. Федчук, П. А. Кондратенко, Я. И. Лепих, Ю. М. Лопаткин, А. А. Свиноаренко

МЕТОД ФУНКЦИЙ ГРИНА И ФУНКЦИОНАЛА ПЛОТНОСТИ В ОПРЕДЕЛЕНИИ КОЛЕБАТЕЛЬНОЙ СТРУКТУРЫ ФОТОЭЛЕКТРОННОГО СПЕКТРА: МОЛЕКУЛЫ СН, HF

Резюме

Улучшенный теоретический метод описания колебательной структуры фотоэлектронных спектров молекул, который базируется на методе функций Грина и теории функционала плотности (ТФП), включая синергетические поправки, применен к количественному описанию фотоэлектронных спектров молекул СН, HF.

Ключевые слова: фотоэлектронный спектр, метод функций Грина, теория функционала плотности, молекулы СН и HF, синергетические поправки.

УДК 539.186

О. В. Глушков, О. П. Федчук, П. О. Кондратенко, Я. І. Лепіх, Ю. М. Лопаткін, А. А. Свиноаренко

МЕТОД ФУНКЦІЙ ГРІНА І ФУНКЦІОНАЛУ ГУСТИНИ У ВИЗНАЧЕННІ ВІБРАЦІЙНОЇ СТРУКТУРИ ФОТОЕЛЕКТРОННОГО СПЕКТРУ: МОЛЕКУЛИ СН, HF

Резюме

Покращений теоретичний метод опису вібраційної структури фотоелектронних спектрів молекул, який базується на методі функцій Гріна та теорії функціоналу густини, включаючи синергетичні поправки, застосовано до кількісного опису фотоелектронних спектрів молекул СН, HF.

Ключові слова: фотоелектронний спектр, метод функцій Гріна, теорія функціоналу густини, молекули СН та HF, синергетичні поправки.

INVESTIGATION OF NANOSTRUCTURED SILICON SURFACES USING FRACTAL ANALYSIS

Fractal analysis was applied to images of nanostructured silicon surfaces which were acquired with a scanning electron microscope. A fractal model describing nanostructured silicon surfaces morphology is elaborated. It were obtained the numerical results for the fractal dimensions for 2 samples with different nanostructured shapes.

INTRODUCTION

Silicon is the dominant material of microelectronics industry. But the serious drawback of silicon is the limitation in optoelectronic applications i. e. produced non-radiative transition. After the discovery of visible photoluminescence (PL) from porous silicon (PS) an intensive research efforts has been taken towards the study of nanostructured silicon. Porous silicon consists of a network of nanometer size silicon crystal-lites in the form of nano-wires and nano-dots. Porous silicon structures has good mechanical robustness, chemical stability and compatibility with existing silicon technology so it has a wide area of potential applications such as waveguides, 1D photonic crystals, chemical sensors, biological sensors, photovoltaic devices etc [1].

In recent years, fractal geometry has been used to characterize the irregular forms of fractured materials. The fracture surface features are determined by the properties of the materials and also by the initial flaw defect sizes and stress states. Fractal objects are characterized by their fractal dimension, D , which is the dimension in which the proper measurement of a fractal object is made. Fractal dimension can be used as a diagnostic parameter characterizing the structure and mechanical properties of the surface layer. Tribological and elastic properties of the surface correlated with the fractal dimension: in areas with high fractal dimension the maximum friction and elasticity of the material is minimal. Also, by modifying the silicon surface by etching the surface, accompanied by an increase in fractal may by an order to increase the sensitivity of sensors based on nanostructured silicon [2, 3]. Therefore, in order to better understand a particular physical process occurring within nanostructured silicon, it is necessary to have detailed knowledge of the internal geometry and topology of the internal pore network. However, the surface area and pore size distribution alone do not meet all requirements to describe the characteristics of the nanostructured of silicon [4–5].

In this article, we review the topological features of nanostructured Si surfaces with two distinctive nanostructures, i. e. nanoislands and roughened shape, obtained by the deformation method [6]. The topological features of silicon surfaces are expressed in terms of the fractal concepts. In this study, we calculated the fractal dimension of the surface by box-counting method.

RESULTS AND DISCUSSION

As a result of high-temperature oxidizing of silicon, and also of some additional reasons, in near-surface layers the complex defect region which consists of disordered silicon and a layer containing dislocation networks is formed [6]. The depth of this defective layer is spread from the interface into the silicon to 10–20 microns. The given defect structure is formed owing to excess of mechanical stresses magnitudes of a threshold of plasticity. Is well known, that intensity of selective chemical etching depends on presence of initial defect structure, prestress processing and orientation of a surface. Etching away of silicon dioxide and treatment by various selective etching agents (Sacco, Sirtl, KOH solution, NaOH solution) surfaces allows to form nanostructures of silicon. It looks like short distance nanoislands of approximately the same size (Fig. 1) or roughened silicon surfaces (Fig. 2). The sizes and the shape of nanostructured silicon depend both on a chemical compound and etching conditions, and from initiating defect structure of near-surface silicon layers. Besides, the given defect structure directly depends on original plastic deformations [7].

As was mentioned above, the box-counting method is used to calculate the fractal dimension of the profile, and the fractal dimension of the surface can be calculated from the dimensions of its profile by adding units. Usually profile prepared by dissecting the test surface and the plane (the direction of fast scan).

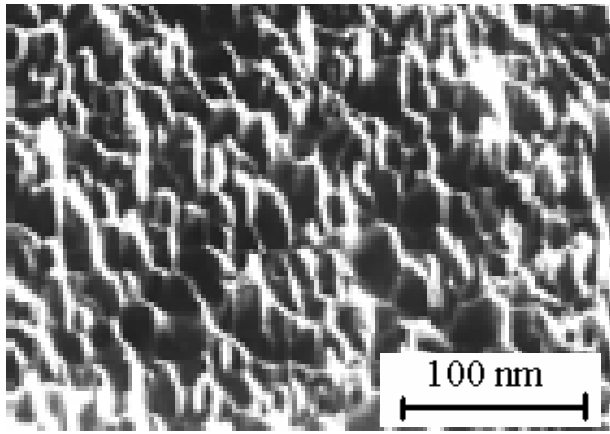


Fig. 1. SEM pattern of nanostructured silicon surface (sample 1)

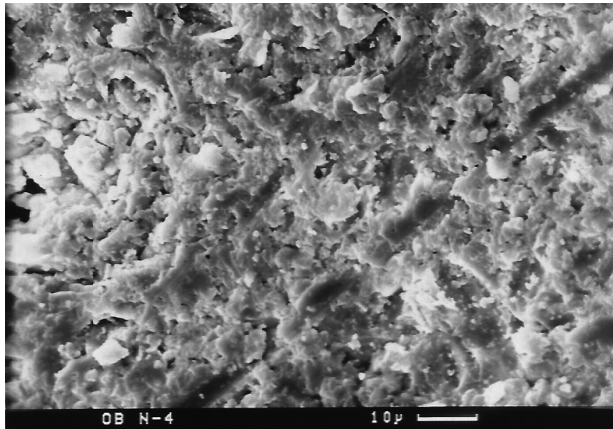


Fig. 2. SEM pattern of roughened silicon surface (sample 2)

To improve the accuracy of calculations can also use the modified the box-counting method, it combines this one and the “lake” algorithm, or method of the perimeter — area (area-perimeter method). Using this method, the surface is cut plane at a fixed level; for example, you can choose the level of:

$$Z_0 = (Z_{\min} + Z_{\max})/2, \quad (1)$$

where Z_{\min} , Z_{\max} — minimum and maximum heights of the points, respectively.

Intersection of the surface with this plane represents a set of closed lines, called “lake”. The perimeter of each “lake” is linked to its area ratio:

$$L(S) = \beta F_d A^{(F_d-1)/2}, \quad (2)$$

where β — constant, F_d — fractal dimension of the line, S — unit of length. Can also be seen in all sections of the “lake” from Z_{\min} up to Z_{\max} . “Lake” formed at the higher level sections, isolated portions of the surface close to the tops of the grains, the terms of the atoms close to the position of atoms in a single crystal, so the value of fractal dimension close to 2.0. The lower section of isolated regions, which

lie at the grain boundaries, where the positions of atoms are arranged like an amorphous material, so the fractal dimension increases. Thus, the fractal dimension is calculated on the expression (2) the slope of the logarithm of the perimeter to the logarithm of the cross-sectional area of the grains. When using the modified method of counting cells (boxes) produce section of the surface plane (1) and get a set of simply connected domains on which to apply the usual method of counting cells. All topograph of the surface under study is filled with square cells with side and count the number of nonempty cells. With a decrease in cell size over non-empty cells are counted. Thus determines the dependence of the number of non-empty cells on their size. The fractal dimension is calculated from the slope depends on a double logarithmic scale [8].

The method was implemented in a software environment Matlab: the processing of the original images (Fig. 1, 2) searches boundaries differential contrast using Canny algorithm, i.e. introduced the following model swings: drop step type (the presence of the interface contrast) was determined by the Heaviside function, white noise at the boundary was set using a Gaussian distribution (Fig. 3). To determine the boundaries were marked with three criteria: the high detection probability drop, the high precision localization of the interface, the unique-



Fig. 3. Convert images to the original surface by Canny algorithm

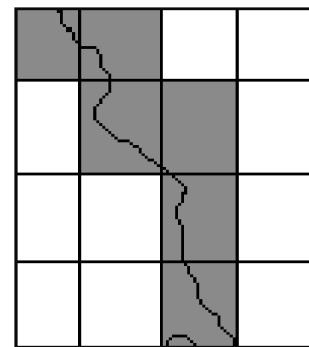


Fig. 4. Model filling in the processed image cells ($N = 16$, $N(S) = 6$)

ness of the existence of the contrast difference. It should be noted that the correct detection of the boundaries is very important because error in determining affects the value of fractal dimension, in most cases in the first decimal place. On the resulting image (Fig. 3) impose a grid of square cells with a given size. Then we count the cells through which the boundary lies $N(S)$ (Fig. 4). With decreasing cell size calculation was performed again.

The fractal dimension determined from the slope of the curve depending on a double logarithmic scale (Fig. 5) as follows:

$$D = \frac{\log N}{\log N(S)}. \quad (3)$$

On figures 5, 6 show plots for samples.

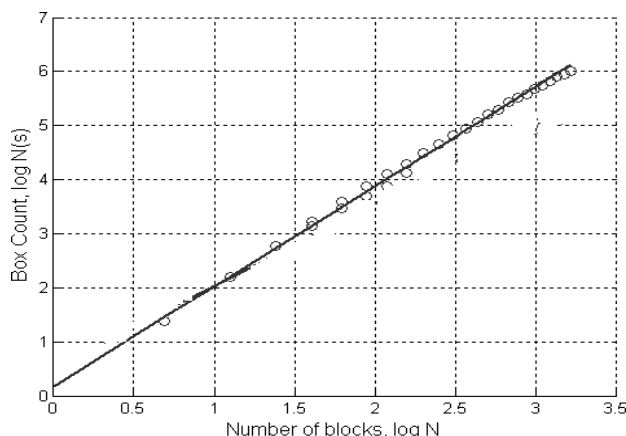


Fig. 5. Calculation of fractal dimension (sample 1)

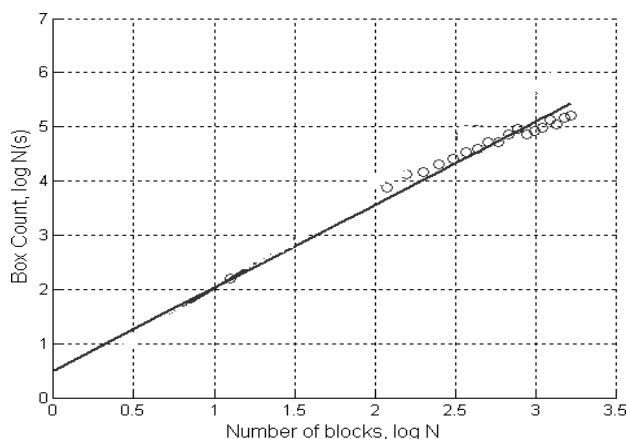


Fig. 6. Calculation of fractal dimension (sample 2)

Numerical results for the fractal dimension are presented in the Table:

Sample	Fractal dimension D
Sample 1	2.53
Sample 2	2.87

CONCLUSIONS

Thus, we can draw following conclusions. In near-surface layers of Si in Si-SiO₂ system the complex defect region which consists of disordered silicon and a layer containing dislocation networks is formed under high-temperature oxidation. After additional chemical treatment it were obtained nanostructured surface with different shapes of silicon. We have studied nanostructured silicon surfaces based on fractal concepts. Our adaptation of the box-counting method for fractal analysis was shown to be effective in accurately extracting the fractal dimension from experimental SEM data on Si surfaces. It were obtained the numerical results for the fractal dimensions for 2 samples with different nanostructured shapes.

REFERENCES

1. R. A. Street, Technology and Applications of Amorphous Silicon, Springer, New York, 2000.
2. H. Saha. Porous Silicon Sensors — Elusive and Eru-dite // Journal of Smart sensing and Intelligent system. — Vol 1, N 1. — 2008. — P. 34—56.
3. T. Nychyporuk, V. Lysenko, and D. Barbier. Fractal nature of porous silicon nanocrystallites // Physical Review B 71, 115402. — 2005. — P. 4021—4024.
4. P. Kumar, M. Kiran. Nanomechanical properties of silicon surfaces nanostructured by excimer laser // Sci. Technol. Adv. Mater. 11. — 2010. — P. 025003—025011.
5. Toyama T., Sobajima Y. and Okamoto H. Fractal study of surface nanostructures of microcrystalline silicon films: From growth kinetics to electronic transport // Philosophical Magazine. — N 89(28). — 2009. — P. 2491—2504.
6. V. A. Smyntyna, O. A. Kulinich, M. A. Glauberman, G. G. Chtmeresyuk, I. R. Yatsunskiy. The structure investigation of near — surface layers in silicon — dioxide silicon structure // Photoelectronics. — N. 17. — 2008. — P. 61—63.
7. V. A. Smyntyna, O. A. Kulinich, I. R. Iatsunskiy, I. A. Marchuk. Factors influencing the yield stress of silicon // Photoelectronics. — 2010. — N. 19. — P. 120—123.
8. Gordienko I. G., Gontareva I. G., Shreiber J. S., Zashimchuk E. E. Two-dimensional and three-dimensional rhombic grids created by self-organization of random nanoextrusions // Adv. Eng. Mater. — V. 6. — 2006. — P. 957—960.

UDC 537.311.33:622.382.33

V. A. Smyntyna, O. A. Kulinich, I. R. Yatsunskiy, I. A. Marchuk, N. N. Pavlenko

INVESTIGATION OF NANOSTRUCTURED SILICON SURFACES USING FRACTAL ANALYSIS

Abstract

Fractal analysis was applied to images of nanostructured silicon surfaces which were acquired with a scanning electron microscope. A fractal model describing nanostructured silicon surfaces morphology is elaborated. It were obtained the numerical results for the fractal dimensions for 2 samples with different nanostructured shapes.

Key words: nanostructured silicon, fractal analysis.

УДК 537.311.33:622.382.33

В. А. Смынтина, О. А. Кулинич, И. Р. Яцунский, И. А. Марчук, Н. Н. Павленко

ИССЛЕДОВАНИЕ НАНОСТРУКТУРИРОВАННОЙ ПОВЕРХНОСТИ КРЕМНИЯ МЕТОДАМИ ФРАКТАЛЬНОГО АНАЛИЗА

Резюме

Фрактальный анализ был применен для исследования электронных изображений наноструктурированных поверхностей кремния, определения их морфологических особенностей. Были получены значения фрактальной размерности для двух образцов с различной формой наноструктурирования.

Ключевые слова: наноструктурированный кремний, фрактальный анализ.

УДК 537.311.33:622.382.33

В. А. Сминтина, О. А. Кулініч, І. Р. Яцунський, І. О. Марчук, Н. Н. Павленко

ДОСЛІДЖЕННЯ НАНОСТРУКТУРОВАНОЇ ПОВЕРХНІ КРЕМНІЮ МЕТОДАМИ ФРАКТАЛЬНОГО АНАЛІЗУ

Резюме

Фрактальний аналіз був застосований для дослідження електронних зображень наноструктурованих поверхонь кремнію, визначення їх морфологічних особливостей. Були отримані значення фрактальної розмірності для двох зразків з різною формою наноструктурування.

Ключові слова: наноструктурований кремній, фрактальний аналіз.

INFLUENCE OF 3D-IMPURITIES (Cr, Fe, Co, Ni) ON THE POSITION OF ABSORPTION EDGE IN ZINC CHALKOGENIDES

The zinc chalcogenides (ZnS, ZnSe, ZnTe) single crystals doped with 3d-impurities (Cr, Fe, Co, Ni) are investigated. The diffusion doping is carried out from metallic nickel and chromium or powderlike iron and cobalt in helium and argon atmosphere. The optical density spectra are investigated in the fundamental absorption range of ZnS, ZnSe, ZnTe crystals. The transition-metal elements doping of crystals results in the absorption edge shift toward lower energies. From the value of the absorption edge shift, the 3d-impurity concentrations in crystals under investigation is determined.

Last years researches of zinc chalcogenides (ZnS, ZnSe, ZnTe) crystals doped with elements of transition metals (Cr, Fe, Co, Ni) are actual. It is related to that for such crystals intracent-er absorption and luminescence transitions are characteristic in unfilled 3d-shells these atoms is characterized by a spectrum in an infra-red (IR) region (1—5 μm) and high quantum output. The explored crystals can used as an active environments for lasers with the reconstructed wave-length IR-emission. Such lasers are applied in medicine, biology, and different spectroscopy researches. Substantial progress in making of the IR-emission lasers is presently attained. The laser generation on the ZnSe and ZnS crystals doped with chrome is realized [1, 2]. In [3], efficient lasing in the spectral range of 3.77—5.05 μm is realized for ZnSe:Fe crystals.

In spite of certain success, there is the row of unresolved important problems, that restrains further application in practice of zinc chalcogenides crystals doped with transition-metal ions. Among them such: perfection of technology obtaining crystals doped with the set concentration of doping impurity, insufficient researches of optical properties in the visible region of spectrum.

There are two basic methods of doping zinc chalcogenides crystals elements of transition-metal is doping during the growing process from a vapour phase and diffusion doping. In [4] ZnSe:Fe and ZnSe:Ni single crystals were obtained from a vapour phase by the free growth method on a single crystal substrate with the use of chemical transport in hydrogen. The possibility of controlling the impurity concentration and doping profile is advantage of the diffusion doping. In [5] the ZnSe:Fe crystals are obtained by the doping from a solid phase metallic source (a metallic layer). The diffusion doping in the iron vapours is carried out in [6]. Duration of diffusion process and small iron impurity concentrations in the obtained crystals are the lacks of these diffusion doping methods.

In this study we describe the diffusion technique of doping which allows to obtaining ZnS, ZnSe, ZnTe single crystals with predicted transition-metals impurities concentration. The optical absorption spectra in the area of fundamental absorption edge has been studied. Basing on the optical absorption edge shift, the impurity concentration has been determined.

The goals of this study is the determination of transition-metal impurities influencing on the fundamental absorption edge position of the ZnS, ZnSe, ZnTe crystals.

1. EXPERIMENTAL

The samples for the study were prepared by the transition-metal elements diffusion doping of pure ZnS, ZnSe and ZnTe single crystals. The undoped crystals were obtained by free growth on a ZnSe single crystal substrate with the (111) growth plane. The method and the main characteristics of the ZnS, ZnSe and ZnTe crystals were described in details in [7]. Selection of temperature profiles and design of the growth chamber excluded the possibility of contact of the crystal with chamber walls. The dislocation density in obtained crystals was no higher than 10^4 cm^{-2} .

Doping of crystals by the nickel or chromium impurity was carried out by diffusion from the metallic nickel or chrome layer deposited on the crystal surface in the He + Ar atmosphere. The nickel or chromium diffusion was carried out under conditions in which the impurity concentration in the source (the metallic nickel or chromium layer) remained nearly constant. A metallic layer sneaked up such thickness, that the condition of impurity diffusion from a source was executed, in which concentration of her during all process remains practically permanent. The crystals were annealed at the temperatures $T_a = 1020\text{—}1270 \text{ K}$. The diffu-

sion process time was about 5—10 hours. After annealing the crystals changed the color: crystals ZnS:Ni, ZnS:Cr got a yellow color, ZnSe:Ni was light-brown, ZnSe:Cr was red-brown and ZnTe:Ni, ZnTe:Cr was dark-brown.

The first experiments with iron and cobalt diffusion were carried out according to a procedure similar for nickel and chromium diffusion. The crystals were doped via impurity diffusion from a metallic layer deposited on the crystal surface. At the same time, this method was ineffective for the receipt of high-doped crystals. It is explained it by the technological problems related to impossibility deposit the thick cobalt or iron layer, from what in the process of annealing all layer dissolved completely in the crystals in the span no longer than 30 minutes. The optical absorption spectra showed that the obtained crystals were lightly doped.

To obtain heavily doped crystals the diffusion by impurity from metal powderlike iron or cobalt in He + Ar atmosphere was carried out. In order to avoid etching of crystals, powderlike ZnS, ZnSe or ZnTe depending on the crystals type in the ratio 1:2 was added to the metallic powder. Crystals were annealed at temperatures from 1070 to 1320 K. The duration of the diffusion process was 10—30 hours. After annealing the ZnS:Fe crystals acquired a yellow-brown colour, ZnS:Co was turquoise, ZnSe:Fe was red-brown, ZnSe:Co was brown and the ZnTe:Fe ZnTe:Co crystals were dark-brown.

The optical density spectra in the visible region were measured by means of an MDR-6 monochromator with diffraction gratings 1200 lines/mm. A FEU-100 hotomultiplier was used as a light flow receiver.

2. INVESTIGATIONS IN THE ABSORPTION EDGE REGION

The absorption spectra (the optical density D^*) of undoped ZnS crystals at 300 K are characterized by an absorption edge with the energy $E_g = 3.75$ eV, ZnSe crystals are characterized by an absorption edge with the energy $E_g = 2.68$ eV and ZnTe are characterized by the energy $E_g = 2.24$ eV.

The transition-metal elements doping of crystals results in the absorption edge shift toward lower energies. Figure 1 shows the absorption spectra of the ZnSe and ZnSe:Co crystals. The absorption edge shift value increased with annealing temperature and conditioned by the Coulomb interaction between impurity states. The absorption edge shift values in the ZnS, ZnSe and ZnTe crystals doped with transition-metal elements are presented in the Tables 1—4. At the change of temperature from 300 to 77 K shift values are saved.

The band gap varies ΔE_g depending on the introduced impurity concentration is determined in [8] by the relation

$$\Delta E_g = -2 \cdot 10^5 \left(\frac{3}{\pi} \right)^{1/3} \frac{eN^{1/3}}{4\pi\epsilon_0\epsilon_s}, \quad (1)$$

where e — electron charge, N — impurity concentration in cm^{-3} , ϵ_s is the static permittivity of ZnS, ZnSe or ZnTe, ϵ_0 — permittivity constant. Using the band gap shift, we calculated the doping impurity concentration in the studied crystals (see Tables 1—4).

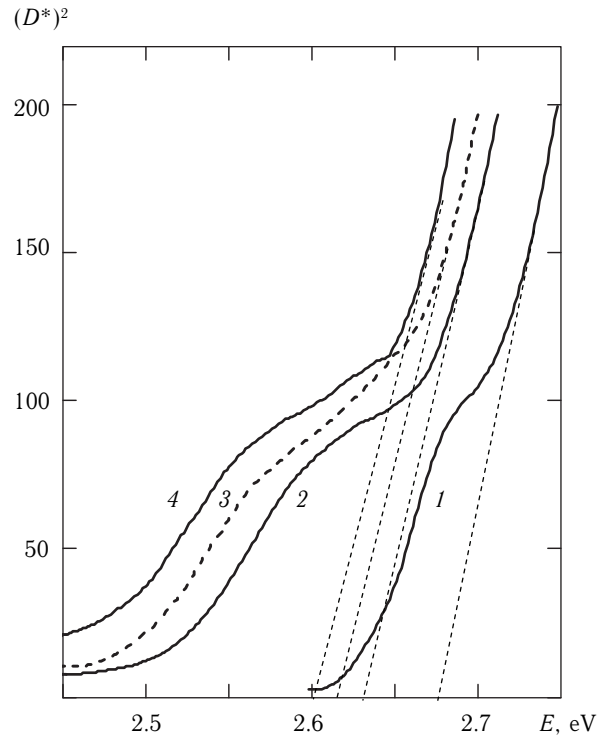


Fig. 1. Spectra of the optical-density D^* of (1) ZnSe, and (2—4) ZnSe:Co crystals obtained at annealing temperature $T_a =$ (2) 1070, (3) 1120, and (4) 1170 K

Tables 1—4 show that the maximal band gap shift value and doping impurity concentration is observed in the crystals doped with cobalt and nickel. In the researches of the ZnSe:Co crystals absorption edge [9] there was band gap shift to 400 meV, that evidenced at formation of the $\text{Zn}_{1-x}\text{Co}_x\text{Se}$ alloy.

Table 1

Results of calculation of the chromium concentration in the ZnS:Cr, ZnSe:Cr, ZnTe:Cr crystals

Annealing temperature, K	Crystal type					
	ZnS:Cr		ZnSe:Cr		ZnTe:Cr	
	ΔE_g , meV	N , cm^{-3}	ΔE_g , meV	N , cm^{-3}	ΔE_g , meV	N , cm^{-3}
1070	—	—	20	$2 \cdot 10^{17}$	30	10^{18}
1120	—	—	30	10^{18}	60	$8 \cdot 10^{18}$
1170	20	$2 \cdot 10^{17}$	70	10^{19}	100	$4 \cdot 10^{19}$
1220	50	$3 \cdot 10^{18}$	90	$2 \cdot 10^{19}$	—	—
1270	—	—	120	$5 \cdot 10^{19}$	—	—

Table 2

Results of calculation of the iron concentration in the ZnS:Fe, ZnSe:Fe, ZnTe:Fe crystals

Annealing temperature, K	Crystal type					
	ZnS:Fe		ZnSe:Fe		ZnTe:Fe	
	ΔE_g , meV	N , cm ⁻³	ΔE_g , meV	N , cm ⁻³	ΔE_g , meV	N , cm ⁻³
1070	—	—	—	—	20	$2 \cdot 10^{17}$
1120	—	—	—	—	40	$3 \cdot 10^{18}$
1170	10	$2 \cdot 10^{16}$	10	$3 \cdot 10^{16}$	100	$4 \cdot 10^{19}$
1220	20	$2 \cdot 10^{17}$	20	$2 \cdot 10^{17}$	130	$8 \cdot 10^{19}$
1270	30	$7 \cdot 10^{17}$	30	$8 \cdot 10^{17}$	—	—
1320	70	$9 \cdot 10^{18}$	40	$2 \cdot 10^{18}$	—	—

Table 3

Results of calculation of the cobalt concentration in the ZnS:Co, ZnSe:Co, ZnTe:Co crystals

Annealing temperature, K	Crystal type					
	ZnS:Co		ZnSe:Co		ZnTe:Co	
	ΔE_g , meV	N , cm ⁻³	ΔE_g , meV	N , cm ⁻³	ΔE_g , meV	N , cm ⁻³
1020	—	—	—	—	90	$3 \cdot 10^{19}$
1070	—	—	40	$2 \cdot 10^{18}$	110	$5 \cdot 10^{19}$
1120	—	—	50	$3 \cdot 10^{18}$	120	$7 \cdot 10^{19}$
1170	—	—	80	10^{19}	—	—
1220	130	$5 \cdot 10^{19}$	120	$5 \cdot 10^{19}$	—	—

Table 4

Results of calculation of the nickel concentration in the ZnS:Ni, ZnSe:Ni, ZnTe:Ni crystals

Annealing temperature, K	Crystal type					
	ZnS:Ni		ZnSe:Ni		ZnTe:Ni	
	ΔE_g , meV	N , cm ⁻³	ΔE_g , meV	N , cm ⁻³	ΔE_g , meV	N , cm ⁻³
1020	—	—	—	—	20	$3 \cdot 10^{17}$
1070	—	—	20	$2 \cdot 10^{17}$	50	$4 \cdot 10^{18}$
1120	10	$4 \cdot 10^{17}$	40	$2 \cdot 10^{18}$	110	$6 \cdot 10^{19}$
1170	100	$2 \cdot 10^{19}$	110	$4 \cdot 10^{19}$	—	—
1220	130	$5 \cdot 10^{19}$	140	$8 \cdot 10^{19}$	—	—
1270	200	$2 \cdot 10^{20}$	160	$1 \cdot 10^{20}$	—	—

Formation of the $\text{Zn}_{1-x}\text{Fe}_x\text{Se}$ alloy was observed in [10]. Careful analysis of optical absorption in the fundamental absorption region of the ZnSe:Fe, ZnSe:Ni crystals, executed by us in [8,11], showed that crystals with doping impurity concentration higher than 10^{18} cm^{-3} showed strong impurity absorption in this re-

gion, that difficult determination of fundamental absorption edge. The impurity absorption bands in the fundamental absorption region were observed in the ZnSe:Cr, ZnSe:Co, ZnS:Co and ZnS:Ni crystals [9, 11–13].

The author is grateful to Drs. Yu. Vaksman and Yu. Purov for their suggestions, and is also thankful to his aspirant V. Yatsun for technical assistance.

4. CONCLUSIONS

The investigations enable us to draw the following conclusions.

1. The diffusion 3d-impurities doping technique is developed for the ZnS, ZnSe, ZnTe single crystals. The method allows to obtaining zinc-chalcogenides single crystals with predicted 3d-impurity concentration.

2. It is shown that doping by transition-metal elements results in diminishment of band gap in the explored crystals.

3. Concentrations of doping impurities in the investigated crystals are determined on values band gap shift. The maximal value of doping impurity concentration ($\sim 10^{20} \text{ cm}^{-3}$) is observed in the crystals doped with cobalt and nickel.

REFERENCES

1. Воронов А. А., Козловский В. И., Коростелин Ю. В., Ландман А. И., Подмарьков Ю. П., Фролов М. П., Лазерные характеристики кристалла Fe: ZnSe в диапазоне температур 85–255 К // Квант. Электроника. — 2005. — В. 35, № 9. — С. 809–812.
2. I. T. Sorokina, E. Sorokin, S. B. Mirov, V. V. Fedorov. Broadly tunable compact continuous-wave Cr^{2+} :ZnS laser // Optics Letters— 2002. — Vol. 27, No. — P. 1040–1042.
3. Fedorov V. V., Mirov S. B. et. al. 3.77–5.05- μm tunable solid-state lasers based on Fe^{2+} -doped ZnSe crystals operating at low and room temperatures // Journal of quantum electronics — 2006. — V. 42, № 9. — P. 907–917.
4. J. Kreissl, H.-J. Schulz. Transition-metal impurities in II–VI semiconductors: characterization and switching of charge states // J. Cryst. Growth. — 1999. — V. 161. — P. 239–249.
5. Кулешов Н. В., Щербицкий В. Г., Кисель В. Э., Левченко В. И., Постнова Л. И. Fe^{2+} :ZnSe — новый материал для пассивных затворов лазеров с длиной волны излучения 3 мкм // Сборник докладов Международной научной конференции «Актуальные проблемы физики твердого тела», <http://iftpp.bas-net.by>.
6. Demirbas U., Sennaroglu A., Somer M. Synthesis and characterization of diffusion-doped Cr^{2+} :ZnSe and Fe^{2+} :ZnSe // Optical Materials — 2006. — V. 28 P. 231–240.
7. Korostelin Yu. V., Kozlovsky V. I., Nasibov A. S., Shapkin P. V. Vapour growth of II–VI solid solution single crystals // J. Cryst. Growth. — 1999. — V. 159. — P. 181–185.
8. Ваксман Ю. Ф., Ницук Ю. А., Яцун В. В., Насибов А. С., Шапкин П. В. Получение и оптические свойства кристаллов ZnSe:Ni // ФТП. — 2010. — Т. 44, В. 2. — С. 149–153.
9. Ваксман Ю. Ф., Павлов В. В., Ницук Ю. А., Пуртов Ю. Н., Насибов А. С., Шапкин П. В. Получение и оптические свойства монокристаллов ZnSe, легированных кобальтом // ФТП. — 2006. — Т. 40, №. 7. — С. 815–818.
10. Chee-Leung Mak, Sooryakumar R., Steiner M. M. Optical transitions in $\text{Zn}_{1-x}\text{Co}_x\text{Se}$ and $\text{Zn}_{1-x}\text{Fe}_x\text{Se}$: Strong concentration-dependent effective p - d exchange // Phys. Rev. B. — 1999. — V. B48. — P. 11743–11747.

11. Ваксман Ю. Ф., Павлов В. В., Ницук Ю. А., Пуртов Ю. Н., Насибов А. С., Шапкин П. В. Оптическое поглощение и диффузия хрома в монокристаллах ZnSe // ФТП. — 2005. — Т. 39, № 4. — С. 401—404.

12. Vaksman Yu. F., Nitsuk Yu. A., Pavlov V. V., Purto-
tov Yu. N., Nasibov A. S., Shapkin P. V. Optical proper-

ties of ZnS single crystals doped with cobalt // Photoelec-
tronics. 2007. — N. 16. — P. 33—36.

13. Vaksman Yu. F., Nitsuk Yu. A., Yatsun V. V., Pur-
tov Yu. N., Nasibov A. S., Shapkin P. V. Optical Properties
of ZnS:Ni Crystals Obtained by Diffusion Doping // Func-
tional Materials. — 2010. — V. 17. — N. 1. — P. 75—79.

UDC 621.315.592

Yu. A. Nitsuk

INFLUENCE OF 3d-IMPURITIES (Cr, Fe, Co, Ni) ON THE POSITION OF ABSORPTION EDGE IN ZINC CHALKOGENIDES

Abstract

The zinc chalcogenides (ZnS, ZnSe, ZnTe) single crystals doped with 3d-impurities (Cr, Fe, Co, Ni) are investigated. The diffusion doping is carried out from metallic chromium and nickel or powderlike iron and cobalt in helium and argon atmosphere. The optical density spectra are investigated in the fundamental absorption range of ZnS, ZnSe, ZnTe crystals. The transition-metal elements doping of crystals results in the absorption edge shift toward lower energies. From the value of the absorption edge shift, the 3d-impurity concentrations in crystals under investigation is determined.

Key words: zinc chalcogenides, 3d-impurities, optical-density, band gap shift.

УДК 621.315.592

Ю. А. Ницук

ВЛИЯНИЕ 3d-ПРИМЕСЕЙ (Cr, Fe, Co, Ni) НА ПОЛОЖЕНИЕ КРАЯ ПОГЛОЩЕНИЯ В ХАЛЬКОГЕНИДАХ ЦИНКА

Резюме

Исследованы монокристаллы халькогенидов цинка (ZnS, ZnSe, ZnTe), легированные 3d-примесями (Cr, Fe, Co, Ni). Диффузионное легирование осуществлялось из металлического хрома и никеля или порошкообразного железа и кобальта в атмосфере гелия и аргона. Исследованы спектры оптической плотности в области фундаментального поглощения кристаллов ZnS, ZnSe, ZnTe. Показано, что легирование элементами переходных металлов приводит к уменьшению ширины запрещенной зоны исследуемых кристаллов. По величине смещения края поглощения определены концентрации 3d-примесей в исследуемых кристаллах.

Ключевые слова: халькогениды цинка, 3d-примеси, оптическая плотность, изменение ширины запрещенной зоны.

УДК 621.315.592

Ю. А. Ницук

ВПЛИВ 3d-ДОМІШОК (Cr, Fe, Co, Ni) НА ПОЛОЖЕННЯ КРАЮ ПОГЛИНАННЯ В ХАЛЬКОГЕНІДАХ ЦИНКУ

Резюме

Досліджено монокристали халькогенідів цинку (ZnS, ZnSe, ZnTe), що леговані 3d-домішками (Cr, Fe, Co, Ni). Дифузійне легування виконувалось з металевого хрому та нікелю або порошкоподібного заліза та кобальту в атмосфері гелію та аргону. Досліджено спектри оптичної густини в області краю фундаментального поглинання кристалів ZnS, ZnSe, ZnTe. Показано, що легування елементами перехідних металів призводить до зменшення ширини забороненої зони в досліджуваних кристалах. За величиною зсуву краю поглинання визначені концентрації 3d-домішок в досліджуваних кристалах.

Ключові слова: халькогеніди цинку, 3d-домішки, оптична густина, зміна ширини забороненої зони.

A. S. KVASIKOVA³, A. V. IGNATENKO², T. A. FLORKO¹, D. E. SUKHAREV²,
Yu. G. CHERNYAKOVA¹

¹ Odessa State Environmental University,

² Odessa National Polytechnical University,

³ Odessa Institute of the Measurement Technique, e-mail: kvasikova@mail.ru

PHOTOEFFECT AND SPECTROSCOPY OF THE HYDROGEN ATOM IN THE CROSSED DC ELECTRIC AND MAGNETIC FIELD

Within the operator perturbation theory a new approach to calculating energies, Stark resonances widths and probabilities of radiative transitions between Stark sublevels in a spectrum of an atom in the crossed DC electric and magnetic fields is presented. The corresponding calculation results are presented for the hydrogen atom.

1. INTRODUCTION

Determination of the energy and radiative characteristics of atom in a strong electric field and crossed electric and magnetic fields is of a great interest for many applications in laser, plasma, atomic, molecular physics, quantum electronics etc and remains very important problem of modern quantum photophysics [1–17]. The key problem is connected with calculation of the energies and widths of the Stark resonances, intensities and probabilities of radiative transitions between Stark sublevels in a spectrum of an atom in a DC electric and magnetic fields [1–3]. In a case of the strong fields, when the corresponding Stark resonances mix and create the Arnold's maps (including the chaos phenomena), this group of problems remains practically unsolved hitherto.

It is well known that the external electric field shifts and broadens the bound state atomic levels. The standard quantum-mechanical approach relates complex eigen-energies (EE) $E = E_r + 0.5iG$ and complex eigen-functions (EF) to the shape resonances [2, 4]. The calculation difficulties in the standard quantum mechanical approach are well known. The WKB approximation overcomes these difficulties for the states, lying far from “new continuum” boundary and, as rule, is applied in the case of a relatively weak electric field. The same is regarding the widespread asymptotic phase method (c. f. [2]). Some modifications has been reached by means of the using WKB method [3]. Quite another calculation procedures are used in the Borel summation of the divergent perturbation theory (PT) series and in the numerical solution of the difference equations following from expansion of the wave function over finite basis [2, 3, 9, 10].

In ref. [4] it has been developed a consistent uniform quantum — mechanical approach to the non-stationary state problems solution including the Stark effect and also scattering problems. The essence of the method is the in-

clusion of the well-known method of “distorted waves approximation” in the frame of the formally exact PT. The zeroth order Hamiltonian H_0 of this PT possesses only stationary bound and scattering states. To overcome formal difficulties, the zeroth order Hamiltonian was defined by the set of the orthogonal EF and EE without specifying the explicit form of the corresponding zeroth order potential. In the case of the optimal zeroth order spectrum, the PT smallness parameter is of the order of G/E , where G and E are the field width and bound energy of the state level. It has been shown that $G/E \leq 1/n$ even in the vicinity of the “new continuum” boundary (n is the principal quantum number). It is very important to note that the hamiltonian H_0 is defined so that it coincides with the total Hamiltonian H at $\epsilon \rightarrow 0$. (ϵ is the electric field strength). Note that perturbation in OPT does not coincide with the electric field potential, though they disappear simultaneously. This method is known as the operator PT (OPT) [2].

In series of the papers [18–22] it has been further developed and applied to the non-hydrogen atoms in the DC electric field. In this paper a new approach, based on the OPT, to calculating energies, Stark resonances widths and probabilities of radiative transitions between Stark sublevels in a spectrum of an atom in the crossed DC electric and magnetic fields is presented. The corresponding calculation results are presented for the hydrogen atom.

2. AN ATOM IN THE CROSSED ELECTRIC AND MAGNETIC FIELDS: PERTURBATION THEORY FORMALISM

The standard Hamiltonian of the atomic system (the hydrogen atom) in the crossed DC electric F and magnetic B fields looks as usually (in atomic units: 1 at. unit $F = 5.14 \cdot 10^9$ V/cm and 1 at. unit $B = 2.35 \cdot 10^5$ T) [3]:

$$H = 1/2(p_p^2 + l_z^2/p^2) + Bl_z/2 + (1/8)B^2p^2 + (1/2)p_z^2 + Fz + V_c(r), \quad (1)$$

where the electron-nucleus potential in a case of the hydrogen atom takes the usual Coulomb form: $-Z/r$ and other notations are the usual.

The standard PT (SPT) formalism in the most effective formulation in application to the hydrogen atom in the crossed electric and magnetic fields has been developed by the Turbiner (c. f. [3]) for sufficiently weak fields. Operator of the “atom-field” interaction is treated as the perturbation one, which should be naturally small. This is the fundamental condition for the application of the SPT formalism.

The energy expansion for the hydrogen atom in the DC crossed electric and magnetic fields in the Turbiner’s PT can be written as follows:

$$E = E_{sz} + E^{(\parallel, \perp)}, \quad (2)$$

where E_{sz} is the sum of energies, corresponding to an electric and magnetic fields with the strengths F and B respectively (in atomic units):

$$E_{sz} = -1 - \frac{9}{2}F^2 + \frac{B^2}{2} - \frac{3555}{32}F^4 - \frac{53}{96}B^4 + \dots \quad (3a)$$

and $E^{\parallel, \perp}$ contains earlier unknown crossed terms for parallel (E^{\parallel}) and perpendicular (E^{\perp}) directions of the fields F and B [3]:

$$E^{\parallel} = \frac{159}{16}F^2B^2 - \frac{1742009}{26880}F^2B^4 + \dots \quad (3b)$$

$$E^{\perp} = \frac{93}{4}F^2B^2 - \frac{22770991}{107520}F^2B^4 + \dots \quad (3c)$$

Surely, the SPT formulae provide very good description of the hydrogen atom in the weak crossed electric and magnetic fields. However, in a case of the strong external fields such an approach obviously falls because of the Dyson phenomenon, asymptotic divergence of the PT set etc. The similar situation occurs in the cases of the separated electric and magnetic fields. As it has been indicated in the introduction, one of the effective methods for the “atom-strong external field” interaction is given by the OPT formalism.

Let us consider some key details of the OPT approach, following to the original refs. [2, 4] and start from the purely DC electric field case. In our theory the magnetic field is treated as perturbation within the OPT formalism at the second step, meanwhile as the electric field is taken into account on the non-perturbative basis. This is a key advancement of our theory. Surely, one could note that our approach can hardly be applied to the strong magnetic field case.

In the OPT formalism the Schrödinger equation for the electron function with taking into account the uniform electric field F and the field of the nucleus (in the original paper the

Coulomb units are used: for length 1 unit is \hbar^2/Ze^2m ; for energy 1 unit is mZ^2e^4/\hbar^2) [4]:

$$[-(1 - N/Z)/r + Fz - 0,5\Delta - E]\psi = 0. \quad (4)$$

Here E is the electron energy, Z is a nucleus charge, N is the number of electrons in atomic core. Naturally, for hydrogen atom: $Z=1$, $N=0$. For multielectron atom one may introduce the ion core charge z^* [2, 18]. As usually in an electric field all the electron states can be classified due to quantum numbers: n, n_1, n_2, m (principal, parabolic, azimuthal: $n = n_1 + n_2 + m + 1$). After separation of variables in the parabolic coordinates $\{\xi = r + z, \eta = r - z, \varphi = \tan^{-1}[y/x]\}$:

$$\psi(\zeta, \eta, \varphi) = f(\zeta)g(\eta)(\zeta \cdot \eta)^{|m|/2} \exp(im\varphi)/(2\pi)^{1/2},$$

equation (1) transformed to the system of two equations for the functions f, g [4]:

$$f'' + \frac{|m|+1}{t} f' + [0,5E + (\beta_1 - N/Z)/t - 0,25F(t)t]f = 0, \quad (5a)$$

$$g'' + \frac{|m|+1}{t} g' + [0,5E + \beta_2/t + 0,25F(t)t]g = 0, \quad (5b)$$

coupled through the constraint on the separation constants: $\beta_1 + \beta_2 = 1$.

For the uniform electric field $F(t) = F$. Potential energy in equation (4) has the barrier. Two turning points for the classical motion along the η axis, t_1 and t_2 , at a given energy E are the solutions of the quadratic equation ($\beta = \beta_1, E = E_0$):

$$t_2 = \{[E_0^2 - 4E(1 - \beta)]^{1/2} - E_0\}/F, \\ t_1 = \{-[E_0^2 - 4E(1 - \beta)]^{1/2} - E_0\}/F, \quad t_1 < t_2.$$

Here and below t denotes the argument common for the whole equation system. In ref. [4] the uniform electric field F in (4) and (5) was substituted by model function $F(t)$ with parameter τ ($\tau = 1,5t_2$). The corresponding function satisfies to necessary asymptotic conditions and is defined as follows [4]:

$$F(t) = \frac{1}{t}F\left[(t - \tau)\frac{\tau^2}{\tau^2 + t^2} + \tau\right]. \quad (6)$$

The final results do not depend on the parameter τ . To calculate the width G of the concrete quasi-stationary state in the lowest PT order it is necessary to know two zeroth order EF of H_0 : bound state function $\Psi_{Eb}(\epsilon, \mathbf{v}, \varphi)$ and scattering state function $\Psi_{Es}(\epsilon, \eta, \varphi)$ with the same EE. First, one has to define the EE of the expected bound state. It is the well known problem of states quantification in the case of the penetrable barrier. We solve the system with total Hamiltonian H under the conditions [4]:

$$f(t) \rightarrow 0 \text{ at } t \rightarrow \infty$$

and

$$\partial x(\beta, E)/\partial E = 0 \quad (7)$$

with

$$x(\beta, E) = \lim_{t \rightarrow \infty} [g^2(t) + \{g'(t)/k\}^2] t^{|m|+1}.$$

These two conditions quantify the bound energy E , separation constant β_1 . The further procedure for this two-dimensional eigen-value problem is resulted in the solving of the system of the ordinary differential equations (2, 3) with probe pairs of E, β_1 . The corresponding EF is:

$$\begin{aligned} & \psi_{Eb}(\zeta, \eta, \varphi) = \\ & = f_{Eb}(\zeta) g_{Eb}(\eta) (\zeta \cdot \eta)^{|m|/2} \exp(i m \varphi) / (2\pi)^{1/2}, \end{aligned}$$

Here $f_{Eb}(t)$ is the solution of (5a) (with the just determined E, β_1) at $t \in (0, \infty)$ and $g_{Eb}(t)$ is solution of (5b) (with the same E, β_1) at $t < t_2$ (inside barrier) and $g(t) = 0$ otherwise. The bound state EE, eigen-value β_1 and EF for the zero order Hamiltonian H_0 coincide with those for the total Hamiltonian H at $\varepsilon \rightarrow 0$. The quantum numbers n, n_1, n_2, m are connected with E, β_1, m by the well known expressions.

The scattering state functions

$$\begin{aligned} & \psi_{Es}(\zeta, \eta, \varphi) = \\ & = f_{Es}(\zeta) g_{Es}(\eta) (\zeta \cdot \eta)^{|m|/2} \exp(i m \varphi) (2\pi)^{1/2}. \end{aligned}$$

The scattering state functions must be orthogonal to the above-defined bound state function and to each other. According to the OPT ideology [4], the following form of g_{Es} is possible:

$$g_{Es}(t) = g_1(t) - z'_2 g_2(t) \quad (8)$$

with f_{Es} and $g_1(t)$ satisfying the differential equations (5a) and (5b). The function $g_2(t)$ satisfies the non-homogeneous differential equation, which differs from (5b) only by the right hand term, disappearing at $t \rightarrow \infty$.

The total equation system, determining the scattering functions looks as follows [4]:

$$\begin{aligned} & f''_{Es} + f'_{Es} + \\ & + [0,5E' + (\beta'_1 - N/Z)/t - 0,25\varepsilon(t)t] f_{Es} = 0, \\ & g''_1 + g'_1 + [0,5E' + \beta'_2/t + 0,25\varepsilon(t)t] g_1 = 0, \\ & g''_2 + g'_2 + [0,5E + \beta'_2/t + 0,25\varepsilon(t)t] g_2 = 2g_{Eb}, \\ & \beta'_1 + \beta'_2 = 1. \end{aligned}$$

The coefficient z'_2 ensures the orthogonality condition and can be defined as:

$$\begin{aligned} z'_2 = & \left\{ \int \int d\zeta d\eta (\zeta + \eta) f_{Eb}^2(\zeta) g_{Eb}(\eta) g_1(\eta) \right\} // \\ & // \left\{ \int \int d\zeta d\eta (\zeta + \eta) f_{Eb}^2(\zeta) g_{Eb}(\eta) g_2(\eta) \right\}. \end{aligned}$$

The imaginary part of energy and resonance width G in the lowest PT order [2]:

$$\text{Im } E = G/2 = \varpi \langle \Psi_{Eb} | H | \Psi_{Es} \rangle^2 \quad (9)$$

with the total Hamiltonian H . The state func-

tions Ψ_{Eb} and Ψ_{Es} are assumed to be normalized to unity and by the $\delta(k - k')$ -condition, accordingly. The intensities of Stark components are defined by the matrix elements of r coordinate of an atomic electron:

$$\begin{aligned} & I(nn_1n_2m \rightarrow n'n_1'n_2'm') = \\ & = \frac{4e^4 \omega_0^4}{3c^3} |\langle nn_1n_2m | r | n'n_1'n_2'm' \rangle|^2, \end{aligned} \quad (10)$$

where ω_0 is non-perturbed frequency of transition $n \rightarrow n_1$. Usually the Stark components are divided on the π and σ -components in dependence upon polarization (linear $\Delta m = 0$, or cycle $\Delta m = \pm 1$). Intensities of the π -components are defined by the matrix elements of z -component r , and intensities of the σ -компонент — by x - (or y -) components r .

As usually, a probability of transition $B(nkm, n')$ from parabolic state $|nkm\rangle$ into all states, belonging to the level n' , is as follows:

$$B(nkm, n') = \omega(n, n') \sum_{k', m'} |\langle nkm | r | n'k'm' \rangle|^2, \quad (11)$$

where

$$\omega(n, n') = \frac{4e^2 a_0^2}{3\hbar c^3} \left(\frac{1}{n^2} - \frac{1}{n'^2} \right)^3. \quad (12)$$

A full probability of transition $B(k, m)$ from definite stark sublevel into all lowest levels is defined as follows:

$$B(k, m) = \sum_{n'=|m|+1}^{n-1} B(nkm, n'), \quad (13)$$

The corresponding life time is:

$$\tau(nkm) = B^{-1}(k, m) \quad (14)$$

A distribution of probabilities of transitions for $m = 0$ is directly defined by the distributions $B(k, m)$ for $m \neq 0$. The last ones are weakly dependent upon the electric quantum number $k = n_1 - n_2$. One can introduce average (on “ k ”) values $B(k, m)$, that are equal:

$$\bar{B}(m) = \frac{1}{n - |m|} \sum_k B(k, m) = \frac{1}{n - |m|} \sum_{l=|m|}^{n-1} A(n, l). \quad (15)$$

Other details can be found in the refs. [19, 20]. Further in all calculation it has been used the known Stark—Superatom program [4], which is freely available and propagated. It is important to note then that the whole calculation procedure of the approach at known resonance energy E and parameter β has been reduced to the solution of single system of the ordinary differential equations [2]. This is its important advancement.

3. RESULTS AND CONCLUSIONS

As example of application of the above developed method, below we present the calculation

Energy (in Ry) of the ground state for hydrogen atom in electric F (1 at. unit = $5.14 \cdot 10^9$ V/cm) and magnetic B (1 at. unit $B = 2.35 \cdot 10^5$ T) fields (look text)

F	B	$B + B^\parallel$ SPT, [3]	$E + E^\perp$ SPT, [3]	$E + E^\parallel$ our theory	$E + E^\perp$ our Theory
0,000	0,000	−1,000000	−1,000000	−1,000000	−1,000000
0,001	0,001	−1,000004	−1,000004	−1,000004	−1,000004
0,005	0,005	−1,000099	−1,000099	−1,000099	−1,000099
0,010	0,010	−1,000402	−1,000401	−1,000401	−1,000401
0,015	0,015	−1,000906	−1,000905	−1,000905	−1,000904
0,020	0,020	−1,001617	−1,001615	−1,001616	−1,001614
0,025	0,025	−1,002542	−1,002537	−1,002540	−1,002535
0,030	0,030	−1,003685	−1,003674	−1,003682	−1,003671
0,035	0,035	−1,005054	−1,005037	−1,005053	−1,005033
0,040	0,040	−1,0066619	−1,006628	−1,006659	−1,006626
0,045	0,045	−1,008520	−1,008465	−1,008517	−1,008463
0,050	0,050	−1,010642	−1,010558	−1,010636	−1,010553

results for energy (in Ry) of the ground state for hydrogen atom in electric F and magnetic B fields (see table 1). For comparison there are also listed the results of the ground state hydrogen atom energy on the basis of the Turbinger's SPT (from ref. [3]).

Analysis shows that the both results are in the physically reasonable agreement, at least till the field strengths values ~ 0.02 atomic units. Further it begins to increase the difference between our theory data and the SPT results.

It is important underline that our results are obtained in the first PT order, i. e. already the first PT order provides the physically reasonable results. From the one hand, for weak field strength values an excellent agreement between both approaches can be easily explained as speech is about by treating the hydrogen atom dynamics in the sufficiently weak fields.

From the other hand, the SPT formalism falls in a case of consideration the strong electric or magnetic or both simultaneously fields. Our theory is absolutely valid in a case of the strong electric field due to using the OPT formalism as the zeroth approximation, where an electric field is taken into account on the non-perturbative basis. However, our theory can hardly applied in a case of the strong external magnetic field. It is obvious that in the last case the non-perturbative treatment in the presented theory is necessary (see [1–3]).

REFERENCES

1. Matter in superintense laser field, Eds. Batani D. And Joachain C. — N.Y: AIP, 2007. — 560 p.
2. Glushkov A. V., Atom in an electromagnetic field. — Kiev: KNT, 2005. — 450 P.
3. Lisitsa V. S., New in effects of Stark and Zeeman // Usp. Phys. Nauk. — 1999. — Vol. 153. — P. 379–422.
4. Glushkov A. V., Ivanov L. N., DC strong-field Stark-effect: New consistent quantum-mechanical approach // J. Phys. B: At. Mol. Opt. Phys. — 1993. — Vol. 26. — P. L379–L386.
5. Stambulchik E., Maron I., Stark effect of high- n hydrogen-like transitions: quasi-continuous approximation // J. Phys. B: At. Mol. Opt. Phys. — 2008. — Vol. 41. — P. 095703 (9 p).
6. Meng H-Y., Zhang Y-X., Kang S., Shi T-Y., Zhan M-S., Theoretical complex Stark energies of lithium by a complex scaling plus the B-spline approach // J. Phys. B: At. Mol. Opt. Phys. — 2008. — Vol. 41. — P. 155003 (12 p).
7. Rao J. Quantum manifestations of scattering orbits in scaled spectrum of non-hydrogenic atom in crossed fields/ Rao J., Delande D., Taylor K. // J. Phys. B: At. Mol. Opt. Phys. — 2002. — V. 35. — P. L1–10.
8. Wang D. Influence of oscillating electric field on the recurrence spectra of a Li Rydberg atom in strong magnetic field / Wang D., Din S., Liu S. // J. Phys. B: At. Mol. Opt. Phys. — 2003. — V. 36. — P. 4225–4232.
9. Silverstone H., Adams B., Cizek J., Otto P., Stark effect in hydrogen: Dispersion relations, asymptotic formulas and calculation of the ionization rate via high-order perturbation theory // Phys. Rev. Lett. — 1979. — Vol. 43. — P. 1498–1501.
10. Zimmerman M. L., Littman M., Kash M., Kleppner D. Stark structure of Rydberg states of alkali-metal atoms // Phys. Rev. A. — 1979. — V. 20. — P. 2251–2275.
11. Plummer M., Noble C. J., Non-hermitian dynamics of argon atoms at 248 nm // J. Phys. B: At. Mol. Opt. Phys. — 2003. — Vol. 36. — P. L219–L226.
12. Glushkov A. V., Ambrosov S. V., Fedchuk O. O., Fedchuk O. P., Stark effect and resonances in the ionization continuum for hydrogen atom and Wannier–Mott excitons in DC electric field // Journ. Phys. Stud. — 2003. — V. 7, N 3. — P. 71–76.
13. Staudt A., Keitel C. H., Stabilization of helium in intense high-frequency laser pulses beyond dipole approximation // J. Phys. B: At. Mol. Opt. Phys. — 2003. — Vol. 36. — P. L203–209.
14. Hasbani R., Cormier E., Bachau H. Resonant and non-resonant ionization of He by XUV ultra-short intense pulses // J. Phys. B: At. Mol. Phys. — 2000. — Vol. 33. — P. 2101–2116.
15. Mercouris T., Nikolaidis C. A. Solution of the many-electron many-photon problem for strong fields: Application to Li^- in one and two-colour laser field // Phys. Rev. A. — 2003. — Vol. 67. — P. 063403-1–063403-12.
16. Harmin D. A. Theory of the Non hydrogenic Stark Effect // Phys. Rev. Lett. — 1982. — Vol. 49. — P. 128–131.
17. Glushkov A. V., Ambrosov S. V., Chaos and regular dynamics of complex atomic systems in magnetic field // J. Techn. Phys. — 1997. — Vol. 37. — P. 347–348.
18. Glushkov A. V., Ambrosov S. V., Ignatenko A. V., Korchevsky D. A., DC Strong Field Stark Effect for Non-hydrogenic Atoms: Consistent Quantum Mechanical Approach // Int. Journ. Quant. Chem. — 2004. — Vol. 99. — P. 936–939.
19. Rusov V. D., Glushkov A. V., Vaschenko V. N., Korchevsky D. A., Ignatenko A. V. Stochastic dynamics of the atomic systems in crossed electric and magnetic field: Rb atom recurrence spectra // Bulletin of Kiev Univ. Ser. phys.-math. — 2004. — № 4. — 433–438.
20. Ignatenko A. V., Probabilities of the radiative transitions between stark sublevels in spectrum of atom in DC electric field: New approach // Photoelectronics. — 2007. — N 16. — P. 71–74.

21. Glushkov A. V., Lepikh Ya. I., Fedchuk A. P., Khetse-
lius O. Yu., Ambrosov S. V., Ignatenko A. V., Wannier-mott
excitons and atoms in a DC electric field: photoionization,
Stark effect, resonances in the ionization continuum // Sensor
Electr. and Microsyst. Techn. — 2008. — N 4. — P. 5—11.

22. Korchevsky D. A., Shpinareva I. M., Ignatenko A. V.,
Sensing stochasticity of atomic systems by analysis of recur-
rence spectra in an crossed dc magnetic and ac electric fields
// Sensor Electr. & Microsyst. Techn. — 2005. — N 1. —
P. 21—26.

UDC 551.515.1

A. S. Kvasikova, A. V. Ignatenko, T. A. Florko, D. E. Sukharev, Yu. G. Chernyakova

PHOTOEFFECT AND SPECTROSCOPY OF THE HYDROGEN ATOM IN THE CROSSED DC ELECTRIC AND MAGNETIC FIELD

Abstract

Within the operator perturbation theory a new approach to calculating energies, Stark resonances widths and probabilities of radiative transitions between Stark sublevels in a spectrum of an atom in the crossed DC electric and magnetic fields is presented. The corresponding calculation results are presented for the hydrogen atom.

Key words: hydrogen atom, DC electric and magnetic fields, standard and operator perturbation theory.

УДК 551.515.1

А. С. Квасикова, А. В. Игнатенко, Т. А. Флорко, Д. Е. Сухарев, Ю. Г. Чернякова

ФОТОЭФФЕКТ И СПЕКТРОСКОПИЯ АТОМА ВОДОРОДА В СКРЕЩЕННЫХ ЭЛЕКТРИЧЕСКОМ И МАГНИТНОМ ПОЛЯХ

Резюме

На основе операторной теории возмущений развит новый подход к расчету энергий уровней, ширин штарковских резонансов, а также вероятностей радиационных переходов между штарковскими подуровнями в спектре атома в скрещенных однородных электрическом и магнитном полях. Приведены данные соответствующего расчета для атома водорода.

Ключевые слова: атом водорода, электрическое и магнитное поле, стандартная и операторная теория возмущений.

УДК 551.515.1

Г. С. Квасикова, Г. В. Ігнатенко, Т. О. Флорко, Д. Є. Сухарев, Ю. Г. Чернякова

ФОТОЕФЕКТ І СПЕКТРОСКОПІЯ АТОМУ ВОДНЮ У СХРЕЩЕНИХ ЕЛЕКТРИЧНОМУ ТА МАГНІТНОМУ ПОЛЯХ

Резюме

На підставі операторної теорії збурень розвинуто новий підхід до розрахунку енергій рівнів, ширин штарківських резонансів, а також ймовірностей радіаційних переходів між штарківськими підрівнями в спектрі атому у схрещених однорідних електричному та магнітному полях. Наведені данні відповідного розрахунку для атому водню.

Ключові слова: атом водню, електричне і магнітне поле, стандартна та операторна теорія збурень.

TECHNIQUE OF DETERMINATION OF MODULES TUBE DIAMETER AND POSSIBLE LENGTHENING OF OPTICAL CABLES CONSTRUCTION

In this work technique for determination of modules tube diameter and possible lengthening of optical cables construction is developed by dependence $\epsilon_c = f(d_{OM}, \Delta R, h)$ researching.

A variety of application areas of optical cables (OC) in systems of fiber optic communication requires the different constructions of cables are to be developed with the proper sizes and materials. Based on the design of optical modules (OM) with hollow shell (plastic tubes-shells with the optical fibres (OF) located in them), there must be selected the appropriate design of the cable core, intermediate shell, power elements, armor and protective hose in order to OF in these cables are not to be damaged due to environment, such as temperature variations and mechanical loading. This design should limit the OM minimum bend radius, tensile and compression OF, so that in a given range of tensile loads and temperature ranges in optic cables wouldn't occur either unacceptable changes in transmission characteristics or damage danger for optical fibers. As known, OF in a tube OM can move freely. In the unloaded state they are located in the center of tube OM (fig. 1) [1].

Free moving of OF is the result of its surplus length in OM. This surplus length of OF is needed for prevention of mechanical influence on OF at the longitudinal lengthening of optical cable, as for as by lengthening of elements of OC there occur the mechanical loadings which can be also applied to the optical fibre.

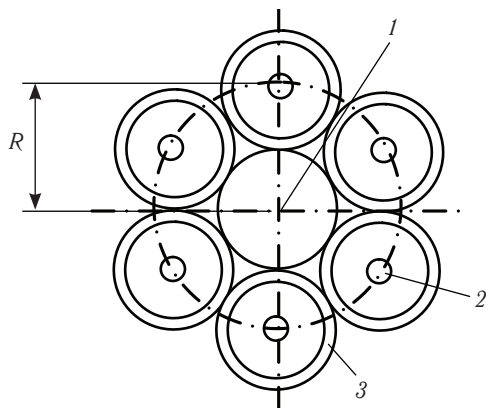


Figure 1. The provisions of OF in the box cover in the absence of tension: 1 — the central power element, 2 — OF, 3 — tube of OM

The size of OF surplus length, as well as the size of air-gap ΔR (fig. 2) between optical fibres, which are in OM centre and the internal surface of module wall determines the measure of lengthening of the whole OC ϵ_c . The size of air-gap ΔR , in its turn, depends on the amount of optical fibres n_{OF} and the diameter of OM, in where these OF are located. At diminishing of air-gap ΔR the limitation of free movement of OF appears in a tube OM, which diminishes the OC lengthening value. At the increase of air-gap all takes a vice versa place. In addition, the size of surplus length of OF in OC depends on the step of twisting of the optical modules h in its core. Consequently, for the optimum designing it is necessary to know the dependence $\epsilon_c = f(d_{OM}, \Delta R, h)$ of OC construction chosen for development.

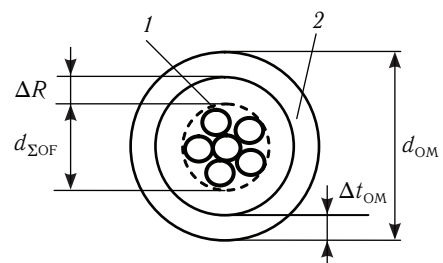


Figure 2. Optical fibres, freely entered into in the tube optical module: 1 — optical fibres, 2 — tube of OM

At present time the analysis of this dependence as well the technique of OM diameter determination are absent in the well-known researches on OC designing [2, 3, 4].

All of aforesaid creates, above all things, a necessity for researching of dependences between OF amount in OM, the OM diameter and the size of OC lengthening in the chosen model of cable construction.

As known, the calculation of possible cable lengthening ϵ_c , depending on the radius of layered OM in cables core, step of twisting OM in a core and value of air-gap between the wall of the module and all of OF, is possible to define with a formula [1]

$$\varepsilon_c = -1 + \sqrt{1 + \frac{4 \cdot \pi^2 \cdot R^2}{h^2} \cdot \left(\frac{2\Delta R}{R} - \frac{\Delta R^2}{R^2} \right)}, \quad (1)$$

Table 1

Values of coefficient k which takes into account the amount of elements in layered of OC

An amount of elements in layered	3	4	5	6	7	8	9	10	11	12
The value of coefficient k	1,155	1,414	1,701	2,000	2,305	2,613	2,924	3,236	3,549	3,864

where ε_c — is the possible lengthening of cable, for what OF loses freedom of moving in a tube OM, that is not yet subjected to the action of the tensile loading; R — is a radius of layer OM in cable core, mm; ΔR — is an air-gap between OF and internal wall of the optical module, mm; h — is a step of twisting of elements core round a central power element, mm.

The size of air-gap between internal wall surface of OM tube and all optical fibres which are placed in it, as it is evident from fig. 2, can be determined with the expression

$$\Delta R = \frac{d_{OM} - 2\Delta t_{OM} - d_{\Sigma OF}}{2}, \quad (2)$$

where ΔR — is an air-gap between the internal wall surface OM tube and all optical fibres, which are accommodated in OM, mm; d_{OM} — is an external OM diameter, mm; Δt_{OM} — is a wall thickness of OM tube, mm; $d_{\Sigma OF}$ — is a diameter of plait of optical fibres in OM, mm.

Radius of OM entering in OC core can be defined with the formula

$$R = \frac{d_{CPE} + d_{OM}}{2}, \quad (3)$$

where d_{CPE} — is a diameter of central power element of OC, mm.

The size of radius of OM entering, as is evident from (3), changes depending on the diameter of the module and diameter of CPE. The last, in its turn, in accordance with [4] depends on the amount of the optical modules in the first layered, that is on the model of cable construction chosen for the development. Taking into account aforesaid, the radius of OM entering in OC core in accordance with the amount of OM in the single-layered cable construction is possible to define with a formula

$$R = \frac{d_{OM}k}{2}, \quad (4)$$

where k — is a coefficient which takes into account the OM amount in the single-layered twisting of OC.

While following work [5] it is possible to define this coefficient for the different number of elements in layered of OC quitting directly proportional dependence d_{CPE} on d_{OM} (Table 4.2).

The results of calculation of coefficient k with the number of elements in layered of OC from 3 to 12 are given in Table 1.

Coming from Eq. (1), (2) and (4), taking into account all of aforesaid, it is possible to present the dependence between the value of OC lengthening, h , k , d_{OM} , Δt_{OM} and $d_{\Sigma OF}$, that is the amount of OF in the module tube.

$$\varepsilon_c = -1 + \sqrt{1 + \frac{4 \cdot \pi^2}{h^2} \cdot (d_{OM}k\Delta R - \Delta R^2)}. \quad (5)$$

From where

$$\varepsilon_c = -1 + \sqrt{1 + \left(\frac{2\pi}{h} \right)^2 \frac{d_{OM} - 2\Delta t_{OM} - d_{\Sigma OF}}{2} \cdot \left(d_{OM}k - \frac{d_{OM} - 2\Delta t_{OM} - d_{\Sigma OF}}{2} \right)}. \quad (6)$$

Coming from expression (6) the diameter of OM tube can be defined with expression

$$ad_{OM}^2 + bd_{OM} + c = 0, \quad (7)$$

where $a = (1 - 2p)(2p + 2k - 1)$, $b = 2d_{\Sigma OF} \times (1 - k - 2p)$, $c = (1 - (\varepsilon_c + 1)^2) \left(\frac{h}{\pi} \right)^2 - d_{\Sigma OF}^2$, d_{OM} — is a diameter of the optical module, mm; p — is a coefficient which takes into account the wall thickness of OM, $p = (0,15...0,2)$; k — is a coefficient which takes into account the amount of elements in to the single-layered cable; h — is a step of OM wring round a central power element (CPE), mm.

Thus, the determination of diameter of the optical module of OC requires:

— setting the construction model of single-layered cable, that is the number of OF, the number of elements in layered (OM, fillers), the step of twisting of elements around CPE, in thickness of OM tubes as well as lengthening of cable, because of which OF loses moving freedom in a tube, that is not yet subject to the action of the tensile loading.

Expression (7) shows by itself the affected quadratic, solving of which gives a value d_{OM} .

For determination of dependence $\varepsilon_c = f(d_{OM}, \Delta R, h)$ it is necessary to analyse the limits of legitimate values of each parameter that enters into Eq. (5), (6) and (7). Taking this into account, the parameters, which enters into (5), (6) and (7) have the following limits of the values in the constructions of modern cables (Table 2).

Table 2

Limits of legitimate values of h , d_{OM} , Δt_{OM}

Parameter	Limits of legitimate values
step of twisting h , mm	80...120
diameter OM d_{OM} , mm	1,8...3,0
thickness of wall of OM Δt_{OM} , mm	(0,15...0,20) d_{OM}
diameter of plait of OF $d_{\Sigma OF}$, mm	0,51...1,53
coefficient k	1,155...3,864

The wall thickness of optical module, as is evident from table 2, as a rule, makes (15...20) % of OM diameter. In this work for calculations of the multimodule OC constructions the thickness of module wall with diameter up to 3 mm was accepted 15 % and in cables with OM diameter over 3 mm — 20 %.

The diameter of plait of optical fibres is possible to define in OM, knowing the amount of OF in a central layer and amount of OF, that are placed in the first layer by analogy with the calculation of diameter of layered of pairs of electric cable [5].

So, in the center of plait of OF can be placed $n = (1...5)$ optical fibres. The diameter of central layer of OF at $n \neq 1$ is possible to define with a formula [5]






$$d_c = d_{OF} \left(1 + \frac{1}{\sin\left(\frac{\pi}{n_{OF}}\right)} \right), \quad (8)$$

where d_c — is a diameter of central layer of OF, mm; d_{OF} — is a diameter of OF, mm; n_{OF} — is an amount of OF.

An exception makes a case when $n_{OF} = 1$, then $d_c = d_{OF}$.

Knowing the amount of OF in the center of plait, it is possible to define their amount in next layers which are round the central layer of OF. So, if there is m of OF in the center of plait, there in accordance with the law of «correct» twisting will be $(m + 6)$ OF in

Table 3

Calculation of diameter of plait of $d_{\Sigma OF}$					
Amount of OF	General view of placing	Placing of OF is in a plait		Formula for calculation $d_{\Sigma OF}$	$d_{\Sigma OF}$, mm (for $d_{OF} = 255 \text{ mkm}$)
		in a center	in 1 layer		
2		2	—	$d_{OF} \left(1 + \frac{1}{\sin\left(\frac{\pi}{2}\right)} \right)$	0,510
4		4	—	$d_{OF} \left(1 + \frac{1}{\sin\left(\frac{\pi}{4}\right)} \right)$	0,615
6		1	5	$d_{OF} \left(1 + \frac{1}{\sin\left(\frac{\pi}{6}\right)} \right)$	0,765
12		3	9	$d_{OF} \left(3 + \frac{1}{\sin\left(\frac{\pi}{3}\right)} \right)$	1,059
16		5	11	$d_{OF} \left(3 + \frac{1}{\sin\left(\frac{\pi}{5}\right)} \right)$	1,199

a next layer, that is, in every next layer the amount of OF is to be increased on 6 comparatively with the previous one.

An exception is the first layer, if in the center of plait there is only one OF. Then, in the first layer the increase will be not 6, but 5 OF.

As known from [7, 8, 9, 10] and taking into account world experience of leading firms-producers of OC, OM can make a diameter from 1,8 to 3 mm, and the amount of OF, located in them, to 16 [11].

When using (8), the formulas for calculation of plait diameter of OF $d_{\Sigma OF}$ as well as its value at n_{OF} from 2 to 16 (Table 3) have been received.

As an example, while using (6), the calculations of possible lengthening of 6-element OC construction ϵ_c and the size of air-gap have been conducted between internal wall surface of OM tube and the plait of optical fibres from 2 to 16 and step of twisting $h = 100 \text{ mm}$ and $\Delta t_{OM} = 0,15 d_{OM}$ and set values d_{OM} , the results are shown at Table 4.

Table 4

The results of calculation of oc lengthening ϵ_c and size of air-gap between the internal wall surface of om tube and the plait of optical fibres

Amount of elements in the layer of OC construction	Amount of OF in a tube OM	Lengthening of OC ϵ_c , % (numerator) and air-gap ΔR , mm (denominator)				
		a diameter is OM, mm (numerator) wall thickness of tube Δt_{OM} , mm (denominator)				
		1,8 0,27	2,0 0,30	2,5 0,35	2,7 0,40	3,0 0,45
six	2	$\frac{0,238}{0,375}$	$\frac{0,312}{0,445}$	$\frac{0,553}{0,645}$	$\frac{0,643}{0,695}$	$\frac{0,813}{0,795}$
	4	$\frac{0,208}{0,323}$	$\frac{0,279}{0,392}$	$\frac{0,514}{0,593}$	$\frac{0,602}{0,643}$	$\frac{0,768}{0,743}$
	6	$\frac{0,164}{0,248}$	$\frac{0,231}{0,317}$	$\frac{0,457}{0,518}$	$\frac{0,540}{0,568}$	$\frac{0,700}{0,667}$
	12	$\frac{0,069}{0,101}$	$\frac{0,129}{0,170}$	$\frac{0,338}{0,371}$	$\frac{0,412}{0,421}$	$\frac{0,561}{0,521}$
	16	$\frac{0,021}{0,030}$	$\frac{0,077}{0,100}$	$\frac{0,278}{0,300}$	$\frac{0,349}{0,351}$	$\frac{0,492}{0,450}$

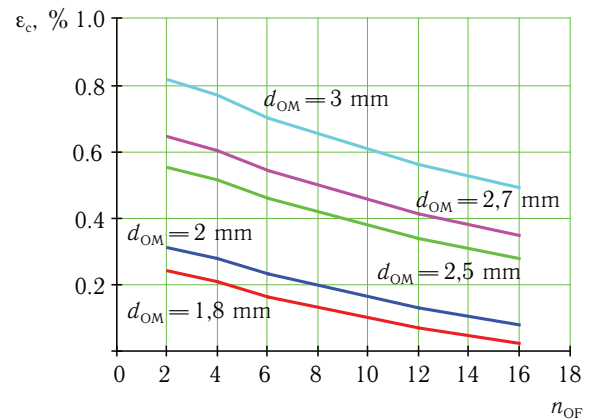


Figure 3. Dependence between possible lengthening of cable ϵ_c and amount of OF in OM for the 6-element construction of OC at the step of twisting $h = 100 \text{ mm}$, $\Delta t_{OM} = 0,15 d_{OM}$

Utilizing expression (7) there were conducted calculations d_{OM} of 6-element single-layered construction of OC at $h=100$ mm and $\Delta t_{OM}=0,15d_{OM}$ depending on the number of OF in the modules (from 2 to 16) and possible lengthenings of OC. Thus k got out from Table 1. The results are presented at fig 3.

CONCLUSION

The given technique of OM diameter determination depending on the amount of OF in the module allows to define the possible lengthening of OC in the construction of cable accepted for development.

The results of researches, executed in this work, have allowed to do the following conclusions:

1. The development of OC construction in order to provide stability of its transmission characteristics and resistibility to mechanical and temperature influences during laying and exploitation periods needs, above all things, choosing of cable core model, determination of tube diameter of optical module and possible lengthening of cable ϵ_c .

2. In this work the technique has been developed for d_{OM} and ϵ_c determination in accordance with characteristics of the chosen model of optical cable (h , n_{OB} , Δt_{OM} and k).

3. It is in-process set that the diameter of the optical module (7) depends on set possible lengthening of cable ϵ_c and characteristics of its construction (p , k , d_{OM} and h).

4. It is set on the example of 6-element single-layered construction of OC:

- the dependence of possible lengthening of cable $\epsilon_c = f(d_{OM}, n_{OF})$ on the diameter of the optical module and number of OF in the module (Table 1 and fig. 3) at the permanent values of step of unidirectional OM twisting round a central power element and thickness of tube of the optical module;

- the character of this dependence shows that with growth of d_{OM} and diminish-

ing of n_{OF} the possible lengthening of OC grows.

5. The developed technique of d_{OM} determination allows while designing of chosen OC model to calculate its geometrical sizes as well as the resistibility to tensile loading.

REFERENCES

1. Мальке Г. Волоконно-оптические кабели: Основы проектирования кабелей, планирование систем / Г. Мальке, П. Гессинг. — Новосибирск: Издатель, 1997. — 264 с.
2. Бондаренко О. В. Методика розрахунку модульної конструкції оптичного кабелю по розтягувальному зусиллю // Сборник научных трудов института проблем моделирования в энергетике им. Г. Е. Пухова НАН Украины. — 2009. — Вып. 54. — С. 31—34.
3. Бондаренко О. В. Розробка методу розрахунку стійкості діелектричних оптичних кабелів до розтягуючих навантажень // Наукові праці Донецького національного технічного університету. Серія: «Обчислювальна техніка та автоматизація». — 2009. — Вип. 17 (148). — С. 64—68.
4. Бондаренко О. В. Выбор конструкции самонесущего оптического кабеля по растягивающим нагрузкам / О. В. Бондаренко, Д. В. Иоргачев, Л. Л. Мурадян // Технология и конструирование в электронной аппаратуре. — 2001. — Вып. № 1. — С. 18—21.
5. Волоконно-оптические кабели. Теоретические основы, конструирование и расчет, технология производства и эксплуатация: монография / [Иоргачев Д. В., Бондаренко О. В., Дашенко А. Ф., Усов А. В.]. — Одесса: Астропринт, 2000. — 536 с.
6. Гроднев И. И., Курбатов Н. Д. Линейные сооружения связи. Учебник для вузов. Изд 3-е, дополненное и переработанное. — М.: Связь, 1974. — 544 с.
7. Каталог фирмы Corning, Fiber Optic Products Catalog, Япония. — Токио, 2004. — 247 с.
8. Каталог фирмы AFL Telecommunications, Fujikura Business, 2007. — 68 с.
9. Кабелі зв'язку оптичні для магістральних, зонних та міських мереж зв'язку. Технічні умови. ТУ У05758730.007-97:1997. — [Чинні від 1997-12-10]. — Одеса: УРУ Держстандарт. Одеський центр стандартизації і метрології, 1997. — 69 с.: табл. 12. — (Технічні умови ВАТ «Одескабель»). О. В. Бондаренко, В. Н. Кугот.
10. Кабелі оптичні для сільських мереж зв'язку. Технічні умови. ТУ У 05758730.008-98:1998. — [Чинні від 1998-04-01]. — Одеса. — УРУ Держстандарт. Одеський центр стандартизації і метрології 1998. — 56 с.: табл. 17. — (Технічні умови ВАТ «Одескабель»). О. В. Бондаренко, В. Ф. Трищенко.
11. Шарле Д. Л. Оптические кабели иностранного производства // Электросвязь. — 2001. — № 11. — С. 6—8.

UDC 621.315.2

O. V. Bondarenko, D. M. Stepanov, O. M. Stastchuk

TECHNIQUE OF DETERMINATION OF MODULES TUBE DIAMETER AND POSSIBLE LENGTHENING OF OPTICAL CABLES CONSTRUCTION

Abstract

In this work technique for determination of modules tube diameter and possible lengthening of optical cables construction is developed by dependence $\epsilon_c = f(d_{OM}, \Delta R, h)$ researching.

Keywords: mechanical loading, possible lengthening of optical cable, diameter of modules tube, plait of optical fibres.

УДК 621.315.2

О. В. Бондаренко, Д. М. Степанов, О. М. Стащук

МЕТОДИКА ВИЗНАЧЕННЯ ДІАМЕТРУ ТРУБКИ МОДУЛЯ ТА ДОПУСТИМОГО ВИДОВЖЕННЯ КОНСТРУКЦІЇ ОПТИЧНОГО КАБЕЛЮ

Анотація

В даній роботі розроблена методика визначення діаметру трубки оптичного модуля та допустимого видовження конструкції оптичного кабелю за допомогою дослідження залежності $\epsilon_k = f(d_{OM}, \Delta R, h)$.

Ключові слова: механічне навантаження, допустиме видовження оптичного кабелю, діаметр трубки модуля, джгут оптичних волокон.

УДК 621.315.2

О. В. Бондаренко, Д. Н. Степанов, О. М. Стащук

МЕТОДИКА ОПРЕДЕЛЕНИЯ ДИАМЕТРА ТРУБКИ МОДУЛЯ И ДОПУСТИМОГО УДЛИНЕНИЯ КОНСТРУКЦИИ ОПТИЧЕСКОГО КАБЕЛЯ

Аннотация

В данной работе разработана методика определения диаметра трубки оптического модуля и допустимого удлинения конструкции оптического кабеля с помощью исследования зависимости $\epsilon_k = f(d_{OM}, \Delta R, h)$.

Ключевые слова: механическая нагрузка, допустимое удлинение оптического кабеля, диаметр трубки модуля, джгут оптических волокон.

THE ELECTROSTATIC FIELD IN THE TWO-DIMENSIONAL REGION BETWEEN UNEVEN ELECTRODES

The problem of the static distribution of the potential ϕ of the electric field in vacuum in the two-dimensional region of space between two uneven electrodes is set and resolved. Their surface irregularities are modeled with the help of arbitrary periodic functions. The approximate solution of the Laplace's equation $\Delta\phi=0$ satisfying corresponding boundary conditions is found to the first order of smallness with respect to the magnitude of small surface irregularities of electrodes. The "theoretical" coordinate dependence of the potential ϕ within established accuracy agrees well with the corresponding "experimental" dependence, which is obtained by methods of computational modeling with the help of the program package "COMSOL Multiphysics" in the simple particular case of the "rectangular" irregularity. The corresponding distribution of the potential ϕ is depicted on the contour plot. In practice obtained results can be applied, in particular, when conductive probes of arbitrary form are placed on the even surface of the cathode at equal distances from each other, and, hence, have direct relevance to the area of scanning tunneling microscopy.

INTRODUCTION

It is well known that the electrostatic field in the two-dimensional region of space between two perfectly even infinite parallel electrodes, to which the voltage (the potential difference) U is applied, is homogenous and possesses the strength

$$\mathbf{E}_0 = (0, E_0), \quad E_0 = -\frac{U}{d}, \quad (1)$$

where d is the distance between considered electrodes, and the potential

$$\phi_0(z) = \frac{U}{d} z, \quad (2)$$

where the coordinate z corresponds to the direction, which is perpendicular to both of electrodes. Its value $z=0$ corresponds to the cathode and the value $z=d$ — to the anode. The subscript "0" indicates that the case of the perfectly even surface of both of electrodes is considered. Besides, it is supposed that the medium, confined between them, only slightly influences on quantities, describing the electric field, and this influence can be neglected, considering the distribution of the potential ϕ in vacuum. If desired the influence of the medium can be taken into account, introducing into denominators of fractions in formulas (1) and (2) the quantity ε — the relative permittivity of the medium.

The natural question arises, how formulas (1) and (2) for the strength \mathbf{E} and the potential ϕ of the considered electric field respectively alter, if surfaces of electrodes are not per-

fectly even. Irregularities, which are peculiar to any real surface, can be interpreted as small deviations of its shape from the flat one. In the analogous way in many cases one can interpret conductive probes of the arbitrary shape, placed on the even surface of the cathode at equal distances from each other [1]. Changing the shape and geometric sizes of probes, as well as the distance between them, one can achieve optimal relations when using them instead of the only one conductive tip in the scanning tunneling microscope and other analogous instruments with the purpose of the improvement of their work. Let us note that some of the latest articles in the area of scanning tunneling microscopy are devoted to carbon nanotubes [2] and graphene [3—7], that is one of the most perspective orientations of modern physics.

The article is constructed in the following way. At first we consider the case of arbitrary surface irregularities of both of electrodes and find in the first order approximation the explicit expression for the potential ϕ of the electric field between them. Then as an example we consider the simple particular case of the "rectangular" irregularity of the surface of the cathode, find in the same first order approximation explicit expressions for the potential ϕ and the component E_z of the strength \mathbf{E} along the direction, which is perpendicular to electrodes, and also graph corresponding contour plots, illustrating obtained formulas. Finally, we compare the "theoretical" dependence with the corresponding "experimental" one, obtained by methods of computational modeling with the help of the program package "COMSOL Multiphysics", and draw conclusions.

ARBITRARY IRREGULARITY

At first let us consider the case of the arbitrary irregularity. The potential $\varphi(x, z)$ of the electric field satisfies the two-dimensional Laplace's equation

$$\Delta_2 \varphi \equiv \frac{\partial^2 \varphi}{\partial x^2} + \frac{\partial^2 \varphi}{\partial z^2} = 0, \quad (3)$$

where $\Delta_2 \equiv \frac{\partial^2}{\partial x^2} + \frac{\partial^2}{\partial z^2}$ is the two-dimensional Laplace's operator, and following boundary conditions:

$$\varphi(x, a(x)) = 0, \quad \varphi(x, b(x)) = U, \quad (4)$$

where $a(x)$ and $b(x)$ are some functions, which define the shape of the surface of the cathode and the anode respectively and are supposed to be known. Thus, it is supposed that the potential, which equals 0, is applied to the cathode and the potential, which equals U , — to the anode. Their difference amounts to U .

The exact solution of the equation (3) with boundary conditions (4) is unknown to us, therefore let us look for its approximate solution in the form

$$\varphi(x, z) \approx \varphi_0(z) + \varphi_1(x, z), \quad (5)$$

where the function $\varphi_0(z)$ is defined by the formula (2) and the additional function $\varphi_1(x, z)$ takes into account the small deviation of the shape of the surface of both of electrodes from the flat one and is supposed to be the quantity of the first order of smallness with respect to this deviation. Thus, in the zero order approximation the potential $\varphi(x, z)$ is defined by the formula (2), corresponding to the case of perfectly even surfaces of both of electrodes, and in the first order approximation — by the formula (5). In the same approximation for functions $a(x)$ and $b(x)$ we obtain

$$\begin{aligned} a(x) &\approx a_0(x) + a_1(x) = a_1(x), \\ b(x) &\approx b_0(x) + b_1(x) = d + b_1(x), \end{aligned} \quad (6)$$

where functions $a_0(x) = 0$ and $b_0(x) = d$ define positions of the cathode and the anode respectively in the zero order approximation and additional functions $a_1(x)$ and $b_1(x)$ take into account their small deviations from values $z = 0$ and $z = d$ respectively and are supposed to be quantities of the first order of smallness with respect to these deviations.

Let us establish the explicit form of functions $a_1(x)$ and $b_1(x)$. Let us suppose that they are periodic with different periods $2l_1$ and $2l_2$ respectively, where l_1 and l_2 are arbitrary positive real numbers, then in accordance with they can be expanded into following Fourier series:

$$a_1(x) = \frac{A_0}{2} + \sum_{k=1}^{+\infty} \left[A_k \cos\left(\frac{k\pi}{l_1} x\right) + C_k \sin\left(\frac{k\pi}{l_1} x\right) \right], \quad (7)$$

$$b_1(x) = \frac{B_0}{2} + \sum_{k=1}^{+\infty} \left[B_k \cos\left(\frac{k\pi}{l_2} x\right) + D_k \sin\left(\frac{k\pi}{l_2} x\right) \right], \quad (8)$$

which coefficients can be found by corresponding well known formulas. They are quantities of the first order of smallness. If deviations of the shape of the surface of both of electrodes from the flat one were on average symmetric with respect to the coordinate z , then equalities

$$A_0 = 0, \quad B_0 = 0 \quad (9)$$

would hold. However, these deviations generally are not symmetric, since in any case there is the electrode itself on the one side from the surface and the medium, in which it is placed, from the other. In spite of this, by the appropriate choice of positions of electrodes one can always achieve fulfillment of equalities (9).

Substituting (5) into (3) and taking into account (2), we obtain the following Laplace's equation with regard to the function $\varphi_1(x, z)$:

$$\frac{\partial^2 \varphi_1}{\partial x^2} + \frac{\partial^2 \varphi_1}{\partial z^2} = 0. \quad (10)$$

Substituting (5) into (4) and taking into account (2), we obtain

$$\begin{aligned} \frac{U}{d} a(x) + \varphi_1(x, a(x)) &\approx 0, \\ \frac{U}{d} b(x) + \varphi_1(x, b(x)) &\approx U. \end{aligned} \quad (11)$$

From (11) in the same first order approximation we obtain

$$\begin{aligned} \frac{U}{d} a_1(x) + \varphi_1(x, 0) &= 0, \\ \frac{U}{d} b_1(x) + \varphi_1(x, d) &= 0. \end{aligned} \quad (12)$$

Thus, the function $\varphi_1(x, z)$ satisfies the Laplace's equation (10) and boundary conditions (12). The set problem permits of the exact solution. Finding it and substituting the obtained expression and (2) into (5), in the first order approximation we finally obtain

$$\begin{aligned} \varphi(x, z) &\approx \frac{U}{d} z + \\ &+ \frac{U}{d} \sum_{k=1}^{+\infty} \frac{1}{\sinh\left(\frac{k\pi}{l_1} d\right)} \left[A_k \cos\left(\frac{k\pi}{l_1} x\right) + C_k \sin\left(\frac{k\pi}{l_1} x\right) \right] \sinh\left[\frac{k\pi}{l_1} (z - d)\right] - \\ &- \frac{U}{d} \sum_{k=1}^{+\infty} \frac{1}{\sinh\left(\frac{k\pi}{l_2} z\right)} \left[B_k \cos\left(\frac{k\pi}{l_2} x\right) + D_k \sin\left(\frac{k\pi}{l_2} x\right) \right] \sinh\left(\frac{k\pi}{l_2} z\right). \end{aligned} \quad (13)$$

"RECTANGULAR" IRREGULARITY

As an example let us consider the case of the "rectangular" surface irregularity of the

cathode. Deviations of the shape of the surface of electrodes from the flat one in this case is described by following functions:

$$a_1(x) = \begin{cases} h, & |x| < r \\ -h', & r < |x| < l_1 \end{cases}, \quad (14)$$

$$b_1(x) = 0, \quad (15)$$

where h , h' and r are positive real numbers, $r < l_1$, h and h' are connected by the relation

$$hr = h'(l_1 - r), \quad h' = \frac{r}{l_1 - r}h, \quad (16)$$

ensuring the fulfillment of the first equality (9). The graph of the function (14) when $x \in [-l_1, l_1]$ and $h = 0.1$ cm, $r = 0.1$ cm, $l_1 = 1$ cm is shown on fig. 1.

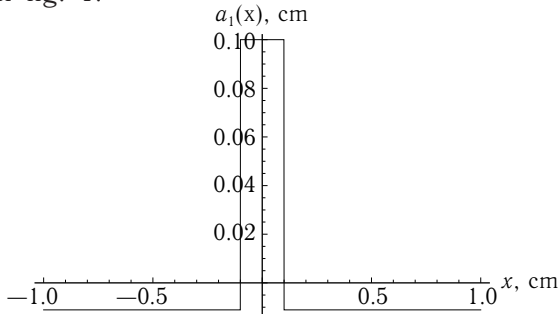


Fig. 1. The graph of the function (14) when $x \in [-l_1, l_1]$ and $h = 0.1$ cm, $r = 0.1$ cm, $l_1 = 1$ cm

Expanding functions (14) and (15) into Fourier series (7) and (8) and substituting coefficients of obtained expansions into (13), we obtain

$$\begin{aligned} \varphi(x, z) \approx & \frac{U}{d}z + \frac{2Uh_1}{\pi d(l_1 - r)} \times \\ & \times \sum_{k=1}^{+\infty} \frac{\sin\left(\frac{k\pi}{l_1}r\right)}{k \sinh\left(\frac{k\pi}{l_1}d\right)} \cos\left(\frac{k\pi}{l_1}x\right) \sinh\left[\frac{k\pi}{l_1}(z - d)\right]. \end{aligned} \quad (17)$$

Obtained function (17) corresponds to the “rectangular” surface irregularity of the cathode. When $h = 0.1$ cm, $r = 0.1$ cm, $l_1 = 1$ cm, $d = 1$ cm, $U = 1$ V from (17) we obtain

$$\begin{aligned} \varphi(x, z) \approx & z + \\ & + \frac{2}{9\pi} \sum_{k=1}^{+\infty} \frac{\sin(0.1k\pi)}{k \sinh(k\pi)} \cos(k\pi x) \sinh[k\pi(z - 1)], \end{aligned} \quad (18)$$

where coordinates x and z are measured in centimeters and the potential φ — in volts. The contour plot of the function (18) when $x \in [-0.5, 0.5]$ and $z \in [0.1, 0.5]$ is shown on fig. 2.

From (17) we obtain in the first order approximation the following expression for the component E_z of the strength \mathbf{E} of the considered electric field along the direction, which is perpendicular to both of electrodes:

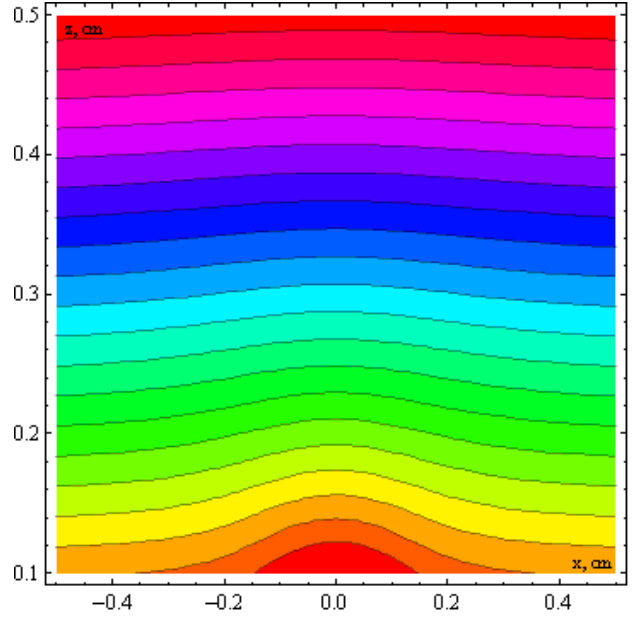


Fig. 2. The contour plot of the function (18) when $x \in [-0.5, 0.5]$ and $z \in [0.1, 0.5]$

$$\begin{aligned} E_z(x, z) = & -\frac{\partial\varphi}{\partial z} \approx -\frac{U}{d} - \frac{2Uh}{d(l_1 - r)} \times \\ & \times \sum_{k=1}^{+\infty} \frac{\sin\left(\frac{k\pi}{l_1}r\right)}{\sinh\left(\frac{k\pi}{l_1}d\right)} \cos\left(\frac{k\pi}{l_1}x\right) \cosh\left[\frac{k\pi}{l_1}(z - d)\right]. \end{aligned} \quad (19)$$

When $h = 0.1$ cm, $r = 0.1$ cm, $l_1 = 1$ cm, $d = 1$ cm, $U = 1$ V from (19) we obtain

$$\begin{aligned} E_z(x, z) \approx & -1 - \frac{2}{9} \times \\ & \times \sum_{k=1}^{+\infty} \frac{\sin(0.1k\pi)}{\sinh(k\pi)} \cos(k\pi x) \cosh[k\pi(z - 1)], \end{aligned} \quad (20)$$

where coordinates x and z are measured in centimeters and the quantity E_z — in volts per centimeter. The contour plot of the function (20) when $x \in [-1, 1]$ and $z \in [0.1, 1]$ is shown on fig. 3.

When $x = 0$ from (20) we obtain

$$E_z(0, z) \approx -1 - \frac{2}{9} \sum_{k=1}^{+\infty} \frac{\sin(0.1k\pi)}{\sinh(k\pi)} \cosh[k\pi(z - 1)]. \quad (21)$$

The graph of the function (21) when $z \in [0.1, 1]$ is shown on fig. 4.

Thus, on fig. 4 the “theoretical” dependence of the function $E_z(0, z)$ on the variable z is depicted. Its comparison with the corresponding “experimental” dependence, which is obtained by methods of computational modeling with the help of the program package “COMSOL Multiphysics” and depicted on fig. 5, shows that within established accuracy they agree well with each other.

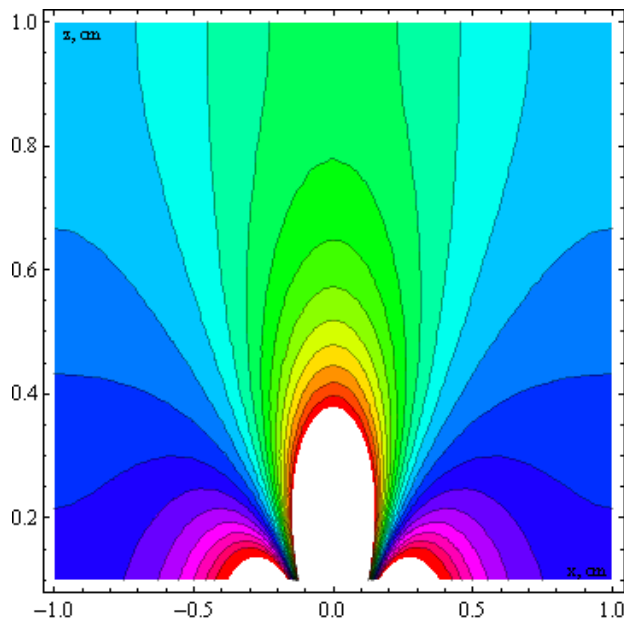


Fig. 3. The contour plot of the function (20) when $x \in [-1, 1]$ and $z \in [0.1, 1]$

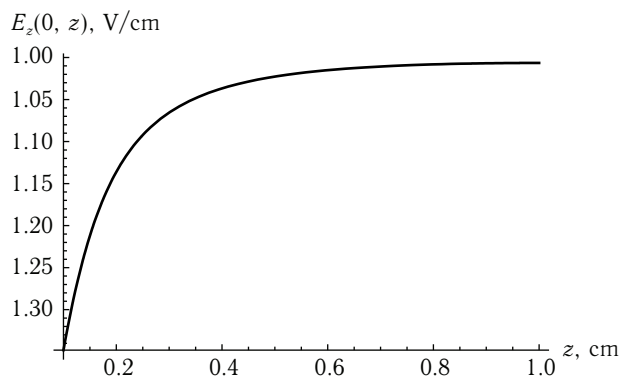


Fig. 4. The graph of the function (21) when $z \in [0.1, 1]$

CONCLUSIONS

Obtained results allow to draw following conclusions:

1. The problem of the static distribution of the potential ϕ of the electric field in vacuum in the two-dimensional region of space between two uneven electrodes is set and resolved in the first order approximation.

2. The simple particular case of the “rectangular” irregularity of the surface of the cathode is considered and explicit expressions for the potential ϕ and the component E_z of the strength \mathbf{E} along the direction, which is perpendicular to electrodes, are found in the first order approximation.

3. Contour plots, illustrating obtained formulas, are graphed and it is shown that the “theoretical” coordinate dependence within established accuracy agrees well with the corre-

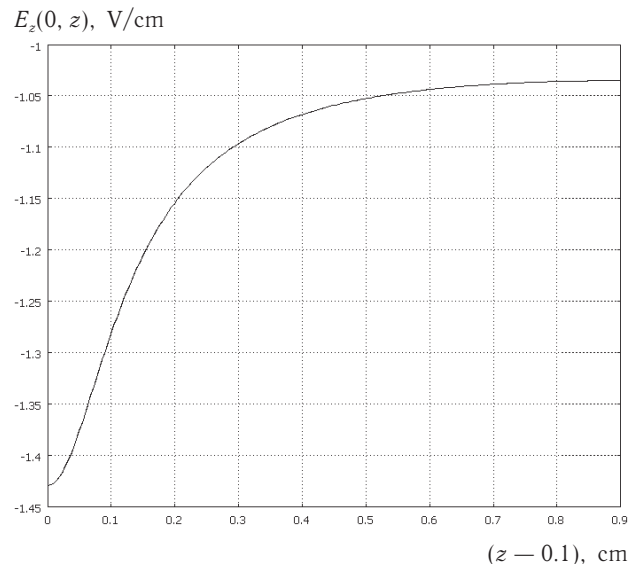


Fig. 5. The graph of the function $E_z(0, z)$ of the variable $(z - 0.1)$ when $z \in [0.1, 1]$, obtained by methods of computational modeling with the help of the program package “COMSOL Multiphysics”

sponding “experimental” dependence, which is obtained by methods of computational modeling with the help of the program package “COMSOL Multiphysics”.

4. In practice obtained results can be applied, in particular, when conductive probes of arbitrary form are placed on the even surface of the cathode at equal distances from each other, and have direct relevance to the area of scanning tunneling microscopy.

REFERENCES

1. И. П. Верещагин, В. И. Левитов, Г. З. Мурзабекян, М. М. Пашин, Основы электрогазодинамики дисперсных систем. — М.: Энергия, 1999. — 480 с.
2. P. Nemes-Incze, Z. Köny, I. Kiricsi, Á. Pekker, Z. E. Horváth, K. Kamarás, L. P. Biró, Mapping of functionalized regions on carbon nanotubes by scanning tunneling microscopy // arXiv: 1009.1290v1.
3. Shyam K. Choudhary, Anjan K. Gupta, Scanning Tunneling Microscopy and Spectroscopy study of charge inhomogeneities in bilayer Graphene. // arXiv: 1007.4417v1.
4. Mayu Yamamoto, Seiji Obata, Koichiro Saiki, Structure and properties of chemically prepared nanographene islands characterized by scanning tunneling microscopy // arXiv: 1006.2654v1.
5. V. Geringer, D. Subramaniam, A. K. Michel, B. Szafraniek, D. Schall, A. Georgi, T. Mashoff, D. Neumaier, M. Liebmann, M. Morgenstern, Electrical transport and low-temperature scanning tunneling microscopy of micro-soldered graphene. // Appl. Phys. Lett. — 2010. — Vol. 96, 082114; arXiv: 0912.2218v1.
6. F. Hiebel, P. Mallet, L. Magaud, J.-Y. Veuillen, Atomic and electronic structure of monolayer graphene on 6H-SiC(000-1)(3 x 3): a scanning tunneling microscopy study. // Phys. Rev. B — 2009. — Vol. 80, 235429; arXiv: 0912.0810v1.
7. N. M. R. Peres, Shan-Wen Tsai, J. E. Santos, R. M. Ribeiro, Scanning Tunneling Microscopy currents on locally disordered graphene. // Phys. Rev. B — 2009. — Vol. 79, 155442; arXiv: 0904.3189v1.

THE ELECTROSTATIC FIELD IN THE TWO-DIMENSIONAL REGION BETWEEN UNEVEN ELECTRODES

Abstract

The problem of the static distribution of the potential ϕ of the electric field in vacuum in the two-dimensional region of space between two uneven electrodes is set and resolved. Their surface irregularities are modeled with the help of arbitrary periodic functions. The approximate solution of the Laplace's equation $\Delta\phi = 0$ satisfying corresponding boundary conditions is found to the first order of smallness with respect to the magnitude of small surface irregularities of electrodes. The "theoretical" coordinate dependence of the potential ϕ within established accuracy agrees well with the corresponding "experimental" dependence, which is obtained by methods of computational modeling with the help of the program package "COMSOL Multiphysics" in the simple particular case of the "rectangular" irregularity. The corresponding distribution of the potential ϕ is depicted on the contour plot. In practice obtained results can be applied, in particular, when conductive probes of arbitrary form are placed on the even surface of the cathode at equal distances from each other, and, hence, have direct relevance to the area of scanning tunneling microscopy.

Key words: electric field, two-dimensional region, electrode.

ЭЛЕКТРОСТАТИЧЕСКОЕ ПОЛЕ В ДВУМЕРНОЙ ОБЛАСТИ МЕЖДУ НЕРОВНЫМИ ЭЛЕКТРОДАМИ

Резюме

Поставлена и решена задача о статическом распределении потенциала ϕ электрического поля в вакууме в двумерной области пространства между двумя неровными электродами. Неровности их поверхностей смоделированы с помощью произвольных периодических функций. Найдено приближенное решение уравнения Лапласа $\Delta\phi = 0$, удовлетворяющее соответствующим граничным условиям, с точностью до первого порядка малости по величине малых неровностей поверхностей электродов. "Теоретическая" зависимость потенциала ϕ от координат в пределах установленной точности хорошо согласуется с соответствующей "экспериментальной" зависимостью, которая получена методами численного моделирования с помощью программного пакета "COMSOL Multiphysics" в простом частном случае "прямоугольной" неровности. Соответствующее распределение потенциала ϕ изображено на контурном графике. На практике полученные результаты могут быть применены, в частности, когда на ровной поверхности катода на равных расстояниях друг от друга установлены проводящие зонды произвольной формы, и, следовательно, имеют прямое отношение к области сканирующей туннельной микроскопии.

Ключевые слова: электрическое поле, двумерная область, электрод.

ЕЛЕКТРОСТАТИЧНЕ ПОЛЕ У ДВОВИМІРНІЙ ОБЛАСТІ МІЖ НЕРІВНИМИ ЕЛЕКТРОДАМИ

Резюме

Поставлена та розв'язана задача про статичний розподіл потенціалу ϕ електричного поля у вакуумі у двовимірній області простору між двома нерівними електродами. Нерівності їх поверхонь змодельовані за допомогою довільних періодичних функцій. Знайдено наближений розв'язок рівняння Лапласа $\Delta\phi = 0$, який задовільняє відповідним граничним умовам, з точністю до першого порядку малості по величині малих нерівностей поверхонь електродів. "Теоретична" залежність потенціалу ϕ від координат у межах встановленої точності добре узгоджується із відповідною "експериментальною" залежністю, яка отримана методами чисельного моделювання за допомогою програмного пакету "COMSOL Multiphysics" у простому окремому випадку "прямокутної" нерівності. Відповідний розподіл потенціалу ϕ зображено на контурному графіку. На практиці отримані результати можуть бути застосовані, зокрема, коли на рівній поверхні катода на рівних відстанях один від одного встановлені провідні зонди довільної форми і, отже, мають пряме відношення до області скануючої тунельної мікроскопії.

Ключові слова: електричне поле, двовимірна область, електрод.

SATURATION CURRENT OF THE THERMOSENSITIVE FIELD FIELD-EFFECT TRANSISTORS UNDER β -IRRADIATION

The influence of β -irradiation on the saturation current of the thermosensitivity of FET has been investigated. It was shown that the change current saturation started from the electron flux $F_e > 10^{13} \text{ cm}^{-2}$ with energy of 1 MeV. The influence of these factors leads to averaging of thermosensitivity.

It is known that transistors are devices useful for temperature sensors [1]. Investigation of thermosensitive properties of field-effect transistor (FET) is rather actual. Study and control of the temperature dependence of saturation current allow to developing temperature sensors with current and potential gate and current stabilization devices with controlled temperature coefficient of output current. Now a days, there is no information of the influence of radiation treatment to thermosensitive properties of FET. At the same time high sensitivity of semiconductor materials and devices to radiation and wide use of microelectronic temperature sensors made this problem as one of actual. In the present work radiation treatment effects on saturation current of thermosensitive FET in passive regime has been investigated.

The influence of radiation treatment on saturation current of FET with p - n junction and MIS transistors with internal channel is determined by the change of bulk resistance of the channel as result of defect formation after radiation treatment. In bipolar connection of FET the changes of saturation drain current (the gate is connected with source) $I_{d, \text{sat}}$ under irradiation don't depend on the life time of minority charge carriers, but are defined by the changes of their concentration and mobility. Therefore, they are less affected by radiation than bipolar transistors. The change of saturation drain current can be described by following equation [2]:

$$\frac{I_{d, \text{sat}, \text{ph}}}{I_{d, \text{sat}, 0}} \approx \exp(-2K_p F_n),$$

where $I_{d, \text{sat}, 0}$ — the saturation current before treatment, $I_{d, \text{sat}, \text{ph}}$ — the saturation current after treatment, K_p — coefficient of conductivity channel change, F_n — neutrons flux. In fig. 1 the calculated dependences of saturation current on neutron flux under different dopant concentrations in conductivity channel are shown.

To investigate the influence of radiation treatment on saturation current 2P202G transis-

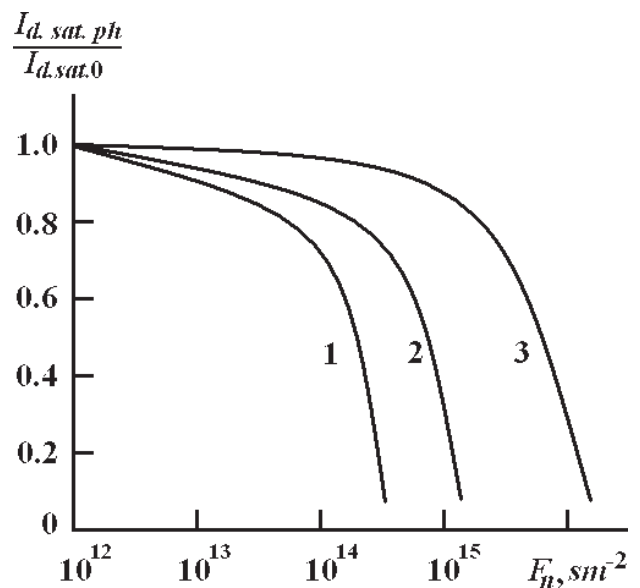


Fig. 1. Theoretical values of saturation current changes. Dopant concentration in channel: 1 — $5 \cdot 10^{15} \text{ cm}^{-3}$, 2 — 10^{16} cm^{-3} , 3 — 10^{17} cm^{-3}

tors were used. After measurements of $I_{d, \text{sat}, 0}$ at $T = 293 \text{ K}$, they have been split on 14 groups with 3 samples in the group. All samples were treated only with one kind of radiation and one intensity. The electron flux F_e had different values: 10^{13} , 10^{14} , $5 \cdot 10^{14}$, 10^{15} , $5 \cdot 10^{15} \text{ cm}^{-2}$ with energy 5 MeV. The measurements were provided on linear accelerator 'Electronica'. The influence of γ -radiation with energy 1 MeV and exposition dose D_γ 10^6 , 10^7 , $3 \cdot 10^7$, $6 \cdot 10^7$, $3 \cdot 10^8 \text{ R}$ was studied on K100000 setup and neutron treatment was provided on reactor VVP-M with neutron flux F_n 10^{13} , $5 \cdot 10^{13}$, 10^{14} , $5 \cdot 10^{14} \text{ cm}^{-2}$ and energy 1.1 MeV.

The radiation treatment was estimated as the changes of saturation current before and after exposition. The results of radiation effects on $I_{d, \text{sat}, 0}$ of FET are shown in fig. 2. As one can see from the curves the experimental data has good correlation with theoretical calculations.

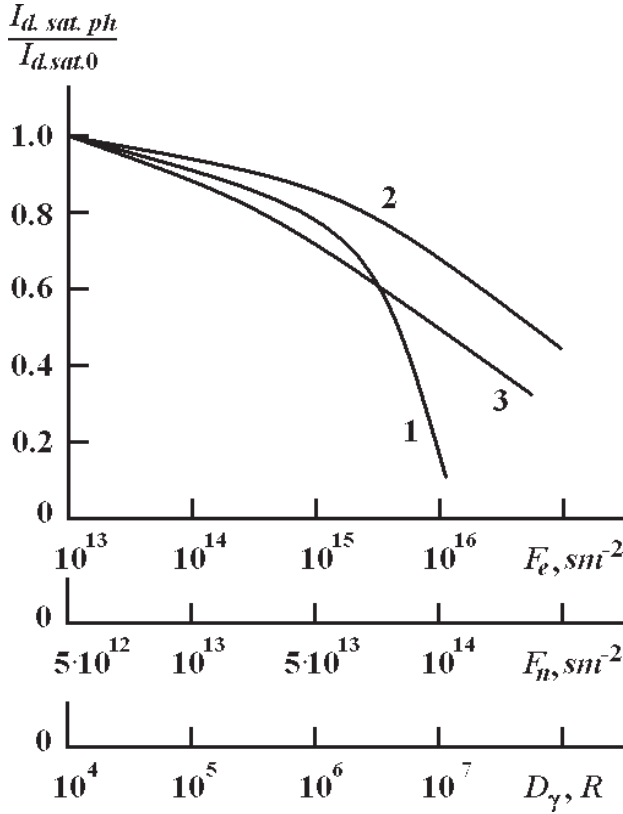


Fig. 2. Saturation current changes under different radiation exposure: electron flux (1), neutron flux (2), γ -radiation (3)

The bridge scheme, consisted of 4 FET, has been used to investigate thermosensitivity of the FET ($\Delta I_{d,sat,0}/\Delta T$). The samples were connected in pairs into diagonal parts of the scheme and then kept into thermostat. At $T=293$ K and $T=303$ K the disbalance of the bridge scheme was measured and the thermosensitivity of the samples was calculated. Then, the samples were exposed to γ -radiation, neutron and electron fluxes and thermosensitivity of the samples was measured again. The annealing of the sample was kept at $T=425$ K during 1 hour. The thermosensitivity of annealed samples was measured under the above mentioned scheme. All results are presented in Table 1.

From the table 1 the one can see that radiation treatment leads to the increase of thermosensitivity and averaging of its value between the samples from different groups. Thus, transistors with high thermosensitivity increased it after lower exposure times than transistors with lower thermosensitivity. The clear dependence of thermosensitivity on radiation level was not revealed. Annealing procedure didn't show the same influence on thermosensitivity changes as well.

The changes of MIS-transistors parameters under irradiation resulted from radioactive defects in dielectric and on dielectric-semiconductor boundary [3]. Under irradiation exposure positive charge is formed in dielectric of MIS structure, which is collected close to dielectric-semiconductor boundary under positive gate potential and to dielectric-metal boundary under

Number of sample	Thermosensitivity $\Delta U/\Delta T$, mV/K			Type of irradiation and doze
	Before radiation treatment	After radiation treatment	After annealing	
1 2	75 25	227 360	383 496	γ -quants $D_\gamma = 3 \cdot 10^7$ R
3 4	83.5 25	265 216	144 186	γ -quants $D_\gamma = 3 \cdot 10^7$ R
5 6	41.5 133	242 148	352 156	γ -quants $D_\gamma = 3 \cdot 10^8$ R
7 8	58.4 83.5	155 230	146 183	electrons $F_e = 10^{14}$ cm $^{-2}$
9 10	66.6 66.6	177 108	176 167	electrons $F_e = 5 \cdot 10^{14}$ cm $^{-2}$
11 12	31.6 41.6	78 177	183 188	electrons $F_e = 10^{15}$ cm $^{-2}$
13 14	12.5 25	62 102	87 114	electrons $F_e = 5 \cdot 10^{15}$ cm $^{-2}$
15 16	41.6 83.5	158 107	181 113	neutrons $F_n = 5 \cdot 10^{13}$ cm $^{-2}$
17 18	75 66.6	161 455	134 436	neutrons $F_n = 10^{14}$ cm $^{-2}$
19 20	83.5 29.2	159 161	140 161	neutrons $F_n = 5 \cdot 10^{14}$ cm $^{-2}$

negative gate potential. The influence of positive charge is stronger in case it is located close to semiconductor surface, what is seen under positive gate potential. Degradation of MIS-transistors at this type of connection is much higher than at other kinds of commutation. Influence of collected positive charge appears in changes of gate voltage threshold $U_{g,th}$, what leads to the saturation current changes. The change of $U_{g,th}$ dependently on radiation doze is much drastically in case of sub gate dielectric, grown in dry air atmosphere [2].

Sensitivity of MIS transistors to radiation increases with the enhance of gate thickness of metallic layer but doesn't depend on Si conductivity type and its dopant content [4]. Degradation of MIS transistors has stable behavior and relies on radiation influence, which has no enough energy to form structural disorders. At room temperatures $I_{d,sat,ph}$ and other parameters can not be restored and to restore it the additional annealing at $T \geq 620$ K is needed.

At the present time there are only few theories, which explain the main experimental results on radiation effects in MIS transistors. However, numerical relations for saturation current and radiation factors are absent.

For experiments KP305 MIS transistors have been used. Thermosensitivity tests under γ -radiation with energy 5 MeV were performed. Saturation current was measured at $T=273$ K and at $T=333$ K. The obtained results are shown in Table 2. It can be seen from the table that exposure dose $D_\gamma < 10^6$ R led to the increase of the saturation current. The doze

Table 2

Parameters values						D_γ , R
Before radiation treatment			After radiation treatment			
$I_{d, sat, 0}$, μA		$\Delta I_{d, sat, 0}/\Delta T$, $\mu A/K$	$I_{d, sat, ph}$, μA		$\Delta I_{d, sat, ph}/\Delta T$, $\mu A/K$	
$T = 273$ K	$T = 333$ K		$T = 273$ K	$T = 333$ K		
4720	4982	4.36	6881	6939	0.9	10^4
1192	12439	8.5	13393	13983	9.8	10^4
11.2	59.6	0.8	19.5	263.4	4.1	10^4
15.6	84.3	1.1	21.4	313.8	4.9	10^5
4137	4161	0.4	6851	7230	6.3	10^5
5077	4925	— 2.5	5857	6290	7.1	10^5
1.38	25.1	0.4	17.4	189	2.9	10^6
3397	3819	7.1	475	1091	10.3	10^6
5050	5300	— 10.9	33.4	342.1	5.2	10^6
6.48	71.5	1.1	22.4	291.3	4.5	10^7
3.719	4.448	12.2	49.8	579	8.8	10^7
4.698	4.864	2.8	81.5	81.5	642	10^7
43.4	128.3	1.4	58.9	603.7	9.1	10^8
4664	4433	-3.8	32.2	439	6.8	10^8
3894	4235	5.5	29.8	415.7	6.4	10^8

$D_\gamma < 10^6$ R led to averaging $I_{d, sat, ph}$ values to narrow region. As result $I_{d, sat, ph}$ of MIS transistors after γ -radiation treatment with $D_\gamma = (10^6 - 10^8)$ R had valued from the region 17—475 μA at $T = 373$ K, but before exposure the values lied in the region of 1—5000 μA . Investigation of stability of radiated samples showed that $I_{d, sat, ph}$ value had no changes within few months. Annealing at $T \approx 400$ K within 3 hours didn't have any influence to $I_{d, sat, ph}$.

Besides the development of restore $I_{d, sat, ph}$ value, γ -radiation influence with $D_\gamma = (10^6 - 10^8)$ R leads also to averaging of thermosensitivity values. Before exposure $\Delta I_{d, sat, 0}/\Delta T$ values were in the range of $-10.9 - +12.2$ $\mu A/K$ but after γ -radiation treatment with $D_\gamma = (10^6 - 10^8)$ R this region narrowed to 2.9...10.3 $\mu A/K$.

Investigation of γ -radiation influence on $I_{d, sat, 0}$ of another MIS transistors showed results similar to the present work data. Analysis of the results points to the fact that γ -radiation $D_\gamma = (10^6 - 10^7)$ R with energy 1.25 MeV leads to good repeatability of saturation current of MIS transistors. Under γ -radiation $D_\gamma < 10^6$ R repeatability of $I_{d, sat, ph}$ and $\Delta I_{d, sat, 0}/\Delta T$ decreases.

Under γ -radiation $D_\gamma > 10^6$ R repeatability of $I_{d, sat, ph}$ and $\Delta I_{d, sat, 0}/\Delta T$ doesn't improve.

On the basis of the results the method to fabrication of MIS transistors was proposed. It is based on radiation treatment of the MIS structures by γ -radiation $D_\gamma = (10^6 - 10^7)$ R. It improves repeatability of $I_{d, sat, 0}$. This method can be used to form photosensitive MIS transistors.

It was shown, that the change of $I_{d, sat, 0}$ starts with electron flux of $F_e \geq 10^{13}$ cm^{-2} with energy 5 MeV, γ -radiation $D_\gamma > 10^5$ R with energy 1.26 MeV, neutron flux $\dot{F}_n \geq 5 \cdot 10^{12}$ cm^{-2} with energy 1 MeV. These factors with high intensity lead to averaging of thermosensitivity.

REFERENCES

1. Датчики. В. М. Шарапов, Е. С. Полищук, Г. Г. Ишанин и др. — Киев: Брама, 2008. — С. 430.
2. Действие проникающей радиации на изделия электронной техники. В. М. Кулаков, Е. А. Ладыгин, В. И. Шаховцов и др., под ред. Е. А. Ладыгина. — М.: Радио и связь, 2001. — С. 135.
3. Вавилов В. С., Ухин Н. А. Радиационные эффекты в полупроводниках и полупроводниковых приборах. — М.: Атомиздат, 2002. — С. 168.
4. Zaininger K. H. Electrical properties of electron bombardment MOS-structures // IEEE Trans. — 2006. — V. 16. — N. 6. — P. 146—148.

UDC 621.315.592

Sh. D. Kurmashev, I. M. Vikulin, A. I. Nimtsovich

SATURATION CURRENT OF THE THERMOSENSITIVE FIELD FIELD-EFFECT TRANSISTORS UNDER β -IRRADIATION

Abstract

The influence of β -radiation treatment to saturation current of thermosensitivity of field-effect transistors has been investigated. It was shown that the change current saturation started from the electron flux $F_e > 10^{13}$ cm^{-2} with energy of 1 MeV. The influence of these factors leads to averaging of thermosensitivity.

Key words: saturation current, transistors, thermosensitivity.

УДК 621.315.592

Ш. Д. Курмашев, И. М. Викулин, А. И. Нимцович

ТОК НАСЫЩЕНИЯ ТЕРМОЧУВСТВИТЕЛЬНЫХ ПОЛЕВЫХ ТРАНЗИСТОРОВ ПРИ ДЕЙСТВИИ РАДИАЦИИ

Резюме

Изучено влияние облучения в пассивном режиме на ток насыщения и термочувствительность полевых транзисторов. Показано, что изменение тока насыщения начинается при воздействии потока электронов $F_e \geq 10^{13} \text{ см}^{-2}$ энергией 5 МэВ, γ -квантов экспозиционной дозой $D_\gamma > 10^5 \text{ Р}$ энергией 1.26 МэВ, потока нейтронов $F_n \geq 5 \cdot 10^{12} \text{ см}^{-2}$ энергией 1 МэВ. Воздействие указанных факторов большой интенсивности приводит к усреднению значений термочувствительности.

Ключевые слова: ток насыщения, транзистор, термочувствительность.

УДК 621.315.592

Ш. Д. Курмашев, І. М. Вікулін, А. І. Німцович

СТРУМ НАСИЧЕННЯ ТЕРМОЧУТЛИВИХ ПОЛЬОВИХ ТРАНЗИСТОРІВ ПІД ВПЛИВОМ РАДІАЦІЇ

Резюме

Вивчено вплив опромінювання у пасивному режимі на струм насичення і термочуйливість польових транзисторів. Доведено, що зміна току насичення починається при впливі потоку електронів $F_e \geq 10^{13} \text{ см}^{-2}$ енергією 5 МеВ, γ -квантів експозиційною дозою $D_\gamma > 10^5 \text{ Р}$ енергією 1.26 МеВ, потоку нейтронів $F_n \geq 5 \cdot 10^{12} \text{ см}^{-2}$ енергією 1 МеВ.

Вплив вказаних факторів великої інтенсивності приводить до усереднення значень термочутливості.

Ключові слова: струм насичення, транзистор, термочутливість.

SPECTROSCOPY OF AUTOIONIZATION RESONANCES IN SPECTRA OF THE LANTHANIDES ATOMS

We applied the generalized energy approach (Gell-Mann and Low S-matrix formalism) to studying the autoionization resonances in heavy atoms, in particular, firstly predicted parameters for the Yb autoionization resonances with accounting for exchange-correlation and relativistic effects.

Traditionally an investigation of spectra, spectral, radiative and autoionization characteristics for heavy and superheavy elements atoms and multicharged ions is of a great interest for further development atomic and nuclear theories and different applications in the plasma chemistry, astrophysics, laser physics, etc. (see Refs. [1–10]). Theoretical methods of calculation of the spectroscopic characteristics for heavy atoms and ions may be divided into a few main groups [1–6]. First, the well known, classical multi-configuration Hartree–Fock method (as a rule, the relativistic effects are taken into account in the Pauli approximation or Breit hamiltonian etc.) allowed to get a great number of the useful spectral information about light and not heavy atomic systems, but in fact it provides only qualitative description of spectra of the heavy and superheavy ions. Second, the multi-configuration Dirac–Fock (MCDF) method is the most reliable version of calculation for multielectron systems with a large nuclear charge. In these calculations the one- and two-particle relativistic effects are taken into account practically precisely. In this essence it should be given special attention to two very general and important computer systems for relativistic and QED calculations of atomic and molecular properties developed in the Oxford group and known as GRASP (“GRASP”, “Dirac”; “BERTHA”, “QED”) (look [1–5] and references there). In particular, the BERTHA program embodies a new formulation of relativistic molecular structure theory within the framework of relativistic QED. This leads to a simple and transparent formulation of Dirac–Hartree–Fock–Breit (DHFB) self-consistent field equations along with algorithms for molecular properties, electron correlation, and higher order QED effects. The DHFB equations are solved by a direct method based on a relativistic generalization of the McMurchie–Davidson algorithm for molecular integrals that economizes memory requirements and is not significantly more expensive computationally than comparable nonrelativistic calculations [4].

In this paper we applied the generalized energy approach (Gell–Mann and Low S-matrix formalism) [8–15] to relativistic calculation of the autoionization characteristics of some heavy atoms on the example of the Yb atom. The generalized gauge-invariant QED version of the energy approach has been further developed by Glushkov–Ivanov–Ivanova (see Refs. [8–10]). The approach is based on the Gell–Mann and Low S-matrix formalism and the gauge-invariant QED PT with using the optimized one-quasiparticle representation and an accurate account of the relativistic, correlation, nuclear, radiative effects. In relativistic case the Gell–Mann and Low formula expressed an energy shift ΔE through the QED scattering matrix including the interaction with as the photon vacuum field as the laser field [11, 12]. The first case is corresponding to definition of the traditional radiative and autoionization characteristics of multielectron atoms and ions. The wave function zeroth basis is found from the Dirac equation with a potential, which includes the ab initio (the optimized model potential or DF potentials, the electric and polarization potentials of a nucleus; the Gaussian or Fermi forms of the charge distribution in a nucleus are usually used) [5]. The correlation corrections of the PT high orders are taken into account within the Green functions method (with the use of the Feynman diagram’s technique). All correlation corrections of the second order and dominated classes of the higher orders diagrams (electrons screening, particle-hole interaction, mass operator iterations) are taken into account [12–14].

Generally speaking, the majority of complex atomic systems possesses a dense energy spectrum of interacting states with essentially relativistic properties. In the theory of the non-relativistic atom a convenient field procedure is known for calculating the energy shifts ΔE of degenerate states. This procedure is connected with the secular matrix M diagonalization [8]. In constructing M , the Gell–Mann and Low adiabatic formula for ΔE is used. A similar approach, using the Gell–Mann and Low formula

with the electrodynamics scattering matrix, is applicable in the relativistic atom theory [8]; the approach is consistently electrodynamic. In contrast to the non-relativistic case, the secular matrix elements are already complex in the second order of the electrodynamic PT (first order of the interelectron interaction). Their imaginary parts are connected with the radiation decay (radiation) possibility. The total energy shift of the state is usually presented in the form:

$$\Delta E = \text{Re} \Delta E + i \text{Im} \Delta E, \text{Im} \Delta E = -\Gamma/2, (1)$$

where Γ is interpreted as the level width, and the decay possibility $P = \Gamma$.

In this approach, the whole calculation of the energies and decay probabilities of a non-degenerate excited state is reduced to the calculation and diagonalization of the complex matrix M . In the papers of different authors, the $\text{Re} \Delta E$ calculation procedure has been generalized for the case of nearly degenerate states, whose levels form a more or less compact group. One of these variants has been previously [8] introduced: for a system with a dense energy spectrum, a group of nearly degenerate states is extracted and their matrix M is calculated and diagonalized. If the states are well separated in energy, the matrix M reduces to one term, equal to ΔE . The non-relativistic secular matrix elements are expanded in a PT series for the interelectron interaction.

The complex secular matrix M is represented in the form [9,10]:

$$M = M^{(0)} + M^{(1)} + M^{(2)} + M^{(3)}. (2)$$

where $M^{(0)}$ is the contribution of the vacuum diagrams of all order of PT, and $M^{(1)}, M^{(2)}, M^{(3)}$ those of the one-, two- and three- quasiparticle diagrams respectively. $M^{(0)}$ is a real matrix, proportional to the unit matrix. It determines only the general level shift. We have assumed $M^{(0)} = 0$. The diagonal matrix $M^{(1)}$ can be presented as a sum of the independent one-quasiparticle contributions. For simple systems (such as alkali atoms and ions) the one -quasiparticle energies can be taken from the experiment. Substituting these quantities into (2) one could have summarised all the contributions of the one -quasiparticle diagrams of all orders of the formally exact QED PT. However, the necessary experimental quantities are not often available. The first two order corrections to $\text{Re} M^{(2)}$ have been analyzed previously [5] using Feynman diagrams. The contributions of the first-order diagrams have been completely calculated. In the second order, there are two kinds of diagrams: polarization and ladder ones. The polarization diagrams take into account the quasiparticle interaction through the polarizable core, and the ladder diagrams account for the immediate quasiparticle interaction. Some of the ladder diagram contributions as well as some of the three-quasiparticle diagram contributions in all PT orders have the same angular sym-

metry as the two-quasiparticle diagram contributions of the first order. These contributions have been summarized by a modification of the central potential, which must now include the screening (anti-screening) of the core potential of each particle by the two others. The additional potential modifies the one-quasiparticle orbitals and energies. Then the secular matrix is as follows:

$$M \simeq \tilde{M}^{(1)} + \tilde{M}^{(2)}, (3)$$

where $\tilde{M}^{(1)}$ is the modified one-quasiparticle matrix (diagonal), and $\tilde{M}^{(2)}$ the modified two-quasiparticle one. $\tilde{M}^{(1)}$ is calculated by substituting the modified one-quasiparticle energies, and $\tilde{M}^{(2)}$ by means of the first PT order formulae for $M^{(2)}$, putting the modified radial functions of the one-quasiparticle states in the radial integrals.

Let us note that in the QED theory, the photon propagator $D(12)$ plays the role of this interaction. Naturally (see above) the analytical form of $D(12)$ depends on the gauge, in which the electrodynamic potentials are written. In general, the results of all approximate calculations depended on the gauge. Naturally the correct result must be gauge invariant. The gauge dependence of the amplitudes of the photoprocesses in the approximate calculations is a well known fact and is in details investigated by Grant, Armstrong, Aymar and Luc—Koenig, Glushkov—Ivanov [1, 2, 5, 8]. Grant has investigated the gauge connection with the limiting non-relativistic form of the transition operator and has formulated the conditions for approximate functions of the states, in which the amplitudes of the photoprocesses are gauge invariant. These results remain true in the energy approach because the final formulae for the probabilities coincide in both approaches. Glushkov-Ivanov have developed a new QED version of the energy approach [9]. Here we applied the generalized version of the energy approach (EA) in QED formulation with using the gauge-invariant procedure for generating the relativistic orbital bases (abbreviator: EA-QEDPT).

The autoionization width is defined by the square of an electron interaction matrix element having the form [8]:

$$V_{1234}^{\omega} = [(j_1)(j_2)(j_3)(j_4)]^{1/2} \times \sum_{\lambda\mu} (-1)^{\mu} \begin{pmatrix} j_1 j_3 & \lambda \\ m_1 - m_3 & \mu \end{pmatrix} \times \text{Re } Q_{\lambda}(1234). (4)$$

The real part of the electron interaction matrix element is determined using expansion in terms of Bessel functions [5, 8]:

$$\frac{\cos|\omega|r_{12}}{r_{12}} = \frac{\pi}{2\sqrt{r_1 r_2}} \times \sum_{\lambda=0} (\lambda) J_{\lambda+1/2}(|\omega|r_{<}) J_{-\lambda-1/2}(|\omega|r_{>}) P_{\lambda}(\cos \mathbf{r}_1 \mathbf{r}_2). (5)$$

The Coulomb part Q_λ^{Coul} is expressed in terms of radial integrals R_λ , angular coefficients S_λ :

$$\begin{aligned} \text{Re } Q_\lambda^{\text{Coul}} = & \frac{1}{Z} \text{Re} \{ R_\lambda(1243) S_\lambda(1243) + \\ & + R_\lambda(\tilde{1}24\tilde{3}) S_\lambda(\tilde{1}24\tilde{3}) + R_\lambda(1\tilde{2}4\tilde{3}) S_\lambda(1\tilde{2}4\tilde{3}) + \\ & + R_\lambda(\tilde{1}\tilde{2}4\tilde{3}) S_\lambda(\tilde{1}\tilde{2}4\tilde{3}) \}. \end{aligned} \quad (6)$$

As a result, the autoionization decay probability is expressed in terms of $\text{Re } Q_\lambda(1243)$ matrix elements:

$$\begin{aligned} \text{Re } R_\lambda(1243) = \\ = \iint dr_1 r_2^2 f(r_1) f(r_1) f(r_2) f(r_2) Z_\lambda^{(1)}(r_-) Z_\lambda^{(1)}(r_+), \end{aligned} \quad (7)$$

where f is the large component of radial part of single electron state Dirac function and function Z is

$$Z_\lambda^{(1)} = \left[\frac{2}{|\omega_{13}| \alpha Z} \right]^{\lambda+1/2} \frac{J_{\lambda+1/2}(\alpha |\omega_{13}| r)}{r^\lambda \Gamma(\lambda+3/2)}. \quad (8)$$

The angular coefficient is defined by standard way as above [3]. The Breit part of Q is defined in the similar way as above, but the contribution of our interest is a real part. The Breit interaction is known to change considerably the Auger decay dynamics in some cases (see, for example, Refs. [8]). The calculation of radial integrals $\text{Re } R_\lambda(1243)$ is reduced to the solution of a system of differential equations:

$$\left. \begin{aligned} y'_1 &= f_1 f_3 Z_\lambda^{(1)}(\alpha |\omega| r) r^{2+\lambda}, \\ y'_2 &= f_2 f_4 Z_\lambda^{(1)}(\alpha |\omega| r) r^{2+\lambda}, \\ y'_3 &= [y_1 f_2 f_4 + y_2 f_1 f_3] Z_\lambda^{(2)}(\alpha |\omega| r) r^{1-\lambda}. \end{aligned} \right\} \quad (9)$$

In addition, $y_3(\infty) = \text{Re } R_\lambda(1243)$, $y_1(\infty) = X_\lambda(13)$. The system of differential equations includes also equations for functions $f/r^{|\alpha|-1}$, $g/r^{|\alpha|-1}$, $Z_\lambda^{(1)}$, $Z_\lambda^{(2)}$. The formulas for the autoionization (Auger) decay probability include the radial integrals $R_\alpha(\alpha k \gamma \beta)$, where one of the functions describes electron in the continuum state. When calculating this integral, the correct normalization of the function Ψ_k is a problem. The correctly normalized function should have the following asymptotic at $r \rightarrow 0$:

$$\left. \begin{aligned} f \} & \rightarrow (\lambda \omega)^{-1/2} \left\{ \begin{aligned} & [\omega + (\alpha Z)^{-2}]^{-1/2} \sin(kr + \delta), \\ & [\omega - (\alpha Z)^{-2}]^{-1/2} \cos(kr + \delta). \end{aligned} \right. \end{aligned} \quad (10)$$

When integrating the master system, the function is calculated simultaneously:

$$\begin{aligned} N(r) = & \left\{ \pi \omega_k [f_k^2 [\omega_k + (\alpha Z)^{-2}] + \right. \\ & \left. + g_k^2 [\omega_k + (\alpha Z)^{-2}] \right\}^{-1/2}. \end{aligned} \quad (11)$$

It can be shown that at $r \rightarrow \infty$, $N(r) \rightarrow N_k$, where N_k is the normalization of functions f_k , g_k of continuous spectrum satisfying the condition (10).

It is important also to note that the calculation is carried out in the jj -coupling scheme representation. The transition to the intermediate coupling scheme has been realized by diagonalization of the secular matrix. Indeed, only $\text{Re } M$ should be diagonalized. The imaginary part is converted by means of the matrix of eigenvectors $\{C_{mk}\}$, obtained by diagonalization of $\text{Re } M$:

$$\text{Im } M_{mk} = \sum_{ij} C_{mi}^* M_{ij} C_{jk}. \quad (12)$$

M_{ij} are the matrix elements in the jj -coupling scheme, and M_{mk} in the intermediate coupling scheme representation. This procedure is correct to terms of the order of $\text{Im } M / \text{Re } M$ [8].

In table 1 we present the experimental data (Letokhov et al [16, 17]) and theoretical results for energies and widths of the autoionization states of the $7s6p$ configuration on YbI (account from the ground state: $6s^2 \text{Yb}$): $E1$, $\Gamma1$ — data by Ivanov et al (EA-RPTMP method) [17, 18]; $E2$, $\Gamma2$ — EA-QED PT data. An analysis shows quite physically reasonable agreement between the values of energies $E1$, $E2$, E_{exp} , however, the values of the widths $\Gamma1$, Γ_{exp} significantly differ. In our opinion, this fact is explained by insufficiently exact estimates of the radial integrals, using the non-optimized bases and some other additional calculation approximations. The EA-QEDPT values for widths are significantly closer to experimental data. It is connected with using more optimized bases of the orbitals and more accurate accounting for the important multi-body exchange-correlation effects. In table 2, 3 the autoionization states energies and widths for YbI with doubly excited valent shell are listed [16—18]: $E1$, $\Gamma1$ — data by Ivanov et al (EA-RPTMP method); $E2$, $\Gamma2$ — EA-QED PT data.

The presented EA-RPTMP and EA-QEDPT data for the energies are in the physically reasonable agreement with experimental data. However, comparison of the corresponding results for widths demonstrates again sufficiently large discrepancy. Analysis shows too that the state $5d_{3/2}5d_{5/2}$, ($J=1$) is really autoionization (hitherto this question remained opened). Its anormal smallness can be explained by the fact that its decay is forbidden in the non-relativistic limit.

Table 1

Energies E (cm $^{-1}$) and widths Γ (cm $^{-1}$) of the YbI $7s6p$ configuration states

Term	Theory				Experiment	
	$E1$	$\Gamma1$	$E2$	$\Delta2$	E_{exp}	Γ_{exp}
$3P_0^0$	59800	0,70	59450	1,25	59130,5	1,1
$3P_1^0$	60000	3,00	60315	1,10	60428,7	0,95
$3P_2^0$	62600	0,70	62587	1,51	62529,1	1,6
$1P_1^0$	63600	1,80	63613	2,48	63655,8	2,6

Energies (in 10^2 cm^{-1}) of autoionization states for Yb with doubly excited valent shell

Conf.	J	Theory		E_{exp}	Conf.	J	Theory		E_{exp}
		$E1$	$E2$				$E1$	$E2$	
$6p_{1/2}^2$	0	—1067	—1064	—1062,7	$6p_{3/2}5d_{5/2}$	3	—963	—962	—
$6p_{3/2}^2$	0	—920	—918	—	$5d_{3/2}^2$	4	—1062	—1061	—
	2	—987	—1004	—1008,9		0	—981	—982	—
$6p_{1/2}6p_{3/2}$	1	—1054	—1050	—1049	$5d_{5/2}^2$	2	—1034	—1032	—101076
	2	—1032	—1036	—1039,5		0	—961	—963	—
$6p_{1/2}5d_{3/2}$	1	—1077	—1072	—		2	—970	—968	—
	2	—1075	—1069	—	$5d_{3/2}5d_{5/2}$	4	—861	—859	—
$6p_{1/2}5d_{5/2}$	2	—1007	—1004	—		1	—980	—982	—
	3	—1119	—1115	—		2	—994	—995	—99463
$6p_{3/2}5d_{3/2}$	0	—1020	—1017	—		3	—1030	—1032	—103247
	1	—1014	—1012	—	$7s_{1/2}6p_{1/2}$	4	—1024	—1026	—
	2	—914	—913	—		0	—889	—886,4	—
	3	—1039	—1035	—	$7s_{1/2}6p_{3/2}$	1	—887	—886	—
$6p_{3/2}5d_{5/2}$	1	—949	—948	—		1	—851	—849	—
	2	—1118	—1116	—		2	—861	—860	—

Table 3

The widths (cm^{-1}) of autoionization states for Yb with doubly excited valent shell

Configurations		Term	Γ_1	Γ_2
	J			
$6p_{3/2}^2$	0	1S_0	5.4	5.69
$6p_{3/2}5d_{5/2}$	1	$^1P_1^0$	5.7	5.95
	3	$^1F_3^0$	1.60	1.98
$5d_{3/2}^2$	0	3P_0	0.01	0.05
$6p_{3/2}5d_{3/2}$	2	$^1D_2^0$	0.20	0.52
$5d_{3/2}5d_{5/2}$	1	3P_1	1(-4)	8(-4)
$5d_{5/2}^2$	0	1S_0	3.30	3.63
$5d_{5/2}^2$	2	3P_2	0.40	0.73
	4	1G_4	0.90	1.74

Note: $0.0008 = 8(-4)$.

REFERENCES

1. Grant I. P., Relativistic Quantum Theory of Atoms and Molecules. — Oxford, 2008. — 650 P.
2. Wilson S., Handbook on Molecular Physics and Quantum Chemistry. — Chichester: Wiley, 2003. — 680 P.
3. Quiney H., Relativistic Quantum Mechanics of Atoms and Molecules // New Trends in Quantum Systems in Chemistry and Physics, Series: Progress in Theoretical Chemistry and Physics (Berlin, Springer). — 2002. — Vol. 6. — P. 135—173.
4. Bell K. L., Berrington K., Crothers D., Hibbert A., Taylor K. T., BERTHA: 4-Component Relativistic Molecular Quantum Mechanics / Supercomputing, Collision Processes, and Application, Series: Physics of Atoms and Molecules (Berlin, Springer). — 2002. — P. 213—224.
5. Glushkov A. V., Relativistic Quantum Theory. Quantum mechanics of Atomic Systems. — Odessa: Astroprint, 2008. — 900 P.
6. Safronova U. I., Safronova M. S., Third-order relativistic many-body calculations of energies, transition rates, hyperfine constants, and blackbody radiation shift in $^{171}\text{Yb}^+$ // Phys. Rev. A. — 2009. — Vol. 79. — P. 022512.
7. Bieron J., Froese-Fischer C., Fritzsche S., Pachucki K., Lifetime and hyperfine structure of 3D_2 state of radium // J. Phys. B: At. Mol. Opt. Phys. — 2004. — Vol. 37. — P. L305—311.
8. Glushkov A. V., Ivanov L. N., Ivanova E. P. // Autoionization Phenomena in Atoms. — M.: Moscow State University. — 1986. — P. 58—160.
9. Ivanova E. P., Ivanov L. N., Aglitsky E. V., Modern Trends in Spectroscopy of Multicharged Ions // Physics Rep. — 1988. — Vol. 166, N 6. — P. 315—390.
10. Glushkov A. V., Ivanov L. N. Radiation Decay of Atomic States: atomic residue and gauge non-invariant contributions // Phys. Lett. A. — 1992. — Vol. 170, N 1. — P. 33—38.
11. Glushkov A. V., Khetselius O. Yu., Svinarenko A. A., Prepelitsa G. P., Energy approach to atoms in a Laser Field and Quantum Dynamics with Laser Pulses of Different Shape // In: Coherence and Ultrashort Pulsed Emission, Ed. Duarte, F. J. — Vienna: InTech. — 2010. — P. 159—186.
12. Glushkov A. V., Khetselius O. Yu., Loboda A. V., Svinarenko A. A., QED approach to atoms in a laser field: Multi-photon resonances and above threshold ionization // Frontiers in Quantum Systems in Chemistry and Physics (Berlin, Springer). — 2008. — Vol. 18. — P. 541—558.
13. Svinarenko A. A., Nikola L. V., Prepelitsa G. P., Tkach T., Mischenko E., The Auger (Autoionization) Decay of Excited States in Spectra of Multicharged Ions: Relativistic Theory//Spectral Lines Shape. — 2010. — Vol. 16. — P. 94—98.
14. Malinovskaya S. V., Glushkov A. V., Khetselius O. Yu., Svinarenko A. A., Bakunina E. V., Florko T. A., Optimized perturbation theory scheme for calculating the interatomic potentials and hyperfine lines shift for heavy atoms in the buffer inert gas // Int. Journ. of Quantum Chemistry. — 2009. — Vol. 109, N 14. — P. 3325—3329.
15. Svinarenko A. A., Mischenko E. V., Loboda A. V., Dubrovskaya Yu. V., Quantum measure of frequency and

sensing the collisional shift of the ytterbium hyperfine lines in medium of helium gas // *Sensor Electronics and Microsystem Techn.* — 2009. — N 1. — P. 25—29.

16. *Ivanov L. N., Letokhov V. S.* Spectroscopy of autoionization resonances in heavy elements atoms // *Com. Mod. Phys. D.: At. Mol. Phys.* — 1999. — Vol. 4. — P. 169—184.

17. *Bekov G. I., Vidolova-Angelova E., Ivanov L. N., Letokhov V. S., Mishin V. I.*, Laser spectroscopy of low excited autoionization states of the ytterbium atom // *JETP.* — 1999. — Vol. 80. — P. 866—878.

18. *Vidolova-Angelova E., Ivanov L. N.*, Autoionizing Rydberg states of thulium. Re-orientation decay due to monopole interaction // *J. Phys. B: At. Mol. Opt. Phys.* — 1999. — Vol. 24. — P. 4147—4158.

UDC 539.183

A. V. Glushkov, A. A. Svinarenko, A. V. Ignatenko

SPECTROSCOPY OF AUTOIONIZATION RESONANCES IN SPECTRA OF THE LANTHANIDES ATOMS

Abstract

We applied the generalized energy approach (Gell—Mann and Low S-matrix formalism) to studying the autoionization resonances in heavy atoms, in particular, firstly predicted parameters for the Yb autoionization resonances with accounting for exchange-correlation and relativistic effects.

Key words: spectroscopy of autoionization resonances, relativistic energy approach.

УДК 539.183

А. В. Глушков, А. А. Свиноренко, А. В. Игнатенко

СПЕКТРОСКОПИЯ АВТОИОНИЗАЦИОННЫХ РЕЗОНАНСОВ В СПЕКТРАХ АТОМОВ ЛАНТАНИДОВ

Резюме

Обобщенный энергетический подход (S-матричный формализм Гелл—Мана и Лоу) применен к изучению автоионизационных резонансов в тяжелых атомах, в частности, на его основе впервые с учетом обменно-корреляционных и релятивистских эффектов предсказаны параметры автоионизационных резонансов в итербии.

Ключевые слова: спектроскопия автоионизационных резонансов, релятивистский энергетический подход.

УДК 539.183

О. В. Глушков, А. А. Свиноренко, Г. В. Игнатенко

СПЕКТРОСКОПІЯ АВТОІОНІЗАЦІЙНИХ РЕЗОНАНСІВ У СПЕКТРАХ АТОМІВ ЛАНТАНІДІВ

Резюме

Узагальнений енергетичний підхід (S-матричний формалізм Гелл—Мана та Лоу) застосовано до вивчення автоіонізаційних резонансів у важких атомах, зокрема, на його основі вперше з урахуванням обмінно-кореляційних і релятивістських ефектів передбачені параметри автоіонізаційних резонансів у ітербії.

Ключові слова: спектроскопія автоіонізаційних резонансів, релятивістський енергетичний підхід.

MICROWAVE IONIZATION OF LITHIUM RYDBERG ATOMS: LINK OF QUASIDISCRETE STATES WITH CONTINUUM

A phenomenon of microwave ionization for the non-hydrogenic Rydberg atoms on example of the lithium atom is studied within new version of the quasi-stationary, quasi-energy states method and model potential one.

1. INTRODUCTION

In last years a phenomenon of multiwave ionization and photoionization of atomic systems in low-frequency electromagnetic fields attracts a great interest (c. f. [1–20]). Above many reasons very essential moment is connected with a possibility of realizing quantum chaos phenomenon in a system. It is obvious that a manifestation of this effect in photo-optical systems may in a significant degree change a functional regime. Earlier it was shown that an ionization process for highly excited hydrogen atom states by a strong, low frequency, electromagnetic field is realized through a mechanism of diffusion on atomic states which are strongly perturbed by a field. An important feature of process is in a stochastic character of electron vibrations. In order to describe a stochastic dynamics of hydrogen atom, several models were developed. The most simplified model uses diffusion like equation [14]. More comprehensive approach must be based on the basis of the Fokker-Plank equation [2, 15]. More sophisticated numerical calculations are presented in refs. [7–15]. Experimental observation of chaotic effect was carried out for the H atom from the state with ground quantum number $n = 60$ in a field of frequency $\omega = 9,9$ GGz. In series of papers by Casati et al (c. f. [15]) a dynamical chaos effect for hydrogen atom in a field was at first correctly described by the non-linear classic mechanics methods. However, an adequate description of the specific features of quantum chaos requires a use of the quantum-mechanical methods. If a hydrogen atom in a field problem is studied in many details, the analogous problem for multi-electron highly excited atoms is far from their adequate solution. In this aspect an especial interest attracts studying the highly excited dynamic Stark resonant states for alkali elements atoms in a electromagnetic field [1, 2]. This problem is also stimulated by experimental discoveries of the near threshold resonances in the photo ionization cross sections for hydrogen and alkali atoms in a electric field (c. f. [1, 2, 15]). Here we study a phenomenon of microwave ionization of the non-hydro-

genic Rydberg atoms on example of the lithium Li atom. All results are obtained by using a new version of the consistent, quantum-mechanical approach — quasi-stationary, quasi-energy states method and the model potential one [16–20].

2. THE COMPLEX ROTATION COORDINATES METHOD: NEW VERSION

Let us give the key moments of the our approach, which bases on the complex rotation coordinates method. The latter is earlier successfully used in solution of the quasi stationary states in static filed problems (c. f. [1, 2, 15, 16]) and connected with transformation of coordinates: $r' = \alpha r \exp(i\varphi)$ in Hamilton operator of a system. Their eigen-values are corresponding to the quasi stationary states, remain unchanged; the eigen functions are transited into a space of quadratically integrated functions. As a result, a problem of defining the energies is led to search of the eigen-values of non-hermit matrix. Let us consider one-quasi-particle atom (i. e. atom with one quasiparticle above the core of closed electron shells) in an external electromagnetic field $F(t) = F_0(t) \cos(\omega t)$ (for circularly polarized wave: $F(t) = F_0 \{\cos \omega t, \sin \omega t, 0\}$). Typical example of such system is an alkali atom. Within the quasi stationary states problem solution, the equation on the quasi stationary states in a field has the following form (atomic units are used):

$$(-1/2 \cdot \nabla^2 - r^{-1} + V_c(r) + \omega L_z + F_0 x) \Psi_E(r) = E \Psi_E(r). \quad (1)$$

Here all notations are standard; $V_c(r)$ is the model potential, which describes an interaction: “Core-Quasiparticle”. After the complex transformation of coordinates the equation (1) on the eigen-values and eigen-functions rewritten as follows:

$$(-1/2 \cdot \nabla^2 e^{-2i\varphi} - r^{-1} e^{-i\varphi} + V_c(r) e^{-i\varphi} + \omega L_z + F_0 x e^{i\varphi}) \Psi_E(r e^{i\varphi}) = (E - E_n^0) \Psi_E(r e^{i\varphi}) \quad (2)$$

Here $E_n^0 = -1/2(n - \delta)^2$ is the non-perturbed energy value; δ is a quantum defect. The quadratic integrality of the quasi-stationary state functions is provided under values of the angle for complex rotation of coordinates φ , and cited values are determined by the following inequalities:

$$|\arg[-(E + N\omega)]^{1/2} < \varphi < \pi/2 - \arg\{-(E + (N - 1)\omega)\}^{1/2}.$$

Here N — is the threshold number of photons needed for ionization. Under choice of the finite basis for diagonalization of (2) the complex eigen-values are dependent upon the angle φ as a parameter. Standard approach is in a choice of the definitive exactness of calculation and in further the basis size is chosen in such a way that their variations do not change the exactness of calculation. In our opinion, the most effective procedure is an use of the optimal basis of the operator perturbation theory in the Stark problem for the non hydrogen atom [7, 16, 17] with application the well known Hellman potential as the potential $V_c(r)$. In further a problem is resulted in stationary task on the eigen-values and eigen-vectors for the matrice \mathbf{A} :

$$\begin{aligned} \mathbf{A}\mathbf{b} &= (E_n^0 - E_n)\mathbf{b} \\ A_{nlm, n_1 l_1 m_1} &= \delta_{l, l_1} \delta_{m, m_1} \{ \langle nlm | n_{1l_1 m_1} \rangle \times \\ &\times [(n_1 + l_1 + 1)/v \cdot \exp(-2i\varphi) - \exp(-i\varphi)] + \\ &+ \delta_{n, n_1} (E_n^0 - 1/2v^2 + \omega m) \} + F_0 \exp(-i\varphi) \times \\ &\times \langle nlm | x | n_{1l_1 m_1} \rangle. \end{aligned} \quad (3)$$

$$(4)$$

Here $|nlm\rangle$ is a radial part of the basis functions. A full diagonalization of the matrice (4) is quite complicated task. As usually, it is possible to make a search for one eigen-value, which is transited to the state E_n^0 under switching on a field. A solution of determining the maximal eigen-value and the corresponding eigen-vector is realized by usual iterative methods (c. f. [2, 7, 10, 16, 17]). Naturally, it's possible the complicating in a case of availability of resonance on atomic levels. Then matrice has several nearest (on absolute value) eigen-values (to separate ones, the q-p algorithm can be used). The shift \mathbf{K} and probability (width) \mathbf{P} of ionization of the atom are defined by the following expressions:

$$K = \alpha F_0^2 / 4 \operatorname{Re} \Delta E, \quad P = \sigma F_0^4 / 2 \operatorname{Im} \Delta E, \quad (5)$$

In whole a solution of the task give a set of the quasi-energies E_j , decay rates Γ_j (energy is the complex variable $E \rightarrow E - i\Gamma/2$) and corresponding eigen vectors $|E_j\rangle$. The characteristics, which is usually measured in the experiment, is ionization probability (after averaging on the initial phase of an external AC field) in dependence upon the time, if initially an atom is in the state $|n_0 l_0 m_0\rangle$. The cited parameter looks as follows:

$$P_{\text{ion}}(t) = 1 - \sum_{E_j} \omega_j \exp(-i\Gamma_j t) \quad (6)$$

with the values ω_j , which define the overlapping the initial state atom function with eigen vectors $|E_j\rangle$ of the “atom-field” system. The summation in eq. (6) is naturally performed over all states in the single Floquet zone. All necessary calculations are performed with using the PC atomic code “Suprator” (Stark blocks) [2, 7, 16].

3. IONIZATION OF LITHIUM RYDBERG ATOM IN A MICROWAVE ELECTROMAGNETIC FIELD

Here we present the results of our studying the microwave ionization of the Li Rydberg atoms. Let us note that detailed experimental investigation of such atoms has been fulfilled by the Virginia group [3—6]. Above theoretical papers one should turn attention on the refs. [7—15], especially numerical calculation [10, 11]. In tables 1—3 we present the results of calculation the ionization probabilities for the lithium atom in the Rydberg states in the microwave electromagnetic field (frequency $\omega/2\pi = 36$ GHz) and different atom-field interaction times t . Here the interaction time is varied from $t = 327 \cdot 2\pi/\omega$ (circles) to $t = 2000 \cdot 2\pi/\omega$ (crosses). In table 1 we present the calculated ionization probabilities values for the lithium atom, which has been initially prepared in the state (states) with the orbital angle moment $l_0 = 0$, moment projection $m_0 = 0$ and principal quantum number $n = 51, 55, 63$ in dependence upon the field amplitude for the atom-field interaction time $t = 327 \cdot 2\pi/\omega$. The similar results of the ref. [10] are presented in the table 1 too. In the table 2, 3 we present the same data, however the atom-field interaction times are as follows: $t = 659 \cdot 2\pi/\omega, 2000 \cdot 2\pi/\omega$. Analyzing the numerical results one could note quite closed agreement with the results of very sophisticated calculations by Krug and Buchleitner [10, 11] for the same atom, chosen state and field amplitude. However, our method looks more effective and simplified in comparison with Krug-Buchleitner approach. The analysis of the obtained data shows that the local violation of the regular dependence of the probability P upon the field amplitude occur for the principal quantum number values $n_0 \sim 51, 63$ (in the comparison with values for $n_0 \sim 51$, namely, for value $n_0 \sim 55$).

The physically reasonable explanation of this phenomenon can be connected with the fact that the Floquet spectrum structure becomes resonantly more complicated. It is important that a link between the quasi-discrete states set and continuum is enhanced. In the recent paper [9] it has been presented a consistent S-matrix theory of similar effects, in particular, the Multiphoton resonances contributions to the ionization parameters of the atom in an electromagnetic field. Speech here is about the perturbative regime, where the field which is experienced by

Table 1

Ionization probabilities for the lithium in the quantum states with $l_0=0$, $m_0=0$, $n_0=51$ —63 for the field amplitude $F=(2.0$ — $3.1) \cdot 10^{-9}$ atomic units (other parameters: $t=327 \cdot 2\pi/\omega$; frequency: $\omega/2\pi=36$ HHZ)

	Our data	Our data	Our data	Our data	Our data	Our data	[10]
n_0	$F=1.6$	$F=2.0$	$F=2.3$	$F=2.5$	$F=2.8$	$F=3.1$	$F=3.1$
51	0,009	0,017	0,024	0,041	0,089	0,147	—
55	0,011	0,021	0,026	0,034	0,045	0,058	—
63	0,124	0,136	0,314	0,312	0,328	0,344	0,362

Table 2

Ionization probabilities for the lithium in the quantum states with $l_0=0$, $m_0=0$, $n_0=51$ —63 for the field amplitude $F=(2.0$ — $3.1) \cdot 10^{-9}$ atomic units (other parameters: $t=659 \cdot 2\pi/\omega$; frequency: $\omega/2\pi=36$ HHZ)

	Our data	Our data	Our data	Our data	Our data	Our data	Our data
n_0	$F=1.6$	$F=2.0$	$F=2.3$	$F=2.5$	$F=2.8$	$F=3.1$	$F=3.1$
51	0,021	0,033	0,040	0,056	0,107	0,154	0,154
55	0,035	0,048	0,055	0,061	0,069	0,074	0,074
63	0,137	0,151	0,339	0,337	0,346	0,369	0,369

Table 3

Ionization probabilities for the lithium in the quantum states with $l_0=0$, $m_0=0$, $n_0=51$ —63 for the field amplitude $F=(2.0$ — $3.1) \cdot 10^{-9}$ atomic units (other parameters: $t=2000 \cdot 2\pi/\omega$; frequency: $\omega/2\pi=36$ HHZ)

	Our data	Our data	Our data	Our data	Our data	Our data	[10]
n_0	$F=1.6$	$F=2.0$	$F=2.3$	$F=2.5$	$F=2.8$	$F=3.1$	$F=3.1$
51	0,063	0,076	0,089	0,106	0,123	0,164	—
55	0,072	0,085	0,102	0,114	0,131	0,148	—
63	0,149	0,178	0,425	0,418	0,448	0,584	0,590

the electron does not induce appreciable ionization. For $n_0 > n_{\text{thr}}$, the ionization probability increases quickly, then the field is sufficiently strong in order to induce a strong coupling of a large number of the atomic bound (discrete) and continuum states. Beyond the perturbative regime the external field (which has cylindrical symmetry) destroys the spherical symmetry of the unperturbed initial atomic state, leading to a large ionization probability. Such a local enhancement of the ionization probability of a given initial state is caused by the complicated structure of the Floquet spectrum; near-degeneracy's between two (or more) atom-field eigen states for the given field amplitude reflect multi-photon resonances between atomic bound states. These resonances enhance the coupling to the atomic continuum and thus the observed total ionization rate has very complicated, non-regular feature (see refs. 20)).

REFERENCES

1. Ullrich C., Erhard S., Gross E. K. U., Superintense Laser Atoms Physics / N.-Y.: Acad. Press., 2007. — 580 p.
2. Glushkov A. V., Atom in an electromagnetic field. — Kiev: KNT, 2005. — 450 P.
3. Gallagher T. F., Mahon C. R., P. Pillet P., Newman J. B., Microwave ionization of hydrogen-like Li and

Na // Phys. Rev. A. — 1999. — Vol. 39. — P. 4545—4554.

4. Mahon C. R., Dexter J. L., Pillet P., Gallagher T. F., Ionization of sodium and lithium Rydberg atoms by 10-MHz to 15-GHz electric fields // Phys. Rev. A. — 1991. — Vol. 44. — P. 1859—1872.

5. Noel M. W., Griffith M. W., Gallagher T. F., Classical subharmonic resonances in microwave ionization of lithium Rydberg atoms // Phys. Rev. A. — 2000. — Vol. 62. — P. 063401.

6. Seng M., Eichmann U., Lange V., Gallagher T. F., Sandner W., Microwave ionization of Rydberg states of the barium ion // Eur. Phys. Journ. D. — 1998. — Vol. 3. — P. 21—26.

7. Glushkov A. V., Ivanov L. N., DC Strong-Field Stark-Effect: consistent quantum-mechanical approach // J. Phys. B: At. Mol. Opt. Phys. — 1993. — Vol. 26. — P. L379—388.

8. Glushkov A. V., Ambrosov S. V., Malinovskaya S. V., Resonances in Quantum Systems in strong external field: New Quantum Approach // Journ. of Techn. Phys. — 1997. — Vol. 38. — P. 215—218.

9. Glushkov A. V., Khetselius O. Yu., Loboda A. V., Svinarenko A. A., QED approach to atoms in a laser field: Multi-photon resonances and above threshold ionization // Frontiers in Quantum Systems in Chemistry and Physics (Berlin, Springer). — 2008. — Vol. 18. — P. 541—558.

10. Krug A., Buchleitner A., Chaotic ionization of non-hydrogenic alkali Rydberg states // Phys. Rev. Lett. — 2001. — Vol. 86. — P. 3538—3541.

11. Krug A., Buchleitner A., Residual symmetries in the spectrum of periodically driven alkali Rydberg states // Europhys. Lett. — 2000. — Vol. 49. — P. 176—180.

12. Dunning F. B., Mestayer J. J., Reinhold C. O., Yoshida S., Burgdorfer J., Engineering atomic Rydberg

states with pulsed electric fields // *J. Phys. B: At. Mol. Opt. Phys.* — 2009. — Vol. 42. — P. 022001. — 22 p.

13. *Grutter M., Zehnder O., Softley T. P., Merkt F.*, Spectroscopic study and multichannel quantum defect theory analysis of the Stark effect in Rydberg states of neon // *J. Phys. B: At. Mol. Opt. Phys.* — 2008. — Vol. 41. — P. 115001.

14. *Dando P. A., Monteiro T. S.*, Atoms in Static Fields: Chaos or Diffraction//In: *Photonic, Elect-ronic, Atomic Collisions.* — Eds. W. Aumyr and H. Winter. — Singapore: World Scientific. — 1999. — P. 621—630.

15. *Benvenuto F., Casati G., Shepelyansky D. L.*, Rydberg Stabilization of atoms in strong fields: “magic”mountain in chaotic sea // *Z. Phys. B.* — 1996. — Vol. 94. — P. 481—486.

16. *Glushkov A. V., Ambrosov S. V., Ignatenko A. V., Korchevsky D. A.*, DC strong field Stark effect for non-hydrogenic atoms: New consistent quantum-mechanical approach // *Int. Journ. Quantum Chem.* — 2004. — Vol. 99. — P. 936—940.

17. *Rusov V. D., Glushkov A. V., Ignatenko A. V., Korchevsky D. A., Vaschenko V. N.*, Stochastic dynamics of the atomic systems in the crossed electric and magnetic field: the rubidium atom recurrence spectra // *Bulletin of the T. Shevchenko Kiev Nat. University. Ser. Phys. — Math.* — 2004. — № 4. — 524—529.

18. *Glushkov A. V., Lepikh Ya. I., Fedchuk A. P., Ignatenko A. V., Khetselius O. Yu., Ambrosov S. V., Wannier—Mott excitons and atoms in a DC electric field: photoionization, Stark effect, resonances in the ionization continuum // Sensor Electronics and Microsyst. Technologies.* — 2008. — N 4. — P. 5—11.

19. *Ignatenko A. V.* Probabilities of the radiative transitions between stark sublevels in spectrum of atom in an DC electric field: new approach // *Photoelectronics.* — 2007. — N 16. — P. 71—74.

20. *Ignatenko A. V.*, Chaotic phenomenon in a multi-wave ionization of the non-Rydberg atoms // *Chaotic Modeling and Simulation.* — 2009. — Vol. 2, Sec. 25. — P. E7 (6 p.).

UDC 551.515.1

A. V. Ignatenko

MICROWAVE IONIZATION OF LITHIUM RYDBERG ATOMS: LINK OF QUASIDISCRETE STATES WITH CONTINUUM

Abstract

A phenomenon of microwave ionization for the non-hydrogenic Rydberg atoms on example of the lithium atom is studied within new version of the quasi-stationary, quasi-energy states method and model potential one.

Key words: microwave ionization, lithium atom, quasi-stationary quasi-energy states method.

УДК 551.515.1

А. В. Игнатенко

МИКРОВОЛНОВАЯ ИОНИЗАЦИЯ АТОМОВ ЛИТИЯ В РИДБЕРГОВСКОМ СОСТОЯНИИ: СВЯЗЬ КВАЗИДИСКРЕТНЫХ СОСТОЯНИЙ С КОНТИНУУМОМ.

Резюме

Феномен микроволновой ионизации для неводородоподобных атомов в ридберговском состоянии на примере атома рубидия изучается с использованием новой версии метода квазистационарных квазиэнергетических состояний и метода модельного потенциала.

Ключевые слова: микроволновая ионизация, атом лития в ридберговском состоянии, метод квазистационарных квазиэнергетических состояний.

УДК 551.515.1

А. В. Ігнатенко

МІКРОХВИЛЬОВА ІОНІЗАЦІЯ АТОМІВ ЛІТІЯ В РІДБЕРГІВСЬКОМУ СТАНІ: ЗВ'ЯЗОК КВАЗІДІСКРЕТНИХ СТАНІВ З КОНТИНУУМОМ

Резюме

Феномен мікрохвильової іонізації для неводнеподібних атомних систем у рідбергівських станах на прикладі атому літія вивчається на підставі нової версії методу квазістаціонарних квазіенергетичних станів та методу модельного потенціалу.

Ключові слова: мікрохвильова іонізація, атом літія у рідбергівському стані, метод квазістаціонарних квазіенергетичних станів.

DETERMINATION OF THE RADIATIVE TRANSITION CHARACTERISTICS IN SPECTRA OF HEAVY IONS: RELATIVISTIC SCHEME

On the basis of new relativistic scheme within the gauge-invariant relativistic multi-body perturbation theory it has been carried out calculating the energies and probabilities of some radiative transitions in spectrum of the complex heavy ion Hg^+ .

INTRODUCTION

The experimental and theoretical studying of the radiation transition characteristics of a whole number of atomic systems is of a great importance and interest from the point of view of as the quantum electronics and atomic physics as plasma physics and thermonuclear fusion science [1—33]). It is also very important for search the optimal candidates and conditions for realization of the X-ray lasing. Besides, the forbidden atomic transitions are attracting from the point of view of sensing new physics behind the well known standard model.

The well known multi-configuration Dirac-Fock (MCDf) approach is widely used in calculations of the atoms and ions. It provides the most reliable version of calculation for atomic systems. Nevertheless, as a rule, detailed description of the method for studying role of the relativistic, gauge-invariant contributions, nuclear effects is lacking. Serious problems are connected with correct definition of the high-order correlation corrections, QED effects etc. The further improvement of this method is connected with using the gauge invariant procedures of generating relativistic orbitals basis's and more correct treating the nuclear and QED effects [1—5].

In refs. [16, 20—24] it has been developed a new ab initio approach to description of the relativistic atomic systems with accurate consistent treating the relativistic, exchange-correlation, nuclear, QED effects, based on the gauge-invariant QED PT [20] and new effective procedures for accounting the nuclear and radiative corrections. This gauge-invariant QED perturbation theory (PT) formalism been used as a basis for development of a new simplified relativistic scheme for determination and sensing the atomic transitions characteristics (energies and probabilities of transitions). In result, a new approach can be treated as the RMBPT scheme. As object of studying here the heavy ion Hg^+ is considered. Earlier it has been carried theoretical studying energy spectra, theoretical determination of the energies and os-

cillator strengths of some electric dipole and forbidden radiative transitions in spectrum of the rare-earth atom of Eu, Ne- and Zn-like multicharged ions [28—33].

1. RELATIVISTIC THEORY OF THE ATOMIC TRANSITION PROBABILITIES

Let us describe in brief the important moment of our theoretical approach. As usually, the wave functions zeroth basis is found from the Dirac equation solution with potential, which includes the core ab initio potential, electric, polarization potentials of nucleus (the gaussian form for charge distribution in the nucleus is used). All correlation corrections of the PT second and high orders (electrons screening, particle-hole interaction etc.) are accounted for. The wavefunction for a particular atomic state

$$\Psi(TPJM) = \sum_r^{NCF} c_r \Phi(r, PJM) \quad (1)$$

is obtained as the above described self-consistent solutions of the Dirac—Fock type equations. Configuration mixing coefficients c_r are obtained through diagonalization of the Dirac Coulomb Hamiltonian

$$H_{DC} = \sum_i c \alpha_i p_i + (\beta_i - 1) c^2 - V_c(r|nlj) + V_{ex} - V_{nuc}(r|R) + \sum_{i>j} \exp(i\omega r_{ij})(1 - \alpha_1 \alpha_2)/r_{ij}. \quad (2)$$

In this equation the potential:

$$V(r) = V_c(r|nlj) + V_{ex} + V_{nuc}(r|R). \quad (3)$$

This potential includes the electrical and polarization potentials of the nucleus. The part V_{ex} accounts for exchange inter-electron interaction. The main exchange effect are taken into account in the equation. The rest of the exchange-correlation effects are accounted for in first two PT orders by the total inter-electron interaction [2]. The effective electron core density (potential V_c) is defined by iteration algorithm within gauge invariant QED procedure [20].

Consider the one-quasiparticle system. A quasiparticle is a valent electron above the core of closed electron shells or a vacancy in the core. In the lowest second order of the EDPT a non-zeroth contribution to the imaginary part of electron energy $\text{Im}\delta E$ (the radiation decay width) is provided by relativistic exchange Fock diagram. In the fourth order of the QED PT there are diagrams, whose contribution into the $\text{Im}\delta E$ accounts for the core polarization effects. It is on the electromagnetic potentials gauge (the gauge non-invariant contribution). Let us examine the multielectron atom with one quasi-particle in the first excited state, connected with the ground state by the radiation transition. In the zeroth QED PT approximation we, as usually (c. f. [2, 20, 28]), use the one electron bare potential

$$V_N(r) + V_C(r), \quad (4)$$

with $V_N(r)$ describing the electric potential of the nucleus, $V_C(r)$, imitating the interaction of the quasi-particle with the core. The core potential $V_C(r)$ is related to the core electron density $\rho_C(r)$ in a standard way. The latter fully defines the one electron representation. Moreover, all the results of the approximate calculations are the functionals of the density $\rho_C(r)$. In ref. [20] the lowest order multielectron effects, in particular, the gauge dependent radiative contribution for the certain class of the photon propagator calibration is treated. This value is considered to be the typical representative of the electron correlation effects, whose minimization is a reasonable criterion in the searching for the optimal one-electron basis of the PT. The minimization of the density functional $\text{Im}\delta E_{\text{niqv}}$ leads to the integral differential equation for the ρ_C , that can be solved using one of the standard numerical codes. In ref. [20] authors treated the function ρ_C in the simple analytic form with the only variable parameter b and substituted it to (6). More accurate calculation requires the solution of the integral differential equation for the ρ_C [2, 28].

The probability is directly connected with imaginary part of electron energy of the system, which is defined in the lowest order of perturbation theory as follows [16]:

$$\text{Im}\Delta E(B) = -\frac{e^2}{4\pi} \sum_{\substack{\alpha > n > f \\ [\alpha < n < f]}} V_{\alpha n \alpha n}^{|\omega_{\alpha n}|}, \quad (5)$$

where $\sum_{\alpha > n > f}$ — for electron and $\sum_{\alpha < n < f}$ — for vacancy. The potential V is as follows:

$$V_{ijkl}^{|\omega|} = \iint dr_1 dr_2 \Psi_i^*(r_1) \Psi_j^*(r_2) \frac{\sin|\omega|r_{12}}{r_{12}} (1 - \alpha_1 \alpha_2) \Psi_k^*(r_2) \Psi_l^*(r_1). \quad (6)$$

The separated terms of the sum in (5) represent the contributions of different channells

and a probability of the dipole transition is:

$$\Gamma_{\alpha_n} = \frac{1}{4\pi} \cdot V_{\alpha_n \alpha_n}^{|\omega_{\alpha_n}|}. \quad (7)$$

The corresponding oscillator strength: $gf = \lambda_g^2 \cdot \Gamma_{\alpha_n} / 6.67 \cdot 10^{15}$, where g is the degeneracy degree, λ is a wavelength in angstroms (Å). Under calculating the matrix elements (5) one could use the angle symmetry of the task and write the expansion for potential $\sin|\omega|r_{12}/r_{12}$ on spherical functions as follows [2, 16]:

$$\frac{\sin|\omega|r_{12}}{r_{12}} = \frac{\pi}{2\sqrt{r_1 r_2}} \times \sum_{\lambda=0}^{\infty} (\lambda) J_{\lambda+1/2}(|\omega|r_1) J_{\lambda+1/2}(|\omega|r_2) P_{\lambda}(\cos \mathbf{r}_1 \mathbf{r}_2), \quad (8)$$

where J — is the Bessell function of first kind and $(\lambda) = 2\lambda + 1$.

This expansion is corresponding to usual multipole one for probability of radiative decay. Substitution of the expansion (7) to matrix element of interaction gives as follows:

$$V_{1234}^{\omega} = [(j_1)(j_2)(j_3)(j_4)]^{1/2} \times \sum_{\lambda \mu} (-1)^{\mu} \begin{pmatrix} j_1 j_3 & \lambda \\ m_1 - m_3 & \mu \end{pmatrix} \times \text{Im} Q_{\lambda}(1234);$$

$$Q_{\lambda} = Q_{\lambda}^{\text{Coul}} + Q_{\lambda}^{\text{Br}}. \quad (9)$$

where j_i are the entire single electron momentums, m_i — their projections; $Q_{\lambda}^{\text{Coul}}$ is the Coulomb part of interaction, Q_{λ}^{Br} — the Breit part. The Coulomb part $Q_{\lambda}^{\text{Coul}}$ is expressed in terms of radial integrals R_{λ} , angular coefficients S_{λ} [16]:

$$Q_{\lambda}^{\text{Coul}} = \frac{1}{Z} \{ R_{\lambda}(1243) S_{\lambda}(1243) + R_{\lambda}(\tilde{1}24\tilde{3}) S_{\lambda}(\tilde{1}24\tilde{3}) + R_{\lambda}(\tilde{1}\tilde{2}43) S_{\lambda}(\tilde{1}\tilde{2}43) + R_{\lambda}(\tilde{1}\tilde{2}\tilde{4}\tilde{3}) S_{\lambda}(\tilde{1}\tilde{2}\tilde{4}\tilde{3}) \}. \quad (10)$$

As a result, the Auger decay probability is expressed in terms of $\text{Re} Q_{\lambda}(1243)$ matrix elements [2]:

$$\text{Re} R_{\lambda}(1243) = \iint dr_1 r_1^2 r_2^2 f_1(r_1) f_3(r_1) f_2(r_2) f_4(r_2) Z_{\lambda}^{(1)}(r_{<}) Z_{\lambda}^{(1)}(r_{>}). \quad (11)$$

where f is the large component of radial part of single electron state Dirac function and function Z is:

$$Z_{\lambda}^{(1)} = \left[\frac{2}{|\omega_{13}| \alpha Z} \right]^{\lambda+1/2} \frac{J_{\lambda+1/2}(\alpha |\omega_{13}| r)}{r^{\lambda} \Gamma(\lambda + 3/2)}. \quad (12)$$

The angular coefficient is defined by standard way [16]. The other items in (3) include small components of the Dirac functions; the sign « \sim » means that in (3) the large radial component f_i is to be changed by the small g_i ; one and the moment l_i is to be changed by $\tilde{l}_i = l_i - 1$ for Dirac number $\alpha_i > 0$ and $\tilde{l}_i + 1$ for $\alpha_i < 0$. The Breit interaction is known to

change considerably the Auger decay dynamics in some cases (c. f. [19]). The Breat part of Q can be defined as the sum:

$$Q_{\lambda}^{\text{Br}} = Q_{\lambda, \lambda-1}^{\text{Br}} + Q_{\lambda, \lambda}^{\text{Br}} + Q_{\lambda, \lambda+1}^{\text{Br}}, \quad (13)$$

where the contribution of our interest is determined as:

$$Q_{\lambda}^{\text{Br}} = \frac{1}{Z} \text{Re} \{ R_{\lambda}(12\tilde{4}\tilde{3})S'_{\lambda}(12\tilde{4}\tilde{3}) + R_{\lambda}(\tilde{1}243)S'_{\lambda}(1243) + R_l(\tilde{1}2\tilde{4}\tilde{3})S'_{\lambda}(\tilde{1}2\tilde{4}\tilde{3}) + R_l(1\tilde{2}4\tilde{3})S'_{\lambda}(1\tilde{2}4\tilde{3}) \}. \quad (14)$$

Radial parts F and G of two components of the Dirac function for electron, which moves in the potential $V(r, R) + U(r, R)$, are defined by solution of the Dirac equations (PT zeroth order). All calculations are carried out using the effective Dirac Superatom code developed by Ivanov et al [16, 19–22].

2. RESULTS AND CONCLUSIONS

We have carried out sensing and calculating energies and probabilities of the radiative transitions for the complex heavy single ionized atom of Hg. This paper goes on our studying of this ion (see ref. [29]). In all calculations we used the Ivanov—Ivanova model potential [19] with defining its parameter within above described an initio QED procedure [20]. In fact this potential imitated the self-consistent Dirac—Fock potential. All details can be found in refs. [2, 20, 28]. In table 1, 2 we present the energies and probabilities of the $5d^{10}7p(P_{1/2}, P_{3/2})—5d^{10}6s(S_{1/2})$, $5d^{10}7p(P_{1/2}, P_{3/2})—5d^{10}7s(S_{1/2})$ transitions in the ions of Hg^+ . For comparison we listed in this table the theoretical Hartree—Fock (HF), Dirac—Fock (DF) and DF (with

fitting to experimental transition energies) values by Ostrovsky—Sheynerman and experimental data by Moore (NBS, Washington) [17, 34]. Analysis of the obtained data allows to make the following conclusions. Firstly, one can see that our approach provides physically reasonable agreement with experiment and significantly more advantageous in comparison with standard Dirac—Fock method and the Hartree—Fock approximation approach.

Secondly, we have checked that the results for oscillator strengths, obtained within our approach in different photon propagator gauges (Coulomb, Babushkon, Landau gauges) are practically equal, that is provided by using an effective QED energy procedure [2]. Thirdly, calculation has confirmed the great role of the interelectron correlation effects of the second and higher QED PT orders, namely, effects of the interelectron polarization interaction and mutual screening.

Acknowledgements. The author would like to thank Prof. A. Glushkov, Prof. A. Ya. Bekshaev, Prof. O. Yu. Khetelius for useful comments and Dr. D. E. Sukharev, Dr. V. N. Polischuk for help in the numerical calculations. The anonymous referee comments are also acknowledged.

REFERENCES

1. *Grant I. P.*, Relativistic Quantum Theory of Atoms and Molecules. — Oxford, 2008. — 650 P.
2. *Glushkov A. V.*, Relativistic Quantum Theory. Quantum, mechanics of Atomic Systems. — Odessa: Astroprint, 2008. — 900 P.
3. *Froese Fischer C., Tachiev G.*, Breit—Pauli energy levels, lifetimes, and transition probabilities for the beryllium-like to neon-like sequences // Atomic Data and Nuclear Data Tables. — 2004. — Vol. 87. — P. 1—184.
4. *Safronova U. I., Safronova M. S.*, Third-order relativistic many-body calculations of energies, transition rates, hyperfine constants, and blackbody radiation shift in $^{171}\text{Yb}^+$ // Phys. Rev. A. — 2009. — Vol. 79. — P. 022512.
5. *Safronova U. I., Safronova A. S., Hamasha, S. M., Beiersdorfer P.*, Relativistic many-body calculations of mul-

Table 1

The energies of the transition $5d^{10}7p(P_{1/2}, P_{3/2})—5d^{10}6s(S_{1/2})$, $5d^{10}7p(P_{1/2}, P_{3/2})—5d^{10}7s(S_{1/2})$ in Hg^+ (in Ry): HF — Hartree—Fock data, DF — Dirac—Fock data, DF(exp) — DF (with fitting to experimental transition energies); RMBPT — our data; experiment — Moore (NBS, Washington)

Method	E_{6s}	$7P_{1/2}-6S_{1/2}$	$7P_{3/2}-6S_{1/2}$	$7P_{1/2}-7S_{1/2}$	$7P_{3/2}-7S_{1/2}$
HF	−1.07	0.721	0.721	0.095	0.095
DF	−1.277	0.904	0.922	0.109	0.127
This work	−1.377	0.986	1.019	0.114	0.147
Experiment	−1.378	0.987	1.020	0.115	0.148

Table 2

The E1 probabilities of the $5d^{10}7p(P_{1/2}, P_{3/2})—5d^{10}6s(S_{1/2})$, $5d^{10}7p(P_{1/2}, P_{3/2})—5d^{10}7s(S_{1/2})$ transition in Hg^+ (in s^{-1}): HF — Hartree—Fock data, DF — Dirac—Fock data, DF(exp) — DF (with fitting to experimental transition energies); RMBPT — our data; experiment — Moore (NBS, Washington)

Method	$7P_{3/2}-6S_{1/2}$	$7P_{1/2}-6S_{1/2}$	$7P_{3/2}-7S_{1/2}$	$7P_{1/2}-7S_{1/2}$
HF	$4.75 \cdot 10^6$	$4.75 \cdot 10^6$	$3.65 \cdot 10^7$	$3.65 \cdot 10^7$
DF	$8.45 \cdot 10^7$	$1.67 \cdot 10^7$	$6.89 \cdot 10^7$	$4.71 \cdot 10^7$
DF (exp)	$1.17 \cdot 10^8$	$2.04 \cdot 10^7$	$1.10 \cdot 10^8$	$5.52 \cdot 10^7$
This work	$1.49 \cdot 10^8$	$2.31 \cdot 10^7$	$1.41 \cdot 10^8$	$6.33 \cdot 10^7$
Experiment	$1.53 \cdot 10^8$	$2.35 \cdot 10^7$	$1.44 \cdot 10^8$	$6.37 \cdot 10^7$

tipole (E1, M1, E2, M2, E3, and M3) transition wavelengths and rates between 31-1 41' excited and ground states in nickel-like ions // *Atomic Data and Nuclear Data Tables*. — 2006. — Vol. 92. — P. 47—104.

6. *Safronova M. S., Johnson W. R., Safronova U. I., Cowan T.*, Relativistic many-body theory calculation of the Stark-induced amplitude of 6p-7p transition in thallium // *Phys. Rev. A*. — 2006. — Vol. 74. — P. 022504 (8 p.).

7. *Biémont E., Fivet V., Quinet P.*, Relativistic Hartree—Fock and Dirac—Fock atomic structure calculations in Fr-like ions Ra^+ , Ac^{2+} , Th^{3+} and $U5^+$ // *J. of Physics B: Atom. Mol. Opt. Phys.* — 2004. — Vol. 37. — P. 4193—4202.

8. *Quinet P., Argante C., Fivet V., Terranova C., Yushchenko A. V., Biémont E.*, Atomic data for radioactive elements Ra I, Ra II, Ac I and Ac II and application to their detection in HD 101065 and HR 465 // *Astr. & Astrophys.* — 2007. — Vol. 474, N 1. — P. 307—314.

9. *Safronova U. I., Cowan T., Safronova M. S.*, Relativistic many-body calculations of electric dipole lifetimes, transition rates, oscillator strengths for 2l-13l' states in Ne-like ions // *J. Phys. B: At. Mol. Opt. Phys.* — 2005. — Vol. 38. — P. 2741—2763.

10. *Semenov R. I., Kapel'kina E. L., Tsygankova G. A., Tsygankov M. A.*, Semiempirical calculation of atomic Characteristics of the 2p53d, 4d, 2p5ns ($n=3-10$) configurations of Ne // *Opt. Spectr.* — 2005. — Vol. 99, N 4. — P. 536—539.

11. *Jamieson M. J., Drake G. W. F., Dalgarno A.*, Variational calculation of the dynamic polarizabilities of rare-earth metal atoms // *Phys. Rev. A*. — 1999. — Vol. 51. — P. 3358—3370.

12. *Bekov G. I., Vidolova-Angelova E., Ivanov L. N., Letokhov V. S., Mishin B.*, Laser spectroscopy of low two-timed excited auto ionization states for ytterbium atom // *JETP*. — 1981. — Vol. 80. — P. 866—878.

13. *Bieron J., Froese-Fischer C., Fritzsche S., Pachucki K.*, Lifetime and hyperfine structure of the 3D_2 state of radium // *J. Phys. B: At. Mol. Opt. Phys.* — 2004. — Vol. 37. — P. L305—311.

14. *Parpia F. A., Froese-Fischer C., Grant I.*, Generalized relativistic atomic structure package: GRASP // *Comp. Phys. Commun.* — 1996. — Vol. 94, N 2. — P. 249—270.

15. *Gurnitskaya E. P.*, Heavy ion storage ring experimental and theoretical determination of the lifetimes for the iron ion levels // *Photoelectronics*. — 2005. — Vol. 14. — P. 50—54.

16. *Glushkov A. V., Ivanov L. N., Ivanova E. P.* // *Autoionization Phenomena in Atoms*. — M.: Moscow State University. — 1986. — P. 58—160.

17. *Östrovsky V. N., Sheynerman S. A.* Radiation transitions in the external shells of ion Hg^+ // *Opt. Spectr.* — 1999. — Vol. 67. — P. 16—22.

18. *Ivanova E. P., Zinoviev N. A.*, The possibility of X-ray lasers based on inner-shell transitions of Ne-like ions // *Phys. Lett. A*. — 2000. — V. 274. — P. 239—246.

19. *Ivanova E. P., Ivanov L. N., Aglitsky E. V.*, Modern Trends in Spectroscopy of Multicharged Ions // *Physics Rep.* — 1999. — Vol. 166, N 6. — P. 315—390.

20. *Glushkov A. V., Ivanov L. N.* Radiation Decay of Atomic States: atomic residue and gauge non-invariant contributions // *Phys. Lett. A*. — 1992. — Vol. 170, N 1. — P. 33—38.

21. *Glushkov A. V., Malinovskaya S. V., Ambrosov S. V.* Spectroscopy of Neutral and Highly-ionized Atoms: Calcula-

tion of the Oscillator Strengths for Na- and Fr-like Ions // *Atomic Spectra and Oscillator Strengths for Astrophysical and Laboratory Plasmas*. — Meudon: Publications de l'Observatoire de Paris. — 1996. — P. 96—99.

22. *Glushkov A. V., Ivanova E. P.*, Theoretical Study of Multicharged Ions Spectra of F- and Ne- Isoelectronic Sequence // *Spectroscopy of multicharged ions*. Ed. Safronova U. I. — Moscow: Nauka, 1986. — P. 5—195.

23. *Glushkov A. V.*, New method of accounting for polarization effects in determination of probabilities of the atomic transitions // *Opt. Spectr.* — 1991. — Vol. 71. — P. 395—397.

24. *Glushkov A. V.*, Relativistic calculation of oscillator strengths in multicharged ions with single electron above closed shells core // *Opt. Spectr.* — 1992. — Vol. 72. — P. 542—547.

25. *Glushkov A. V., Malinovskaya S. V., Svinarenko A. A., Chernyakova Yu. G.*, QED calculation of electron satellites spectra in an intense laser field in multicharged ion // *Int. J. Quant. Chem.* — 2004. — Vol. 99, N 5. — P. 673—678.

26. *Glushkov A. V., Ambrosov S. V., Loboda A. V., Gurnitskaya E. P., Prepelitsa G. P.*, Consistent QED approach to calculation of electron-collision excitation cross-sections and strengths: Ne-like ions // *Int. Journ. Quant. Chem.* — 2005. — Vol. 104, N 4. — P. 562—569.

27. *Glushkov A. V., Ambrosov S. V., Loboda A. V., Gurnitskaya E. P., Khetselius O. Yu.*, QED calculation of heavy multicharged ions with account for correlation, radiative and nuclear effects // *Recent Advances in Theor. Phys. & Chem. Systems (Springer)*. — 2006. — Vol. 15. — P. 285—300.

28. *Glushkov A. V., Khetselius O. Yu., Gurnitskaya E. P., Loboda A. V., Florko T. A., Sukharev D. E., Lovett L.*, Gauge-invariant QED perturbation theory approach to calculating nuclear electric quadrupole moments, hyperfine structure constants for heavy atoms and ions // *Frontiers in Quantum Systems in Chemistry and Physics (Springer)*. — 2008. — Vol. 18. — P. 505—522.

29. *Florko T. A., Loboda A. V., Svinarenko A. A.*, Sensing forbidden transitions in spectra of some heavy atoms and multicharged ions: new theoretical scheme / *Sensor Electronics and Microsyst. Techn.* — 2009. — N 3. — P. 21—26.

30. *Malinovskaya S. V., Glushkov A. V., Khetselius O. Yu., Svinarenko A. A., Mischenko Bakunina E. V., Florko T. A.*, Optimized perturbation theory scheme for calculating the interatomic potentials and hyperfine lines shift for heavy atoms in the buffer inert gas // *Int. Journ. of Quantum Chemistry*. — 2009. — Vol. 109, N 14. — P. 3325—3329.

31. *Florko T. A.*, Theoretical determination of oscillator strengths of some transitions in rare-earth atom of Eu // *Photoelectronics*. — 2007. — N16. — P. 98—101.

32. *Florko T. A., Gurnitskaya E. P., Polischuk V. N., Seredenko S. S.*, Dipole transitions of rare earth atoms in inert medium in a weak electromagnetic field and quasi-molecular term // *Photoelectronics*. — 2007. — N 16. — P. 26—32.

33. *Florko T. A.*, Theoretical determination of the radiative transition probabilities in spectra of Ne-like multicharged ions // *Photoelectronics*. — 2010. — N 19. — P. 51—55.

34. *Martin W.*, NIST Spectra Database, version 2.0 // NIST. — Washington. — 2004; *Moore C.*, NBS Spectra Database // NBS. — Washington. — 2007.

UDC 539.184

T. A. Florko

DETERMINATION OF THE RADIATIVE TRANSITIONS CHARACTERISTICS IN SPECTRA OF HEAVY IONS: RELATIVISTIC SCHEME

Abstract

On the basis of new relativistic scheme within the gauge-invariant relativistic multi-body perturbation theory it has been carried out calculating the energies and probabilities of some radiative transitions in spectrum of the complex heavy ion Hg^+ .

Key words: radiative transitions, heavy ions, new relativistic approach.

УДК 539.184

Т. А. Флорко

**ОПРЕДЕЛЕНИЕ ХАРАКТЕРИСТИК РАДИАЦИОННЫХ ПЕРЕХОДОВ В СПЕКТРАХ ТЯЖЕЛЫХ ИОНОВ:
РЕЛЯТИВИСТСКАЯ СХЕМА**

Резюме

Выполнен расчет энергий и вероятностей радиационных переходов в спектре сложного тяжелого иона Hg^+ на основе новой релятивистской схемы в рамках калибровочно-инвариантной релятивистской многочастичной теории возмущений.

Ключевые слова: радиационные переходы, тяжелые ионы, новая релятивистская схема.

УДК 539.184

Т. О. Флорко

**ВИЗНАЧЕННЯ ХАРАКТЕРИСТИК РАДІАЦІЙНИХ ПЕРЕХОДІВ У СПЕКТРАХ ВАЖКИХ ІОНІВ:
РЕЛЯТИВІСТСЬКА СХЕМА**

Резюме

Виконано розрахунок енергій, ймовірностей радіаційних переходів у спектрі складного важкого іону Hg^+ на основі нової релятивістської схеми в межах калібровочно-інваріантної релятивістської багаточастинкової теорії збурень.

Ключові слова: радіаційні переходи, важкі іони, нова релятивістська схема.

RESONANT AUGER SPECTROSCOPY OF THE ATOMS OF INERT GASES

The results of determination and analysis of the resonant Auger transition spectra characteristics for atoms of the inert gases are obtained within the relativistic multi-body theory and compared with available experimental and other theoretical data. A number of the Auger transition parameters have been firstly presented.

1. INTRODUCTION

The Auger electron spectroscopy remains an effective method to study the chemical composition of solid surfaces and near-surface layers [1–8]. Sensing the Auger spectra in atomic systems and solids gives the important data for the whole number of scientific and technological applications. So called two-step model is used most widely when calculating the Auger decay characteristics [1–5]. Since the vacancy lifetime in an inner atomic shell is rather long (about 10^{-17} to 10^{-14} s), the atom ionization and the Auger emission are considered to be two independent processes. In the more correct dynamic theory of the Auger effect [2, 3] the processes are not believed to be independent from one another. The fact is taken into account that the relaxation processes due to Coulomb interaction between electrons and resulting in the electron distribution in the vacancy field have no time to be over prior to the transition.

In fact, a consistent Auger decay theory has to take into account correctly a number of correlation effects, including the energy dependence of the vacancy mass operator, the continuum pressure, spreading of the initial state over a set of configurations etc [1–19]. The most widespread theoretical studying the Auger spectra parameters is based on using the multi-configuration Dirac–Fock (MCDF) calculation [2, 3]. The theoretical predictions based on MCDF calculations have been carried out within different approximations and remained hitherto non-satisfactory in many relations. Earlier [8–13] it has been proposed relativistic perturbation theory (PT) method of the Auger decay characteristics for complex atoms, which is based on the Gell-Mann and Low S-matrix formalism energy approach) and QED PT formalism [4–7]. The novel element consists in an using the optimal basis of the electron state functions derived from the minimization condition for the calibration-non-invariant contribution (the second order PT polarization diagrams contribution) to the imaginary part of the multi-electron system energy already at the first non-disappearing approximation of the PT. Earlier it has been applied in

studying the Auger decay characteristics for a set of neutral atoms, quasi-molecules and solids. Besides, the ionization cross-sections of inner shells in various atoms and the Auger electron energies in solids were estimated. Here we present new results of determination and analysis of the resonant Auger transition spectra characteristics for atoms of the inert gases (Ne, Xe), which are obtained within the relativistic multi-body theory [8–13] and compared with available experimental and other theoretical data. A number of the Auger transition parameters has been firstly presented.

2. THEORETICAL APPROACH TO DETERMINATION OF THE AUGER DECAY CHARACTERISTICS

Within the frame of QED PT approach the Auger transition probability and the Auger line intensity are defined by the square of an electron interaction matrix element having the form [5]:

$$V_{1234}^{\omega} = [(j_1)(j_2)(j_3)(j_4)]^{1/2} \times \\ \times \sum_{\mu} (-1)^{\mu} \begin{pmatrix} j_1 j_3 & \lambda \\ m_1 - m_3 & \mu \end{pmatrix} \times \text{Re } Q_{\lambda}(1234); \\ Q_{\lambda} = Q_{\lambda}^{\text{Quil}} + Q_{\lambda}^{\text{Br}}. \quad (1)$$

The terms $Q_{\lambda}^{\text{Quil}}$ and Q_{λ}^{Br} correspond to subdivision of the potential into Coulomb part $\cos|\omega|r_{12}/r_{12}$ and Breit one, $\cos|\omega|r_{12}\alpha_1\alpha_2/r_{12}$. The real part of the electron interaction matrix element is determined using expansion in terms of Bessel functions:

$$\frac{\cos|\omega|r_{12}}{r_{12}} = \frac{\pi}{2\sqrt{r_1 r_2}} \times \\ \times \sum_{\lambda=0} (\lambda) J_{\lambda+1/2}(|\omega|r_{<}) J_{-\lambda-1/2}(|\omega|r_{>}) P_{\lambda}(\cos \mathbf{r}_1 \mathbf{r}_2), \quad (2)$$

where J is the 1st order Bessel function, $(\lambda) = 2\lambda + 1$. The Coulomb part $Q_{\lambda}^{\text{Quil}}$ is ex-

pressed in terms of radial integrals R_λ , angular coefficients S_λ [4]:

$$\begin{aligned} \text{Re } Q_\lambda^{\text{oul}} = & \frac{1}{Z} \text{Re} \{ R_\lambda(1243) S_\lambda(1243) + \\ & + R_\lambda(\tilde{1}2\tilde{4}\tilde{3}) S_\lambda(\tilde{1}2\tilde{4}\tilde{3}) + R_\lambda(1\tilde{2}\tilde{4}\tilde{3}) S_\lambda(1\tilde{2}\tilde{4}\tilde{3}) + \\ & + R_\lambda(\tilde{1}\tilde{2}\tilde{4}\tilde{3}) S_\lambda(\tilde{1}\tilde{2}\tilde{4}\tilde{3}) \}. \end{aligned} \quad (3)$$

As a result, the Auger decay probability is expressed in terms of $\text{Re } Q_\lambda(1243)$ matrix elements:

$$\text{Re } R_\lambda(1243) = \iint dr_1 r_1^2 r_2^2 f_1(r_1) f_3(r_1) f_2(r_2) f_4(r_2) Z_\lambda^{(1)}(r_-) Z_\lambda^{(1)}(r_+), \quad (4)$$

where f is the large component of radial part of single electron state Dirac function; function Z and angular coefficient are defined in refs. [4–7]. The other items in (3) include small components of the Dirac functions; the sign « \sim » means that in (3) the large radial component f_i is to be changed by the small g_i one and the moment l_i is to be changed by $\tilde{l}_i = l_i - 1$ for Dirac number $\alpha_1 > 0$ and $l_i + 1$ for $\alpha_i < 0$.

The Breat interaction is known to change considerably the Auger decay dynamics in some cases. The Breat part of Q is defined in [4, 5]. The Auger width is obtained from the adiabatic Gell–Mann and Low formula for the energy shift [5]. The direct contribution to the Auger level width with a vacancy $n_\alpha l_\alpha j_\alpha m_\alpha$ is as follows:

$$\sum_\lambda \frac{2}{(\lambda)(j_\alpha)} \sum_{\beta\gamma \leq j} \sum_{k > f} Q_\lambda(\alpha k \gamma \beta) Q_\lambda(\beta \gamma k \alpha), \quad (5)$$

while the exchange diagram contribution is:

$$\frac{2}{(j_\alpha)} \sum_{\lambda_1 \lambda_2} \sum_{\beta\gamma \leq j} \sum_{k > f} Q_{\lambda_1}(\alpha k \gamma \beta) Q_{\lambda_2}(\beta \gamma k \alpha) \begin{Bmatrix} j_\alpha & j_\gamma & \lambda_2 \\ j_k & j_\beta & \lambda_1 \end{Bmatrix}. \quad (6)$$

The partial items of the $\sum_{\beta\gamma} \sum_k$ sum answer

to contributions of $\alpha^{-1} \rightarrow (\beta\gamma)^{-1} K$ channels resulting in formation of two new vacancies $\beta\gamma$ and one free electron k : $\omega_k = \omega_\alpha + \omega_\beta - \omega_\alpha$. The final expression for the width in the representation of jj -coupling scheme of single-electron moments has the form:

$$\Gamma(2j_1^o l_1^o, 2j_2^o l_2^o; J) = 2 \sum_{jkl} |\Gamma(2j_1^o l_1^o, 2j_2^o l_2^o; l_o, kjl)|^2. \quad (7)$$

Here the summation is made over all possible decay channels.

Contribution of the main polarization diagrams (the particle-hole interaction) of the second and higher orders of the PT to the energy can be presented as follows:

$$E(A) = \iint dr_1 dr_2 \cdot \mathbf{p}_1(r_1) \cdot V_{\text{pol}}^d(r_1 r_2) \cdot \mathbf{p}_2(r_2) \quad (8)$$

with effective two-quasiparticle interaction [3]:

$$\begin{aligned} V_{\text{pol}}^d(r_1 r_2) = & X \left\{ \frac{dr'(\rho_c^{(0)}(r'))^{1/3} \theta(r')}{|r_1 - r'| \cdot |r' - r_2|} - \right. \\ & \left. \int \frac{dr'(\rho_c^{(0)}(r'))^{1/3} \theta(r')}{|r_1 - r'|} \times \int \frac{dr''(\rho_c^{(0)}(r''))^{1/3} \theta(r'')}{|r'' - r_2|} \right\} / \langle (\rho_c^{(0)})^{1/3} \rangle, \\ \langle (\rho_c^{(0)})^{1/3} \rangle = & \int dr (\rho_c^{(0)}(r))^{1/3} \theta(r), \quad (9) \\ \theta(r) = & \left\{ 1 + \frac{[3\pi^2 \cdot \rho_c^{(0)}(r)]^{2/3}}{c^2} \right\}^{1/2}, \end{aligned}$$

where ρ_c^0 is the core (“Fermi sea”) electron density (without quasiparticles), X is the numerical coefficient, c is the velocity of light. The similar potential representation can be obtained for the exchange polarization quasiparticle interaction (see details in ref. [3, 11, 13]).

The basis of the particle state functions is defined by the solution of the Dirac–Fock equation (integrated numerically using the Runge–Cutt method). Novel element is connected with using ab initio paoptimized Dirac–Fock potential with the formal parameter which is determined on the basis of the QED optimization procedure (see details in refs. [4–6, 11, 13]).

The calculation of radial integrals $\text{Re } R_\lambda(1243)$ is reduced to the solution of a system of differential equations [5]:

$$\begin{aligned} y_1' = & f_1 f_3 Z_\lambda^{(1)}(\alpha|\omega|r) r^{2+\lambda}; \\ y_2' = & f_2 f_4 Z_\lambda^{(1)}(\alpha|\omega|r) r^{2+\lambda}; \\ y_3' = & [y_1 f_2 f_4 + y_2 f_1 f_3] Z_\lambda^{(2)}(\alpha|\omega|r) r^{1-\lambda}. \end{aligned} \quad (8)$$

In addition,

$$y_3(\infty) = \text{Re } R_\lambda(1243), \quad y_1(\infty) = X_\lambda(13).$$

The formulae for the Auger decay probability include the radial integrals $R_\alpha(\alpha k \gamma \beta)$, where one of the functions describes electron in the continuum state. The energy of an electron formed due to a transition jkl is defined by the difference between energies of atom with a hole at j level and double-ionized atom at kl levels in final state:

$$E_A(jkl, {}^{2S+1}L_J) = E_A^+(j) - E_A^{2+}(kl, {}^{2S+1}L_J). \quad (10)$$

To single out the above-mentioned correlation effects, the equation (12) can be presented as [8, 9]:

$$\begin{aligned} E_A(jkl, {}^{2S+1}L_J) = & E(j) - E(k) - E(l) - \\ & - \Delta(k, l; {}^{2S+1}L_J), \end{aligned} \quad (11)$$

where the item Δ takes into account the dynamic correlation effects (relaxation due to hole screening with electrons etc.) To take these effects into account, the set of procedures elaborated in the atomic theory [8–13] is used.

3. RESULTS AND CONCLUSIONS

In tables 1 we present the data on the transition energies and angular anisotropy parameter β (for each parent state) for the resonant

Auger decay to the $2s^1 2p^5(^1P) np$ and $2s^0 p^6(^2S) np$ ($n = 3, 4$) states of Ne^+ . There are listed the experimental data by De Fanis et al [18] and Pahler et al [15], theoretical *ab initio* Hartree-Fock results [18] and our data, obtained within the relativistic many-body PT with using the gauge-invariant QED PT method for generating relativistic functions basis's. In table 2 we the data on the widths (meV) for the $2s^1 2p^5(^1P) np$ and $2s^0 p^6(^1S) np$ ($n = 3, 4$) states of Ne^+ . There are listed the experimental data by [18], theoretical *ab initio* multi configuration Hartree-Fock results by Sinanis et al [16], single-configuration Hartree-Fock data by Armen—Larkins

[17] and our data, obtained within the relativistic many-body PT.

In table 3 we present data on the initial and final states of the most intense $4d^{-2} \rightarrow 4d^{-1} \rightarrow 5p^{-2}$ and $4d^{-1} 5p^{-2} \rightarrow 5p^{-4}$ Auger transitions in the neutral xenon. The calculated intensities are given relative to the creation of one 3d hole, and only intensities ≥ 0.005 are listed. Our theoretical data (the relativistic many-body PT) and the theoretical pseudorelativistic Hartree Fock data by Jonauskas et al [19], semiempirical (with using the Cowan code) [20] and experimental [19] kinetic energies of the Auger transitions are also given.

Table 1

Transition energies E_k , angular anisotropy parameters β (for each parent state for the resonant Auger decay to the $2s^1 2p^5(^1P) np$ and $2s^0 p^6(^2S) np$ ($n = 3, 4$) states of Ne^+ : the experimental data [18, 15], theoretical *ab initio* Hartree-Fock results [18] and our data, obtained within the relativistic many-body PT

Final state	Exp. E_k , [18]	Theory: E_k , [18]	Theory: E_k , our	β ; Exp. [18]	Theory: β , [18]	Theory: β — our data
$2s^1 2p^5(^1P) 3p^2 S$	778.79	776.43	778.52	1.7 ± 0.3	2.000	1.832
$2s^1 2p^5(^1P) 3p^2 P$	778.54	776.40	778.27	-0.94 ± 0.06	-0.996	-0.959
$2s^1 2p^5(^1P) 3p^2 D$	778.81	776.66	778.57	0.20 ± 0.06	0.200	0.202
$2s^1 2p^5(^1P) 3p^2 S$	788.16	786.51	787.88	1.5 ± 0.1	1.998	1.678
$2s^1 2p^5(^1P) 3p^2 P$	788.90	787.52	788.69	-0.91 ± 0.06	-0.928	-0.916
$2s^1 2p^5(^1P) 3p^2 D$	789.01	787.64	788.82	0.06 ± 0.05	0.156	0.074
$2s^1 2p^5(^1P) 4p^2 S$	773.60		773.48	0.96 ± 0.28		0.972
$2s^1 2p^5(^1P) 4p^2 P$	773.48		773.25	-0.92 ± 0.06		-0.928
$2s^1 2p^5(^1P) 4p^2 D$	773.56		773.33	0.15 ± 0.06		0.156
$2s^1 2p^5(^3P) 4p^2 S$	783.72		783.54	1.97 ± 0.40		2.045
$2s^1 2p^5(^3P) 4p^2 P$	783.95		783.78	-0.43 ± 0.09		-0.444
$2s^1 2p^5(^3P) 4p^2 D$	784.01		783.82	0.09 ± 0.20		0.102
$2s^0 2p^6(^1S) 3p^2 P$	—		754.93	0.05 ± 0.14		0.061
$2s^0 2p^6(^1S) 4p^2 P$	—		749.85	0.07 ± 0.18		0.082

Table 2

Widths (meV) for the $2s^1 2p^5(^1P) np$ and $2s^0 p^6(^1S) np$ ($n = 3, 4$) states of Ne^+ : the experimental data [18], theoretical *ab initio* multi configuration Hartree-Fock results by Sinanis et al [16], single-configuration Hartree-Fock data by Armen—Larkins [17] and our data, obtained within the relativistic many-body PT

final state	Exp. [18]	Exp. [15]	Theory [17]	Theory [16]	Theory: Our data
$2s^1 2p^5(^1P) 3p^2 S$	530 ± 50	410 ± 50	687	510	524
$2s^1 2p^5(^1P) 3p^2 P$	42 ± 3	—	20.7	—	38
$2s^1 2p^5(^1P) 3p^2 D$	34 ± 4	—	40.2	—	32
$2s^1 2p^5(^3P) 3p^2 S$	120 ± 10	110 ± 40	18.8	122	118
$2s^1 2p^5(^3P) 3p^2 P$	19 ± 5	—	10.3	—	16
$2s^1 2p^5(^3P) 3p^2 D$	80 ± 10	—	62.3	—	72
$2s^1 2p^5(^1P) 4p^2 S$	135 ± 20	—	—	—	121
$2s^1 2p^5(^1P) 4p^2 P$	—	—	—	—	3
$2s^1 2p^5(^1P) 4p^2 D$	—	—	—	—	8
$2s^1 2p^5(^3P) 4p^2 S$	—	—	—	—	27
$2s^0 2p^6(^1S) 3p^2 P$	80 ± 5	—	—	—	78
$2s^0 2p^6(^1S) 4p^2 P$	20 ± 3	—	—	—	18

Table 3

Calculated and experimental intensities I , kinetic energies E_k for Xe (*see text*)

	Initial state	Final state	I [19]	I , our	Theor E [19]	Theor E , our	Theor E [20]	Exp. [19]
a	$4d^2\ ^1G_4 \rightarrow$	$4d^{-1}\ 5p^2(^1D)\ ^2F_{5/2}$	0.005	0.006	31.5	31.3		}
a	$4d^2\ ^1G_4 \rightarrow$	$4d^{-1}\ 5p^2\ (^3P)\ ^2F_{7/2}$	0.013	0.014	31.2	31.0		} 30.8
a	$4d^2\ ^1G_4 \rightarrow$	$4d^{-1}\ 5p^2\ (^1D)\ ^2G_{9/2}$	0.009	0.010	30.9	30.6		}
b	$4d^2\ ^1D_2 \rightarrow$	$4d^{-1}\ 5p^2\ (^3P)\ ^2D_{5/2}$	0.005	0.006	30.5	30.3		30.3
c	$4d^2\ ^1G_4 \rightarrow$	$4d^{-1}\ 5p^2\ (^3P)\ ^2D_{3/2}$	0.007	0.007	30.1	30.0		29.9
d	$4d^2\ ^1G_4 \rightarrow$	$4d^{-1}\ 5p^2\ (^1D)\ ^2D_{5/2}$	0.005	0.006	29.3	29.2		}
d	$4d^2\ ^1D_2 \rightarrow$	$4d^{-1}\ 5p^2\ (^1D)\ ^2F_{7/2}$	0.008	0.009	29.1	29.1		} 29.1
d	$4d^2\ ^1G_4 \rightarrow$	$4d^{-1}\ 5p^2\ (^1D)\ ^2F_{7/2}$	0.008	0.009	29.1	29.1		}
d	$4d^2\ ^3F_4 \rightarrow$	$4d^{-1}\ 5p^2\ (^3P)\ ^4F_{9/2}$	0.006	0.007	29.1	29.1		}
e	$4d^2\ ^3F_4 \rightarrow$	$4d^{-1}\ 5p^2\ (^3P)\ ^4F_{5/2}$	0.007	0.006	28.4	28.3		
e	$4d^2\ ^3F_4 \rightarrow$	$4d^{-1}\ 5p^2\ (^3P)\ ^2F_{5/2}$	0.005	0.005	28.1	28.0		} 28.3
f	$4d^2\ ^1G_4 \rightarrow$	$4d^{-1}\ 5p^2\ (^1S)\ ^2D_{5/2}$	0.018	0.019	27.8	27.8		27.9
g	$4d^2\ ^3F_2 \rightarrow$	$4d^{-1}\ 5p^2\ (^1D)\ ^2G_{9/2}$	0.005	0.006	27.4	27.3		} 27.1
g	$4d^2\ ^3P_1 \rightarrow$	$4d^{-1}\ 5p^2\ (^1S)\ ^2D_{5/2}$	0.005	0.006	27.0	26.9		
h	$4d^2\ ^3F_4 \rightarrow$	$4d^{-1}\ 5p^2\ (^3P)\ ^2F_{5/2}$	0.008	0.009	26.5	26.5		} 26.5
h	$4d^2\ ^1D_2 \rightarrow$	$4d^{-1}\ 5p^2\ (^1S)\ ^2D_{3/2}$	0.009	0.010	26.1	26.2		
h	$4d^2\ ^1G_4 \rightarrow$	$4d^{-1}\ 5p^2\ (^1S)\ ^2D_{3/2}$	0.008	0.008	26.1	26.2		
h	$4d^2\ ^3P_2 \rightarrow$	$4d^{-1}\ 5p^2\ (^1S)\ ^2D_{5/2}$	0.006	0.006	25.9	26.0		
i	$4d^2\ ^3F_4 \rightarrow$	$4d^{-1}\ 5p^2\ (^1D)\ ^2G_{9/2}$	0.008	0.008	25.6	25.9		—
j	$4d^2\ ^3F_2 \rightarrow$	$4d^{-1}\ 5p^2\ (^1S)\ ^2D_{5/2}$	0.005	0.006	24.3	24.6		24.7
k	$4d^2\ ^3F_4 \rightarrow$	$4d^{-1}\ 5p^2\ (^1S)\ ^2D_{5/2}$	0.006	0.007	22.5	22.9		
l	$4d^{-1}\ 5p^2(^1S)\ ^2D_{3/2}$	$5p^4\ ^1D_2$	0.010	0.010	20.8	20.9	20.9	21.0
m	$4d^{-1}\ 5p^2(^1S)\ ^2D_{5/2}$	$5p^4\ ^1D_2$	0.021	0.022	19.2	19.3	19.5	} 19.3
m	$4d^{-1}\ 5p^2(^1D)\ ^2S_{1/2}$	$5p^4\ ^1D_2$	0.005	0.006	18.9	19.0	18.9	
n	$4d^{-1}\ 5p^2(^1S)\ ^2D_{3/2}$	$5p^4\ ^1S_0$	0.014	0.015	18.3	18.7	18.9	18.9
o	$4d^{-1}\ 5p^2(^1D)\ ^2P_{3/2}$	$5p^4\ ^1D_2$	0.009	0.009	17.9	18.3		
o	$4d^{-1}\ 5p^2(^3P)\ ^4D_{5/2}$	$5p^4\ ^3P_0$	0.017	0.018	17.9	18.3		
o	$4d^{-1}\ 5p^2(^3P)\ ^2F_{5/2}$	$5p^4\ ^3P_1$	0.005	0.005	17.8	18.2		} 18.6
o	$4d^{-1}\ 5p^2(^3P)\ ^2F_{7/2}$	$5p^4\ ^3P_2$	0.011	0.012	17.7	18.1		
o	$4d^{-1}\ 5p^2(^1D)\ ^2D_{5/2}$	$5p^4\ ^1D_2$	0.009	0.009	17.6	18.0	18.4	
p	$4d^{-1}\ 5p^2(^3P)\ ^2F_{5/2}$	$5p^4\ ^3P_2$	0.006	0.007	17.1	17.6		
q	$4d^{-1}\ 5p^2(^1S)\ ^2D_{5/2}$	$5p^4\ ^1S_0$	0.017	0.017	16.7	17.3	17.5	} 17.5
q	$4d^{-1}\ 5p^2(^3P)\ ^2D_{5/2}$	$5p^4\ ^1D_2$	0.009	0.009	16.4	17.0		
r	$4d^{-1}\ 5p^2(^1D)\ ^2G_{9/2}$	$5p^4\ ^1D_2$	0.020	0.021	16.0	16.6	16.6	16.6
s	$4d^{-1}\ 5p^2(^3P)\ ^2F_{7/2}$	$5p^4\ ^1D_2$	0.008	0.009	15.7	16.3		
s	$4d^{-1}\ 5p^2(^1D)\ ^2F_{7/2}$	$5p^4\ ^1S_0$	0.005	0.005	15.4	15.9		
s	$4d^{-1}\ 5p^2(^3P)\ ^2F_{5/2}$	$5p^4\ ^1D_2$	0.005	0.005	15.2	15.7		
t	$4d^{-1}\ 5p^2(^3P)\ ^2D_{3/2}$	$5p^4\ ^1S_0$	—	0.005	—	14.9		
u	$4d^{-1}\ 5p^2(^1D)\ ^2G_{9/2}$	$5p^4\ ^1S_0$	—	0.006	—	14.1		

The analysis of the presented results in tables 1—3 allows to conclude that the précised description of the Auger processes requires the detailed accurate accounting for the exchange-correlation effects, including the particle-hole interaction, screening effects and iterations of the mass operator. The relativistic many-body

PT approach provides more accurate results that is due to a considerable extent to more correct accounting for complex inter electron exchange-correlation effects. It is important to note that using the more correct gauge-invariant procedure of generating the relativistic orbital basis's directly linked with correctness of accounting

for the correlation effects. The same is regarding the procedure of accounting the relativistic effects (especially for Xe).

REFERENCES

1. Kulekshov V. F., Kukharev Yu. A., Fridrikhov S. A. et al. Spectroscopy and Electron Diffraction in Solid Surfaces Studies. Nauka: Moscow, 1985.
2. Aberg T., Hewat G. Theory of Auger effect. Springer-Verlag: Berlin, 1999.
3. Aglitsky E. V., Safronova U. I. Spectroscopy of Autoionization states of atomic systems. Energoatomizdat: Moscow, 1992.
4. Glushkov A. V., Relativistic Quantum Theory. Quantum, mechanics of Atomic Systems. — Odessa: Astroprint, 2008. — 900 P.
5. Glushkov A. V., Ivanov L. N., Ivanova E. P., Generalized energy approach to radiation and autoionization decay of the atomic states // Autoionization Phenomena in Atoms. — Univ. Press, Moscow. — 1986. — P. 58—160.
6. Glushkov A. V., Ivanov L. N. Radiation decay of atomic states: Atomic residue and gauge non-invariant contributions // Phys. Lett. A. — 1992. — Vol. 170, N 1. — P. 33—37.
7. Glushkov A. V., Khetselius O. Yu., Gurnitskaya E. P., Loboda A. V., Lovett L., et al. Gauge-invariant QED perturbation theory approach to calculating nuclear electric quadrupole moments, hyperfine structure constants for heavy atoms and ions // Frontiers in Quantum Systems in Chemistry and Physics (Springer). — 2008. — Vol. 18. — P. 505—558.
8. Nikola L. V., Quantum calculation of Auger spectra for Na, Si atoms and solids // Photoelectronics. — 2007. — N 16. — P. 102—105.
9. Ambrosov S. V., Glushkov A. V., Nikola L. V., Sensing the Auger spectra for solids: New quantum approach // Sensor Electr. and Microsyst. Techn. — 2006. — N 3. — P. 46—50.
10. Tjurin A. V., Nikola L. V., Khetselius O. Yu., Sukharev D. E., Sensing the finite size nuclear effect in calculation of the Auger spectra for atoms and solids // Sensor Electr. and Microsyst. Techn. — 2007. — N 1. — P. 18—21.
11. Glushkov A. V., Svinarenko A. A., Malinovskaya S. V., Khetselius O. Yu., Loboda A. V., Lopatkin Yu. M., Nikola L. V., Perelygina T. B., Generalized energy approach to calculating electron collision cross-sections for multicharged ions in a plasma: Debye shielding model // Internat. Journal of Quantum Chem. — 2011. — Vol. 111, N 2. — P. 288—296.
12. Svinarenko A. A., Nikola L. V., Prepelitsa G. P., Tkach T., Mischenko E., The Auger decay of excited states in spectra of multicharged ions: relativistic theory // Spectral Lines Shape (AIP, USA). — 2010. — Vol. 16. — P. 94—98.
13. Nikola L. V., Ignatenko A. V., Shakhman A. N., Relativistic theory of the Auger (autoionization) decay of excited states in spectrum of multicharged ion // Photoelectronics. — 2010. — N19. — P. 61—64.
14. Osmekhin S., Fritzsche S., Grum-Grzhimailo A. N., Huttula M., Aksela H., Aksela S., Angle-resolved study of the Ar $2p^{-1}_{1/2}3d$ resonant Auger decay // J. Phys. B: At. Mol. Opt. Phys. — 2008. — Vol. 41. — P. 145003.
15. Pahler M., Caldwell C. D., Schaphorst S. J., Krause M., Intrinsic linewidths of neon $2s2p^{(1,3P)}nl^2L$ correlation satellites // J. Phys. B: At. Mol. Opt. Phys. — 1993. — Vol. 26. — P. 1617—1622.
16. Sinanis C., Aspromalis G., Nicolaidis C., Electron correlation in the Auger spectra of the Ne⁺ K $2s2p^{(3,1P^0)}3p^2S$ satellites // J. Phys. B: At. Mol. Opt. Phys. — 1995. — Vol. 28. — P. L423—428.
17. Armen G. B., Larkins F. P., Valence Auger and X-ray participator and spectator processes for neon and argon atoms // J. Phys. B: At. Mol. Opt. Phys. — 1991. — Vol. 24. — P. 741—760.
18. De Fanis A., Tamenori Y., Kitajima M., Tanaka H., Ueda K., Doppler-free resonant Auger Raman spectroscopy on atoms and molecules at Spring-8 // Journ. of Phys. CS. — 2004. — Vol. 183. — P. 63—72.
19. Jonauskas V., Partanen L., Kucas S., Karazija R., Huttula M., Aksela S., Aksela H., Auger cascade satellites following 3d ionization in xenon // Journ. of Phys. B: At. Mol. Opt. Phys. — 2003. — Vol. 36. — P. 4403—4416.
20. Cowan D., Methods of atomic structure calculations. — N. Y., 1999. — 280 P.

UDC 535.42

L. V. Nikola

RESONANT AUGER SPECTROSCOPY OF THE ATOMS OF INERT GASES

Abstract

The results of determination and analysis of the resonant Auger transition spectra characteristics for atoms of the inert gases are obtained within the relativistic multi-body theory and compared with available experimental and other theoretical data. A number of the Auger transition parameters have been firstly presented.

Key words: Auger spectroscopy, atom of inert gas, relativistic theory

УДК 535.42

Л. В. Нікола

РЕЗОНАНСНА ОЖЕ СПЕКТРОСКОПІЯ АТОМІВ ІНЕРТНИХ ГАЗІВ

Резюме

Представлені результати теоретичного визначення в рамках релятивістської многочастинкової теорії та аналізу характеристик резонансних спектрів Оже переходів для атомів інертних газів і проведено їх порівняння з наявними експериментальними та альтернативними теоретичними даними. Для ряду Оже переходів характерні параметри отримані вперше.

Ключові слова: Оже спектроскопія, атом інертного газу, релятивістська теорія.

УДК 535.42

Л. В. Нікола

РЕЗОНАНСНА ОЖЕ СПЕКТРОСКОПІЯ АТОМІВ ІНЕРТНИХ ГАЗІВ

Резюме

Наведені результати теоретичного визначення у межах релятивістської багаточастинкової теорії та аналізу характеристик резонансних спектрів Оже переходів для атомів інертних газів і проведено їх порівняння з наявними експериментальними та альтернативними теоретичними даними. Для ряду Оже переходів характерні параметри отримані вперше.

Ключові слова: Оже спектроскопія, атом інертного газу, релятивістська теорія.

ELECTROMAGNETIC AND STRONG INTERACTIONS EFFECTS IN X-RAY SPECTROSCOPY OF PIONIC ATOMS

it is given an analysis of the electromagnetic and strong interactions contributions to the transitions energies in the X-ray spectra of the pionic atomic systems. It is considered an advanced approach to redefinition of the meson-nucleon phenomenological optical model potential parameters and increasing an accuracy of the hadronic transitions energies definition.

In this paper we give an analysis of the electromagnetic, hyperfine, electroweak and strong interactions contributions to the transitions energies in the X-ray spectra of hadronic atomic systems and discuss the X-ray standards status. Besides, it is considered an advanced approach to redefinition of the pion-nucleon phenomenological optical model potential parameters and increasing an accuracy of the hadronic X-ray transitions energies definition. As it is known, one of the fundamental questions in the modern hadron's physics is that the hadron masses being much higher than the mass of their quark content. The current mass of the up (u) and down (d) quarks is two orders of magnitude smaller than a typical hadron's mass of about 1 GeV. This extraordinary phenomenon is proposed to originate from spontaneous breaking of chiral symmetry of massless quarks in strong interaction physics [1—5]. At present time one of the most sensitive tests for the chiral symmetry breaking scenario in the modern hadron's physics is provided by studying the exotic hadron-atomic systems. One could turn the attention on the some differences between the pionic and kaonic systems. In the kaonic case one deals with the strangeness sector, and, for example, the strong interaction effect amounts to a very small shift and width in pionic hydrogen of 7 and 1 eV respectively. Nowadays the transition energies in pionic (kaonic, muonic etc.) atoms are measured with an unprecedented precision and from studying spectra of the hadronic atoms it is possible to investigate the strong interaction at low energies measuring the energy and natural width of the ground level with a precision of few meV [1—20].

The mechanism of creation of the hadronic atoms is well known now (e. g. [1, 2]). Really, such an atom is formed when a negative pion enters a medium, loses its kinetic energy through ionization and excitation of the atoms and molecules and eventually is captured, replacing the electron, in an excited atomic orbit. The further de-excitation scenario includes the different cascade processes such as the Auger transitions, Coulomb de-excitation, scat-

tering etc. When a pion reaches a low-n state with the little angular momentum, strong interaction with the nucleus causes its absorption. The strong interaction is the reason for a shift in the energies of the low-lying levels from the purely electromagnetic values and the finite lifetime of the state corresponds to an increase in the observed level width. The possible energy shifts caused by the pion-induced fluorescence X-rays were checked in the measurement of the pion beams at PSI in Switzerland. The systematic error of the fit functions is found to be 2 eV.

The most known theoretical models to treating the hadronic atomic systems are presented in refs. [9—11, 16—20]. In refs. [6, 20] there were developed an effective *ab initio* schemes to the Klein—Gordon equation solution and further definition of the X-ray spectra for multi-electron kaonic atoms with the different schemes for account for the nuclear, radiative, correlation effects. The theoretical studying the strong interaction shifts and widths from X-ray spectroscopy of kaonic atoms (U, Pb etc) was fulfilled. The most difficult aspects of the theoretical modeling are reduced to the correct description of the kaon (pion)-strong interaction as the electromagnetic part of the problem is reasonably accounted for in models [16—20]. Besides, quite new aspect is linked with the possible, obviously, very tiny electroweak and hyperfine interactions.

All available theoretical models to treating the hadronic (kaonic, pionic) atoms are naturally based on the using the Klein—Gordon equation (e. g. [2]):

$$m^2 c^2 \Psi(x) = \left\{ \frac{1}{c^2} [i\hbar \partial_t + eV_0(r)]^2 + \hbar^2 \nabla^2 \right\} \Psi(x), \quad (1)$$

where c is a speed of the light, \hbar is the Planck constant, and $\Psi_0(x)$ is the scalar wave function of the space-temporal coordinates. Usually one considers the central potential $[V_0(r), 0]$ approximation with the stationary solution:

$$\Psi(x) = \exp(-iEt/\hbar) \varphi(x), \quad (2)$$

where $\varphi(x)$ is the solution of the stationary equation.

$$\left\{ \frac{1}{c^2} [E + eV_0(r)]^2 + \hbar^2 \nabla^2 - m^2 c^2 \right\} \varphi(x) = 0. \quad (3)$$

Here E is the total energy of the system (sum of the mass energy mc^2 and binding energy ϵ_0). In principle, the central potential V_0 naturally includes the central Coulomb potential, the vacuum-polarization potential, the strong interaction potential. Standard approach to treating the last interaction is provided by the well known optical potential model (c. g. [11]). Practically in all works the central potential V_0 is the sum of the following potentials. The nuclear potential for the spherically symmetric density $\rho(r|R)$ is:

$$V_{\text{nuc}}(r|R) = -((1/r) \int_0^r dr' r'^2 \rho(r') R) + \int_r^\infty dr' r' \rho(r') R. \quad (4)$$

The most popular Fermi-model approximation the charge distribution in the nucleus $\rho(r)$ (c. f. [1, 2]) is as follows:

$$\rho(r) = \rho_0 / \{1 + \exp[(r - c)/a]\}, \quad (5)$$

where the parameter $a = 0.523$ fm, the parameter c is chosen by such a way that it is true the following condition for average-squared radius: $\langle r^2 \rangle^{1/2} = (0.836 \cdot A^{1/3} + 0.5700)$ fm. The effective algorithm for its definition is used in refs. [7, 18–20] and reduced to solution of the following system of the differential equations:

$$V'_{\text{nuc}}(r, R) = (1/r^2) \int_0^r dr' r'^2 \rho(r', R) \equiv (1/r^2) y(r, R),$$

$$y'(r, R) = r^2 \rho(r, R), \quad (6)$$

$$\rho'(r) = (\rho_0/a) \exp[(r - c)/a] \{1 + \exp[(r - c)/a]\}^2$$

with the boundary conditions:

$$V_{\text{nuc}}(0, R) = -4/(\pi r), \quad y(0, R) = 0, \\ \rho(0) = \rho_0 / \{1 + \exp[-c/a]\}. \quad (7)$$

Another, probably, more consistent approach is in using the relativistic mean-field (RMF) model, which been designed as a renormalizable meson-field theory for nuclear matter and finite nuclei [21–24]. To take into account the radiation corrections, namely, the effect of the vacuum polarization there are traditionally used the Ueling potential and its different modifications such as [1–7]. The most difficult aspect is an adequate account for the strong interaction.

In the pion-nucleon state interaction one should use the following pulse approximation expression for scattering amplitude of a pion on the “i” nucleon [1, 2]:

$$f_i(r) = \{b'_0 + b'_1(t\tau) + [c'_0 + c'_1(t\tau)]kk'\} \times \\ \times \delta(r - r_i), \quad (10)$$

where t and τ are the isospines of pion and nucleon. The nucleon spin proportional terms of the kind $\sigma[kk']$ are omitted. The constants in (10) can be expressed through usual s-wave (α_{2T}) and p-wave ($\alpha_{2T, 2I}$) scattering length (T and I -isospin and spin of the system πN). The corresponding parameters in the Compton wave length λ_π terms are as follows:

$$b'_0 = (\alpha_1 + 2\alpha_3)/3 = -0.0017\lambda_\pi, \\ b'_1 = (\alpha_3 - \alpha_1)/3 = -0.086\lambda_\pi, \\ c'_0 = (4\alpha_{33} + 2\alpha_{13} + 2\alpha_{31} + \alpha_{11})/3 = \\ = -0.208(\lambda_\pi)^3, \\ c'_1 = (2\alpha_{33} - 2\alpha_{13} + \alpha_{31} - \alpha_{11})/3 = \\ = -0.184(\lambda_\pi)^3.$$

The scattering amplitude for pion on a nucleus is further received as a coherent sum of the πN -scattering lengths. πN -scattering. In approximation of the only s-wave interaction the corresponding potential can be written in the Dezer form [1, 2]:

$$V_N(r) = -2\pi\hbar^2\mu_\pi^{-1} [ZA^{-1}a_p + (A - Z)A^{-1}a_n] \rho(r). \quad (11)$$

The s-wave lengths of the $\pi^{-1}p$ -scattering $a_p = (2\alpha_1 + \alpha_3)/3$ и $\pi^{-1}n$ -scattering $a_n = \alpha_3$; scattering are introduced to Eq. (11). Because of the equality between $a_n = b'_0 + b'_1$ and $a_p = b'_0 + b'_1$ (with an opposite sign) the theoretical shift of the s-level with $T = 0$ ($A = 2Z$) from Eq. (12) is much less than the observed shift. So, the more correct approximation must take into account the effects of the higher orders.

In whole the energy of the hadronic atom is represented as the sum:

$$E \approx E_{KG} + E_{FS} + E_{VP} + E_N; \quad (12)$$

here E_{KG} — is the energy of a pion in a nucleus (Z, A) with the point-like charge (dominant contribution in (12)), E_{FS} is the contribution due to the nucleus finite size effect, E_{VP} is the radiation correction due to the vacuum-polarization effect, E_N is the energy shift due to the strong interaction V_N . The last contribution can be defined from the experimental energy values as:

$$E_N = E - (E_{KG} + E_{FS} + E_{VP}). \quad (13)$$

From the other side the strong pion-nucleus interaction contribution can be found from the solution of the Klein—Gordon equation with the corresponding meson-nucleon potential. In this case, this contribution E_N is the function of the potentials (8)–(11) parameters.

Let us further to analyse some theoretical and experimental results and present some proposals on the further improvement of the available theoretical approaches. In tables 1 the data on the transition energies in some pionic atoms (from. Refs. [1–3]): the measured

Transition energies (keV) in the spectra of some pionic atoms

Element	E_{EXP} , keV			E_{KGF}	E_{th1}^N	E_{th2}^N
	Berkley	CERN	Virgginia			
Transition $2p - 1s$						
He ⁴			$10,69 \pm 0,06$	10,731	10,70	10,68
Li ⁶	$23,9 \pm 0,2$		$24,18 \pm 0,06$	24,472	24,09	24,06
Li ⁷	$23,8 \pm 0,2$		$24,06 \pm 0,06$	24,538	23,95	23,85
Transition $3d - 2p$						
Cl		$150,55 \pm 0,15$	$24,18 \pm 0,06$	149,051	150,38	150,46
K	$188,6 \pm 0,3$	$188,77 \pm 0,18$	$24,06 \pm 0,06$	186,445	188,43	188,53
Cu		$446,1 \pm 2,0$		437,424	444,24	445,03
Transition $4f - 3d$						
Cs ¹³³	$560,5 \pm 1,1$	$562,0 \pm 1,5$		553,330	561,47	562,12
Transition $5g - 4f$						
Tl		$561,67 \pm 0,25$		556,562	560,93	561,63
Pb		$575,56 \pm 0,25$		570,614	575,21	575,78
U ²³⁸	$731,4 \pm 1,1$	$732,0 \pm 0,4$	$730,88 \pm 0,75$	724,317	729,80	730,52

values form the Berkley, CERN and Virginea laboratories, theoretical values for the $2p - 1s$, $3d - 2p$, $4f - 3d$, $5g - 4f$ pionic transitions (E_{th1}^N — values from the Klein—Gordon—Fock equation with the pion-nucleus potential [3, 9, 17]; E_{KGF} — values from the Klein—Gordon—Fock equation with the finite size nucleus potential (our data), E_{th2}^N — values from the Klein—Gordon—Fock equation with the generalized pion-nucleus potential [20]: our data). It is easily to understand that when there is the close agreement between theoretical and experimental shifts, the corresponding energy levels are not significantly sensitive to strong nuclear.

interaction, i. e the electromagnetic contribution is dominative. In the opposite situation the strong-interaction effect is very significant. The analysis of the presented data indicate on the necessity of the further more exact experimental investigations and further improvement of the pion-nuclear potential modelling. Really, under availability of the "exact" values of the transitions energies one can perform the comparison of the theoretically and experimentally defined transition energies in the X-ray spectra in order to make a redefinition of the pion-nucleon model potential parameters using Eqs. (8)—(11). Taking into account the increasing accuracy of the X-ray pionic atom spectroscopy experiments, one can conclude that the such a way will make more clear the true values for parameters of the pion-nuclear potentials and correct the disadvantage of widely used parameterization of the potentials (8)—(11). The importance of the presented energy parameters is provided not only its great role in the X-ray spectroscopy of the hadronic systems. The high accuracy of the theoretical modelling and new experimental results can give an important infor-

mation about properties of the nuclei and hadrons (see below), in particular, masses, magnetic moments, spins and parity of some hadrons. Sensing the key parameters of the hyperfine, electromagnetic and strong interactions is of a great importance too.

In conclusion, the author would like to thank anonymous referee for invaluable comments and advices.

REFERENCES

1. Deslattes R., Kessler E., Indelicato P., de Billy L., Lindroth E., Anton J., Exotic atoms // *Rev. Mod. Phys.* — 2003. — Vol. 75. — P. 35—70.
2. Deloff A., Fundamentals in Hadronic Atom Theory, Singapore: World Scientific, 2003. — 352 P.
3. Menshikov L. I., Evseev, M. K., Some questions of physics of the exotic atoms // *Sov. Phys. — Uspekhi.* — 2001. — Vol. 171. — P. 150—184.
4. Hayano R. S., Hori M., Horvath D., Widman E., Antiprotonic helium and CPT invariance // *Rep. Prog. Phys.* — 2007. — Vol. 70. — P. 1995—2065.
5. Mohr P. J. Quantum Electrodynamics Calculations in few-Electron Systems // *Phys. Scripta.* — 1999. — Vol. 46, N 1. — P. 44—52.
6. Pavlovich V. N., Zelentsova T. N., Serga I. N., Analysis of the electromagnetic and strong interactions effects in x-ray spectroscopy of hadronic atoms and «kaonic helium puzzle» // *Photoelectronics.* — 2010. — N 19. — P. 65—69.
7. Glushkov A. V., Rusov V. D., Ambrosov S. V., Loboda A. V., Resonance states of compound super-heavy nucleus and EPPP in heavy nucleus collisions // *New Projects and New Lines of research in Nuclear Physics.* Eds. Fazio G. and Hanappe F.: Singapore, World Sci. — 2003. — P. 142—154.
8. Gall K. P., Austin E., Miller J. P., et al, Precision measurements of K- and Σ -masses // *Phys. Rev. Lett.* — 1999. — Vol. 60. — P. 186—190.
9. Anagnostopoulos D. F., Biri S., Boissourdain V., Demeter M., Borchert G., Egger J., Fuhrmann H., Gotta D., Gruber A., Hennebach M. et al // *Low-energy X-ray standards from pionic atoms* // *Nucl. Instrum. Methods B.* — 2003. — Vol. 205. — P. 9—18.
10. Anagnostopoulos D. F., Gotta D., Indelicato P., Simons L. M., Low-energy X-ray standards from hydrogenlike pionic atoms // *Arxiv: phys.* — 2003. — 0312090v1-P. 1—4.

11. Batty C. J., Eckhause M., Gall K. P., et al. Strong interaction effects in high Z- K⁻ atoms // Phys. Rev. C. — 1999. — Vol. 40. — P. 2154—2160.
12. S. Okada, G. Beer, H. Bhang, M. Cargnelli, J. Chiba, Seonho Choi, C. Curceanu, Y. Fukuda, T. Hanaki, R. S. Hayano, M. Iio, T. Ishikawa, S. Ishimoto, T. Ishiwatari, K. Itahashi, M. Iwai, M. Iwasaki, B. Juhasz, P. Kienle, J. Marton, Y. Matsuda, H. Ohnishi, H. Outa, M. Sato, P. Schmid, S. Suzuki, T. Suzuki, H. Tatsuno, D. Tomono, E. Widmann, T. Yamazaki, H. Yimc and J. Zmeskal, Precision measurement of the 3d → 2p x-ray energy in kaonic ⁴He // Phys. Lett. B. — 2007. — Vol. 653, N 5—6. — P. 387—391.
13. Ito T. M., Hayano R. S., Nakamura S. N., Tera-da T. P., Observation of kaonic hydrogen atom x rays // Phys. Rev. C. — 1999. — Vol. 58. — P. 2366—2382.
14. Ishiwatari T. on behalf of the SIDDHARTA Collaboration, Silicon drift detectors for the kaonic atom X-ray measurements in the SIDDHARTA experiment // Nucl. Instr. and Methods in Physics. Research Sec. A. Accelerators, Spectrometers, Detectors and Associated Equipment. — 2007. — Vol. 581, N 1—2. — P. 326—329.
15. M. Cargnelli, T. Ishiwatari, P. Kienle, J. Marton, E. Widmann, J. Zmeskal, G. Beer, A. M. Bragadireanu, T. Ponta, M. Bazzi, M. Catitti, C. Curceanu (Petrascu), C. Guaraldo, M. Iliescu, P. Levi Sandri, V. Lucherini, D. Pietreanu, D. L. Sirghi, F. Sirghi, P. Lechner, H. Soltau, L. Bombelli, C. Fiorini, T. Frizzi, A. Longoni, F. Ghio, B. Girolami, and L. Struder, Kaonic hydrogen X rays — experiments at DAFNE // Proc. KAON Int. Conf., Laboratori Nazionali di Frascati dell'INFN (Rome, Italy). — 2007. — 5 P.
16. Santos J. P., Parente F., Boucard S., Indelicato P., Desclaux J. P., X-ray energies of circular transitions and electron scattering in kaonic atoms // Phys. Rev. A. — 2005. — Vol. 71. — P. 032501.
17. Indelicato P., Trassinelli M., From heavy ions to exotic atoms // arXiv:physics. — 2005. — V1-0510126v1. — 16 P.
18. Sukharev D. E., Khetselius O. Yu., Dubrovskaya Yu. V., Sensing strong interaction effects in spectroscopy of hadronic atoms // Sensor Electr. and Microsyst. Techn. — 2009. — N 3. — P. 16—21.
19. Sukharev D. E., Florko T. A., Khetselius O. Yu., Dubrovskaya Yu. V., Bremsstrahlung and X-ray spectra for kaonic and pionic hydrogen and nitrogen // Photoelectronics. — 2009. — N 18. — P. 16—20.
20. Pavlovich V. N., Zelentsova T. N., Tarasov V. A., Serga I. N., Mudraya N. V., Interplay of the hyperfine, electroweak and strong interactions in heavy hadron-atomic systems and x-ray standards status // Sensor Electr. and Microsyst. Techn. — 2010. — N 2. — P. 20—26.
21. Serot B. D., Walecka J. D., Advances in Nuclear Physics Vol. 16: The Relativistic Nuclear Many Body Problem. Plenum Press, New York, 1999.
22. Ring P., Schuck P., The Nuclear Many-Body Problem. — Berlin: Springer, 2000.
23. Gambhir Y. K., Bhagwat A., The relativistic mean field and some of its recent applications // Physics of Elem. Part. and Atom. Nucl. — 2006. — Vol. 37. — P. 366—436.
24. Khetselius O. Yu., Relativistic perturbation theory calculation of the hyperfine structure parameters for some heavy-element isotopes // Int. Journ. of Quantum Chemistry. — 2009. — Vol. 109. — P. 3330—3335.

UDC 539.17

I. N. Serga

ELECTROMAGNETIC AND STRONG INTERACTIONS EFFECTS IN X-RAY SPECTROSCOPY OF PIONIC ATOMS

Abstract

It is given an analysis of the electromagnetic and strong interactions contributions to the transitions energies in the X-ray spectra of the pionic atomic systems. It is considered an advanced approach to redefinition of the meson-nucleon phenomenological optical model potential parameters and increasing an accuracy of the hadronic transitions energies definition.

Keywords: X-ray spectra, pionic atoms, relativistic theory.

УДК 539.17

И. Н. Серга

ЭФФЕКТЫ ЭЛЕКТРОМАГНИТНОГО И СИЛЬНОГО ВЗАИМОДЕЙСТВИЙ В РЕНТГЕНОВСКОЙ СПЕКТРОСКОПИИ ПИОННЫХ АТОМОВ

Резюме

Проанализированы вклады электромагнитного и сильного взаимодействий в энергии переходов в рентгеновских спектрах пион-атомных систем. Рассмотрен эффективный подход к переопределению параметров оптического модельного пион-нуклонного потенциала и увеличению точности определения энергий переходов в рентгеновских спектрах адронных атомов.

Ключевые слова: рентгеновские спектры, пионные атомы, релятивистская теория.

УДК 539.17

І. М. Серга

ЕФЕКТИ ЕЛЕКТРОМАГНІТНОЇ І СИЛЬНОЇ ВЗАЄМОДІЇ У РЕНТГЕНІВСЬКІЙ СПЕКТРОСКОПІЇ ПІОННИХ АТОМІВ

Резюме

Проаналізовані внески електромагнітної та сильної взаємодії в енергії переходів у рентгенівських спектрах піон-атомних систем. Розглянуто ефективний підхід до пере- визначення параметрів оптичного модельного піон-нуклонного потенціалу і збільшенню точності визначення енергій переходів у рентгенівських спектрах адронних атомів.

Ключові слова: рентгенівські спектри, піонні атоми, релятивістська теорія.

RELATIVISTIC THEORY OF THE BETA DECAY: ENVIRONMENT AND FINAL STATE INTERACTION EFFECTS

Theoretical schemes for estimating the atomic chemical environment effect and final state interaction on the β decay characteristics are considered. As method of calculation of the relativistic atomic fields and electron wave functions, the gauge invariant Dirac-Fock type approach is used. The numerical results for β decay parameters for a number of nuclei are presented.

Though in a modern nuclear physics there is a number of principally new problems, connected with an unprecedented progress in the physical experiment, nevertheless the classical problems, including the beta decay or low energy nucleus-nucleus collision etc. are remained under intensive theoretical and experimental interest (c. f. [1–12]). This paper is devoted to carrying out new schemes for estimating the beta decay characteristics and sensing an influence of the chemical environment on the β decay parameters with using new theoretical schemes (c. f. [1–5, 11–18]). In last years a calculating the β decay processes and sensing an influence of the chemical environment on the beta β characteristics attracts a great interest especially due to the new experimental studies of the β decay for a number of nuclei [1–5]. A number of experimental and theoretical papers appeared where the different aspects of the β decay theory and accounting for different factors are considered. One of the important topics is problem to get the data about the neutrino mass from the beta decay spectra shape. An exact value of the half-decay period for the whole number of heavy radioactive nuclei is important for standardisation of data about their properties. Disagreement between different experimental data regarding the β -decay in heavy radioactive nuclei is provided by different chemical environment radioactive nucleus. For example, such disagreement in data on the half-decay period for the ^{241}Pu (see, for example, ref. [4, 5, 8, 9]) is explained in some papers by special beta decay channel. The beta particle in this channel does not transit into free state, but it occupies the external free atomic level. According to ref. [1–5], differences in population of these levels are to be a reason of an influence of the chemical environment on the beta decay. So, a sensing the chemical environment effect on the beta decay is very important to be studied as within a consistent, high accurate theoretical calculation scheme as experimental high precise measurement. Under theoretical consideration of the problem, one has to consider the following effects: i.). A changing electron wave functions because of the changing atomic elec-

tric field due to the difference in the valence shells occupation numbers in different chemical substances; ii). A changing up limit of integration under calculating the Fermi integral function in different chemical substances [5]. As a rule, the beta particle and neutrino bring away the difference between energies of the mother and daughter atoms. This difference energy is equal to sum of values, provided by atomic nucleus reconstruction and atomic electron shell reconstruction. The entire energy of electron shell of an atom in the different chemical compounds is different. Due to the changing the nuclear charge Z on unite during the beta decay, this entire energy of electron shell of an atom changes in different chemical compounds by different way; iii). Together with beta decay and ejection of the beta particle out atom it is possible additional channel when the beta electron occupies non-occupied place on the bonded external orbitals of atom. As a rule, special tables [9] for the Fermi function and integral Fermi function is used for calculating the beta spectrum shape. In ref. [9] calculation scheme is based on the non-relativistic Hartree—Fock—Slater approach, but the finite size of nucleus is taken into account. In paper [4] the relativistic Dirac—Fock (DF) method was used. Note that the DF approach is the most wide spread method of calculation, but, as a rule, the corresponding orbitals basis's are not optimized. Some problems are connected with correct definition of the nuclear size effects, QED corrections etc. We are applying below the gauge invariant DF (GIDF) type approach [10–12] for estimating the atomic chemical environment effect and final state interaction on the β decay characteristics

As it is well known a distribution of the β particles on energy in the permitted transitions is as follows [9]:

$$dW_{\beta}(E)/dE = \frac{1}{2\pi^3} G^2 \cdot F(E, Z) \cdot E \cdot p \cdot (E_0 - E)^2 \cdot |M|^2. \quad (1)$$

Here G is the weak interaction constant; E and $p = (E^2 - 1)^{1/2}$ are an entire energy and pulse

of beta particle; $E_0 = 1 + (E_{bn}/m_e c^2)$, E_{bn} is the boundary energy of β -spectrum; $|M|$ is a matrix element, which is not dependent upon an energy in a case of the permitted β -transitions.

As usually for calculation of the β decay shape and decay half period one should use the tables of the Fermi function and integral Fermi function. The Fermi function F and integral Fermi function f are defined as follows:

$$F(E, Z) = \frac{1}{2p^2} (g_{-1}^2 + f_{+1}^2), \quad (2a)$$

$$f(E_0, Z) = \int_1^{E_0} F(E, Z) \cdot E \cdot p \cdot (E_0 - E)^2 dE. \quad (2b)$$

Here $f_{\pm 1}$ and $g_{\pm 1}$ are the relativistic electron radial functions; the indexes $\pm l = \chi$, where $\chi = (l - j)/(2j + 1)$. Two schemes of calculation are usually used: i). the relativistic electron radial wave functions are calculated on the boundary of the spherical nucleus with radius R_0 (it has done in ref. [4]); ii). the values of these functions in the zero are used (see ref. [9]).

The normalisation of electron radial functions f_i and g_i provides the behaviour of these functions for large values of radial valuable as follows:

$$g_i(r) \rightarrow r^{-1}[(E + 1)/E]^{1/2} \sin(pr + \delta_i), \quad (3a)$$

$$f_i(r) \rightarrow r^{-1}(i/|i|)[(E - 1)/E]^{1/2} \cos(pr + \delta_i). \quad (3b)$$

An effect of interaction in the final state between beta electron and atomic electrons with an accuracy to $(\alpha Z/v)^2$ is manifested and further accounted for in the first non-vanishing approximation [8]. This contribution changes the energy distribution of the beta electron on value:

$$\frac{dW_\beta(E)/dE}{dW_\beta^{(0)}(E)/dE} = 1 - (\alpha E/p)^2 \langle \Psi_{in} | \sum_j^z (a_B/|r_j|) | \Psi_{in} \rangle.$$

Here Ψ_{in} — the wave function of atom initial state, z is a number of electrons, a_B is the Bohr radius. As method of calculation of the relativistic atomic fields and electron wave functions, we have used the GIDF approach [10, 11]. The potential of Dirac equation includes also the electric and polarization potentials of a nucleus (the gaussian form of charge distribution in the nucleus was used). All correlation corrections of the PT second and high orders (electrons screening, particle-hole interaction etc.) are accounted for [5]. The GIDF equations for N-electron system are written and contain the potential: $V(r) = V(r|nlj) + V_{ex} + V(r|R)$, which includes the electrical and polarization potentials of the nucleus. The part V_{ex} accounts for exchange inter-electron interaction. Note that a procedure of the exchange account in the GIDF scheme is similar to one in the usual DF approach. Regarding the GIDKS scheme, it is similar to usual DKS scheme. The optimization of the orbital bases is realized by iteration algorithm within gauge invariant QED procedure

(look its application in the beta-decay theory [5]). Approach allows calculating the continuum wave functions, taking into account fully an effect of exchange of the continuum electron with electrons of the atom. Note that this is one of the original moments of the paper. Another original moment is connected with using the consistent QED gauge invariant procedure for optimization of the electron functions bases. Numerical calculation and analysis shows that used methods allow getting the results, which are more precise in comparison with analogous data, obtained with using non-optimized bases. The details of the numerical procedure are presented in ref. [10—12].

Firstly, we present the results of estimating the final state interaction effects on the β decays for super allowed transition $O^+ \rightarrow O^+$ (nuclei: ^{42}Se , ^{46}V). In table 1 we present our results for corrections ft to probability of the super allowed transitions $O^+ \rightarrow O^+$ due to the final state interaction effect (FSI).

Table 1

Corrections to probability of the super allowed transitions $O^+ \rightarrow O^+$ due to the final state interaction effect (FSI)

Nucleus	Compiled data (without FSI) [12]	Calculation with FSI [12]	Calculation with FSI Our data
^{42}Se	$3089,3 \pm 7,5$	3097,8	3095,2
^{46}V	$3088,6 \pm 4,3$	3098,4	3095,9

There are also presented the compiled data (without accounting for the final state interaction effect) and the estimates from ref. [8] within the Durand approach. The FSI correction may not be directly defined in the heavy nuclei due to the great indefiniteness in nuclear matrix elements. Exception is the super allowed transition $O^+ \rightarrow O^+$. These transitions are used for definition of the weak interaction constant $G_V(ft \sim G_V^2)$. As one can see there is quite significant difference between presented values for different nuclei. One can suppose that there is systematic defect of existing theory of accounting corrections, which increase with the growth of Z . As an analysis shows, our data can be considered as the most correct ones.

In table 2 we present some data on the atomic chemical environment effect on the β decay probability $^{241}\text{Pu} \rightarrow ^{241}\text{Am}$. Analysis shows that it has taken a place the significant changing of the $T_{1/2}$ value for ^{241}Pu . According to our calculation, the Fermi function under double ionization is less on 0,33—0,90 %. Let us note that our results are in reasonable agreement with data of refs. [4, 5]. It means, naturally, that the decay of ^{241}Pu runs more slowly. The typical example of the Pu compounds is pair PuO_2 and PuO . The detailed analysis shows that an account of the possible channel of the β decay with occupying external atomic orbitals, in

The atomic chemical environment effect on the β decay probability $^{241}\text{Pu} \rightarrow ^{241}\text{Am}$. Changing the half-period $T_{1/2}$ (GIDF calculation)

Decay of neutral atom			Decay of ionized atom			$\Delta f/f = -\Delta T_{1/2}/T_{1/2}, \%$
Atom	E_{ip}, eV	$f(E_{\text{ip}}, Z)$	Ion	E_{ip}, eV	$f(E_{\text{ip}}, Z)$	
$\text{Pu}^{(0)}$	20800	1,72164(-3)	$\text{Pu}^{(+2)}$	20783	1,71596(-3)	—0,33
	20817	1,72522(-3)		20800	1,71953(-3)	—0,33
	20800	1,72164(-3)	$\text{Pu}^{(+2)}$	20767	1,71148(-3)	—0,59
	20833	1,72952(-3)		20800	1,71931(-3)	—0,59
	20800	1,72164(-3)	$\text{Pu}^{(+4)}$	20748	1,70615(-3)	—0,90
	20852	1,73403(-3)		20800	1,71842(-3)	—0,90

our opinion, gives a reasonable explanation of dependence of the plutonium half decay period upon the chemical composition than version without account of this channel.

REFERENCES

1. Tegen R., Beta decay of the free neutron and a (near) degenerate neutrino mass // Nucl. Phys. A. — 2002. — Vol. 706. — P. 193—202.
2. Izosimov I. N., Kazimov A. A., Kalinnikov V. G., Solnyshkin A. A. and Suhonen J., Beta-decay strength measurement, total beta-decay energy determination and decay-scheme completeness testing by total absorption gamma-ray spectroscopy // Phys. Atom. Nucl. — 2004. — Vol. 67, N 10. — 1876—1882.
3. Kopytin I. V., Karelin K. N., and Nekipelov A. A. Exact inclusion of the coulomb field in the photobeta decay of a nucleus and problem of bypassed elements // Phys. Atom. Nucl. — 2004. — Vol. 67, N 8. — P. 1429—1441.
4. Band I. M., Listengarten M. A., Trzhaskovskaya M. B., Possibility of beta decay in model of atom of the Hartree—Fock—Dirac and influence of chemical composition on the beta decay // Izv. AN USSR. — 1987. — Vol. 51, N 11. — P. 1999—200.
5. Glushkov A. V., Khetselius O. Yu., Lovett L., Electron- β -Nuclear Spectroscopy of Atoms and Molecules and Chemical Environment Effect on the β -Decay parameters // Advances in the Theory of Atomic and Molecular Systems (Berlin, Springer). — 2009. — Vol. 20. — P. 125—172.
6. Karpeshin F., Trzhaskovskaya M. B., Gangrskii Yu. P., Resonance Internal Conversion in Hydrogen-Like Ions // JETP. — 2004. — Vol. 99, N 2. — P. 286—289.
7. Kaplan I., Endpoint energy in the molecular beta spectrum, atomic mass defect and the negative m_{ν}^2 puzzle // J. Phys. G.: Nucl. Part. Phys. — 1999. — Vol. 23. — P. 683—692.
8. Drukarev E. G., Strikman M. I., Final state interactions of beta electrons and related phenomena // JETP. — 1999. — Vol. 64(10). — P. 1160—1168.
9. Gelepov B. C., Zyryanova L. N., Suslov Yu. P. Beta processes. — Leningrad: Nauka, 1999. — 372 p.
10. Malinovskaya S. V., Dubrovskaya Yu. V., Vitavetskaya L. A., Advanced quantum mechanical calculation of the beta decay probabilities // Low Energy Antiproton Phys. (AIP). — 2005. — Vol. 796. — P. 201—205.
11. Malinovskaya S. V., Dubrovskaya Yu. V., Zelentsova T. N., The atomic chemical environment effect on the β decay probabilities: Relativistic calculation // Kiev University Bulletin. Series Phys. — Math. — 2004. — № 4. — C. 427—432.
12. Glushkov A. V., Malinovskaya S. V., Dubrovskaya Yu. V., Sensing the atomic chemical composition effect on the β decay probabilities // Sensor Electr. & Microsyst. Techn. — 2005. — N 1. — P. 16—20.

UDC 539.135

Yu. V. Dubrovskaya, D. E. Sukharev, L. A. Vitavetskaya

RELATIVISTIC THEORY OF THE BETA DECAY: ENVIRONMENT AND FINAL STATE INTERACTION EFFECTS

Abstract

Theoretical schemes for estimating the atomic chemical environment effect and final state interaction on the β decay characteristics are considered. As method of calculation of the relativistic atomic fields and electron wave functions, the gauge invariant Dirac—Fock type approach is used. The numerical results for β decay parameters for a number of nuclei are presented.

Key words: β decay probability, relativistic theory, environment effect.

УДК 539.135

Ю. В. Дубровская, Д. Е. Сухарев, Л. А. Витавецкая

РЕЛЯТИВИСТСКАЯ ТЕОРИЯ β -РАСПАДА: ЭФФЕКТЫ ХИМИЧЕСКОГО ОКРУЖЕНИЯ И ВЗАИМОДЕЙСТВИЯ В КОНЕЧНОМ СОСТОЯНИИ

Резюме

Рассмотрены теоретические схемы определения характеристик β распада и оценки влияния эффекта химического окружения и взаимодействия в конечном состоянии. В качестве метода вычисления релятивистского атомного поля и волновых функций использована обобщенная калибровочно-инвариантная версия метода Дирака—Фока. Приведены оценки характеристик бета распада для ряда ядер.

Ключевые слова: вероятность β -распада, релятивистская теория, эффект химического окружения.

Ю. В. Дубровська, Д. Є. Сухарев, Л. А. Вітавецька

РЕЛЯТИВІСТСЬКА ТЕОРІЯ β -РОЗПАДУ: ЕФЕКТИ ХІМІЧНОГО ОТОЧЕННЯ ТА ВЗАЄМОДІЇ У КІНЦЕВОМУ СТАНІ

Резюме

Розглянуті теоретичні схеми розрахунку характеристик β розпаду та оцінки впливу ефекту хімічного оточення та взаємодії у кінцевому стані. Як метод розрахунку релятивістських атомних полів і електронних хвильових функцій використані узагальнені калібровочно-інваріантні схеми Дірака—Фока і Дірака—Кона—Шема. Наведені чисельні результати характеристик бета розпаду для низки ядер.

Ключові слова: імовірність β розпаду, релятивістська теорія, ефект хімічного оточення.

*N. G. SERBOV*², *V. KUZAKON*³, *O. Yu. KHETSELIUS*¹, *G. P. PREPELITSA*²,
*E. P. SOLYANIKOVA*³

¹ I. I. Mechnikov Odessa National University,

² Odessa State Environmental University, e-mail: nikserbov@mail.ru

³ Odessa National Academy of Food Technologies

NON-LINEAR ANALYSIS METHODS OF SIGNAL'S TEMPORAL SERIES IN MODELING OF INTERACTIONS IN THE NON-LINEAR VIBRATIONAL SYSTEMS OF THE QUANTUM GENERATORS TYPE

The actual problem of the modern quantum electronics is studying a dynamics of the coupled quantum generators and identifying the presence of chaotic dynamics in this time (frequency) series. Here we review the elements of advanced techniques of using the non-linear analysis methods to dynamics, such as the wavelet analysis, multi-fractal formalism, mutual information approach, correlation integral analysis, false nearest neighbour algorithm, Lyapunov exponent's analysis, and surrogate data method.

1. INTRODUCTION

As it is well known in the modern quantum electronics, photoelectronics etc there are many physical systems (multielement semiconductors and gas lasers, different radiotechnical devices etc), which should be considered in the first approximation as set of autogenerators, coupled by different way (c. f. [1, 2]). The typical schemes of different autogenerators (semiconductor quantum generators, coupled by means optical waveguide etc) are presented in refs. [1, 2]. The key aspect of studying the dynamics of these systems is analysis of the temporal set for characteristic signals. In refs. [1–4] it has been numerically studied a regular and chaotic dynamics of the system of the Vander–Poll autogenerators with account of finiteness of the signals propagation time between them and also with special kind of inter-oscillators interaction forces. Chaos theory establishes that apparently complex irregular behaviour could be the outcome of a simple deterministic system with a few dominant nonlinear interdependent variables. The past decade has witnessed a large number of studies employing the ideas gained from the science of chaos to characterize, model, and predict the dynamics of various systems phenomena (c. f. [1–23]). The outcomes of such studies are very encouraging, as they not only revealed that the dynamics of the apparently irregular phenomena could be understood from a chaotic deterministic point of view but also reported very good predictions using such an approach for different systems. Here we review the elements of advanced techniques of using the non-linear analysis methods to dynamics, such as the wavelet analysis, multi-fractal formalism, mutual information approach, correlation integral analysis, false nearest neighbour algorithm, Lyapunov exponent's analysis, and surrogate data method.

2. INVESTIGATION OF CHAOS IN THE VIBRATION DYNAMICS

In ref. [2–4, 19] it has been studied a regular and chaotic dynamics of the system of the autogenerators. Figure 1 illustrates the typical vibration dynamics time series for a grid of autogenerators [4]. As it can be seen in Fig. 1, the systems exhibits significant variations without any apparent cyclicity. It is clear that a visual inspection of the (irregular) amplitude level series does not provide any clues regarding its dynamical behaviour, whether chaotic or stochastic. To detect some regularity (or irregularity) in the time series, the Fourier power spectrum is often analyzed, however it often fails too. Chaotic signals may also have sharp spectral lines but even in the absence of noise there will be continuous part (broadband) of the spectrum. The broad power spectrum falling as a power of frequency is a first indication of chaotic behaviour, though it alone does not characterize chaos [5, 15, 18]. From this point of view, the corresponding series analyzed in this study is presumably chaotic [8]. However, more well-defined conclusion on the dynamics of the time series can be made after the data will be treated by methods of chaos theory.

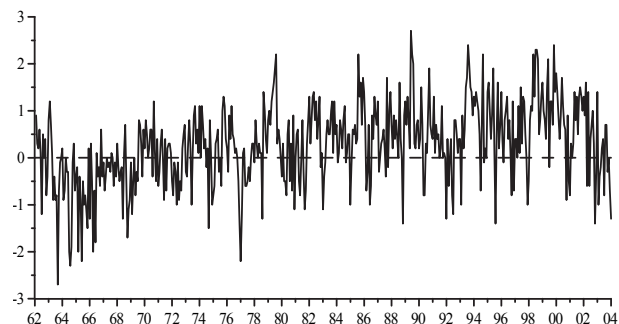


Fig. 1. The typical vibration dynamics time series for a grid of autogenerators

2.1. Introducing remarks

Let us consider scalar measurements $s(n) = s(t_0 + n\Delta t) = s(n)$, where t_0 is the start time, Δt is the time step, and n is the number of the measurements. In a general case, $s(n)$ is any time series, particularly the amplitude level. Since processes resulting in the chaotic behaviour are fundamentally multivariate, it is necessary to reconstruct phase space using as well as possible information contained in the $s(n)$. Such a reconstruction results in a certain set of d -dimensional vectors $\mathbf{y}(n)$ replacing the scalar measurements. Packard et al. [7] introduced the method of using time-delay coordinates to reconstruct the phase space of an observed dynamical system. The direct use of the lagged variables $s(n + \tau)$, where τ is some integer to be determined, results in a coordinate system in which the structure of orbits in phase space can be captured. Then using a collection of time lags to create a vector in d dimensions,

$$\mathbf{y}(n) = [s(n), s(n + \tau), s(n + 2\tau), \dots, s(n + (d - 1)\tau)], \quad (1)$$

the required coordinates are provided. In a nonlinear system, the $s(n + j\tau)$ are some unknown nonlinear combination of the actual physical variables that comprise the source of the measurements. The dimension d is called the embedding dimension, d_E . Example of the Lorenz attractor given by Abarbanel et al. [5, 6] is a good choice to illustrate the efficiency of the method.

2.2. Choosing time lag

According to Mañé [13] and Takens [12], any time lag will be acceptable is not terribly useful for extracting physics from data. If τ is chosen too small, then the coordinates $s(n + j\tau)$ and $s(n + (j + 1)\tau)$ are so close to each other in numerical value that they cannot be distinguished from each other. Similarly, if τ is too large, then $s(n + j\tau)$ and $s(n + (j + 1)\tau)$ are completely independent of each other in a statistical sense. Also, if τ is too small or too large, then the correlation dimension of attractor can be under- or overestimated respectively [8, 18]. It is therefore necessary to choose some intermediate (and more appropriate) position between above cases. First approach is to compute the linear autocorrelation function

$$C_L(\delta) = \frac{\frac{1}{N} \sum_{m=1}^N [s(m + \delta) - \bar{s}][s(m) - \bar{s}]}{\frac{1}{N} \sum_{m=1}^N [s(m) - \bar{s}]^2}, \quad (2)$$

where $\bar{s} = \frac{1}{N} \sum_{m=1}^N s(m)$,

and to look for that time lag where $C_L(\delta)$ first passes through zero (see [18]). This gives a good hint of choice for τ at that $s(n + j\tau)$ and

$s(n + (j + 1)\tau)$ are linearly independent. However, a linear independence of two variables does not mean that these variables are nonlinearly independent since a nonlinear relationship can differs from linear one. It is therefore preferably to utilize approach with a nonlinear concept of independence, e. g. the average mutual information. Briefly, the concept of mutual information can be described as follows. Let there are two systems, A and B , with measurements a_i and b_k . The amount one learns in bits about a measurement of a_i from a measurement of b_k is given by the arguments of information theory [9] as

$$I_{AB}(a_i, b_k) = \log_2 \left(\frac{P_{AB}(a_i, b_k)}{P_A(a_i)P_B(b_k)} \right), \quad (3)$$

where the probability of observing a out of the set of all A is $P_A(a_i)$, and the probability of finding b in a measurement B is $P_B(b_k)$, and the joint probability of the measurement of a and b is $P_{AB}(a_i, b_k)$. The mutual information I of two measurements a_i and b_k is symmetric and non-negative, and equals to zero if only the systems are independent. The average mutual information between any value a_i from system A and b_k from B is the average over all possible measurements of $I_{AB}(a_i, b_k)$,

$$I_{AB}(\tau) = \sum_{a_i, b_k} P_{AB}(a_i, b_k) I_{AB}(a_i, b_k). \quad (4)$$

To place this definition to a context of observations from a certain physical system, let us think of the sets of measurements $s(n)$ as the A and of the measurements a time lag τ later, $s(n + \tau)$, as B set. The average mutual information between observations at n and $n + \tau$ is then

$$I_{AB}(\tau) = \sum_{a_i, b_k} P_{AB}(a_i, b_k) I_{AB}(a_i, b_k). \quad (5)$$

Now we have to decide what property of $I(\tau)$ we should select, in order to establish which among the various values of τ we should use in making the data vectors $\mathbf{y}(n)$. In ref. [11] it has been suggested, as a prescription, that it is necessary to choose that τ where the first minimum of $I(\tau)$ occurs. On the other hand, the autocorrelation coefficient failed to achieve zero, i. e. the autocorrelation function analysis not provides us with any value of τ . Such an analysis can be certainly extended to values exceeding 1000, but it is known [15] that an attractor cannot be adequately reconstructed for very large values of τ . The mutual information function usually [4] exhibits an initial rapid decay (up to a lag time of about 10) followed more slow decrease before attaining near-saturation at the first minimum.

One could remind that the autocorrelation function and average mutual information can be considered as analogues of the linear redundancy and general redundancy, respectively, which

was applied in the test for nonlinearity. If a time series under consideration have an n -dimensional Gaussian distribution, these statistics are theoretically equivalent as it is shown by Paluš (see [15]). The general redundancies detect all dependences in the time series, while the linear redundancies are sensitive only to linear structures. Further, a possible nonlinear nature of process resulting in the vibrations amplitude level variations can be concluded.

2.3. Choosing embedding dimension. Grassberger and Procaccia algorithm

The goal of the embedding dimension determination is to reconstruct a Euclidean space R^d large enough so that the set of points d_A can be unfolded without ambiguity. In accordance with the embedding theorem, the embedding dimension, d_E , must be greater, or at least equal, than a dimension of attractor, d_A , i. e. $d_E \geq d_A$. In other words, we can choose a fortiori large dimension d_E , e. g. 10 or 15, since the previous analysis provides us prospects that the dynamics of our system is probably chaotic. However, two problems arise with working in dimensions larger than really required by the data and time-delay embedding [5, 6, 18].

First, many of computations for extracting interesting properties from the data require searches and other operations in R^d whose computational cost rises exponentially with d . Second, but more significant from the physical point of view, in the presence of noise or other high dimensional contamination of the observations, the extra dimensions are not populated by dynamics, already captured by a smaller dimension, but entirely by the contaminating signal. In too large an embedding space one is unnecessarily spending time working around aspects of a bad representation of the observations which are solely filled with noise. It is therefore necessary to determine the dimension d_A .

There are several standard approaches to reconstruct the attractor dimension (see, e. g., [5, 6, 15]), but let us consider in this study two methods only. The correlation integral analysis is one of the widely used techniques to investigate the signatures of chaos in a time series. The analysis uses the correlation integral, $C(r)$, to distinguish between chaotic and stochastic systems. To compute the correlation integral, the algorithm of Grassberger and Procaccia [10] is the most commonly used approach. According to this algorithm, the correlation integral is

$$C(r) = \lim_{N \rightarrow \infty} \frac{2}{N(n-1)} \sum_{\substack{i,j \\ (1 \leq i < j \leq N)}} H(r - \|y_i - y_j\|), \quad (6)$$

where H is the Heaviside step function with $H(u) = 1$ for $u > 0$ and $H(u) = 0$ for $u \leq 0$, r is the radius of sphere centered on y_i or y_j , and N is the number of data measurements. If the time series is characterized by an attrac-

tor, then the integral $C(r)$ is related to the radius r given by

$$d = \lim_{\substack{r \rightarrow 0 \\ N \rightarrow \infty}} \frac{\log C(r)}{\log r}, \quad (7)$$

where d is correlation exponent that can be determined as the slope of line in the coordinates $\log C(r)$ versus $\log r$ by a least-squares fit of a straight line over a certain range of r , called the scaling region. If the correlation exponent attains saturation with an increase in the embedding dimension, then the system is generally considered to exhibit chaotic dynamics. The saturation value of the correlation exponent is defined as the correlation dimension (d_2) of the attractor. The nearest integer above the saturation value provides the minimum or optimum embedding dimension for reconstructing the phase-space or the number of variables necessary to model the dynamics of the system. On the other hand, if the correlation exponent increases without bound with increase in the embedding dimension, the system under investigation is generally considered stochastic. As the characteristic illustration in figure 2, 3 we present the characteristic behaviour of the ionization probability for the hydrogen atom in the

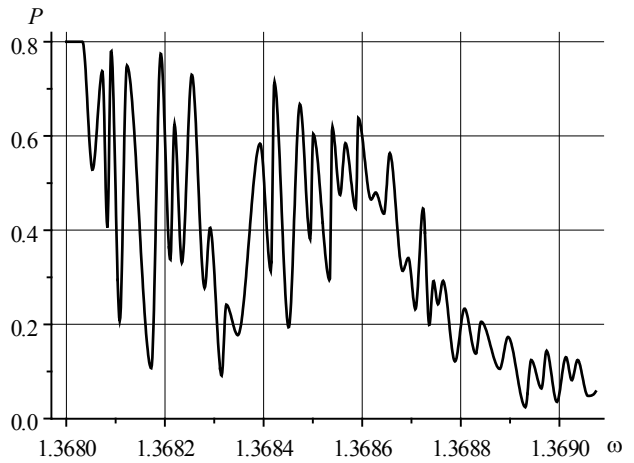


Fig. 2. Characteristic behaviour of the ionization probability for the hydrogen atom in the microwave electromagnetic field [23]

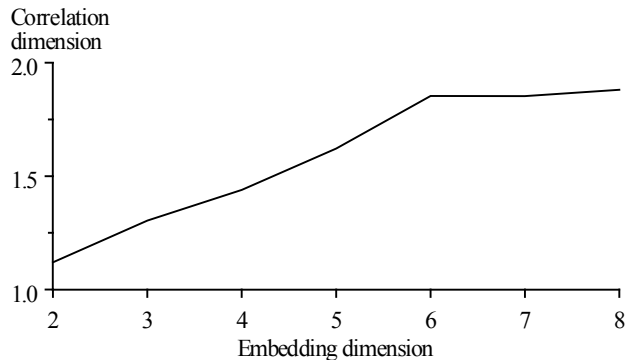


Fig. 3. The relationship between the correlation exponent and embedding dimension values the hydrogen atom in the microwave electromagnetic field)

microwave electromagnetic field and correlation dimension results for chaotic dynamics (the relationship between the correlation exponent and embedding dimension values) [23].

As it can be seen, the correlation exponent value increases with embedding dimension up to a certain value, and then saturates beyond that value. The saturation of the correlation exponent beyond a certain embedding dimension is an indication of the existence of deterministic dynamics. The saturation value of the correlation exponent, i. e. correlation dimension of attractor, for the amplitude level series is about 1.8 and occurs at the embedding dimension value of 6. The low, non-integer correlation dimension value indicates the existence of low-dimensional chaos in the dynamics of the hydrogen atom in the microwave electromagnetic field. The same picture has been found for the vibrations dynamics of the autogenerators [4]. The nearest integer above the correlation dimension value can be considered equal to the minimum dimension of the phase-space essential to embed the attractor. The value of the embedding dimension at which the saturation of the correlation dimension occurs is considered to provide the upper bound on the dimension of the phase-space sufficient to describe the motion of the attractor. Furthermore, the dimension of the embedding phase-space is equal to the number of variables present in the evolution of the system dynamics. The results of such studying can indicate that to model the dynamics of process resulting in the amplitude level variations the minimum number of variables essential is equal to 4 and the number of variables sufficient is equal to 6. Therefore, the amplitude level attractor should be embedded at least in a four-dimensional phase-space.

The results can indicate also that the upper bound on the dimension of the phase-space sufficient to describe the motion of the attractor, and hence the number of variables sufficient to model the dynamics of process resulting in the level variations is equal to 6.

There are certain important limitations in the use of the correlation integral analysis in the search for chaos. For instance, the selection of inappropriate values for the parameters involved in the method may result in an underestimation (or overestimation) of the attractor dimension [8]. Consequently, finite and low correlation dimensions could be observed even for a stochastic process [18]. To verify the results obtained by the correlation integral analysis, we use surrogate data method.

The method of surrogate data [16] is an approach that makes use of the substitute data generated in accordance to the probabilistic structure underlying the original data. This means that the surrogate data possess some of the properties, such as the mean, the standard deviation, the cumulative distribution function, the power spectrum, etc., but are otherwise postulated as random, generated according to a specific null hypothesis. Here, the null hy-

pothesis consists of a candidate linear process, and the goal is to reject the hypothesis that the original data have come from a linear stochastic process. One reasonable statistics suggested by Theiler et al. [16] is obtained as follows.

If we denote Q_{orig} as the statistic computed for the original time series and Q_{s_i} for the i th surrogate series generated under the null hypothesis and let μ_s and σ_s denote, respectively, the mean and standard deviation of the distribution of Q_s , then the measure of significance S is given by

$$S = \frac{|Q_{\text{orig}} - \mu_s|}{\sigma_s}. \quad (8)$$

An S value of ~ 2 cannot be considered very significant, whereas an S value of ~ 10 is highly significant [16]. The details on the null hypothesis and surrogate data generation are described in ref. [18]. To detect nonlinearity in the amplitude level data, the one hundred realizations of surrogate data sets were generated according to a null hypothesis in accordance to the probabilistic structure underlying the original data. The correlation integrals and the correlation exponents, for embedding dimension values from 1 to 20, were computed for each of the surrogate data sets using the Grassberger—Procaccia algorithm as explained earlier. Figure 2 shows the relationship between the correlation exponent values and the embedding dimension values for the original data set and mean values of the surrogate data sets as well as for one surrogate realization.

Often, a significant difference in the estimates of the correlation exponents, between the original and surrogate data sets, can be observed. In the case of the original data, a saturation of the correlation exponent is observed after a certain embedding dimension value (i. e., 6), whereas the correlation exponents computed for the surrogate data sets continue increasing with the increasing embedding dimension. The high significance values of the statistic indicate that the null hypothesis (the data arise from a linear stochastic process) can be rejected and hence the original data might have come from a nonlinear process.

It is worth consider another method for determining d_E that comes from asking the basic question addressed in the embedding theorem: when has one eliminated false crossing of the orbit with itself which arose by virtue of having projected the attractor into a too low dimensional space? By examining this question in dimension one, then dimension two, etc. until there are no incorrect or false neighbours remaining, one should be able to establish, from geometrical consideration alone, a value for the necessary embedding dimension. Such an approach was described by Kennel et al. [6]. In dimension d each vector

$$\mathbf{y}(k) = [s(k), s(k + \tau), s(k + 2\tau), \dots, s(k + (d - 1)\tau)] \quad (9)$$

has a nearest neighbour $\mathbf{y}^{NN}(k)$ with nearness in the sense of some distance function. The Euclidean distance in dimension d between $\mathbf{y}(k)$ and $\mathbf{y}^{NN}(k)$ we call $R_d(k)$:

$$R_d^2(k) = [s(k) - s^{NN}(k)]^2 + [s(k + \tau) - s^{NN}(k + \tau)]^2 + \dots + [s(k + \tau(d - 1)) - s^{NN}(k + \tau(d - 1))]^2. \quad (10)$$

$R_d(k)$ is presumably small when one has a lot of data, and for a dataset with N measurements, this distance is of order $1/N^{1/d}$. In dimension $d + 1$ this nearest-neighbour distance is changed due to the $(d + 1)$ st coordinates $s(k + d\tau)$ and $s^{NN}(k + d\tau)$ to

$$R_{d+1}^2(k) = R_d^2(k) + [s(k + d\tau) - s^{NN}(k + d\tau)]^2. \quad (11)$$

We can define some threshold size R_T to decide when neighbours are false. Then if

$$\frac{|s(k + d\tau) - s^{NN}(k + d\tau)|}{R_d(k)} > R_T, \quad (12)$$

the nearest neighbours at time point k are declared false. Kennel et al. [6] showed that for values in the range $10 \leq R_T \leq 50$ the number of false neighbours identified by this criterion is constant. In practice, the percentage of false nearest neighbours is determined for each dimension d . A value at which the percentage is almost equal to zero can be considered as the embedding dimension. In ref. [4] under studying the chaotic dynamics of the quantum generators was shown that the percentage of false neighbours drops to almost zero at 4 or 5, i. e. a four or five-dimensional phase-space is necessary to represent the dynamics (or unfold the attractor) of the amplitude level series. From the other hand, the mean percentage of false nearest neighbours computed for the surrogate data sets decreases steadily but at 20 is about 35 %. Such a result seems to be in close agreement with that was obtained from the correlation integral analysis, providing further support to the observation made earlier regarding the presence of low-dimensional chaotic dynamics in the amplitude level variations.

2.4. Lyapunov exponents

Lyapunov exponents are the dynamical invariants of the nonlinear system. In a general case, the orbits of chaotic attractors are unpredictable, but there is the limited predictability of chaotic physical system, which is defined by the global and local Lyapunov exponents. A negative exponent indicates a local average rate of contraction while a positive value indicates a local average rate of expansion. In the chaos theory, the spectrum of Lyapunov exponents is considered a measure of the effect of perturbing the initial conditions of a dynamical system. Note that both positive and negative Lyapunov exponents can co-

exist in a dissipative system, which is then chaotic.

Since the Lyapunov exponents are defined as asymptotic average rates, they are independent of the initial conditions, and therefore they do comprise an invariant measure of attractor. In fact, if one manages to derive the whole spectrum of Lyapunov exponents, other invariants of the system, i. e. Kolmogorov entropy and attractor's dimension can be found. The Kolmogorov entropy, K , measures the average rate at which information about the state is lost with time. An estimate of this measure is the sum of the positive Lyapunov exponents. The inverse of the Kolmogorov entropy is equal to the average predictability. The estimate of the dimension of the attractor is provided by the Kaplan and Yorke conjecture (see [15, 18]):

$$d_L = j + \frac{\sum_{\alpha=1}^j \lambda_\alpha}{|\lambda_{j+1}|}, \quad (13)$$

where j is such that $\sum_{\alpha=1}^j \lambda_\alpha > 0$ and $\sum_{\alpha=1}^{j+1} \lambda_\alpha < 0$,

and the Lyapunov exponents λ_α are taken in descending order.

There are several approaches to computing the Lyapunov exponents (see, e. g., [5, 6, 18]). One of them [18] is in computing the whole spectrum and based on the Jacobin matrix of the system function [14]. To calculate the spectrum of Lyapunov exponents from the amplitude level data, one could determine the time delay τ and embed the data in the four-dimensional space. In this point it is very important to determine the Kaplan—Yorke dimension and compare it with the correlation dimension, defined by the Grassberger—Procaccia algorithm.

The estimations of the Kolmogorov entropy and average predictability can further show a limit, up to which the amplitude level data can be on average predicted. Surely, the important moment is a check of the statistical significance of results. It is worth to remind that results of state-space reconstruction are highly sensitive to the length of data set (i. e. it must be sufficiently large) as well as to the time lag and embedding dimension determined. Indeed, there are limitations on the applicability of chaos theory for observed (finite) time series arising from the basic assumptions that the time series must be infinite. A finite and small data set may probably results in an underestimation of the actual dimension of the process. The statistical convergence tests, described here, together with surrogate data approach that, was above applied, can provide the satisfactory significance of the investigated data regarding the state-space reconstruction.

3. CONCLUSIONS AND DISCUSSION

Thus, we have considered the elements of advanced techniques of using the non-linear

analysis methods to dynamics, such as the multi-fractal formalism, mutual information approach, correlation integral analysis, false nearest neighbour algorithm, Lyapunov exponent's analysis, and surrogate data method. Their using allows to study in details an existence of chaotic behaviour in the non-linear vibrational systems on the basis of temporal series. The mutual information approach provided a time lag which is needed to reconstruct phase space. Such an approach allowed concluding the possible nonlinear nature of process resulting in the amplitude level variations. The correlation dimension method provided a low fractal-dimensional attractor thus suggesting a possibility of the existence of chaotic behaviour. The method of surrogate data, for detecting nonlinearity, provided significant differences in the correlation exponents between the original data series and the surrogate data sets. This finding indicates that the null hypothesis (linear stochastic process) can be rejected. The main conclusion is that the system exhibits a nonlinear behaviour and possibly low-dimensional chaos. Thus, a short-term prediction based on nonlinear dynamics is possible. The Lyapunov exponents analysis usually can support this conclusion. In any case the hypothesis of chaos in is reasonable and can provide an alternative approach for characterizing and modelling the dynamics of processes resulting in the vibrations processes in the complicated system such as different semiconductors and quantum electronics devices, corresponding nano-devices, classical and quantum systems in an electromagnetic field etc.

REFERENCES

1. Vedenov A. A., Ezhov A. A., Levchenko E. B., Non-linear systems with memory and functions of neuron ensembles, In: Non-linear waves. Structure and bi-furcations Eds Gaponov-Grekhov A. V., Rabinovich M. I., pp. 53–69, Nauka, Moscow (1987).
2. Serbov N. G., Svinarenko A. A., Wavelet and multi-fractal analysis of oscillations in system of coupled autogenerators in chaotic regime // Photoelectronics. — 2006. — N 15. — P. 27–30.
3. Serbov N. G., Svinarenko A. A., Wavelet and multi-fractal analysis of oscillations in a grid of coupled autogenerators // Photoelectronics. — 2007. — N16. — P. 53–56.
4. Svinarenko A. A., Loboda A. V., Serbov N. G., Modeling and diagnostics of interaction of the non-linear vibrational systems on the basis of temporal series (application to semiconductor quantum generators) // Photoelectronics. — 2009. — N 18. — P. 76–84.
5. Abarbanel H., Brown R., Sidorowich J., Tsimring L., The analysis of observed chaotic data in physical systems // Rev Modern Phys. — 1993. — Vol. 65. — P. 1331–1392.
6. Kennel M., Brown R., Abarbanel H., Determining embedding dimension for phase-space reconstruction using a geometrical construction // Phys Rev A. — 1992. — Vol. 45. — P. 3403–3411.
7. Packard N., Crutchfield J., Farmer J., Shaw R., Geometry from a time series // Phys Rev Lett. — 1988. — Vol. 45. — P. 712–716.
8. Havstad J., Ehlers C., Attractor dimension of non-stationary dynamical systems from small data sets // Phys Rev A. — 1989. — Vol. 39. — P. 845–853.
9. Gallager R. G., Information theory and reliable communication, Wiley, New York. — 1999.
10. Grassberger P., Procaccia I., Measuring the strangeness of strange attractors // Physica D. — 1983. — Vol. 9. — P. 189–208.
11. Fraser A., Swinney H., Independent coordinates for strange attractors from mutual information // Phys Rev A. — 1986. — Vol. 33. — P. 1134–1140.
12. Takens F (1981) Detecting strange attractors in turbulence. In: Rand DA, Young LS (eds) Dynamical systems and turbulence, Warwick 1981. (Lecture notes in mathematics No 898). Springer, Berlin Heidelberg New York, pp 366–381.
13. Mañé On the dimensions of the compact invariant sets of certain non-linear maps. In: Rand DA, Young LS (eds) Dynamical systems and turbulence, Warwick 1981 Springer, Berlin Heidelberg N. — Y, p. 230–242
14. Sano M, Sawada Y (1985) Measurement of the Lyapunov spectrum from a chaotic time series // Phys Rev. Lett. — 1995. — Vol. 55. — P. 1082–1085.
15. Sivakumar B., Chaos theory in geophysics: past, present and future // Chaos, Solitons & Fractals. — 2004. — Vol. 19. — P. 441–462.
16. Theiler J., Eubank S., Longtin A., Galdrikian B., Farmer J., Testing for nonlinearity in time series: The method of surrogate data // Physica D. — 1992. — Vol. 58. — P. 77–94.
17. Glushkov A. V., Khokhlov V. N., Tsenenko I. A. Atmospheric teleconnection patterns: wavelet analysis // Nonlin. Proc. in Geophys. — 2004. — V. 11, N3. — P. 285–293.
18. Khokhlov V. N., Glushkov A. V., Loboda N. S., Serbov N. G., Zhurbenko K., Signatures of low-dimensional chaos in hourly water level measurements at coastal site // Stoch. Environ. Res. Risk Assess. (Springer). — 2008. — Vol. 22. — P. 777–788.
19. Bunyakova Yu. Ya., Glushkov A. V., Fedchuk A. P., Serbov N. G., Svinarenko A. A., Tsenenko I. A., Sensing non-linear chaotic features in dynamics of system of coupled autogenerators: standard multifractal analysis // Sensor Electr. and Microsyst. Techn. — 2007. — N 1. — P. 14–17.
20. Glushkov A. V., Khokhlov V. N., Loboda N. S., Bunyakova Yu. Ya., Short-range forecast of atmospheric pollutants using non-linear prediction method // Atmospheric Environment (Elsevier). — 2008. — Vol. 42. — P. 7284–7292.
21. Gutzwiller M., Chaos in Classical and Quantum Mechanics. — N.-Y.: Springer-Verlag, 1999. — 720 p.
22. Ott E. Chaos in dynamical systems. Cambridge: Cambridge Univ. Press, 2002. — 490 p.
23. Khetselius O. Yu., Prepelitsa G. P., Ignatenko A. V. Ionization of H atom in a microwave field // Proc. ESF REHE Workshop. — Torun (Poland). — 1998. — P. 31.

UDC 539.124:541.47

N. G. Serbov, V. M. Kuzakon, O. Yu. Khetselius, G. P. Prepelitsa, E. P. Solyanikova,

NON-LINEAR ANALYSIS METHODS OF SIGNAL'S TEMPORAL SERIES IN MODELING OF INTERACTIONS IN THE NON-LINEAR VIBRATIONAL SYSTEMS OF THE QUANTUM GENERATORS TYPE

Abstract

The actual problem of the modern quantum electronics is studying a dynamics of the coupled quantum generators and identifying the presence of chaotic dynamics in this time (frequency) series. Here we review the elements of advanced techniques of using the non-linear analysis methods to dynamics, such as the wavelet analysis, multi-fractal formalism, mutual information approach, correlation integral analysis, false nearest neighbour algorithm, Lyapunov exponent's analysis, and surrogate data method.

Key words: vibrational systems, quantum generators, non-linear analysis techniques.

УДК 539.124:541.47

Н. Г. Сербов, В. М. Кузаконь, О. Ю. Хецелиус, Г. П. Препелица, Е. П. Соляникова

НЕЛИНЕЙНЫЕ МЕТОДЫ АНАЛИЗА ВРЕМЕННЫХ РЯДОВ СИГНАЛОВ В МОДЕЛИРОВАНИИ ВЗАИМОДЕЙСТВИЙ В НЕЛИНЕЙНЫХ КОЛЕБАТЕЛЬНЫХ СИСТЕМАХ ТИПА КВАНТОВЫХ ГЕНЕРАТОРОВ

Резюме

Актуальная проблема современной квантовой электроники связана с изучением динамики связанных квантовых генераторов и идентификацией хаоса в соответствующих временных рядах. В статье изложены элементы усовершенствованной техники использования нелинейных методов анализа динамики систем таких как вейвлет анализ мультифрактальный формализм, методика взаимной информации, метод корреляционных интегралов, алгоритм «ложных ближайших соседей», анализ на основе экспонент Ляпунова, метод суррогатных данных.

Ключевые слова: колебательные системы, квантовые генераторы, нелинейные методы анализа.

УДК 539.124:541.47

М. Г. Сербов, В. М. Кузаконь, О. Ю. Хецелиус, Г. П. Препелица, О. П. Солянікова

НЕЛІНІЙНІ МЕТОДИ АНАЛІЗУ ЧАСОВИХ РЯДІВ СИГНАЛІВ У МОДЕЛЮВАННІ ВЗАЄМОДІЙ У НЕЛІНІЙНИХ КОЛИВАЛЬНИХ СИСТЕМАХ ТИПУ КВАНТОВИХ ГЕНЕРАТОРІВ

Резюме

Актуальна проблема сучасної квантової електроніки пов'язана з вивченням динаміки зв'язаних квантових генераторів та ідентифікацією хаосу у відповідних часових рядах. У статті викладені елементи удосконаленої техніки використання нелінійних методів аналізу динаміки систем таких як вейвлет аналіз, мульти-фрактальний формалізм, методика взаємної інформації, метод кореляційних інтегралів, алгоритм «хибних найближчих сусідів», аналіз на підставі експонент Ляпунова, метод сурогатних даних.

Ключові слова: коливальні системи, квантові генератори, нелінійні методи аналізу.

SENSING ELECTROMAGNETIC AND STRONG INTERACTIONS EFFECTS IN SPECTROSCOPY OF KAONIC ATOMS

The theoretical studying the transition energies widths from X-ray spectroscopy of kaonic atoms is fulfilled. Sensing the electromagnetic and strong interaction effects and theoretical estimating spectra of kaonic atomic systems can be considered as a new tool for studying nuclear structure.

1. INTRODUCTION

Studying the exotic hadronic atomic systems such as kaonic atoms is of a great as theoretical as practical interest for further development of atomic and nuclear theories as well as new tools for sensing the nuclear structure and fundamental kaon-nucleus strong interactions. Besides, studying these systems is very important for further check of the Standard model [1–16]. In the last few years transition energies in the kaonic atoms [1–7] have been measured with an unprecedented precision. The spectroscopy of kaonic hydrogen allows to study the strong interaction at low energies by measuring the energy and natural width of the ground level with a precision of few meV [6, 7]. Besides, light kaonic atoms can additionally be used to find new low-energy X-ray standards and to evaluate the kaon (pion) mass using high accuracy X-ray spectroscopy. The collaborators of the E570 experiment [6, 7] measured X-ray energy of a kaonic helium atom, which is an atom consisting of a kaon (a negatively charged heavy particle) and a helium nucleus. Batty et al [5] had performed theoretical and experimental studying the strong-interaction effects in spectra of high Z kaonic atoms. These authors had presented the naive phenomenological optical model estimates. Now new exciting experiments are been preparing in order to make sensing the strong interaction effects in other hadronic atoms. Studying the low-energy kaon-nuclear strong interaction with strangeness have been performed by measurements of the kaonic atom X-rays with atomic numbers $Z = 1–92$ [1]. It is known that the shifts and widths due to the strong interaction can be systematically understood using phenomenological optical potential models. Nevertheless, one could mention a large discrepancy between the theories and experiments on the kaonic helium 2p state. A large repulsive shift (about -40 eV) has been measured by three experimental groups in the 1970's and 80's, while a very small shift (< 1 eV) was obtained by the optical models calculated from the kaonic atom

X-ray data with $Z > 2$ [1–6]. This significant disagreement (a difference of over 5 standard deviations) between the experimental results and the theoretical calculations is known as the “kaonic helium puzzle”. A possible large shift has been predicted using the model assuming the existence of the deeply bound kaonic nuclear states. However, even using this model, the large shift of 40 eV measured in the experiments cannot be explained. A re-measurement of the shift of the kaonic helium X-rays is one of the top priorities in the experimental research activities. In the theory of the kaonic and pionic atoms there is an important task, connected with a direct calculation of the X-ray transition energies within consistent relativistic quantum mechanical atomic and nuclear theory methods. The standard way is based on solution of the Klein—Gordon equation, but there are many important problems connected with accurate accounting for as kaon-nuclear strong interaction effects as QED radiative corrections (firstly, the vacuum polarization effect etc.) [11, 12]. This topic has been a subject of intensive theoretical and experimental interest (see [1, 3]). In the present paper an effective ab initio approach to quantum Klein—Gordon equation calculation of X-ray spectra for multi-electron kaonic atoms with an account of the nuclear, radiative effects [13–16] is used and the theoretical studying the X-ray electromagnetic transitions energies in the kaonic atoms is performed.

2. THE KLEIN—GORDON EQUATION APPROACH IN THE KAONIC ATOMS THEORY

Let us describe the key moments of our new approach to quantum calculation of the spectra for multi-electron kaonic atoms with an account of nuclear and radiative effects (more details applying to the multi-electron heavy atoms can be found in refs. [13–16]). It is well known that the relativistic dynamic of a spinless particle can be described by the Klein—Gordon

equation. The electromagnetic interaction between a negatively charged spin-0 particle with a charge equal to $q = -e$ and the nucleus can be taken into account introducing the nuclear potential A_v in the KG equation via the minimal coupling $p_v \rightarrow p_v - qA_v$. The wave functions of the zeroth approximation for kaonic atoms are found from the Klein—Gordon equation:

$$m^2 c^2 \Psi(x) = \left\{ \frac{1}{c^2} [i\hbar \partial_t + eV_0(r)]^2 + \hbar^2 \nabla^2 \right\} \Psi(x), \quad (1)$$

where \hbar is the Planck constant, c the velocity of the light and the scalar wavefunction $\Psi_0(x)$ depends on the space-time coordinate $x = (ct, r)$. Here it is considered a case of a central Coulomb potential ($V_0(r), 0$). A usually, We consider here the stationary solution of Eq. (1). In this case, we can write:

$$\Psi(x) = \exp(-iEt/\hbar) \varphi(x) \quad (2)$$

and Eq. (1) becomes:

$$\left\{ \frac{1}{c^2} [E + eV_0(r)]^2 + \hbar^2 \nabla^2 - m^2 c^2 \right\} \varphi(x) = 0, \quad (3)$$

where E is the total energy of the system (sum of the mass energy mc^2 and binding energy ϵ_0). In principle, the central potential V_0 should include the central Coulomb potential, the vacuum-polarization potential as well as the kaon-nucleus strong interaction potential (optical model potential). Earlier we have calculated some characteristics of hydrogen-like and other multi-electron ions with using the nuclear charge distribution in the form of a uniformly charged sphere and Gaussian form (c. f. [10, 12]). The advantage of the Gaussian form nuclear charge distribution is provided by using the smooth function instead of the discontinuous one as in the model of a uniformly charged sphere [16]. It is obvious that it simplifies the calculation procedure and permits to perform a flexible simulation of the real distribution of the charge in a nucleus. In last years to define the nuclear potential it is usually used the Fermi model for the charge distribution in the nucleus $\rho(r)$ (c. f. [12]):

$$\rho(r) = \rho_0 / \{1 + \exp[(r - c)/a]\}, \quad (4)$$

where the parameter $a = 0.523$ fm, the parameter c is chosen by such a way that it is true the following condition for average-squared radius: $\langle r^2 \rangle^{1/2} = (0.836 \cdot A^{1/3} + 0.5700)$ fm. Further let us present the formulas for the finite size nuclear potential and its derivatives on the nuclear radius. If the point-like nucleus has the central potential $W(R)$, then a transition to the finite size nuclear potential is realized by exchanging $W(r)$ by the potential [12]:

$$W(r|R) = W(r) \int_0^r dr' r'^2 \rho(r') + \int_r^\infty dr' r'^2 W(r') \rho(r'). \quad (5)$$

We assume it as some zeroth approximation. Further the derivatives of various characteristics on R are calculated. They describe the interaction of the nucleus with outer electron; this permits recalculation of results, when R varies within reasonable limits. The Coulomb potential for the spherically symmetric density $\rho(r|R)$ is:

$$V_{\text{nuc}}(r|R) = -((1/r)) \int_0^r dr' r'^2 \rho(r') + \int_r^\infty dr' r' \rho(r'). \quad (6)$$

It is determined by the following system of differential equations [19]:

$$\begin{aligned} V'_{\text{nuc}}(r, R) &= (1/r^2) \int_0^r dr' r'^2 \rho(r', R) \equiv (1/r^2) y(r, R), \\ y'(r, R) &= r^2 \rho(r, R), \\ \rho'(r) &= (\rho_0/a) \exp[(r - c)/a] \{1 + \exp[(r - c)/a]\}^2 \end{aligned} \quad (7)$$

with the boundary conditions:

$$\begin{aligned} V_{\text{nuc}}(0, R) &= -4/(\pi r), \quad y(0, R) = 0, \\ \rho(0) &= \rho_0 / \{1 + \exp[-c/a]\}. \end{aligned} \quad (8)$$

The new important topic is connected with a correct accounting the radiation QED corrections and, first of all, the vacuum polarization correction. Procedure for an account of the radiative QED corrections in a theory of the multi-electron atoms is given in detail in refs. [11, 12]. Regarding the vacuum polarization effect let us note that this effect is usually taken into account in the first PT order by means of the Uehling potential:

$$\begin{aligned} U(r) &= -\frac{2\alpha}{3\pi r} \int_1^\infty dt \exp(-2rt/\alpha Z) (1 + 1/2t^2) \frac{\sqrt{t^2 - 1}}{t^2} \equiv \\ &\equiv -\frac{2\alpha}{3\pi r} C(g), \end{aligned} \quad (9)$$

where $g = \frac{r}{\alpha Z}$. In our calculation we usually use more exact approach [12]. The Uehling potential, determined as a quadrature (9), may be approximated with high precision by a simple analytical function. The use of new approximation of the Uehling potential [12] permits one to decrease the calculation errors for this term down to 0.5—1 %. Besides, using such a simple analytical function form for approximating the Uehling potential allows its easy inclusion into the general system of differential equations [12, 14, 15].

3. RESULTS AND CONCLUSIONS

In ref. [13—16] we have presented some results of calculation for a selection of kaonic atom transitions. The kaon mass was assumed to be 493.677 ± 0.013 MeV [1]. In table 1 we present the calculated electromagnetic (EM) X-ray energies of kaonic atoms for transitions between

Calculated electromagnetic (E_c) and measured (E_m) energies (keV) of the X-ray transitions in the KA: the Batty et al theory EM1,2 [5] with using simple cascade Fermi—Teller model (Leon—Seki code), data by Indelicato et al (theory EM3) [3, 4] and our data (theory EM4)

KA	Transition	E_c , our theory EM4	E_c , [5] theory EM1	E_c , [5] theory EM2	E_c , [3, 4] theory EM3	E_m , [1, 5]
Li	3—2	15.335	15.392	15.319	15.330	15.320 (24) 15.00 (30)
K	5—4	105.962	105.970	—	105.952	105.86 (28)
W	8—7	346.586	346.54	—	346.571	346.624 (25)
W	7—6	535.180	535.24	—	535.240	534.886 (92)
Pb	8—7	426.1748	426.15	426.201	426.180	426.221 (57)
U	8—7	538.520	538.72	538.013	537.44	538.315 (100)

circular levels. The transitions are identified by the initial (n_i) and final (n_f) quantum numbers. The calculated values of transition energies are compared with available measured (E_m) and other calculated (E_c) values [1–7].

In a case of the close agreement between theoretical and experimental data, the corresponding levels are less sensitive to strong nuclear interaction. In the opposite case one could point to a strong-interaction effect in the exception cited above. Then it is of a great importance to determine correctly the strong-interaction contribution. It requires determination of the proton and neutron densities [17, 18]. In ref. [13] it has been shown that our theory allows to reproduce quite correctly the measured strong interaction parameters. To understand further information on the low-energy kaon-nuclear interaction, new experiments to determine the shift and width of kaonic atoms are now in preparation in J-Parc and in LNF, respectively (look, for example, refs. [1, 8]).

REFERENCES

1. Deloff A., Fundamentals in Hadronic Atom Theory, Singapore: World Scientific, 2003. — 352 P.
2. Hayano R. S., Hori M., Horvath D., Widman E., Antiprotonic helium and CPT invariance // Rep. Prog. Phys. — 2007. — Vol. 70. — P. 1995–2065.
3. Deslattes R., Kessler E., Indelicato P., de Billy L., Lindroth E., Anton J., Exotic atoms // Rev. Mod. Phys. — 2003. — Vol. 75. — P. 35–70.
4. Santos J. P., Parente F., Boucard S., Indelicato P., Desclaux J. P., X-ray energies of circular transitions and electron scattering in kaonic atoms // Phys. Rev. A. — 2005. — Vol. 71. — P. 032501.
5. Batty C. J., Eckhause M., Gall K. P., et al. Strong interaction effects in high Z-K⁻ atoms // Phys. Rev. C. — 1999. — Vol. 40. — P. 2154–2160.
6. Ito T. M., Hayano R. S., Nakamura S. N., Terada T. P., Observation of kaonic hydrogen atom x rays // Phys. Rev. C. — 1999. — Vol. 58. — P. 2366–2382.
7. Ishiwatari T. on behalf of the SIDDHARTA Collaboration, Silicon drift detectors for the kaonic atom X-ray measurements in the SIDDHARTA experiment // Nucl. Instr. and Methods in Physics. Research Sec. A. Accelerators, Spectrometers, Detectors and Associated Equipment. — 2007. — Vol. 581, N 1–2. — P. 326–329.
8. Okada S., Beer G., Bhang H., et al, Precision measurement of the $3d \rightarrow 2p$ x-ray energy in kaonic ^4He // Phys. Lett. B. — 2007. — Vol. 653, N 5-6. — P. 387–391.
9. Glushkov A. V., Makarov I. T., Nikiforova E. S., Pravdin M. I., Sleptsov I. Ye., Muon component of EAS with energies above 10^{17} eV // Astropart. Phys. — 1995. — Vol. 4. — P. 15–22.
10. Glushkov A. V., Malinovskaya S. V., Dubrovskaya Yu. V., Vitavetskaya L. A., Quantum calculation of cooperative muon-nuclear processes: discharge of metastable nuclei during negative muon capture // Recent Advances in Theory of Phys. and Chem. Systems (Springer). — 2006. — Vol. 15. — P. 301–318.
11. Grant I., Relativistic Quantum Theory of Atoms and Molecules Theory and Computation, Springer Series on Atomic, Optical, and Plasma Physics. 2007. — Vol. 40. — P. 670 P.
12. Glushkov A. V., Relativistic quantum theory. Quantum mechanics of atomic systems, Odessa: Astroprint, 2008. — 900 P.
13. Sukharev D. E., Khetselius O. Yu., Dubrovskaya Yu. V., Sensing strong interaction effects in spectroscopy of hadronic atoms // Sensor Electr. & Microsyst. Techn. — 2009. — N 3. — P. 16–21.
14. Glushkov A. V., Khetselius O. Yu., Gurnitskaya E. P., Loboda A. V., Sukharev D. E., Relativistic Quantum Chemistry of Heavy Ions and Hadronic Atomic Systems: Spectra and Energy Shifts // Theory and Applications of Computational Chemistry (AIP). — 2009. — Vol. 1. — P. 131–134.
15. Glushkov A. V., Malinovskaya S. V., Khetselius O. Yu., Loboda A. V., Sukharev D. E., Lovett L., The Green's functions method in quantum chemistry: New numerical algorithm for Dirac equation with complex energy and Fermi-model nuclear potential // Internat. Journal of Quantum Chemistry (USA). — 2009. — Vol. 109. — P. 1717–1727.
16. Turin A. V., Khetselius O. Yu., Sukharev D. E., Florko T. A., Estimating of X-ray spectra for kaonic atoms as tool for sensing the nuclear structure // Sensor Electr. and Microsyst. Techn. — 2009. — N 1. — P. 30–35.
17. Serot B. D., Walecka J. D., Advances in Nuclear Physics Vol. 16: The Relativistic Nuclear Many Body Problem. Plenum Press, New York, 1999.
18. Glushkov A. V., Rusov V. D., Ambrosov S. V., Loboda A. V., Resonance states of compound super-heavy nucleus and EPPP in heavy nucleus collisions // New Projects and New Lines of research in Nuclear physics. Eds. Fazio G. and Hanappe F.: Singapore, World Sci. — 2003. — P. 142–154.

UDC 539.132

D. E. Sukharev

SENSING ELECTROMAGNETIC AND STRONG INTERACTIONS EFFECTS IN SPECTROSCOPY OF KAONIC ATOMS

Abstract

The theoretical studying the transition energies from X-ray spectroscopy of kaonic atoms is fulfilled. Sensing the electromagnetic and strong interaction effects and theoretical estimating spectra of kaonic atomic systems can be considered as a new tool for studying nuclear structure.

Keywords: electromagnetic and strong interaction effects, spectroscopy, kaonic atoms.

УДК 539.132

Д. Е. Сухарев

ДЕТЕКТИРОВАНИЕ ЭФФЕКТОВ ЭЛЕКТРОМАГНИТНОГО И СИЛЬНОГО ВЗАИМОДЕЙСТВИЯ В СПЕКТРОСКОПИИ КАОННЫХ АТОМОВ

Резюме

Выполнено теоретическое изучение энергий переходов в спектрах каонных атомов в рамках рентгеновской спектроскопии каонных систем. Детектирование эффектов электромагнитного и сильного взаимодействия и оценка спектров каонных атомов являются одним из новых подходов к изучению структуры ядер.

Ключевые слова: эффекты электромагнитного и сильного взаимодействия, спектроскопия, каонные атомы.

УДК 539.132

Д. Є. Сухарев

ДЕТЕКТУВАННЯ ЕФЕКТІВ ЕЛЕКТРОМАГНІТНОЇ ТА СИЛЬНОЇ ВЗАЄМОДІЇ У СПЕКТРОСКОПІЇ АДРОННИХ АТОМІВ

Резюме

Виконано теоретичне вивчення енергій переходів у спектрах каонних атомів у межах рентгенівської спектроскопії каонних систем. Детектування ефектів електромагнітної та сильної взаємодії і оцінка спектрів каонних атомів є одним з нових підходів до вивчення структури ядер.

Ключові слова: ефекти електромагнітної та сильної взаємодії, спектроскопія, каонні атоми.

QUANTUM-CHEMICAL SIMULATION OF THE OXIDATION PROCESS OF ETHYLENE GLYCOL TO GLYOXAL AT PRESENCE OF COPPER NANOCATALYSTS

Within the methods of electron density functional and *ab initio* pseudopotential we have obtained the distributions of the density of valence electrons and the electron energy spectra for Cu nanocatalysts with the adsorbed on him molecule of ethylene glycol with the participation of the adsorbed in different position oxygen atoms. Position of the ethylene glycol molecule on the top atom of cube fragment of the catalyst has the least energy.

INTRODUCTION AND STATEMENT OF THE PROBLEM

Among various nanostructure materials, metallic nanostructures of the Cu group have received great interest primarily due to their unique properties and possible applications in catalysis, photonics, electronics, information storage [1–5]. Nanocatalysts are interesting objects of fundamental researches in catalysis. Comprehensive study of the structure of catalytically active materials, chemisorptions phenomena, kinetics and mechanisms of catalytic processes are necessary components of optimization of catalysts. The catalysis act starts with the binding of reagents (substratum), then with they are occurred a row of the change and, finally, a product appears. Herewith, a catalyst organizes the process, alters the potential energy of components, and moves atoms. Nevertheless, as an inorganic catalyst works, as it attacks the substratum, as it moves electrons, these facts remain not understood. Researches of the catalyst activity are carried out by using a simplified model experiments (for instance, such experiments present consequent transition from faces of single crystal to different surface defects and, finally, to the appropriate additives). In the case of physical adsorption with its relatively small interaction energies and, hence, a small violation of the molecular structure of adsorbent, the efficiency of the catalyst, obviously, mainly depends on the joint transfer of reagents to the surface, on which a weak transformation of molecular structure can be. Similar mechanisms probably are bases of the biological reactions when enzyme and substratum in the adsorbed state are in close proximity to each other (complementarities). In the case of chemisorptions that differs by strongly interaction molecules with a rigid surface of the catalyst, the situation is different. As follows from the results of mass spectrometry, the intermediates (intermediate compounds) of these reactions play an important role in the formation of

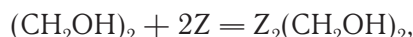
required products. Different crystallographic faces of catalyst have different catalyst reactivity, that of them in which the surface atoms weakly interact with substratum are most catalytically active. Studies show that the steps of the growing and the lattice defects, which leave on surface, have high catalytic activity by comparison with the atomic-smooth surface of the catalyst.

Significantly, that there is possibility to influence upon the nanocatalysts properties, improving their varied applications, by controlling their size, shape, compositeness and porosity. For example, the authors of the study [6] demonstrated a relationship between the catalytic activity of Au particles and their morphology, that is to say the particles with a more open structure and thin walls had a higher catalytic activity than Au nanoparticles with the continuous crystalline structure. The objects of their study were Au-based nanocages of 50 nm in edge length and 5nm in wall thickness as new catalysts for the reduction of p-nitrophenol by sodium borohydride (NaBH_4).

In a number of works in which were used various physic-chemical (e. g., [7]) and computing (e. g. [8, 9]) methods, the mechanisms of the interaction of the silver surface (and other catalysts of group of copper) with molecular and atomic oxygen (and other molecules as the participants processes) were studied. Understanding an essence of the processes, which occur at the interaction, is important since it allows predicting the behavior of systems with adsorbed atomic oxygen in the presence of other components of the process (gas phases molecules, active intermediate particles, etc.). It allows also getting information on the interaction energy of the participants of the adsorption process with the active centers on the catalyst surface and the structure of the arising intermediates and the transition states. One of the ways to study such interactions there are a theoretical quantum-chemical calculations that use the electron density functional theory and *ab initio* pseudopotential.

MODELS AND METHODS OF CALCULATION

Direct partial oxidation of ethylene glycol allows to get glyoxal which is a valuable product used in a number of organic syntheses, but this process in industry is not implemented due to lack of efficient catalytic systems [10]. Searching for of the active catalysts of glyoxal synthesis brings about nanoparticles which contains metals of copper subgroup [11] and which become the objects of our study. With provision for the experimental data on the composition of products, as well as based on representations about the mechanism of the synthesis process of glyoxal by means of the ethylene glycol oxidation on the catalysts of copper group [2–5], this mechanism can be described by the determined set of reactions. The first of them is:



Z marks the active center of the catalyst surface, $\text{Z}_2(\text{CH}_2\text{OH})_2$ marks the two-center adsorption of ethylene glycol.

Adsorption of the symmetrical oxygen-containing compounds with two carbon atoms (such as ethylene glycol) is accompanied destructive chemisorption and oxidation of adsorbed molecules on the mechanism of dehydrogenation. Accumulation of single-carbon adsorbate, which formed because of destruction of organic molecules on the C—C or C—O—C bonds, is observed in all studies on the collapse of the symmetrical oxygen-containing compounds with two carbon atoms. Copper is the perfect catalyst for dehydrogenation, which is the initial stage of oxidation of organic molecules, but for the oxidation of organic molecules to the outgoing products must also present at the surface of oxygen-containing particles (reactive oxygen species).

In this work, the catalytic influence of Cu nanostructures investigated in calculations from first principles. The results were obtained with the help of the authors' program code [12] which realizes the Car—Parrinello quantum-mechanical dynamics with the use of a local approximation in the formalism of the electron density functional and *ab initio* norm-conserving pseudopotential [13]. The ground state of electron-nucleus systems were determined by the algorithm of quantum dynamics if variables of electron and nuclear subsystems are simultaneously optimized or by means of the diagonalization of the Kohn—Sham matrix of a system if only electron variables are determined at fixed atomic cores. Following Kohn-Sham ideology the electron density recorded in terms of occupied orthonormalized one-particle wave functions:

$$n(\vec{r}) = \sum_i |\psi_i(\vec{r})|^2. \quad (1)$$

In the Born—Oppenheimer approximation, a point on the potential energy surface was deter-

mined by a minimum with respect to the wave functions of the energy functional:

$$E[\{\psi_i\}, \{\vec{R}_j\}, \{\alpha_v\}] = \sum_i \int_{\Omega} d^3r \psi_i^*(\vec{r}) \left[-\frac{\hbar^2}{2m} \nabla^2 \right] \psi_i(\vec{r}) + U[\{n(\vec{r})\}, \{\vec{R}_j\}, \{\alpha_v\}], \quad (2)$$

where $\{\vec{R}_j\}$ are the coordinates of cores and $\{\alpha_v\}$ stands for all possible external influences on the system.

In the commonly accepted approach, the minimization of an energy functional (2) with respect to one-particle orbitals $\psi_i(\vec{r})$ under additional conditions of orthonormalization imposed on $\psi_i(\vec{r})$ leads to the Kohn—Sham self-consistent one-particle equations:

$$\left\{ -\frac{\hbar^2}{2m} \nabla^2 + \frac{\delta U}{\delta n(\vec{r})} \right\} \psi_i(\vec{r}) = \epsilon_i \psi_i(\vec{r}). \quad (3)$$

We expand the one-particle wave function $\psi_i(\vec{r})$ in a series in plane wave. The series length was chosen to be such that about 20 plane waves correspond to one atom (the number of waves was limited by the power of a computer). The valence electron-core interaction has been modeled by *ab initio* norm-conserving pseudopotential. Artificial super lattice was created for use accounting advantage of inverse space. The atomic basis of the primitive tetragonal unit cell of the super lattice reflected features of the investigating system. In the case where only the electron variables were sought at fixed atomic cores, we calculated the Kohn—Sham matrix for equation (3) at a certain value of the wave vector \vec{k} from the Brillouin zone of the artificial super lattice. The matrix is composed from elements on the operators of the kinetic energy and the ion pseudopotential, which is screened dielectric function $\epsilon(\vec{G})$ in the Thomas-Fermi approximation. The diagonalization of the Kohn—Sham matrix allows us to obtain coefficients in the expansions of the wave function and the energy spectrum $E_i(\vec{k})$. The authors' computer programs dispose of the possibility of visualization of the electron density (1) in the manner of the space projection or the cross section. Furthermore, they have possibility for display of the electron density particulars in the neighborhood of any atom with any resolution

To reproduce a wall of copper nanocages from 5 and 7 atomic layers and surfaces (100) which is covered the adsorbed molecules of ethylene glycol in the presence of oxygen it was created the atomic basis of the primitive tetragonal cell of the artificial superlattice. The atomic basis comprised to 200 atoms. The parameters of the primitive cell were chosen such that in the directions X, Y and Z, the surfaces of the wall of copper nanocages simulated as free. In addition, the sizes of the primitive cell were chosen such that the translationally repeated atomic systems do not influence

on one another. The Cu (100) surface was not used reconstructed.

On results of our calculation were defined the ground state energy, the spectral characteristics of systems including cluster Cu and adsorbed molecules, the distribution of electron density, and the positions on the surface of the catalyst for the most best for ethylene glycol adsorption with the participation of the adsorbed in different position oxygen atoms.

THE RESULTS OF CALCULATIONS AND DISCUSSION

In Fig. 1 and Fig. 2 the spatial distribution of the density of valence electrons for fragments of the walls of the copper nanocages containing five (seven) atomic layers (62 or 172 atoms)

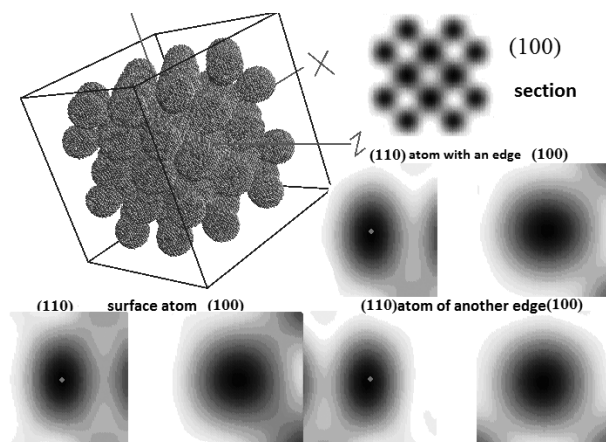


Fig. 1. The density distribution of valence electrons in the 62 atomic Cu fragment: spatial distribution of electron density for izo-value 0.7 of the maximum and the cross section in the (100) plane and (110) plane of spatial distribution of the whole fragment and in the vicinity of the surface atoms

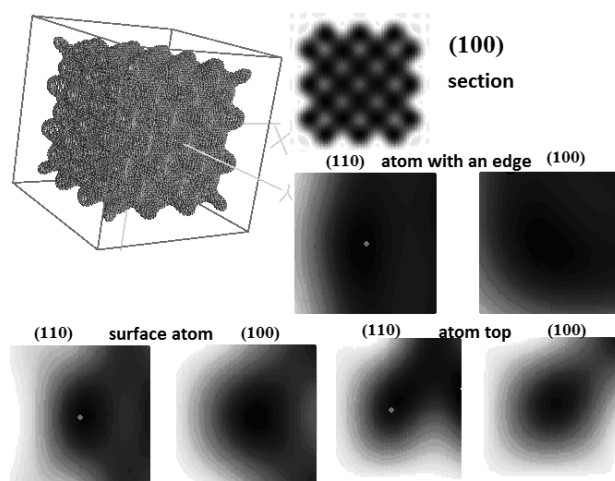


Fig. 2. The distribution of valence electron density of 172 atomic Cu fragment: the spatial distribution of electron density for izo-value 0.6—0.7 from the maximum and the cross-sections in the (100) plane and (110) plane of the spatial distribution of the whole fragment and in the vicinity of the surface atoms

presents. These fragments differ in surface layers, as follows, the 62-atom fragment contains no atom at the top, whereas the 172-atom fragment contains such atom, and that it has the most attenuated connection with the fragment.

To be able to determine what changes occur in current of the adsorption of ethylene glycol molecules on the catalyst the density distributions of valence electrons of isolated molecules were calculated (Fig. 3). It is seen that the bonds O—N, O—C are more crucial for the molecule than the bond C—C.

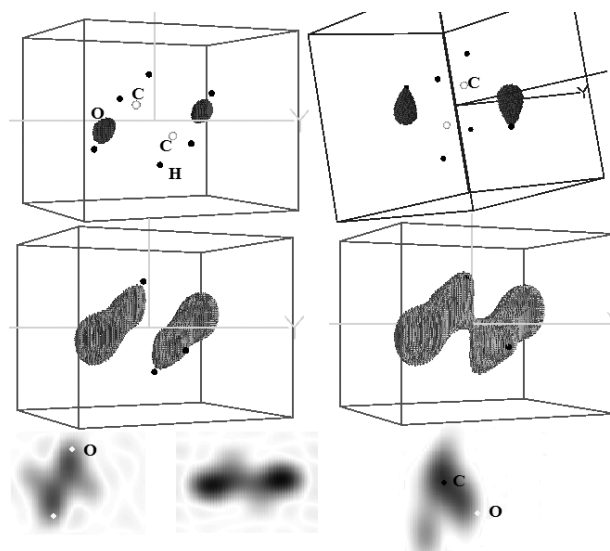


Fig. 3. The density distribution of valence electrons in the ethylene glycol molecule: spatial distribution of electron density for izo-value 0.9—1.0 from the maximum, for izo-value 0.7—0.8 from the maximum, for izo-value 0.6—0.7 from the maximum, for izo-value 0.5—0.6 from the maximum (left to right, from top to bottom) and the cross sections in the (100) plane and (110) plane of spatial distribution (lower row)

Following calculations were carried out for the nanocatalysts fragments with molecules in different positions and in the presence of the oxygen atoms on which was decomposed the oxygen molecule. So from Fig. 4 possible to get information on possible position of adsorbents to atoms of Cu nanoclusters and also research change in the electron density at adsorptions of the oxygen atoms by the catalysts surface. As follows, the formation of the general electron cloud is seen from Fig. 4.

On Fig. 4 they are shown adsorptions in the A positions and the B positions (determination of positions are realized on left part drawing). About the C positions, possible say that it on the electron distribution and energy is befitted to the B positions. As to the D positions that it is characterized more low energy then rest positions have an alike energies. From above said possible to draw a conclusion that adsorptions of the oxygen atoms in the A, B, C positions there is physical, but in the D positions there is chemical. Consequently, the oxygen atom in the D positions follows to consider be-

ing lost for the following interaction with the organic molecules.

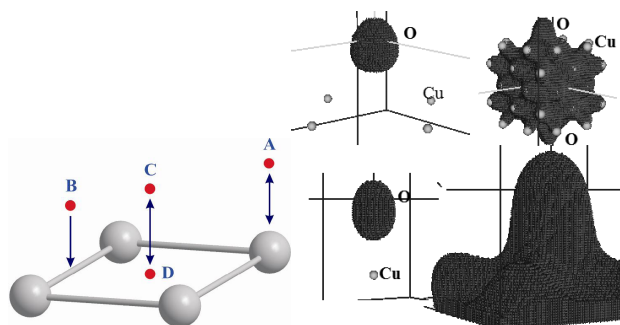


Fig. 4. Positions of the location of the molecules on catalyst surface: A — "top", B — "bridge", C — "hollow" on distances not less 1,4 Å, D — "in plane" (at location of the ethylene glycol molecule was defined position of its centre, more exactly centre of the C—C bound) (on the left); the spatial distribution of electron density for iso-value 0.9—1.0 from the maximum and for iso-value 0.7—0.8 in vicinity of the oxygen atom in the B position on the catalyst surface (on the right at the top) and the oxygen atom in the A position on the catalyst surface (on the right at the bottom)

Fig. 5 shows fragments of the density space partial distributions of valence electrons in the 5-monoatom layer catalyst with the ethylene glycol molecule that adsorbed in the C positions without presence the free oxygen. On Fig. 6 and Fig. 7 the ethylene glycol molecule is oriented comparatively atom of the catalyst in the A positions and comparatively edge of the Cu nanocage fragments accordingly. Comparing these results possible to draw a conclusion that location of the molecule by its centre on the between atomic emptiness (the C positions) and near edge of the Cu nanocage fragments more effectively destroys the C—C bound of molecule under its decomposition than under the location of the molecule in the A positions (on Cu atom). As can be seen from Fig. 6 in the last case on the line of the C—C bound is saved significant electron density.

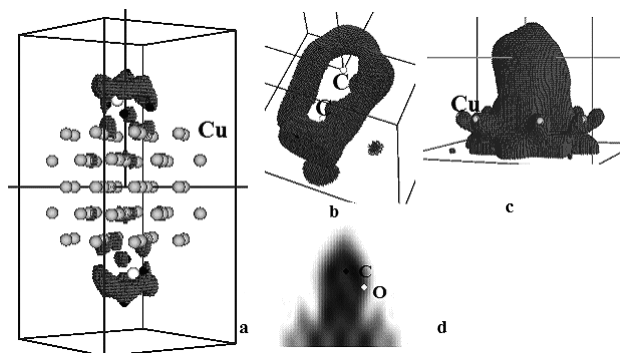


Fig. 5. The density distribution of valence electrons in 62 atomic Cu fragment with the ethylene glycol molecule on surface in the C position: a) spatial distribution of electron density for iso-value 0.9—1.0 from the maximum; b) look at molecule from above with the electron density for iso-value 0.9—1.0; c) look at molecule from the side with the electron density for iso-value 0.6—0.7; d) the cross section in the (110) plane of spatial distribution in the vicinity of the surface atoms

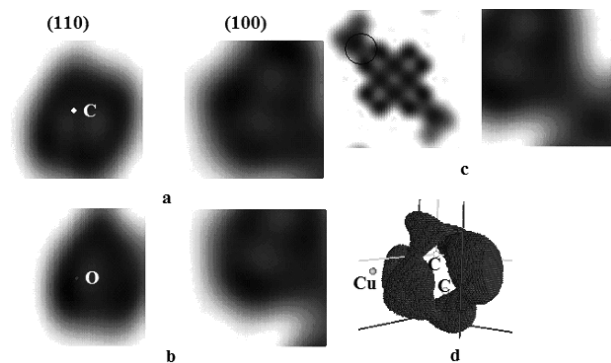


Fig. 7. The density distributions of valence electrons in 62 atomic Cu fragment with the ethylene glycol molecule near edge of the Cu fragment: a), b) the cross sections in the (110) plane and the (100) plane of spatial distribution in the vicinity of the C and O atoms of molecule; c) the cross sections in the (100) plane of spatial distribution of the whole atomic composition and in the vicinity of the C from edge (magnified scene of the area, which is marked around); d) look at molecule from above with the electron density for iso-value 0.9—1.0

On Fig. 8 and Fig. 9 the calculation results for atoms system consisting of catalysts with the ethylene glycol molecule that adsorbed in the C positions in presence the free oxygen that adsorbed in the A positions ("top") on distance 1,7 Å before centre of the molecule presents.

Oxygen adsorptions on the A positions ("top"), that which are considered on Fig. 8 and Fig. 9, are realized on miscellaneous Cu atoms between which is located a centre of the ethylene glycol molecule. Whereas, molecule is not flat and is oriented for catalysts surfaces under corner, that its atoms are found in different positions to atoms of catalysts surfaces, but signifies and to oxygen atom, which on them are located (adsorbed).

On Fig. 10—11 the calculation results for atoms system consisting of the 7-monoatom layer catalysts (the 172 Cu atom fragment of nanocage wall) with the ethylene glycol mol-

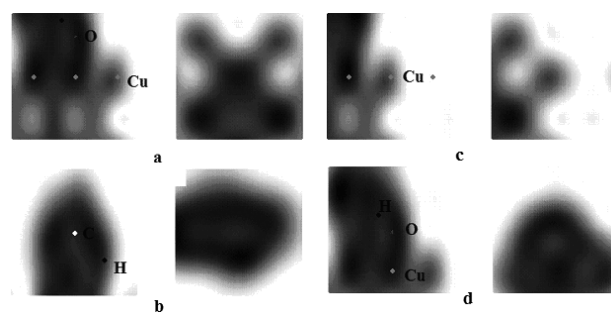


Fig. 8. The cross sections in the (110) plane and the (100) plane of spatial distribution in the 62 atomic Cu fragment with the ethylene glycol molecule in the C position and the oxygen atom in the A position which is found on distance 1,7 Å from molecule: a) in the vicinity of the Cu atom from the catalyst surface on which is located the free oxygen atom (radius of the area of the survey is 2,7 Å); b) in the vicinity of the C atom from the ethylene glycol molecule; c) in the vicinity of the Cu atom from the catalyst surface near which is located the ethylene glycol molecule; d) in the vicinity of the free oxygen atom (Cu atom from the catalyst surface and O atom, H atom of the ethylene glycol molecule get in area of the survey)

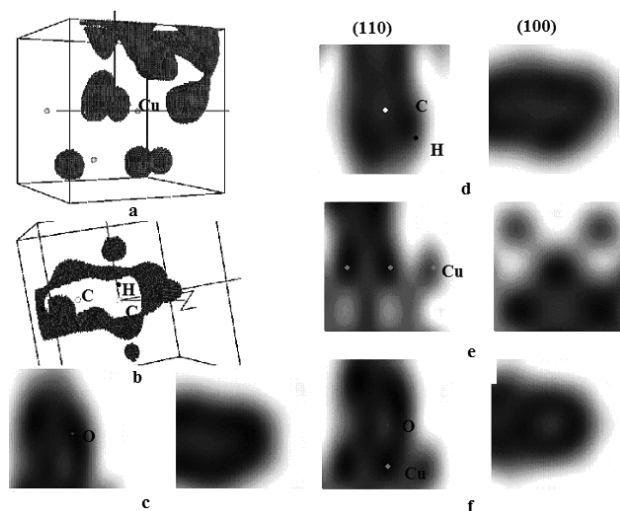


Fig. 9. The density distributions of valence electrons and its the cross sections distribution in the 62 atomic Cu fragment with the ethylene glycol molecule in the C position and the oxygen atom in the A position which is found on distance 1,7 Å from molecule: a), e) in the vicinity of the Cu atom from the catalyst surface (radius of the area of the survey is 2,7 Å); b), d) in the vicinity of the C atom from the ethylene glycol molecule; c) in the vicinity of the Cu atom from the catalyst surface near which is located the ethylene glycol molecule; c) in the vicinity of the O atom from the ethylene glycol molecule; f) in the vicinity of the free oxygen atom

ecule which differently for catalyst is oriented or near edge or on surface in the C position or near atom of the top of cube fragment of catalysts presents. Follows to note that above-described system contains completely 192 atoms

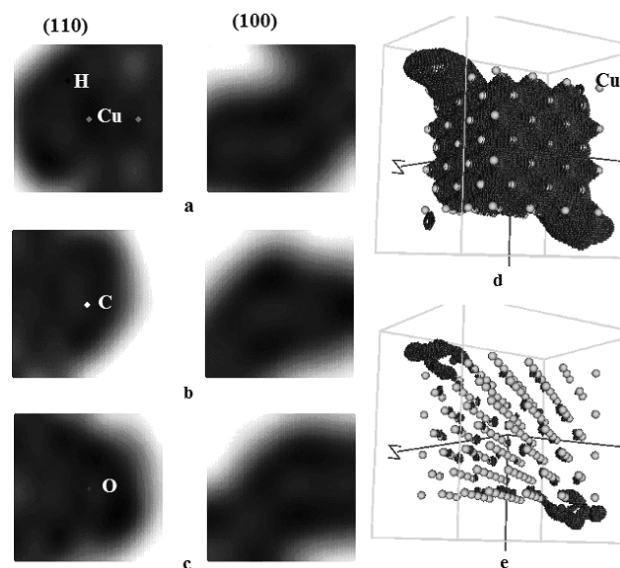


Fig. 10. The density distributions of valence electrons and its the cross sections distribution in the 172 atomic Cu fragment with the ethylene glycol molecule near edge of the catalyst fragment: a) in the vicinity of the Cu atom from the catalyst edge (radius of the area of the survey is 2,7 Å); b) in the vicinity of the C atom from the ethylene glycol molecule; c) in the vicinity of the O atom from the ethylene glycol molecule; d), e) the spatial distribution of electron density of whole atomic composition for isovalue 0.7–0.8 from the maximum and 0.9–1.0, accordingly

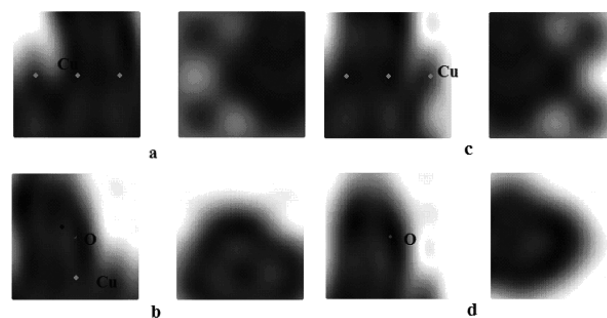


Fig. 11. The cross sections in the (110) plane and the (100) plane of spatial distribution in the 172 atomic Cu fragment with the ethylene glycol molecule in the C position and the oxygen atom in the A position which is found on distance 1,7 Å from molecule: a), c) in the vicinity of the Cu atoms from the catalyst surface on which is located the ethylene glycol molecule (radius of the area of the survey is 2,7 Å); b) in the vicinity of the free oxygen atom d) in the vicinity of the O atom from the ethylene glycol molecule

and 1892 electrons, but this vastly enlarges arrays data and amount accounting operation. Therefore, under limited power of the computing machinery, which was in our use, we happened to reduce the amount of the plane waves in decomposition of the wave function of the system that has influenced upon separate ability of the maps to density of the electronic charge and has done the complex comparison results. The comparison to full energy last variant, for massive fragment of the catalyst allows to select the position of the molecule on top atom of fragment as the least energy as to smaller fragment for size, that such characteristic has a position of the molecule near edge.

CONCLUSIONS

Within the methods of electron density functional and pseudopotential with *ab initio* we have obtained the distributions of the density of valence electrons and the electron energy spectra for Cu nanocatalysts with the adsorbed on him molecule of ethylene glycol with the participation of the adsorbed in different position oxygen atoms.

Adsorptions of the oxygen atoms in the different positions on Cu nanocatalysts can be physical or chemical.

Location of the organic molecule by its centre on the between atomic emptiness of surface of Cu nanocatalysts and near edge of the Cu nanocage fragments more effectively destroys the C-C bound of organic (ethylene glycol) molecule under its decomposition than under the location of the molecule on Cu atom of surface of nanocatalyst.

Position of the ethylene glycol molecule on the top atom of massive fragment of the catalyst has the least energy in contrast with smaller fragment for size, also such characteristic has a position of the molecule near edge of cube fragment.

REFERENCES

1. Ghosh S. K., Pal T. Structure/Function Relationships of [NiFe]- and [FeFe]-Hydrogenases // *Chemical Rev.* — 2007. — 107. — P. 4273—4303.
2. Lee J. S., Ulmann P. A., Han M. S., Mirkin C. A. A DNA-gold nanoparticle-based colorimetric competition assay for the detection of cysteine // *Nano Lett.* — 2008. — 8(2). — P. 529—533.
3. Hirsch L. R., Stafford R. J., Bankson J. A., Sershen S. R., Rivera B., Price R. E., Hazle J. D., Halas N. J., West J. L. Nanoshell-mediated near-infrared thermal therapy of tumors under magnetic resonance guidance // *Proc. Natl. Acad. Sci. U. S. A.* — 2003. — 100. — P. 54—62.
4. Murphy C. J., Gole A. M., Hunyadi S. C., Orendorff C. J. Colloidal One-Dimensional Gold and Silver Nanostructures // *Inorg. Chem.* — 2006. — 45. — P. 7544—7554.
5. Zeng J., Huang J., Lu W., Wang X., Wang B., Zhang S. J. A new method for probing spin-flip scattering in ballistic nanosystems // *Physics (in Chinese)*. — 2007. — 36. — P. 199—205.
6. Jie Zeng, Qiang Zhang, Jingyi Chen, Younan Xia. A Comparison Study of the Catalytic Properties of Au-Based Nanocages, Nanoboxes, and Nanoparticles // *Nano Lett.* — 2010. — 10. — P. 30—35.
7. Greeley J., Mavrikakis M. J. On the role of subsurface oxygen and ethylenedioxy in ethylene epoxidation on silver // *Phys. Chem.* — 2007. — 111. — P. 7992—8017.
8. Qin C., Whitten J. L. Adsorption of O, H, OH and H₂O on Ag(100) // *Phys. Chem. B.* — 2005. — 109. — P. 8852—8856.
9. Салаев М. А., Полещук О. Х., Курина Л. Н. Теоретический анализ адсорбции молекулярного кислорода на кластере серебра Ag₄ // *Бутлеровские сообщения.* — 2010. — 21. — № 7. — С. 34—41.
10. Магаева А. А., Шмотин В. С., Водянкина О. В., Князев А. С., Саланов А. Н., Чесалов Ю. А., Одегова Г. В., Курина Л. Н. // *Журн. физ. химии.* — 2006. — 80. — № 5. — С. 818—902.
11. Magaev O. V., Knyazev A. S., Vodyankina O. V., Dorofeeva N. V., Salanov A. N., Boronin A. E. Active surface formation and catalytic activity of phosphorous-promoted electrolytic silver in the selective oxidation of ethylene glycol to glyoxal // *Applied Catalysis A: General.* — 2008. — 344. — P. 142—149.
12. Балабай Р. М. Обчислювальні методи із перших принципів у фізиці твердого тіла: квантово-механічна молекулярна динаміка. — *Кривий Ріг: Видавничий дім*, 2009. — С. 123.
13. Bachelet G. B., Hamann D. R., Schluter M. Pseudopotentials that work: from H to Pu // *Phys. Rev. B — Solid State.* — 1982. — 26(8). — P. 4199—4228.

UDC 539.142; 539.184

R. M. Balabai, E. N. Chernikova

QUANTUM-CHEMICAL SIMULATION OF THE OXIDATION PROCESS OF ETHYLENE GLYCOL TO GLYOXAL AT PRESENCE OF COPPER NANOCATALYSTS

Abstract

Within the methods of electron density functional and *ab initio* pseudopotential we have obtained the distributions of the density of valence electrons and the electron energy spectra for Cu nanocatalysts with the adsorbed on him molecule of ethylene glycol with the participation of the adsorbed in different position oxygen atoms. Position of the ethylene glycol molecule on the top atom of cube fragment of the catalyst has the least energy.

Key words: the *ab initio* pseudopotential, the electron density functional, the valence electron density, nanocatalysts, copper, adsorption, the ethylene glycol molecule, the oxygen atom.

УДК 539.142; 539.184

Р. М. Балабай, О. М. Чернікова

КВАНТОВО-ХИМИЧЕСКОЕ МОДЕЛИРОВАНИЕ ПРОЦЕССОВ ОКИСЛЕНИЯ ЭТИЛЕНГЛИКОЛЯ В ГЛИОКСАЛЬ НА НАНОКАТАЛИЗАТОРАХ ГРУППЫ МЕДИ

Резюме

Методами функционала электронной плотности и псевдопотенциала из первых принципов получены распределения плотности валентных электронов и энергетические спектры электронов для нанокатализаторов Си с адсорбированными молекулами этиленгликоля и кислорода в различных позициях на поверхности катализатора. Определено, что ориентация молекулы этиленгликоля у вершины кубического фрагмента катализатора имеет наименьшую энергию.

Ключевые слова: Псевдопотенциал из первых принципов, функционал электронной плотности, плотность валентных электронов, нанокатализатор, медь, адсорбция, молекула этиленгликоля, атом кислорода.

УДК 539.142; 539.184

Р. М. Балабай, О. М. Чернікова

КВАНТОВО-ХІМІЧНЕ МОДЕЛЮВАННЯ ПРОЦЕСІВ ОКИСЛЕННЯ ЕТИЛЕНГЛІКОЛЮ У ГЛІОКСАЛЬ НА НАНОКАТАЛІЗАТОРАХ ГРУПИ МІДІ

Резюме

Методами функціоналу електронної густини та псевдопотенціалу із перших принципів отримані розподіли густини валентних електронів і їх енергетичні спектри для нанокаталізаторів Си із адсорбованими молекулами етиленгліколю та атомів кисню у різних позиціях на поверхні каталізатору. Визначено, що орієнтація молекули етиленгліколю біля вершини кубічного фрагменту каталізатора має найменшу енергію.

Ключові слова: псевдопотенціал із перших принципів, функціонал електронної густини, густини валентних електронів, нанокаталізатори, мідь, адсорбція, молекула етиленгліколю, атом кисню.

INFORMATION FOR CONTRIBUTORS OF "PHOTOELECTRONICS" ARTICLES

"Photoelectronics" Articles publishes the papers which contain the results of scientific research and technical designing in the following areas:

- Physics of semiconductors, hetero- and low-dimensional structures;
- Physics of microelectronic devices;
- Quantum optics and spectroscopy of nuclei, atoms, molecules and solids;
- Optoelectronics, quantum electronics and sensorics;
- Photophysics of nucleus, atoms and molecules;
- Interaction of intense laser radiation with nuclei, atomic systems, substance.

"Photoelectronics" Articles is defined by the decision of the Highest Certifying Commission as the specialized edition for physical-mathematical and technical sciences and published and printed at the expense of budget items of Odessa I. I. Mechnikov National University.

"Photoelectronics" Articles is published in English. Authors send two copies of papers in English. The texts are accompanied by 3.5" diskette with text file, tables and figures. Electronic copy of a material can be sent by e-mail to the Editorial Board and should meet the following requirements:

1. The following formats are applicable for texts — MS Word (rtf, doc).
2. Figures should be made in formats — EPS, TIFF, BMP, PCX, JPG, GIF, WMF, MS Word I MS Gif, Micro Calc Origin (opj). Figures made by packets of mathematical and statistic processing should be converted into the foregoing graphic formats.

The papers should be sent to the address:

Kutalova M. I., Physical Faculty of Odessa I. I. Mechnikov National University, 42 Pastera str, 65026 Odessa, Ukraine, e-mail: wadz@mail.ru, tel. +38-0482-7266356.

Information is on the site:

<http://www.photoelectronics.onu.edu.ua>

The title page should contain:

1. Codes of PACS.
2. Surnames and initials of authors.
3. TITLE OF PAPER.
4. Name of institution, full postal address, number of telephone and fax, electronic address.

Equations are printed in MS Equation Editor.

References should be printed in double space and should be numbered in square brackets consecutively throughout the text. References for literature published in 1999—2011 years are preferential.

Illustrations will be scanned for digital reproduction. Only high-quality illustrations will be taken for publication. Legends and symbols should be printed inside. Neither negatives, nor slides will be taken for publication. All figures (illustrations) should be numbered in the sequence of their record in text.

An abstract of paper should be not more than 200 words. Before a text of summary a title of paper, surnames and initials of authors should be placed.

For additional information please contact with the Editorial Board.

ІНФОРМАЦІЯ ДЛЯ АВТОРІВ НАУЧНОГО ЗБОРНИКА «PHOTOELECTRONICS»

В збірникі «Photoelectronics» публікуються статті, які містять результати наукових досліджень і технічних розробок в наступних напрямках:

- Фізика напівпровідників, гетеро- і низкорозмірних структур;
- Фізика мікроелектронних пристроїв;
- Квантова оптика і спектроскопія ядер, атомів, молекул і твердих тел;
- Оптоелектроніка, квантова електроніка і сенсорика;
- Фотофізика ядра, атомів, молекул;
- Взаємодія інтенсивного лазерного випромінювання з ядрами, атомними системами, речовиною.

Збірник «Photoelectronics» видається на англійській мові. Рукопис подається автором в двох екземплярах на англійській і російській мовах. К рукопису додаються дискета з текстовим файлом і малюнками. Електронна копія матеріалу може бути надіслана в редакцію по електронній пошті.

Електронна копія статті повинна відповідати наступним вимогам:

1. Електронна копія (або дискета) матеріалу надсилається одночасно з твердою копією тексту і малюнків.
2. Для тексту допустимі наступні формати — MS Word (rtf, doc).
3. Малюнки приймаються в форматах — EPS, TIFF, BMP, PCX, JPG, GIF, CDR, WMF, MS Word I MS Gif, Micro Calc Origin (opj). Малюнки, виконані пакетами математическої і статистическої обробки повинні бути конвертовані в вищезазначені графіческіе формати.

Рукописи присилаються в адрес:

Отв. секр. Куталовой М. И., ул. Пастера, 42, физ. факультет ОНУ им. И. И. Мечникова, г. Одесса, 65026. E-mail: wadz@mail.ru, тел. (0482) 726-63-56.

Аннотации статей сб. «Photoelectronics» находятся на сайте: <http://photoelectronics.onu.edu.ua>

К рукопису прилагается

Титульная страница:

1. Коды PAC и УДК.
2. Фамилия и инициалы автора(ов).

3. Учреждение, полный почтовый адрес, номер телефона, номер факса, адреса электронной почты для каждого из авторов.

4. Название статьи

Текст должен печататься шрифтом 14 пунктов через два интервала на белой бумаге формата А4.

Уравнения необходимо печатать в редакторе формул MS Equation Editor. Необходимо давать определение величин, которые появляются в тексте впервые.

Таблицы подаются на отдельных страницах. Должны быть выполнены в соответствующих табличных редакторах или представленные в текстовом виде с использованием разделителей (точка, запятая, запятая с точкой, знак табуляции).

Ссылки на литературу должны печататься через два интервала, нумероваться в квадратных дужках последовательно в порядке их появления в тексте статьи. Ссылаться необходимо на литературу, которая издана позднее 2000 года. Для ссылок используются следующие форматы:

Книги. Автор(ы) (инициалы, потом фамилии), название книги курсивом, издательство, город и год издания. (При ссылке на главу книги, указывается название главы, название книги курсивом, номера страниц). *Журналы.* Автор(ы) (инициалы, потом фамилии), название статьи, название журнала (используются аббревиатуры только для известных журналов), год издания, номер выпуска, номер страниц. *Иллюстрации* будут сканироваться цифровым сканером. Принимаются в печать только высококачественные иллюстрации. Подписи и символы должны быть в печатании. Не принимаются в печать негативы, слайды, транспаранты.

Рисунки должны иметь соответствующий к формату журнала размер не больше 160×200 мм. Текст на рисунках должен выполняться шрифтом 12 пунктов. На графиках единицы измерения указываются через запятую. Все рисунки (иллюстрации) нумеруются и размещаются в тексте статьи.

Резюме объемом до 200 слов пишется на английском, русском языках и на украинском (для авторов из Украины). Перед текстом резюме соответствующим языком указываются УДК, фамилии и инициалы всех авторов, название статьи.

ІНФОРМАЦІЯ ДЛЯ АВТОРІВ НАУКОВОГО ЗБІРНИКА «PHOTOELECTRONICS»

У науковому збірнику «Photoelectronics» друкуються статті, які містять результати наукових досліджень та технічних розробок у таких напрямках:

- Фізика напівпровідників, гетеро- і низькорозмірні структури;
- Фізика мікроелектронних приладів;
- Квантова оптика і спектроскопія ядер, атомів, молекул та твердих тіл;
- Оптоелектроніка, квантова електроніка і сенсоріка;
- Фотофізика ядра, атомів, молекул;
- Взаємодія інтенсивного лазерного випромінювання з ядрами, атомними системами, речовиною.

Збірник «Photoelectronics» видається англійською мовою. Рукопис подається автором у двох примірниках англійською мовою. До рукопису додається дискета з текстовим файлом і малюнками. Електронна копія матеріалу може бути надіслана до редакції електронною поштою.

Електронна копія статті повинна відповідати наступним вимогам:

1. Електронна копія (або дискета) матеріалу надсилається одночасно з твердою копією тексту та малюнків.
2. Для тексту припустимі наступні формати — MS Word (rtf, doc).

3. Малюнки приймаються у форматах — EPS, TIFF, BMP, PCX, JPG, GIF, CDR, WMF, MS Word і MS Graf, Micro Calc Origin (orj). Малюнки, виконані пакетами математичної та статистичної обробки, повинні бути конвертовані у вищевказані графічні формати.

Рукописи надсилаються на адресу:

Відп. секр. Куталовій М. І., вул. Пастера, 42, фіз. факультет ОНУ ім. І. І. Мечникова, м. Одеса, 65026.
E-mail: wadz@mail.ru 6, тел. (0482) 726-63-56.

Всі довідки на нашому сайті:

<http://www.photoelectronics.onu.edu.ua>

До рукопису додається:

Титульна сторінка:

1. Коды РАС та УДК. Допускається використання декількох шифрів, що розділяються комою. У випадку, коли автором (авторами) не буде вказано жоден шифр, редакція збірника встановлює шифр статті за своїм вибором.

2. Прізвище (-а) та ініціали автора (-ів).

3. Установа, повна поштова адреса, номер телефону, номер факсу, адреса електронної пошти для кожного з авторів

4. Назва статті

Текст повинен друкуватися шрифтом 14 пунктів через два інтервали на білому папері формату А4. Назва статті, а також заголовки підрозділів друкуються прописними літерами і відзначаються напівжирним шрифтом.

Рівняння необхідно друкувати у редакторі формул MS Equation Editor. Необхідно давати визначення величин, що з'являються в тексті вперше.

Таблиці повинні бути виконані у відповідних табличних редакторах або представлені у текстовому вигляді з використанням роздільників (крапка, кома, кома з крапкою, знак табуляції).

Посилання на літературу повинні друкуватися через два інтервали, нумеруватись в квадратних дужках, послідовно у порядку їх появи в тексті статті. Необхідно посилатись на літературу, яка вийшла з друку пізніше 2000 року. Для посилань використовуються наступні формати:

Книги. Автор(и) (ініціали, потім прізвища), назва книги курсивом, видавництво, місто і рік видання. *Журнали.* Автор(и) (ініціали, потім прізвища), назва статті, назва журналу курсивом (використовуються аббревіатури тільки для відомих журналів), номер тому і випуску, номер сторінки і рік видання

Ілюстрації будуть скануватися цифровим сканером. Приймаються до друку тільки високоякісні ілюстрації. Підписи і символи повинні бути вдруковані. Не приймаються до друку негативи, слайди, транспаранти.

Рисунки повинні мати відповідний до формату журналу розмір не більше 160×200 мм. Текст на рисунках повинен виконуватись шрифтом 10 пунктів. На графіках одиниці виміру вказуються через кому. Усі рисунки (ілюстрації) нумеруються і розміщуються у тексті статті.

Резюме друкується англійською, російською і українською мовами (для авторів з України). Перед текстом резюме відповідною мовою вказуються УДК, прізвища та ініціали всіх авторів, та назва статті.

Наукове видання

ФОТО ЕЛЕКТРОНІКА

№ 20 — 2011

**МЕЖВІДОМЧИЙ
НАУКОВИЙ ЗБІРНИК**

Англійською мовою

Надруковано з готового оригінал-макета

Підп. до друку 05.12.2011. Формат 60×84/8. Папір офсетний. Гарнітура «Літературна». Друк офсетний. Ум. друк. арк. 15,81. Тираж 300 прим. Зам. № 871.

Видавництво і друкарня «Астропринт»
65091, м. Одеса, вул. Разумовська, 21
Тел.: (0482) 37-07-95, 37-14-25, 33-07-17, (048) 7-855-855
www.astroprint.odessa.ua

Свідоцтво суб'єкта видавничої справи
ДК № 1373 від 28.05.2003 р.